Theory and Measurement of Bistatic Scattering of X-band Microwaves from Rough Dielectric Surfaces

by

Roger Dean De Roo

A dissertation submitted in partial fulfillment
of the requirements for the degree of
Doctor of Philosophy
(Electrical Engineering)
in The University of Michigan
1996

Doctoral Committee:
Professor Fawwaz T. Ulaby, Chair
Professor Anthony W. England
Professor Linda P. Katehi
Assistant Professor Kamal Sarabandi
Professor John F. Vesecky

To my father and mother

ACKNOWLEDGEMENTS

I would like to thank my committee for their time and their help. In particular, I thank my advisor, Prof. Fawwaz Ulaby, for his enduring patience toward me and his (seemingly sometimes misplaced) faith in me. In addition, I would like to thank Prof. Chen-To Tai, who showed me so many wonderful things.

I also owe a great deal to those with whom I've toiled in the fields (sometimes literally): Dr. Leland Pierce, Dr. Michael Whitt, Dr. Kyle McDonald, Dr. Emilie van Deventer, Dr. Richard Austin, Dr. John Kendra, Dr. Adib Nashashibi, Dr. James Stiles, Dr. Yisok Oh, Prof. Yasuo Kuga, Craig Dobson, Paul Siqueira, Eric Li, Tsen-Chieh Chiu, Yanni Kouskoulas, Bryan Hauck, Neil Peplinski, Andrew Zambetti, Josef Kellndorfer, Kathleen Bergen, Sebastian Lauer, Martin Kuttner, Ron Oliver, and Mike Prozinski. My deepest apologies to those few whom I must have missed.

Credit belongs to Ralf Zaar for the photo in Figure 3.1 and thanks go to Mike McCurdy for providing me with this photo (and other things).

Special appreciation goes to three of my dearest friends: Jon English, for always being there, and to Dr. Valdis Liepa and Ron Hartikka, who provided me with an engineering education which could not be learned in a classroom.

TABLE OF CONTENTS

LIST OF TABLES

Table

LIST OF FIGURES

Figure

LIST OF APPENDICES

APPENDIX

CHAPTER 1

Introduction

1.1 Objectives

The backscattering of electromagnetic fields from random rough surfaces has many uses and has been experimentally investigated often in the past few decades. Experimental investigations into *bistatic* electromagnetic scattering from random rough surfaces have been few, in part because the applications of bistatic scattering are not as straightforward as for backscattering. The many theoretical developments for scattering from random rough surfaces, while developed for the bistatic case, have only been extensively used and tested for backscattering. The usefulness and validity of these theories for bistatic scattering is largely unknown. Therefore, a detailed investigation into the bistatic nature of these theories is expected to yield insights that are invaluable to their application to backscattering. An experimental investigation of bistatic rough surface scattering is valuable in the prediction of the performance of antennas operating in the presence of the ground [9, 3]. Moreover, recent developments in the modeling of terrain for radar backscattering indicate that bistatic scattering from a rough ground combined with a scattering overstructure (eg. trees or crops) can contribute significantly to the backscattering from the terrain as a whole. Therefore an

understanding of the nature of bistatic radar scattering and knowledge of the behavior of bistatic scattering theories are needed. The inversion of measurements involving such bistatic scattering mechanisms may yield new insights into the determination of important scattering parameters in the target of interest.

This dissertation is an experimental and theoretical investigation into the nature of bistatic rough surface scattering. While many theoretical approaches to modeling rough surface scattering have been developed, an exhaustive investigation into vector dielectric bistatic scattering of each of these approaches would be prohibitive, as many have been completed only for scalar scattering or Dirichlet boundary problems. Emphasis, therefore, is on the various Kirchhoff approaches and the Small Perturbation Method, which are sufficiently mature that minor extensions, at most, are required.

In addition to experimental verifications of the ranges of validity for these scattering models, some curious aspects of rough surface scattering require theoretical and experimental investigation. The nature of the vertical component of the scattered field when the angle of incidence or the angle of scattering is the Brewster angle for the relatively smooth dielectric is unknown. The range of validity of the prediction of depolarization of radiation by these theories, both single scattering and multiple scattering, must be determined. The source of phase shifts between scattered components must be investigated. In addition to the theoretical issues above, a bistatic polarimetric radar must be calibrated.

1.2 Structure of this Dissertation

Chapter 2 presents the surface scattering problem, and an outline of three traditional approaches to solving it: the Geometric Optics solution, the Physical Optics solution, and the Small Perturbation Model. An overview of previous experimental investigations of bistatic scattering is given.

Chapter 3 describes a Bistatic Measurement Facility which was constructed to make accurate measurements of bistatic scattering at X-band frequencies. Data obtained from this facility is used elsewhere in this dissertation.

Chapter 4 describes the theory and techniques to calibrate the Bistatic Measurement Facility. A separate technique is presented for the backscattering calibration and the bistatic calibration. While the backscattering calibration is presented elsewhere, the bistatic calibration is developed for this facility. Unique verification measurements demonstrate the validity of the calibrations.

Chapter 5 presents a modified Physical Optics approach to the surface scattering problem, which explains some observations which involves the Brewster angle, and reconciles a fundamental difference in the predictions for relative levels of σ^0_{vv} and σ^0_{hh} in backscattering by the Small Perturbation Method and Physical Optics.

Chapter 6 presents a comparison of measurements made in the Bistatic Measurement Facility with theoretical models outlined in Chapter 2 and the modified Physical Optics approach developed in Chapter 5. The coherent component of the modified Physical Optics approach is shown to be better at predicting measured data than the approaches in Chapter 2.

Chapter 7 develops an application of bistatic surface scattering, namely a model exten-

sion for backscattering from forests. The extension includes bistatic surface scattering with scattering from tree trunks.

Chapter 8 contains the results of this investigation, as well as suggestions for potential future research.

CHAPTER 2

Background

Traditional radar systems operate in the monostatic mode in which the transmit and receive antennas are located very close to each other or a single antenna is used for both functions. Monostatic scattering, also called backscattering, is a special case of the more general case of bistatic scattering which includes all possible combinations of illumination and scattering direction. Whereas extensive backscattering data exists in both the open literature and in classified data bases for point and distributed targets, bistatic data is practically nonexistent by comparison. Moreover, our current understanding of the applicability and ranges of validity of available scattering models and theoretical formulations to the general case of bistatic scattering is equally poor, primarily because these models have not been tested against accurate bistatic scattering data.

This chapter provides a basic background to the problem of bistatic scattering from rough surfaces, from basic definitions and the problem description to the three classic solutions to the problem and conclusions which can be drawn from the existing databases.

2.1 Bistatic Scattering

2.1.1 Wave Polarization

Figure 2.1 depicts an object, which may be a point or a distributed target, located at the center of an (x, y, z) coordinate system. In bistatic scattering, we have an incident wave generated by a transmit antenna pointed towards the target along the wave direction $\hat{\mathbf{k}}_i$, as well as a receive antenna whose boresight is pointed towards the target along the direction $-\hat{\mathbf{k}}_s$. Both $\hat{\mathbf{k}}_i$ and $\hat{\mathbf{k}}_s$ are unit vectors. The transmit direction propagation vector $\hat{\mathbf{k}}_i$ is specified by the incidence angle θ_i, defined as the angle between $-\hat{\mathbf{k}}_i$ and the positive z-axis, and the incident azimuth angle ϕ_i, defined as the angle in the x-y plane between the x-axis and the projection of $\hat{\mathbf{k}}_i$ onto the x-y plane,

$$\hat{\mathbf{k}}_i = \hat{\mathbf{x}}\cos\phi_i \sin\theta_i + \hat{\mathbf{y}}\sin\phi_i \sin\theta_i - \hat{\mathbf{z}}\cos\theta_i \tag{2.1}$$

A similar definition applies to $\hat{\mathbf{k}}_s$ in terms of the scattering (receive) angle θ_s:

$$\hat{\mathbf{k}}_s = \hat{\mathbf{x}}\cos\phi_s \sin\theta_s + \hat{\mathbf{y}}\sin\phi_s \sin\theta_s + \hat{\mathbf{z}}\cos\theta_s \tag{2.2}$$

The incident wave is represented by an electric field vector $\mathbf{E}$ which may lie anywhere in the plane orthogonal to the direction of propagation $\hat{\mathbf{k}}_i$. We characterize $\mathbf{E}$ in terms of a horizontal polarization components, $E_h^i \hat{\mathbf{h}}_i$, and a vertical polarization component, $E_v^i \hat{\mathbf{v}}_i$, where $\hat{\mathbf{h}}_i$ and $\hat{\mathbf{v}}_i$ are unit vectors denoting the directions of the respective polarizations. The direction $\hat{\mathbf{h}}_i$ is parallel to the x-y plane chosen to coincide with the $\hat{\phi}$-direction in the spherical

coordinate system and is given by:

$$\hat{\mathbf{h}}_i = \frac{\hat{\mathbf{z}} \times \hat{\mathbf{k}}_i}{|\hat{\mathbf{z}} \times \hat{\mathbf{k}}_i|} = \hat{\mathbf{y}} \cos\phi_i - \hat{\mathbf{x}} \sin\phi_i \tag{2.3}$$

and the vector $\hat{\mathbf{v}}_i$, which coincides with $\hat{\theta}$, completes the orthogonal set $(\hat{\mathbf{k}}_i, \hat{\mathbf{v}}_i, \hat{\mathbf{h}}_i)$. Thus,

$$\hat{\mathbf{v}}_i = \hat{\mathbf{h}}_i \times \hat{\mathbf{k}}_i = -(\hat{\mathbf{x}} \cos\phi_i \cos\theta_i + \hat{\mathbf{y}} \sin\phi_i \cos\theta_i + \hat{\mathbf{z}} \sin\theta_i) \tag{2.4}$$

The electric field of the incident wave, $\mathbf{E}^i$, is given by:

$$\mathbf{E}^i = \hat{\mathbf{v}}_i E_v^i + \hat{\mathbf{h}}_i E_h^i, \tag{2.5}$$

or in matrix notation as:

$$\mathbf{E}^i = \begin{bmatrix} E_v^i \\ \\ E_h^i \end{bmatrix}. \tag{2.6}$$

Similarly, the received electric field, $\mathbf{E}^s$, is given by:

$$\begin{aligned} \mathbf{E}^s &= \hat{\mathbf{v}}_s E_v^s + \hat{\mathbf{h}}_s E_h^s \\ &= \begin{bmatrix} E_v^s \\ \\ E_h^s \end{bmatrix}, \end{aligned} \tag{2.7}$$

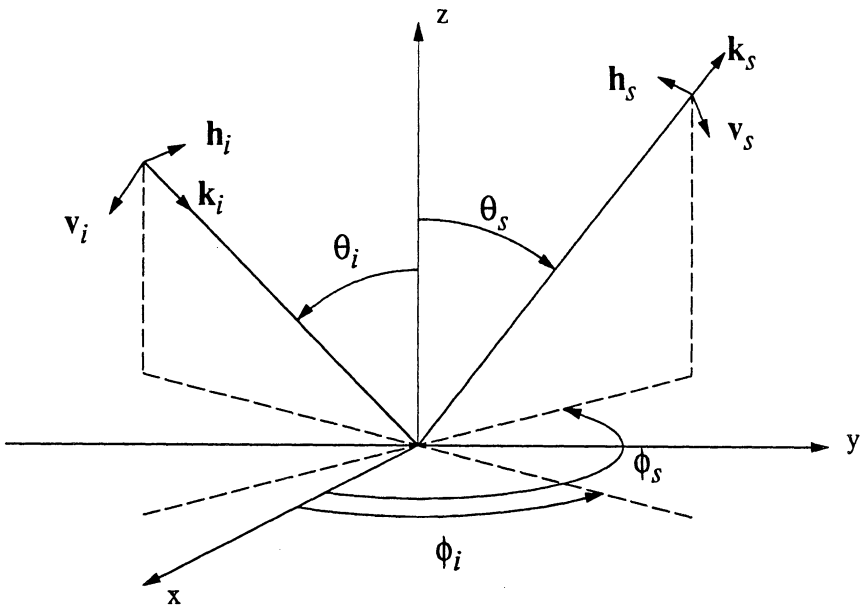

Figure 2.1: General Bistatic Coordinate System

with the polarization unit vectors given by:

$$\hat{\mathbf{h}}_s = \frac{\hat{\mathbf{z}} \times \hat{\mathbf{k}}_s}{|\hat{\mathbf{z}} \times \hat{\mathbf{k}}_s|} = \hat{\mathbf{y}} \cos\phi_s - \hat{\mathbf{x}} \sin\phi_s \tag{2.8}$$

$$\hat{\mathbf{v}}_s = \hat{\mathbf{h}}_s \times \hat{\mathbf{k}}_s = \hat{\mathbf{x}} \cos\phi_s \cos\theta_s + \hat{\mathbf{y}} \sin\phi_s \cos\theta_s - \hat{\mathbf{z}} \sin\theta_s \tag{2.9}$$

Throughout this document a subscript of i refers to a quantity associated with the incident wave, and s is associated with the scattered wave. This system of notation is neither the Forward Scattering Alignment (FSA) nor the Backscattering Alignment (BSA) as found in [47]; it could be denoted the Specular Scattering Alignment since the condition $\theta_i = \theta_s$ and $\phi_i = \phi_s$ is the specular direction, much like the same conditions in the FSA correspond to the forward scattering direction. It is most closely related to the FSA with the difference being that the angle of incidence of the FSA is replaced by its supplement. In other words, $\theta_i = \pi - \theta_{i\,FSA}$ (see figure 2.1 of Ulaby and Elachi [47]).

In addition to the direct representation of the fields *via* the matrix in (2.6) and (2.7),

there exists a modified Stokes vector notation [47]:

$$\mathbf{F}_m^i = \begin{bmatrix} \left\langle \left| E_v^i \right|^2 \right\rangle \\ \left\langle \left| E_h^i \right|^2 \right\rangle \\ 2\left\langle \Re e\left\{ E_v^i \; E_h^{i\,*} \right\} \right\rangle \\ 2\left\langle \Im m\left\{ E_v^i \; E_h^{i\,*} \right\} \right\rangle \end{bmatrix}$$

$$\mathbf{F}_m^s = \begin{bmatrix} \left\langle \left| E_v^s \right|^2 \right\rangle \\ \left\langle \left| E_h^s \right|^2 \right\rangle \\ 2\left\langle \Re e\left\{ E_v^s \; E_h^{s\,*} \right\} \right\rangle \\ 2\left\langle \Im m\left\{ E_v^s \; E_h^{s\,*} \right\} \right\rangle \end{bmatrix}$$

where $\langle x \rangle$ denotes the expected value of x. The first element of the Stokes vector represents the total intensity polarized in the $\hat{\mathbf{v}}$ direction, while the second represents the total intensity polarized in the $\hat{\mathbf{h}}$ direction. The third element is the difference in intensity of that polarized in the $\frac{1}{\sqrt{2}}\left(\hat{\mathbf{v}}+\hat{\mathbf{h}}\right)$ direction from that polarized in the $\frac{1}{\sqrt{2}}\left(\hat{\mathbf{v}}-\hat{\mathbf{h}}\right)$ direction. The fourth element is the difference in intensity of that right hand circularly polarized to that left hand circularly polarized (as defined by IEEE).

The advantage of the Stokes notation is that it can correctly account for partial polarization of waves while that of the direct notation cannot. The cost of this notation is that the absolute phase of the electric field is lost; however, this is usually so difficult to measure that its utility is minimal.

2.1.2 Azimuthally Symmetric Targets

In general, the bistatic-scattering geometry is specified in terms of the four angles θ_i, ϕ_i, θ_s and ϕ_s. The values of ϕ_s and ϕ_i are not nearly as important as the difference between them, since their values are subject to the choice of the $\hat{\mathbf{x}}$ and $\hat{\mathbf{y}}$-directions and the surface is assumed azimuthally symmetric. Since the Cartesian coordinate system will be associated with the surface, and in the measurements described in this dissertation the surface is rotated under the radar antennas, the distinction between ϕ_i and ϕ_s will be preserved. Therefore, a new quantity is introduced: $\phi_\Delta = \phi_s - \phi_i$. Thus, the angular set for bistatic scattering geometry is reduced to three angles θ_i, θ_s and ϕ_Δ for the special case of azimuthally symmetric targets.

Many functions in the surface scattering theories will not be dependent directly on either $\mathbf{k}_i$ or $\mathbf{k}_s$, but rather on their difference, as projected normally or tangentially to the surface:

$$\kappa_x = \hat{\mathbf{x}} \cdot (\mathbf{k}_s - \mathbf{k}_i) = k_1(\sin\theta_s \cos\phi_s - \sin\theta_i \cos\phi_i) \tag{2.10}$$

$$\kappa_y = \hat{\mathbf{y}} \cdot (\mathbf{k}_s - \mathbf{k}_i) = k_1(\sin\theta_s \sin\phi_s - \sin\theta_i \sin\phi_i) \tag{2.11}$$

$$\kappa_z = \hat{\mathbf{z}} \cdot (\mathbf{k}_s - \mathbf{k}_i) = k_1(\cos\theta_s + \cos\theta_i) \tag{2.12}$$

$$\kappa_t = \sqrt{\kappa_x^2 + \kappa_y^2} = k_1\sqrt{\sin^2\theta_i + \sin^2\theta_s - 2\sin\theta_i \sin\theta_s \cos\phi_\Delta} \tag{2.13}$$

For backscattering, $\theta_s = \theta_i$ and $\phi_\Delta = 180°$. Specular scattering corresponds to $\theta_s = \theta_i$ and $\phi_\Delta = 0°$. Scattering in the plane of incidence is specified by $\phi_\Delta = 0°$ or $\phi_\Delta = 180°$, with no restrictions on the values of θ_s or θ_i.

2.1.3 Time Convention

Throughout this dissertation, a time harmonic solution is assumed with a time dependence of $e^{j\omega t}$, where ω is the angular frequency. This time dependence is suppressed in the expressions herein.

2.1.4 Scattering Matrix S

When a q-polarized transmit antenna, where $q = h$ or v, illuminates a target in the direction (θ_i, ϕ_i) with an electric field E_q^i, and a p-polarized receive antenna at a distance r from the target receives a field E_p^s (where $p = h$ or v) in the direction (θ_s,ϕ_s), the two fields are related to one another by the scattering amplitude of the target $S_{pq}(\theta_s, \phi_s; \theta_i, \phi_i, \theta_j, \phi_j)$:

$$E_p^s(\theta_s, \phi_s) = \frac{e^{-jkr}}{r} S_{pq}(\theta_s, \phi_s; \theta_i, \phi_i; \theta_j, \phi_j) E_q^i(\theta_i, \phi_i) \tag{2.14}$$

where the direction (θ_j, ϕ_j) denotes the orientation of the target relative to a reference coordinate system, and $k = 2\pi/\lambda$ is the propagation wavenumber. Note that the first subscript of S_{pq} denotes the polarization of the received antenna and the second one denotes the polarization of the transmit antenna. In the $(\hat{\mathbf{h}}, \hat{\mathbf{v}})$ polarization space, there are four complex scattering amplitudes: S_{vv}, S_{vh}, S_{hv}, and S_{hh}. To accommodate the general case wherein the incident wave may have any polarization, and therefore may consist of both vertical and horizontal polarization components, we use the matrix form:

$$\begin{bmatrix} E_v^s \\ E_h^s \end{bmatrix} = \frac{e^{-jkr}}{r} \begin{bmatrix} S_{vv} & S_{vh} \\ S_{hv} & S_{hh} \end{bmatrix} \begin{bmatrix} E_v^i \\ E_h^i \end{bmatrix} \tag{2.15}$$

or equivalently,

$$\mathbf{E}^s = \frac{e^{-jkr}}{r}\mathbf{S}\mathbf{E}^i \tag{2.16}$$

The matrix **S** is called the scattering matrix of the target.

2.1.5 Modified Mueller Matrix L

The analogous quantity to the scattering matrix for the modified Stokes vector notation is the modified Mueller matrix:

$$\mathbf{F}^s = \frac{1}{r^2}\mathbf{L}\mathbf{F}^i \tag{2.17}$$

where the modified Mueller matrix **L** is given by

$$\mathbf{L} = \begin{bmatrix} \left\langle |S_{vv}|^2 \right\rangle & \left\langle |S_{vh}|^2 \right\rangle & \left\langle \Re e\{S_{vh}^* S_{vv}\} \right\rangle & -\left\langle \Im m\{S_{vh}^* S_{vv}\} \right\rangle \\ \left\langle |S_{hv}|^2 \right\rangle & \left\langle |S_{hh}|^2 \right\rangle & \left\langle \Re e\{S_{hh}^* S_{hv}\} \right\rangle & -\left\langle \Im m\{S_{hh}^* S_{hv}\} \right\rangle \\ 2\left\langle \Re e\{S_{vv} S_{hv}^*\} \right\rangle & 2\left\langle \Re e\{S_{vh} S_{hh}^*\} \right\rangle & \left\langle \Re e\{S_{vv} S_{hh}^* + S_{vh} S_{hv}^*\} \right\rangle & \left\langle \Im m\{S_{vh} S_{hv}^* - S_{vv} S_{hh}^*\} \right\rangle \\ 2\left\langle \Im m\{S_{vv} S_{hv}^*\} \right\rangle & 2\left\langle \Im m\{S_{vh} S_{hh}^*\} \right\rangle & \left\langle \Im m\{S_{vv} S_{hh}^* + S_{vh} S_{hv}^*\} \right\rangle & \left\langle \Re e\{S_{vv} S_{hh}^* - S_{vh} S_{hv}^*\} \right\rangle \end{bmatrix} \tag{2.18}$$

and has the advantage over the scattering matrix in that it incorporates the average properties of the scattering target. Again, the cost of the modified Mueller matrix is in the absence of an absolute phase, which describes how a target modifies the absolute phase of the scattered field relative to the absolute phase of the incident field. Since both of these quantities are difficult to measure, even relative to each other, little of value is lost by using this notation.

2.1.6 Radar Cross Section (RCS) σ

The scattering matrix **S** completely specifies the bistatic scattering behavior of the target for the specified incident and scattering direction. The *pq*-polarized radar cross section (RCS) of a point target is given by:

$$\sigma_{pq} = 4\pi |S_{pq}|^2 \tag{2.19}$$

The RCS for transmit and receive polarization combinations other than horizontal and vertical (such as circular and elliptical) can be calculated in terms of **S** using polarization synthesis [47].

2.1.7 Bistatic Scattering Coefficient σ^0

For a distributed target, such as a soil surface, the quantity of interest is the RCS per unit area, also called the bistatic scattering coefficient σ^0. Because a distributed target is a collection of many scattering points, the scattered signal exhibits scintillation effects as a function of spatial position. Hence, to determine σ^0, it is necessary to perform measurements of **S** for many spatial locations across the surface and then calculate the variance:

$$\sigma^0_{pq} = \lim_{A \to 0} \frac{4\pi}{A} \left\langle |S_{pq} - \langle S_{pq} \rangle|^2 \right\rangle \tag{2.20}$$

where A is the area of illumination. The limit exists because the bistatic scattering coefficient is a differential quantity. Mathematically, S_{pq} must be calculated over an area which extends to infinity in order to evaluate the expected value before the limit can be applied. This definition usually appears more like

$$\sigma^0_{pq} = \frac{4\pi}{A} \left\langle |S_{pq}|^2 \right\rangle \tag{2.21}$$

because S_{pq} is assumed to have zero mean, which is not true in the specular direction for surfaces, and the area is not part of a limiting process because a fundamental assumption of a statistical radar measurement is that a large number of independent scatterers is observed.

If N observations are performed, then a practical application of (2.21) is

$$\sigma_{pq}^{0} = \frac{4\pi}{A_{ill}} \sum_{i=1}^{N} \left(|S_{pq}|^2 \right)_i \tag{2.22}$$

where A_{ill} is the total effective illuminated area of the distributed target (see Section 4.5 of Chapter 4). In equations (2.21) and (2.22), **S** is assumed to have zero mean.

2.1.8 Bistatic Scattering from Rough Surfaces

Surface scattering theory refers to the development of models for the prediction of the scattering of waves from a rough interface between two homogeneous media. Much development of these theories has occurred in the last few decades because scattering of acoustic and electromagnetic waves from surfaces has been an important physical phenomenon in many fields of science and engineering. Acoustical scattering theory has perhaps seen the most development, partly because the physics of the acoustical case require only scalar mathematics for the scattering equations. For the general case of electromagnetic scattering from rough surfaces separating two electrically dissimilar media, a vector equation is formulated for the modeling of the physics. Under certain circumstances, however, such as one medium being perfectly electrically conducting, the vector nature of the scattering problem can be reduced to a scalar equation. Many electromagnetic rough surface scattering publications are restricted to this important scalar problem. In the following discussion of approaches to modeling and solving the electromagnetic scattering problems, I will outline the full vector approaches to the surface scattering theories as they are commonly used.

2.2 Surface Description

The surfaces under consideration in this dissertation can be mathematically modeled as separating two homogeneous but electrically dissimilar half-spaces. The surface constitutes the boundary between the two half-spaces, and the loci of this surface are assumed to be described as a random height above a mean planar surface. The height of the surface above or below this mean surface is unique for every transverse location on the mean surface. In other words, the surface height z is described by the function $z = f(x,y)$ where f is a random function of the lateral coordinates x and y. This is not a strictly appropriate model for naturally occurring surfaces like bare soils, however, which may include concavities in the surface, small clumps of soil above the surface, and possibly air bubbles within the soil. It is also not appropriate for soil surfaces covered with a thin layer of dead vegetative matter such as the litter found on a forest floor. Nor is it appropriate for surfaces separating a heterogeneous material from a homogeneous one, like a bare soil which is drying in the sun after a storm. Accurate analysis of the scattering of electromagnetic waves from these types of surfaces is beyond the scope of this dissertation; for wavelengths sufficiently large or natural surfaces which do not support the features described above, the assumption that the surface can be described by a single-valued function is valid.

An example of such a surface, or at least a one dimensional slice of the surface, is shown in Figure 2.2. This figure represents the measured profile of a surface from which bistatic scattering has been measured. Results from the characterization and the radar measurements of this surface will be used throughout the remainder of this chapter to illustrate some of the surface scattering phenomenon which are investigated further in later chapters.

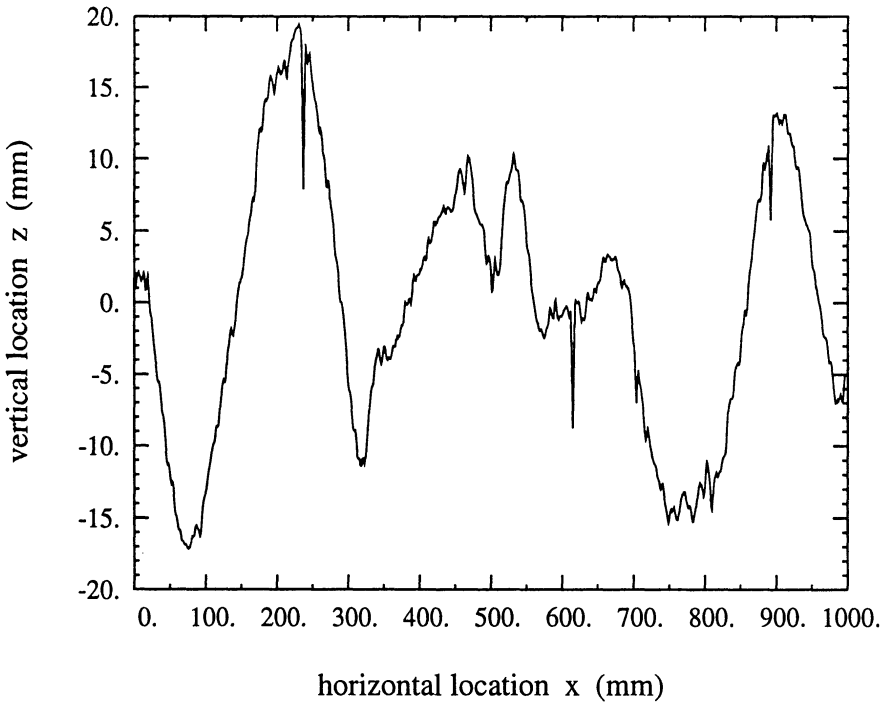

Figure 2.2: A one-dimensional slice of a profile of a surface used in bistatic scattering experiments in this study.

Calculating the scattering from every possible surface configuration is impossible. For this reason we are interested not in the actual scattering from each possible surface, but in expected values of the scattering of waves from a class of surfaces which could be described with the same statistical parameters. The shape of a random rough surface is described by the surface height distribution function and the surface height correlation function. For a surface whose height is given by $z = f(x, y)$, the surface height distribution function is given by $p_f(z)$, which is a probability distribution function for surface heights. While this height distribution function may take many possible forms, it is assumed in most analyses of rough

surface scattering to be Gaussian:

$$p_f(z) = \frac{1}{\sqrt{2\pi}\sigma} e^{-\frac{1}{2}\frac{z^2}{\sigma^2}} \tag{2.23}$$

Measurements by this and other experimenters [31, 29] indicate that this assumption is quite valid. Figure 2.3 shows the fit between a histogram of measured surface heights for the rough surface in Figure 2.2 and equation (2.23). As a result of this form of the surface height probability distribution function, the surface height characteristics can be specified by a single parameter, σ, which is the root-mean-squared surface deviation from the mean planar surface located at $z = 0$.

Another statistical descriptor of random rough surfaces is the correlation function, denoted by ρ. It describes the degree to which the height at one location given by $z = f(x,y)$, is correlated to the height at another location, given by $z' = f(x',y')$. The mathematical definition for the correlation function is

$$\rho = \frac{\langle zz' \rangle}{\sigma^2} \tag{2.24}$$

where the brackets indicate an expected value and the σ^2 in the denominator normalizes the correlation function to unity when the two points on the surface are the same (that is, when $x = x'$ and $y = y'$). For surfaces described by a stationary random process, the correlation ρ can be expressed in terms of the lateral separations $u = x - x'$ and $v = y - y'$ between the two locations on the surface. Moreover, if the surface statistics are symmetric under azimuthal rotations, the correlation function can be described by a single variable $\xi = \sqrt{u^2 + v^2}$, which

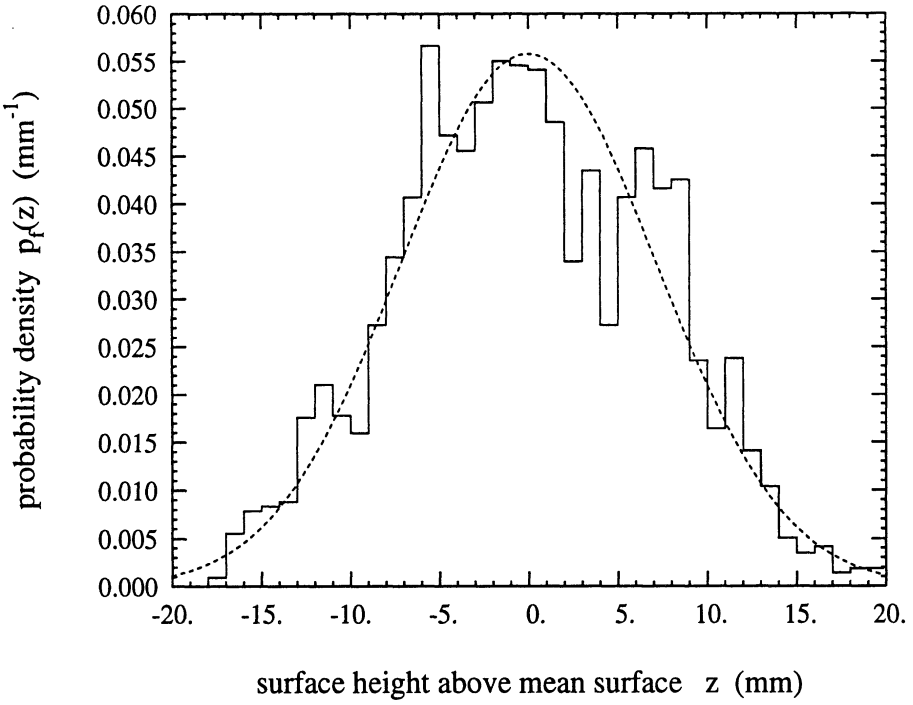

Figure 2.3: A histogram of measured heights for a rough surface and the Gaussian probability distribution used to model it. $\sigma = 6.9$ mm for this surface; N=4353

specifies the absolute value of the lateral separation. Unlike the surface height distribution function, the correlation function may take several forms for naturally occurring randomly rough surfaces. The vast majority of the literature on rough surface scattering assumes that the surface statistics are azimuthally symmetric and Gaussian, while many measurements of natural surfaces in microwave remote sensing situations indicate that a power law correlation function may be more appropriate. While not all surfaces in nature are azimuthally symmetric (a wind driven sea is an example of such a non-symmetric surface), a good number are symmetric and this dissertation will be limited to such surfaces.

The correlation length l is a measure of the lateral extent of the correlation between sur-

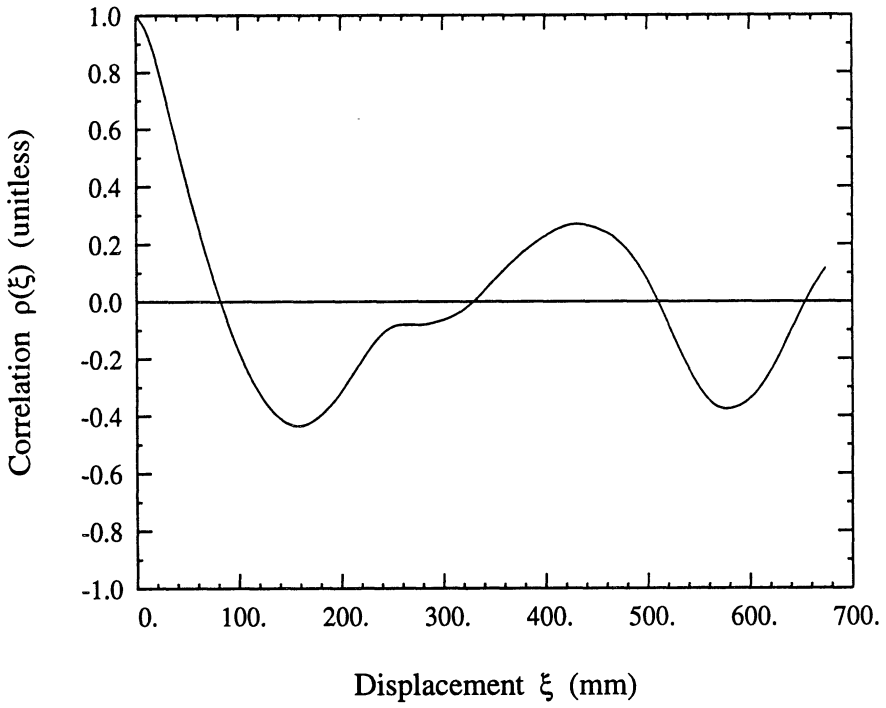

Figure 2.4: Correlation function of surface in previous figure.

face heights. If two points on a surface are sufficiently close such that $\xi < l$, then the heights at those two points are considered correlated. Likewise, if those two points are sufficiently distant such that $\xi > l$, then the heights are considered uncorrelated. When two points are separated by the correlation length, ie. when $\xi = l$, the value of the correlation is approximately given by $\rho = 1/e$.

The correlation function for the surface in Figure 2.2 is shown in Figure 2.4. It has a correlation length of 52.5 mm. In spite of the fact that a number of profiles that were taken of the surface were used to generate this average correlation, more profiles are needed to demonstrate that the correlation function tends toward zero beyond a few correlation lengths. As a result of the negative values of the correlation function, several of the integrals used to predict scattering characteristics (for example, (2.69) and (2.78)) may yield values which

are obviously incorrect. Austin [1] describes at length the data requirements for accurate characterization of a complete correlation function. However, only a few surface profiles are needed to determine the shape of the correlation function within one correlation length, and if the rest of the correlation function tends towards zero, this portion of the correlation function dominates the integrals. The effect of the shape of the correlation function within one correlation length can be explored by considering several analytical forms for the correlation function.

Four correlation functions will be considered as valid for random rough surfaces in this dissertation. They are the Gaussian, the exponential, the Gaussian exponential, and the power-law correlation functions:

$$\rho_g(\xi) = e^{-\xi^2/l^2} \tag{2.25}$$

$$\rho_e(\xi) = e^{-|\xi|/l} \tag{2.26}$$

$$\rho_{ge}(\xi) = e^{-\xi^2/(l_1^2+|\xi|l_2)} \tag{2.27}$$

$$\rho_{pl}(\xi) = \frac{1}{\left(1+\frac{\xi^2}{l^2}\right)^{\frac{3}{2}}} \tag{2.28}$$

The Gaussian, exponential and power law correlation functions are plotted for comparison in Figure 2.5 with the correlation length l normalized to unity. At the correlation length, all forms of the correlation function are nearly equal to $1/e$.

From the nature of the correlation functions, we would expect that a Gaussian surface would have very few short term variations (the correlation is relatively high for $\xi < l$) and many long term variations (the correlation is very low for $\xi > l$). An exponential surface, on

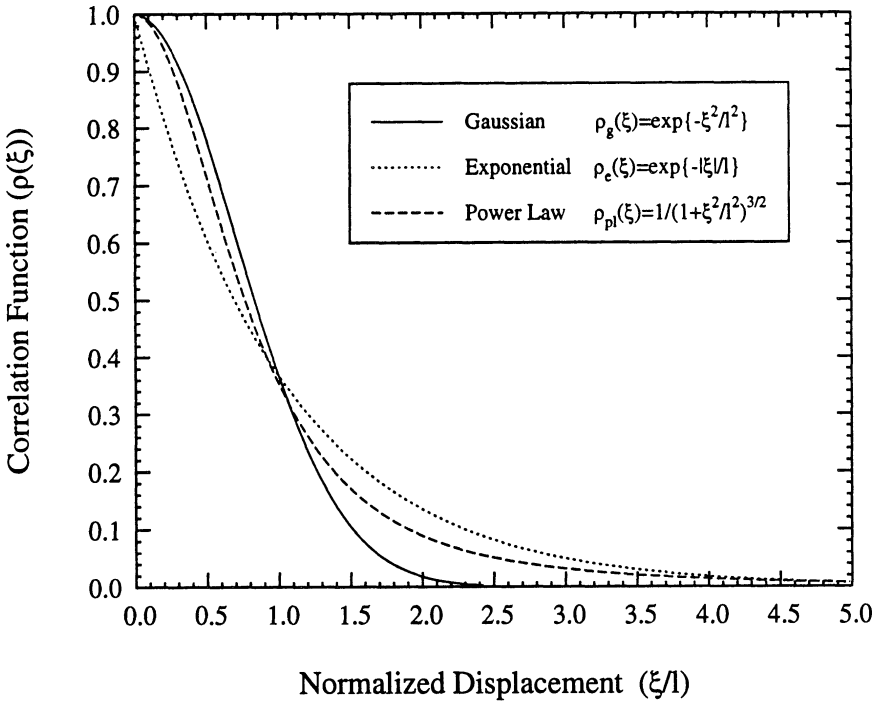

Figure 2.5: Forms of normalized correlation functions

the other hand, would have more short term variations and fewer long term variations than a Gaussian surface because, for $\xi < l$, the correlation is not quite so high and, for $\xi > l$, not quite so low as a Gaussian surface. A power law surface would have short and long term variations between those of a Gaussian and exponential surface.

The rms surface slope m, which is a useful quantity in the Geometric Optics approach below, is related to the second derivative of the correlation function at zero displacement, which is always negative for realizable correlation functions. In general, it is given by

$$m^2 = -\sigma^2 \rho''(0) \tag{2.29}$$

The values for the rms slope for the correlation functions given above are:

$$m_g = \sqrt{2}\sigma/l \tag{2.30}$$

$$m_{ge} = \sqrt{2}\sigma/l_1 \tag{2.31}$$

$$m_{pl} = \sqrt{3}\sigma/l \tag{2.32}$$

It must be emphasized that the exponential correlation function is not strictly valid as a correlation function, since it is not doubly differentiable at $\xi = 0$. For this reason the Gaussian-exponential correlation function is used when a correlation function is needed which has the proper characteristics at the origin (well defined rms slope) and yet has exponential characteristics away from the origin. Unfortunately, the Gaussian-exponential correlation function does not lend itself to analytical manipulation as readily as does the exponential correlation function. Therefore, models which appear in this dissertation which assume an exponential correlation should be considered to have a Gaussian-exponential correlation for which $l_2 \gg l_1$. The correlation length l for the Gaussian-exponential is given by

$$l = \frac{1}{2}\left(l_2 + \sqrt{l_2^2 + 4l_1^2}\right) \tag{2.33}$$

and, in light of (2.33) and (2.31), the Gaussian-exponential correlation function can be expressed in terms of the more useful parameters of the slope and correlation length:

$$\rho_{ge}(\xi) = e^{-\xi^2 m_{ge}^2/\left(2\sigma^2(1-|\xi|/l)+|\xi| l m_{ge}^2\right)} \tag{2.34}$$

This list of correlation functions is not exhaustive. There are many other forms for the correlation function which are not considered appropriate for microwave rough surface scattering from soils. One example of such a rough surface is a wind roughened sea surface, which is best described with 'Pierson-Moskowitz' surface statistics [43].

While the Kirchhoff approaches to characterizing scattering use correlation functions, the perturbation approaches use the Fourier transform of the correlation functions, which is also known as the spectral density. The spectral densities can be calculated from these correlation functions by

$$W(k_x, k_y) = \frac{1}{(2\pi)^2} \int_{-\infty}^{\infty} \int_{-\infty}^{\infty} \rho(u, v) e^{-j(k_x u + k_y v)} du dv \tag{2.35}$$

which, if the correlation functions are azimuthally symmetric, can be reexpressed as

$$W(k) = \frac{1}{2\pi} \int_0^{\infty} \rho(\xi) J_0(k\xi) \xi d\xi \tag{2.36}$$

where $k = \sqrt{k_x^2 + k_y^2}$. The spectral densities which correspond to the correlation functions in (2.25) (2.26) and (2.28) are given by

$$W_g(k) = \frac{l^2}{2\pi} e^{-k^2 l^2/4} \tag{2.37}$$

$$W_e(k) = \frac{l^2}{2\pi} \frac{1}{(1 + k^2 l^2)^{\frac{3}{2}}} \tag{2.38}$$

$$W_{pl}(k) = \frac{l^2}{2\pi} e^{-kl} \tag{2.39}$$

Examples of one-dimensional surfaces with different statistics are shown in Figure 2.6

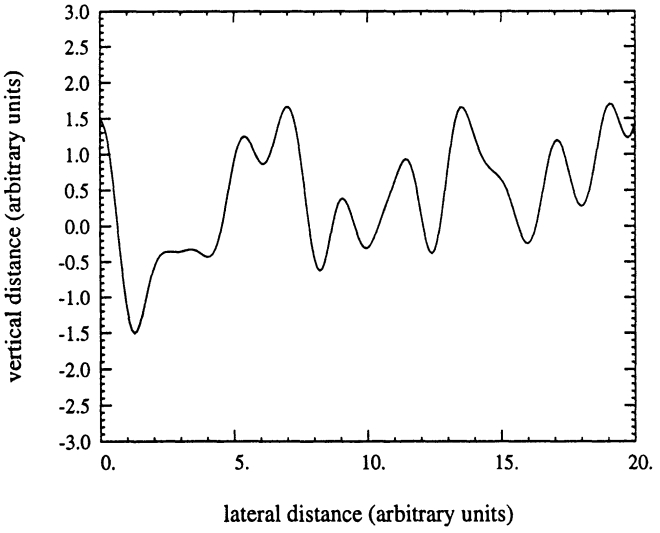

Figure 2.6: Example of one-dimensional surface with Gaussian correlation. $\sigma = 1, l = 1$

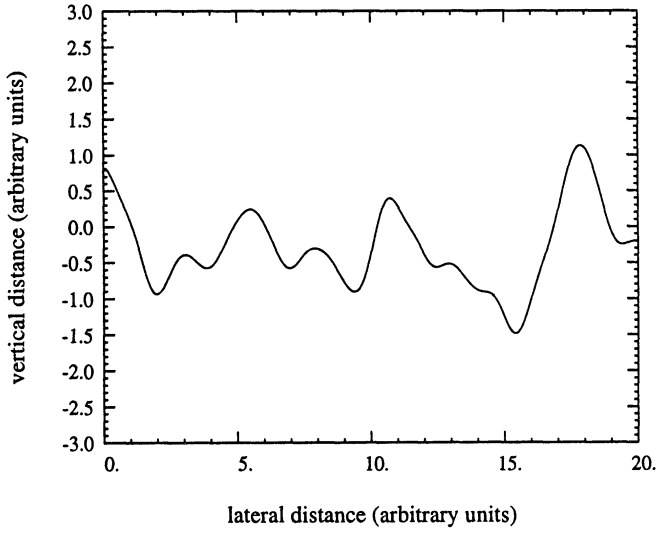

Figure 2.7: Example of one-dimensional surface with Gaussian correlation. $\sigma = .5, l = 1$

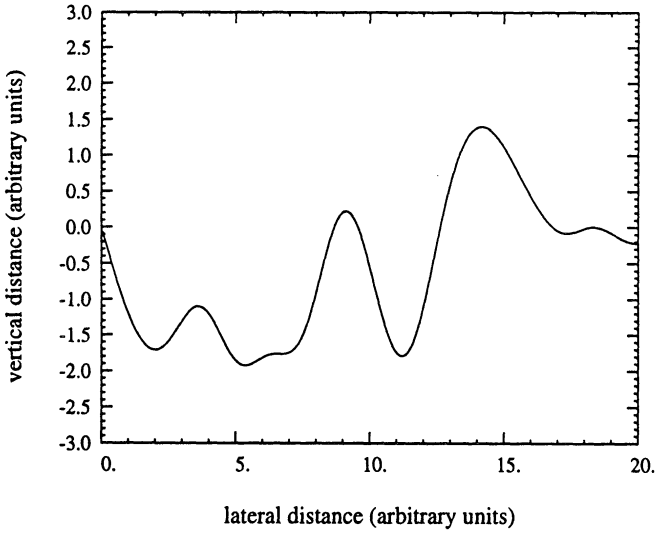

Figure 2.8: Example of one-dimensional surface with Gaussian correlation. $\sigma = 1, l = 2$

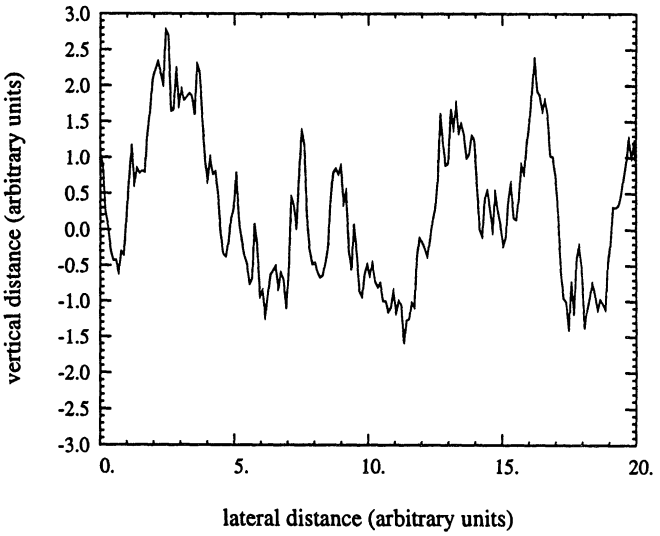

Figure 2.9: Example of one-dimensional surface with exponential correlation. $\sigma = 1$, $l = 1$

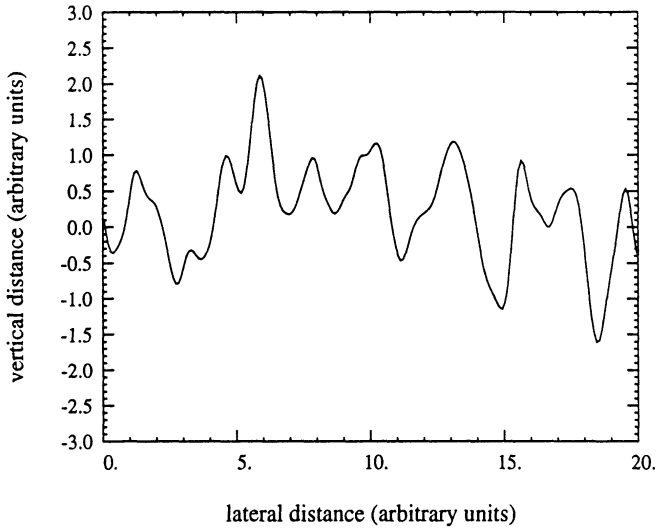

Figure 2.10: Example of one-dimensional surface with power law correlation. $\sigma = 1$, $l = 1$

through Figure 2.10. These surface profiles were computer generated by loading an array with the square root of the appropriate spectral density, randomly perturbing the magnitude and phase, and inverse Fourier transforming the spectrum into a real profile. On average, such a generated surface has the underlying spectral density and corresponding correlation function. Figure 2.6 shows a surface with a Gaussian correlation function with unit rms surface height and unit correlation length. Figure 2.7 and Figure 2.8 show how the shape of the surface changes when the Gaussian statistics are maintained, but when the rms surface height is halved and the correlation length is doubled, respectively. Figure 2.9 is of a surface with unit rms surface height and unit correlation length, but with an exponential correlation function. Note how the precise shape of the exponential correlation surface of Figure 2.9 shows the effect of sampling; the slope at each point is not well defined since it so strongly depends on the sampling of the surface used to generate the plot. This effect corresponds

to the fact that the rms slope m for this class of surfaces does not exist. Figure 2.10 is of a surface with unit rms surface height and unit correlation length, but with a power law correlation. Its short and long term characteristics fall between the characteristics of that of the Gaussian and exponential correlation surfaces.

2.3 Notations and Conventions

This section outlines the notation that is used throughout the rest of this dissertation. The surface separates space into two regions denoted as medium 1 and medium 2. Medium 1 has complex permittivity ε_1, complex permeability μ_1, complex impedance $\eta_1 = \sqrt{\mu_1/\varepsilon_1}$; medium 2 has complex permittivity ε_2, complex permeability μ_2, complex impedance $\eta_2 = \sqrt{\mu_2/\varepsilon_2}$. A wave of angular frequency ω has a complex wavenumber $k_1 = \omega\sqrt{\mu_1\varepsilon_1}$ in medium 1, and a complex wavenumber $k_2 = \omega\sqrt{\mu_2\varepsilon_2}$ in medium 2. Constitutive parameters with a subscript r refer to those of medium 2 relative to medium 1: for example, $\varepsilon_r = \varepsilon_2/\varepsilon_1$. The incident (excitation) wave has its source in medium 1. The surface is a perturbation from a mean surface lying in the $x-y$ plane; ie. the mean value of the surface height is zero: $\langle z \rangle = 0$. Therefore the $\hat{\mathbf{z}}$ direction defines a global normal unit vector to the rough surface; it is not, however, necessarily a local normal unit vector to the surface at any particular point.

In addition to a global coordinate system shown in Figure 2.1, analyses of rough surface scattering are facilitated by a description of a coordinate system local to a small portion of the surface. One unit vector that is important on the small scale of a surface is a unit vector normal to the surface. Two such vectors exist; one points into medium 1 and the other into

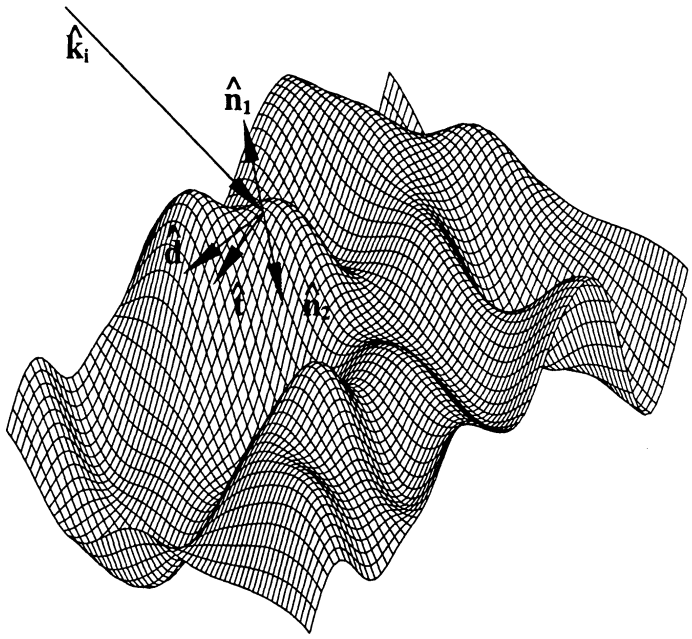

Figure 2.11: Local right-handed coordinate system at the surface. Shown is a Gaussian surface with an arbitrary incident unit vector $\hat{\mathbf{k}}_i$. Unit vectors $\hat{\mathbf{n}}_1$ and $\hat{\mathbf{n}}_2$ point normally to the surface into the upper and lower medium respectively. The tangential unit vector $\hat{\mathbf{t}}$ is orthogonal to both $\hat{\mathbf{k}}_i$ and $\hat{\mathbf{n}}_1$. The unit vector $\hat{\mathbf{d}}$ completes the right-handed coordinate system $(\hat{\mathbf{k}}_i, \hat{\mathbf{t}}, \hat{\mathbf{d}})$ which is local to the surface. Two unit vectors ($\hat{\mathbf{n}}_2$ and $\hat{\mathbf{d}}$) are shown in halftone to clarify that they lie beneath the surface.

medium 2, and are denoted as $\hat{\mathbf{n}}_1$ and $\hat{\mathbf{n}}_2$ respectively. Since they point in opposite directions, $\hat{\mathbf{n}}_1 = -\hat{\mathbf{n}}_2$. In terms of the function that defines the surface, the unit normal can be expressed in the global coordinate system as follows:

$$\hat{\mathbf{n}}_1 = \frac{\hat{\mathbf{z}} - Z_x\hat{\mathbf{x}} - Z_y\hat{\mathbf{y}}}{\sqrt{1+Z_x^2+Z_y^2}} \tag{2.40}$$

where $Z_x = \frac{\partial f(x,y)}{\partial x}$ and $Z_y = \frac{\partial f(x,y)}{\partial y}$ are the surface slopes in the $\hat{\mathbf{x}}$ and $\hat{\mathbf{y}}$-directions, respectively. The Physical Optics approach below is developed in a Taylor series in surface slopes longitudinal and transverse to the incident and scattered waves. The surface slopes longitu-

dinal and transverse relative to an incoming wave direction are given by

$$Z_l = Z_x \cos\phi_i + Z_y \sin\phi_i \tag{2.41}$$

$$Z_t = Z_y \cos\phi_i - Z_x \sin\phi_i \tag{2.42}$$

Similarly, the longitudinal and transverse slopes relative to the scattered direction are

$$Z_{ls} = Z_x \cos\phi_s + Z_y \sin\phi_s = Z_l \cos\phi_\Delta + Z_t \sin\phi_\Delta \tag{2.43}$$

$$Z_{ts} = Z_y \cos\phi_s - Z_x \sin\phi_s = Z_t \cos\phi_\Delta - Z_l \sin\phi_\Delta \tag{2.44}$$

In addition to the unit normal, the Physical Optics approach makes use of a local right handed coordinate system $(\hat{\mathbf{k}}_i, \hat{\mathbf{t}}, \hat{\mathbf{d}})$. This coordinate system is shown in Figure 2.11, and the unit vectors are given by [48],

$$\begin{aligned}
\hat{\mathbf{t}} &= \frac{\hat{\mathbf{k}}_i \times \hat{\mathbf{n}}_1}{\left|\hat{\mathbf{k}}_i \times \hat{\mathbf{n}}_1\right|} \\
&= \frac{\hat{\mathbf{x}}(\sin\theta_i \sin\phi_i - Z_y \cos\theta_i) - \hat{\mathbf{y}}(\sin\theta_i \cos\phi_i - Z_x \cos\theta_i) - \hat{\mathbf{z}} Z_{ti} \sin\theta_i}{\sqrt{(\sin\theta_i - Z_{li}\cos\theta_i)^2 + Z_{ti}^2}}
\end{aligned} \tag{2.45}$$

$$\begin{aligned}
\hat{\mathbf{d}} &= \hat{\mathbf{k}}_i \times \hat{\mathbf{t}} \\
&= (\hat{\mathbf{x}}(-\sin\theta_i \cos\theta_i \cos\phi_i + Z_x \cos^2\theta_i - Z_{ti} \sin^2\theta_i \sin\phi_i) \\
&\quad + \hat{\mathbf{y}}(-\sin\theta_i \cos\theta_i \sin\phi_i + Z_y \cos^2\theta_i + Z_{ti} \sin^2\theta_i \cos\phi_i) \\
&\quad + \hat{\mathbf{z}}(-\sin^2\theta_i + Z_{li} \sin\theta_i \cos\theta_i)) / \sqrt{(\sin\theta_i - Z_{li}\cos\theta_i)^2 + Z_{ti}^2}
\end{aligned} \tag{2.46}$$

In the scalar approximation to the Physical Optics approach these expressions are simplified by assuming all slopes are zero; the zeroth order terms in the Physical Optics expres-

sions do not depend on the surface slopes. However, higher order terms which describe such phenomenon as cross-polarized scattering in the plane of incidence and *vv* scattering at the Brewster angle require the full vector development.

2.4 Review of Surface Scattering Models

2.4.1 Stratton-Chu Integral Equation

All electromagnetic surface scattering theories are approximate solutions of the Stratton-Chu integral equation [40, 46]

$$\mathbf{E}^s(\mathbf{r}) = \int_{S'} [\nabla \times \mathbf{G}(\mathbf{r},\mathbf{r}') \cdot (\hat{\mathbf{n}} \times \mathbf{E}(\mathbf{r}')) - jk_s\eta_s \mathbf{G}(\mathbf{r},\mathbf{r}') \cdot (\hat{\mathbf{n}} \times \mathbf{H}(\mathbf{r}'))] dS' \tag{2.47}$$

where $\mathbf{r}$ is the point of observation, $\mathbf{r}'$ is a point on the rough surface S', $\hat{\mathbf{n}}$ is a unit surface normal vector from the surface S' into the observation medium, and k_s and η_s are the wavenumber and impedance, respectively, of the (scattered) electromagnetic field in the observation medium. The dyadic Green's function in the observation medium is given by

$$\mathbf{G}(\mathbf{r},\mathbf{r}') = \left[\mathbf{I} - \frac{\nabla\nabla}{k_s^2}\right] g(\mathbf{r},\mathbf{r}') \tag{2.48}$$

$$g(\mathbf{r},\mathbf{r}') = \frac{e^{-jk_s|\mathbf{r}-\mathbf{r}'|}}{4\pi|\mathbf{r}-\mathbf{r}'|} \tag{2.49}$$

An analytic solution to this equation, or its scalar equivalent, does not exist for surfaces which are randomly rough; i.e., whose loci $\mathbf{r}'$ are described by a stochastic process.

2.4.2 Form of the Incident Wave

The first assumption in the solution of (2.47) is the form of the incident (excitation) wave upon the rough surface. The scattering pattern of radiation from the surface will depend upon how it is illuminated, and so the choice of incident wave becomes important. In the vast majority of the literature, the incident wave is assumed to be a plane wave:

$$\mathbf{E}^i(\mathbf{r}_i) = \hat{\mathbf{q}} E_0 e^{-j\mathbf{k}_i \cdot \mathbf{r}_i} \tag{2.50}$$

where $\mathbf{k}_i$ and $\mathbf{r}_i$ are the wavenumber and location, respectively, in the medium containing the incident wave, E_0 is the amplitude of the incident wave electric field, and $\hat{\mathbf{q}}$ is the polarization vector of the incident wave. This choice for the incident radiation is appropriate for nearly all practical problems involving rough surface scattering. For surfaces sufficiently far from the source of illumination the incident field at the surface is very nearly planar. One important exception is the measurement of the coherently scattered field: standard analyses of the coherent scattering of plane waves yields radar cross sections which are delta distributions in solid angle and are not directly applicable or interpretable for practical measurement systems [49, 17]. The plane wave assumption also breaks down when the source of illumination is not distant from the surface. Papers by Fung and Eom [17] and Eom and Boerner [13] are examples of scalar analyses of electromagnetic rough surface scattering in which non-planar incident waves are assumed. The plane wave assumption engenders no loss in generality, however, much as the assumption of a time harmonic solution does not imply loss of generality, since most functions which could describe realistic propagating electromagnetic radiation are Fourier transformable in both time and space. Kojima [26] analyzes

the scalar surface scattering of electromagnetic Hermite-Gaussian beams by decomposing the incident wave into plane wave components.

2.4.3 Kirchhoff Approach

Under many circumstances, knowledge of the scattered field very distant from the rough surface is sufficient. Under the far field approximation, the Stratton-Chu integral equation (2.47) takes the form [39, 48, 46]:

$$\mathbf{E}^s(\mathbf{r}) = -j\frac{e^{-jk_sR_0}}{4\pi R_0}\mathbf{k}_s \times \int_{S'}[\hat{\mathbf{n}} \times \mathbf{E}(\mathbf{r}') - \eta_s\hat{\mathbf{k}}_s \times (\hat{\mathbf{n}} \times \mathbf{H}(\mathbf{r}'))]e^{j\mathbf{k}_s\cdot\mathbf{r}}dS' \tag{2.51}$$

where R_0 is the distance from the surface S' to the observation point $\mathbf{r}$. Unfortunately, this formulation is still very difficult to solve, and further approximations are required. The Kirchhoff approach is a solution in which the tangential fields on the surface at a particular location $\mathbf{r}' = \hat{\mathbf{x}}x + \hat{\mathbf{y}}y + \hat{\mathbf{z}}f(x,y)$ are approximated in some way from the incident field on the surface at that point. The most direct and common of the Kirchhoff approaches to solving (2.51) is the tangent-plane approximation [48, 46], in which the tangential fields at the surface are approximated by those that would exist if, for at each local surface point $\mathbf{r}'$, the surface was replaced with one which was plane and passed through $\mathbf{r}'$ with the same slope as does S' at that point. In other words, the local tangential fields are composed of the tangential component of the incident field plus the tangential component of the local reflected field as found by Fresnel reflection. To express the tangent-plane approximation mathematically, we must decompose the incident radiation into components which are locally transverse electric and transverse magnetic at the surface. Using the local surface right-handed

coordinate system (2.45) and (2.46), the electric field at the surface is expressed as

$$\begin{aligned}\hat{\mathbf{q}}E_0 &= ((\hat{\mathbf{t}}\cdot\hat{\mathbf{q}})\hat{\mathbf{t}}+(\hat{\mathbf{d}}\cdot\hat{\mathbf{q}})\hat{\mathbf{d}})E_0 \\ &= \mathbf{E}^i_\perp + \mathbf{E}^i_\parallel \end{aligned} \tag{2.52}$$

Then the local reflected fields at the surface under the tangent-plane approximation are given by

$$\begin{aligned}\mathbf{E}^r_\perp(\mathbf{r}') &= R_h\mathbf{E}^i_\perp(\mathbf{r}') \\ \mathbf{E}^r_\parallel(\mathbf{r}') &= -R_v\mathbf{E}^i_\parallel(\mathbf{r}') \end{aligned} \tag{2.53}$$

where the Fresnel reflection coefficients are

$$R_h = \frac{\eta_2\cos\theta_{l1}-\eta_1\cos\theta_{l2}}{\eta_2\cos\theta_{l1}+\eta_1\cos\theta_{l2}} \tag{2.54}$$

$$R_v = \frac{\eta_1\cos\theta_{l1}-\eta_2\cos\theta_{l2}}{\eta_1\cos\theta_{l1}+\eta_2\cos\theta_{l2}} \tag{2.55}$$

and θ_{l1}, θ_{l2} refer to the local angles of incidence and transmission, respectively and are related by Snell's law:

$$k_1\sin\theta_{l1} = k_2\sin\theta_{l2} \tag{2.56}$$

Also,

$$\cos\theta_{l1} = -\hat{\mathbf{n}}_1\cdot\hat{\mathbf{k}}_i \tag{2.57}$$

Thus the total tangential electric field on the surface is given by

$$\begin{aligned}\hat{\mathbf{n}}_1 \times \mathbf{E}(\mathbf{r}') &= \hat{\mathbf{n}}_1 \times (\mathbf{E}^i(\mathbf{r}') + \mathbf{E}^r(\mathbf{r}')) \\ &= \hat{\mathbf{n}}_1 \times ((1+R_h)\mathbf{E}^i_\perp + (1-R_v)\mathbf{E}^i_\parallel) \\ &= [(1+R_h)(\hat{\mathbf{t}}\cdot\hat{\mathbf{q}})(\hat{\mathbf{n}}_1 \times \hat{\mathbf{t}}) + (1-R_v)(\hat{\mathbf{d}}\cdot\hat{\mathbf{q}})(\hat{\mathbf{n}}_1 \times \hat{\mathbf{d}})]E_0 \qquad (2.58)\end{aligned}$$

Similarly, the tangential magnetic field on the surface is given by

$$\eta_1 \hat{\mathbf{n}}_1 \times \mathbf{H}(\mathbf{r}') = [(1-R_h)(\hat{\mathbf{t}}\cdot\hat{\mathbf{q}})(\hat{\mathbf{n}}_1 \times \hat{\mathbf{d}}) - (1+R_v)(\hat{\mathbf{d}}\cdot\hat{\mathbf{q}})(\hat{\mathbf{n}}_1 \times \hat{\mathbf{t}})]E_0 \qquad (2.59)$$

These fields are the total tangential electric and magnetic fields on the surface subject to the tangent-plane approximation. They have the same value in medium 1 and in medium 2, because tangential fields are continuous across the surface, but for convenience they could be expressed in terms of the constitutive parameters of medium 2 if the transmitted fields, instead of the reflected fields, are of interest.

2.4.3.1 Validity of the Tangent Plane Approximation

The tangent-plane approximation is appropriate only if the surface is locally smooth with respect to the wavelength of the electromagnetic wave for all surface loci $\mathbf{r}'$. This condition is usually expressed as

$$\left\langle 2kr_s \cos^3 \theta_{li} \right\rangle \gg 1 \qquad (2.60)$$

where r_s is the radius of curvature of the surface [3, 42, 23]. Some authors [3, 48] have slightly different expressions for the region of validity of the tangent-plane approximation.

This criterion is not expressed in terms that are usually used to describe rough surfaces, namely the rms surface height σ and the correlation length l. Ulaby *et al.* [48] reduce this condition of validity to $l^2/2.76\sigma \gg \lambda$ for a Gaussian surface, together with a simultaneous condition $kl \gg 6$ which is not derived.

Thorsos [42], Thorsos and Jackson [44], and Chen and Fung [8] have numerically tested the regions of validity of the Kirchhoff approach and the Small Perturbation method for perfectly conducting Gaussian rough surfaces. It is difficult to say if the region of validity reported by Thorsos is strictly due to the tangent-plane approximation or from other approximations, like Physical Optics or Geometric Optics, used to derive useful scattering expressions in the Kirchhoff approach. At any rate, Thorsos concludes that $kl > 2\pi$ alone is a condition of validity for the Kirchoff approach, except when the angle of incidence is too close to grazing. Corrections to various parameters are also presented to extend the region of validity of the Kirchhoff formulation. Thorsos' definition of validity is that the theory is to agree with the numerical results with a maximum error of 1 dB. Chen restricted his study of the Kirchhoff region of validity to incidence angles such that $\theta_i < 20°$ to avoid the effects of shadowing. His definition of validity is the sum of the deviations of the theory from the numerical results at $0°, 10°$ and $20°$ is to not exceed 3 dB for both co-polarizations. From Chen's graphics one can conclude that the Kirchhoff approach accurately predicts incoherent scattering for $kl > 4$ and $l^2/2.4\sigma > \lambda$, which is very close to the region outlined in Ulaby *et al.* [48]. In addition, Chen demonstrates that the Kirchhoff approach accurately predicts coherent scattering for sufficiently small $k\sigma$ and kl, a result not previously shown. The three

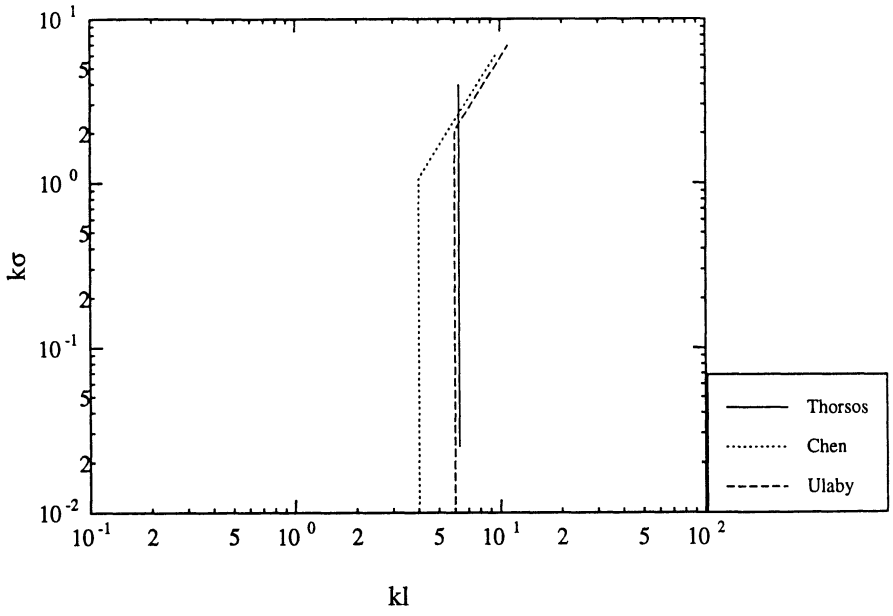

Figure 2.12: Regions of validity for the Kirchhoff approach as described by several authors. The valid region is to the right of the lines.

descriptions of the region of validity of the Kirchhoff approach are shown in Figure 2.12.

A more exact and more complicated approach to analyzing the validity of the Kirchhoff approach is to analyze the error introduced by assuming the surface fields to be only dependent on the incident fields at that point. The true surface fields are due to all currents that exist in the model environment: the fields scattered by the surface at other locales as well as the incident fields at that point. Several papers [6, 7, 18] attempt to analyze the Kirchhoff type scattering of electromagnetic waves from perfectly conducting rough surfaces by using conditions more exact than the tangent-plane approximation. In particular, the magnetic field on a perfectly conducting surface is expressed as a virtual electric current:

$$\mathbf{J}(\mathbf{r}') = 2\hat{\mathbf{n}} \times \mathbf{H}^i(\mathbf{r}') + \frac{1}{2\pi}\hat{\mathbf{n}} \times \int \nabla g(\mathbf{r}', \mathbf{r}'') \times \mathbf{J}(\mathbf{r}'') dS'' \tag{2.61}$$

where the first term gives the (single scattering) Physical Optics current. Further approximations to this expression are required, because the current **J** appears on both sides of the equation. Chen and Fung [7] suggest iteratively solving for the current, using the Physical Optics current as an initial guess. This technique has been called the Second Order Kirchhoff approach or Improved Kirchhoff approach. Fung and Pan [18] solve the scattering problem using this technique for the three dimensional case and shows that it predicts depolarization in the backscattering direction, but does not compare the results to measurements, as he does for co-polarized backscatter. He claims that this approach extends the region of validity for the scattering coefficients to shorter correlation lengths, and agrees with the small perturbation solution in its region of validity. This approach has been extensively described in Fung [15] where it is called the Integral Equation Method, and is applied to dielectric surfaces. Ishimaru and Chen [22] use this same starting point to extend the Kirchhoff approach for a two-dimensional problem, but uses a novel expansion of the Green's function which yields predictions of backscattering enhancement for appropriate surface conditions.

2.4.3.2 Choice of Surface Fields

Some debate has been raised in the literature as to which fields the symbols **E** and **H** in (2.51) on the surface actually refer to: the scattered fields or the total (incident plus scattered) fields. Holzer and Sung [21] discuss the implications of each choice of fields, and conclude that the scattered fields alone are the proper choice for **E** and **H**, although the total fields are also valid for some scattering problems, such as the Geometric Optics solution or scattering from a perfectly conducting surface. The choice of fields should not matter if an exact solution could be found [46], as the integral of the incident fields over the surface

will only yield the incident field elsewhere. The process of approximating a solution to the equation with the total field may give rise to errors which are obvious when the special case of a rough surface separating identical regions is considered [21]. In this case, the rough surface is fictitious, and the scattering should be zero. If the scattered fields alone are used, the tangential fields in the integral in (2.51) reduce to zero and thus the scattering is zero; scattering is not zero if the total fields are used.

2.4.3.3 Geometric Optics

The Geometric Optics approach to the solution of (2.51) under the tangent-plane approximation is valid as $k \to \infty$, or more specifically, as $\kappa_z = \hat{\mathbf{z}} \cdot (\mathbf{k}_s - \mathbf{k}_i) \to \infty$. It is derived using the stationary-phase approximation, hence it is also known as the stationary phase method. The Geometric Optics approach to electromagnetic scattering assumes that all electromagnetic waves travel like ray tubes, and are scattered by (smooth) objects only into the specular direction. The stationary phase method as applied directly to (2.51) yields $\langle \mathbf{E}^s \rangle = 0$, meaning that there is no coherent component of the Geometric Optics scattered field. If it is applied to the expected value of the variance of the field, however, we discover that

$$\left\langle S_{pq} S_{mn}^* \right\rangle = \frac{k^2}{(4\pi)^2} U_{pq} U_{mn}^* \left\langle |I|^2 \right\rangle \tag{2.62}$$

where p, m are receive polarizations and q, n are transmit polarizations; $\left\langle |I|^2 \right\rangle$ is the stationary phase integral over the phase on the surface, and U_{pq} are polarization amplitude coefficients which are constant with respect to surface slopes, subject to the stationary phase

condition. Explicitly,

$$U_{pq} = -\frac{\kappa}{k_i\left(\left(\hat{\mathbf{k}}_i\cdot\hat{\mathbf{v}}_s\right)^2+\left(\hat{\mathbf{k}}_i\cdot\hat{\mathbf{h}}_s\right)^2\right)}\left[R_v\left(\left(\hat{\mathbf{h}}_s\delta_{ph}+\hat{\mathbf{v}}_s\delta_{pv}\right)\cdot\hat{\mathbf{k}}_i\right)\left(\left(\hat{\mathbf{h}}_i\delta_{hq}+\hat{\mathbf{v}}_i\delta_{vq}\right)\cdot\hat{\mathbf{k}}_s\right)\right.$$
$$\left.+R_h\left(\left(\hat{\mathbf{v}}_s\delta_{ph}-\hat{\mathbf{h}}_s\delta_{pv}\right)\cdot\hat{\mathbf{k}}_i\right)\left(\left(\hat{\mathbf{v}}_i\delta_{qh}-\hat{\mathbf{h}}_i\delta_{qv}\right)\cdot\hat{\mathbf{k}}_s\right)\right] \tag{2.63}$$

where δ_{pq} is the Kronecker delta function ($\delta_{pq}=1$ iff $p=q$ and $\delta_{pq}=0$ iff $p\neq q$), and

$$\left\langle |I|^2\right\rangle = \frac{4\pi^2 A_0\kappa^2}{\kappa_z^4}p(Z_{x0},Z_{y0}) \tag{2.64}$$

where $\kappa^2=\kappa_x^2+\kappa_y^2+\kappa_z^2=2k^2(1+\cos\theta_i\cos\theta_s-\sin\theta_i\sin\theta_s\cos\phi_\Delta)$ (see Physical Optics, below) and $p(Z_x,Z_y)$ is the probability density that the surface has points with slopes of Z_x and Z_y in the $\hat{\mathbf{x}}$- and $\hat{\mathbf{y}}$-directions respectively. Z_{x0} and Z_{y0} are slopes that correspond to specular scattering for the given values of θ_i,θ_s,ϕ_i and ϕ_s. For an isotropic surface,

$$p(Z_x,Z_y)=\frac{1}{2m^2}e^{-\kappa_t^2/2\kappa_z^2m^2} \tag{2.65}$$

where m is the root-mean-squared surface slope.

Scattering coefficients of the Geometric Optics solution are proportional to the magnitude of the Fresnel reflection coefficients for the pair of directions chosen, and to the probability that the slopes will occur to facilitate scattering in those directions. In the plane of incidence, depolarization is zero because scattering is assumed to arise only from points on the surface which have no lateral slope. In backscattering there is not only a lack of depolarization, but the co-polarized scattering coefficients are identical. This prediction origi-

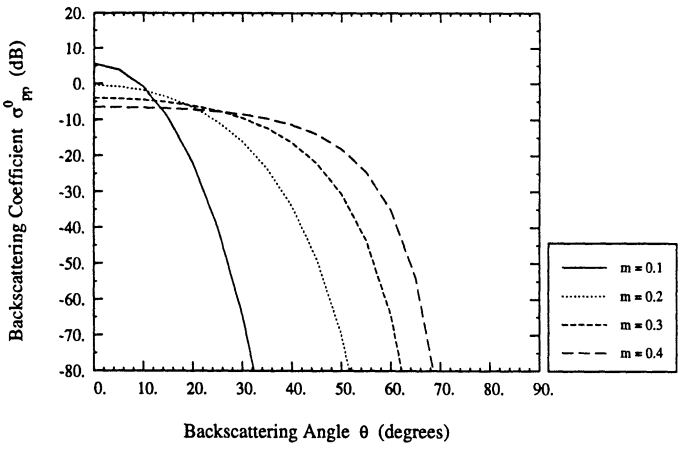

Figure 2.13: Geometric Optics backscattering coefficients vs. incidence angle with rms slope m varied from 0.1 to 0.4. $\varepsilon_r = 3.0 - j0.0$ The co-polarized terms are identical and cross-polarized terms are zero.

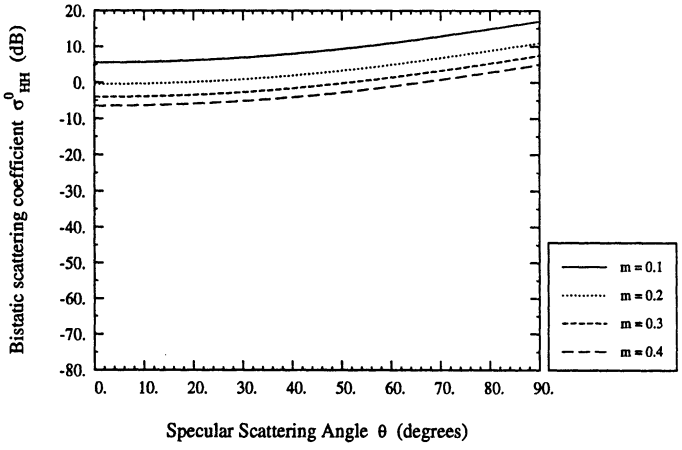

Figure 2.14: Geometric Optics bistatic scattering coefficients in the specular scattering direction for *hh* polarization vs. incidence angle with rms slope m varied from 0.1 to 0.4. $\varepsilon_r = 3.0 - j0.0$ The cross-polarized terms are zero.

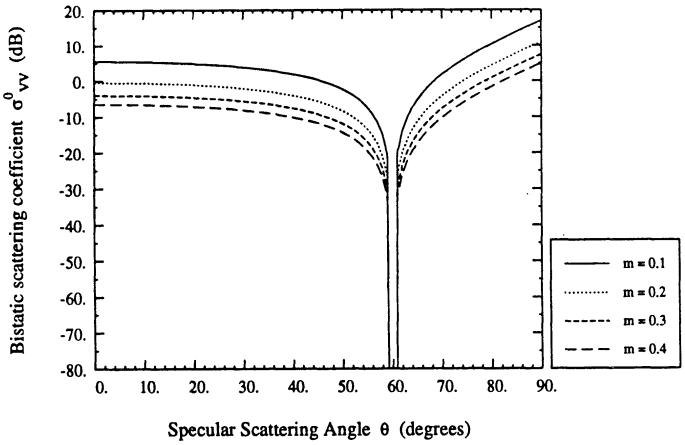

Figure 2.15: Geometric Optics bistatic scattering coefficients in the specular scattering direction for *vv* polarization vs. incidence angle with rms slope m varied from 0.1 to 0.4. $\varepsilon_r = 3.0 - j0.0$. The Brewster angle is clearly evident.

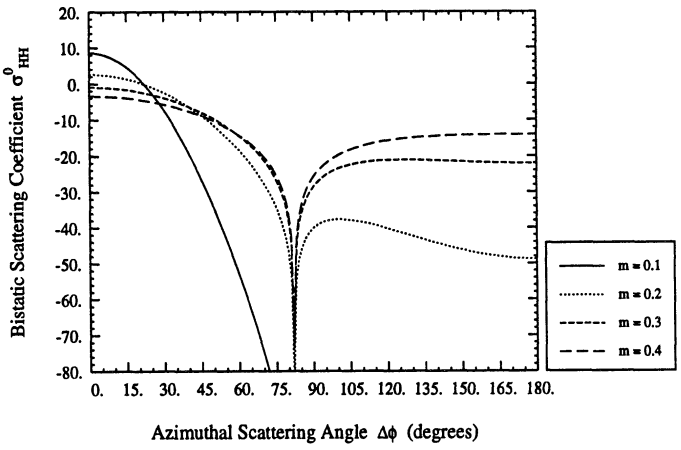

Figure 2.16: Geometric Optics bistatic scattering coefficients for *hh* polarization vs. azimuthal scattering angle with rms slope m varied from 0.1 to 0.4. $\theta_i = \theta_s = 45°$, $\varepsilon_r = 3.0 - j0.0$. Backscattering corresponds to $\phi_\Delta = 180°$ and specular scattering corresponds to $\phi_\Delta = 0°$.

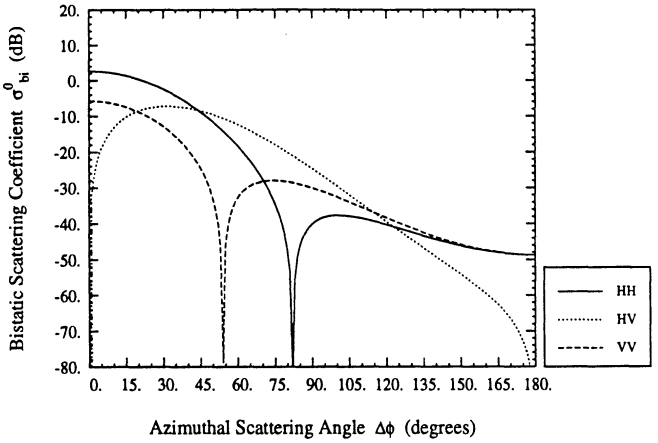

Figure 2.17: Geometric Optics bistatic scattering coefficients for all polarizations vs. azimuthal scattering angle with rms slope fixed at $m = 0.1$, $\sigma^0_{vh} = \sigma^0_{hv}$ for Geometric Optics $\varepsilon_r = 3.0 - j0.0$, $\theta_i = \theta_s = 45°$. Backscattering corresponds to $\phi_\Delta = 180°$ and specular scattering corresponds to $\phi_\Delta = 0°$.

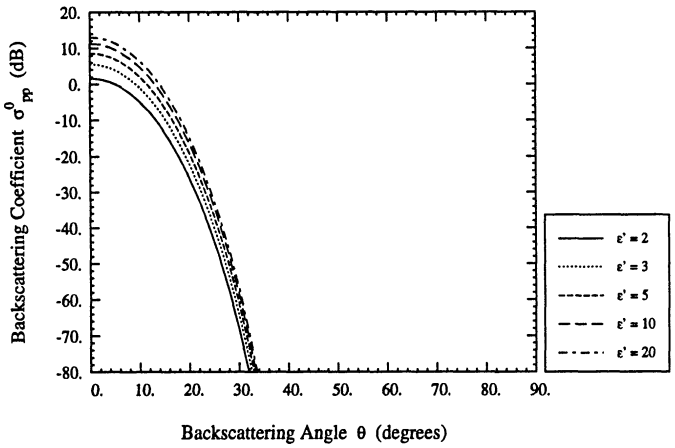

Figure 2.18: Geometric Optics backscattering coefficients vs. incidence angle with surface dielectric varied. Surface slope fixed at $m = 0.1$. The co-polarized terms are identical and cross-polarized terms are zero.

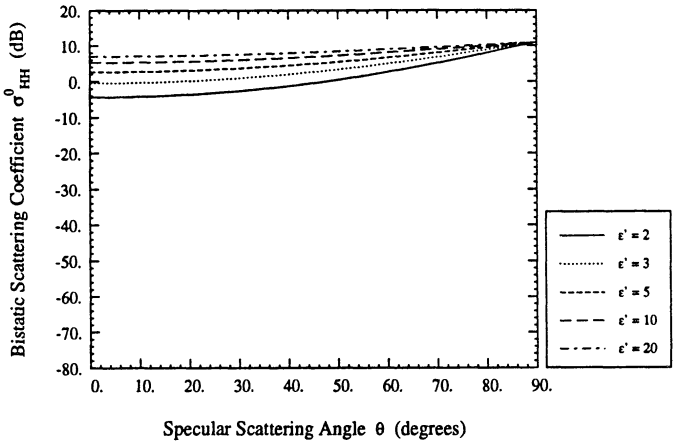

Figure 2.19: Geometric Optics bistatic scattering coefficients in the specular scattering direction for *hh* polarization with surface dielectric varied. Surface slope fixed at $m = 0.1$. The cross-polarized terms are zero.

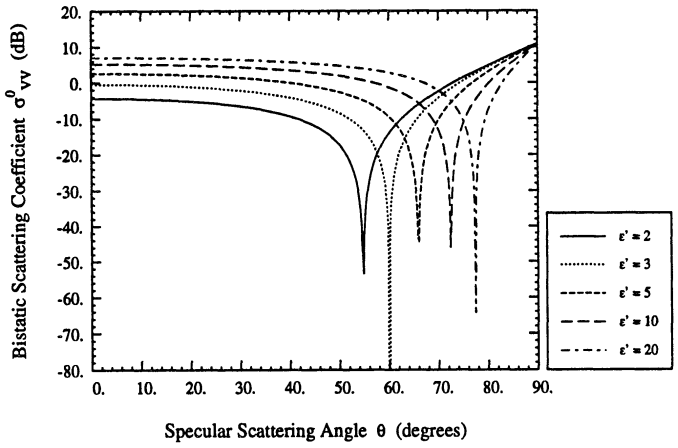

Figure 2.20: Geometric Optics bistatic scattering coefficients in the specular scattering direction for *vv* polarization with surface dielectric varied. Surface slope fixed at $m = 0.1$. The cross-polarized terms are zero.

nates from the assumption that only specular points on the surface contribute to scattering; thus backscatter is due to locally normal incidence, and the Fresnel coefficients are independent of polarization for normal incidence. The co-polarized scattering coefficients are not necessarily the same away from backscattering. Due to the formulation of the Geometric Optics solution, the scattering coefficients are reciprocal. That is, the scattering coefficients are the same if the incident and scattered directions and polarizations are reversed. Figure 2.13 through Figure 2.20 show several Geometric Optics bistatic scattering coefficients for a number of different conditions of roughness and polarization. Figure 2.13 shows the rapid decrease in backscattering as the incidence angle is increased. For a large angle of incidence, the probability that a surface facet exists which is oriented to backscatter energy is small for a surface with a small rms surface slope. As the rms slope is increased, however, the point of drop-off extends out to larger backscattering angles. Scattering in the specular direction for *hh* polarization is shown in Figure 2.14. Scattering in the specular direction is caused by facets which have zero slope. As a result, scattering is large at all angles of incidence. The probability that the slope at any one point is zero decreases only modestly as the rms slope is increased. Specular scattering is also shown in Figure 2.15, except that in this case the polarization is *vv*. In the specular direction, the polarization dependence of Geometric Optics scattering is identical to that of the reflectivity. The effect of the Brewster angle is clearly evident; all other characteristics mimic that of *hh* polarization.

Figure 2.16 shows the Geometric Optics scattering dependence on the azimuthal angle ϕ_Δ. For the very smooth surface, the *hh*-polarized scattering is very sharply limited to the specular direction, while for the rougher surfaces the scattering simultaneously decreases in the specular direction and increases in the backscattering direction. A sharp null occurs in

the pattern which is independent of the roughness, but as Figure 2.17 shows, is dependent on the polarization. For cross-polarization, the nulls occur only in the plane of incidence ($\phi_\Delta = 0°$ or 180°). The nulls for co-polarization exist due to a rotation the electric field by the appropriately oriented facets. Out of the plane of incidence the field polarizations local to the surface no longer coincide with the incident or scattered polarizations. The combination of local *v* and *h* polarized scattering generates linearly polarized scattering. The difference in the local reflection coefficients as a function of polarization insures that the angle at which the scattered polarization is orthogonal to the receiver polarization are different for the different incident polarizations. The Brewster angle in the specular direction is a very special case of this phenomenon.

The dependence of the Geometric Optics scattering on the dielectric is shown for backscattering in Figure 2.18, for *hh* polarized specular scattering in Figure 2.19, and for *vv* polarized specular scattering in Figure 2.20. Except for the scattering beyond the Brewster angle, an increase in the dielectric increases scattering. This is due solely to the change in the reflection coefficients due to the change in dielectric.

The limit of validity on the stationary phase approximation according to Ulaby *et al.* [48] is:

$$\kappa_z \sigma > \sqrt{10} \tag{2.66}$$

where κ_z is defined by (2.12). The region of validity for Geometric Optics is therefore defined by a combination of the stationary phase validity condition and that for the tangent-plane approximation. The Geometric Optics region of validity as given by Ulaby is shown

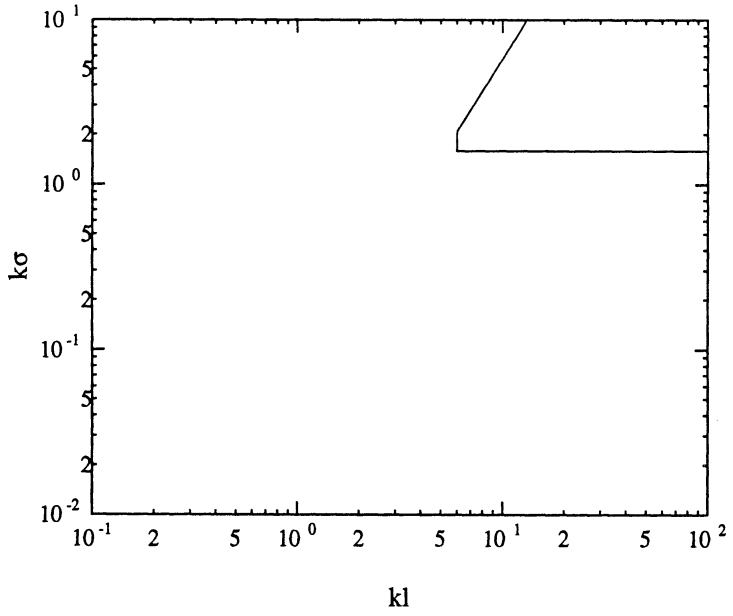

Figure 2.21: Region of validity for the Geometric Optics Approach as described by Ulaby *et al.*. The valid region includes the upper right corner in the diagram.

in Figure 2.21 for the condition that $\theta_i, \theta_s \rightarrow 0°$ so that $\kappa_z \rightarrow 2k$. For combinations of angles away from nadir, the minimum value of the roughness parameter $k\sigma$ must be greater for (2.66) to hold.

Under this stationary phase condition that the surface be sufficiently rough, we would expect that the coherent scattering coefficient would be negligibly small. If we were to use this condition in the coherent component of the Physical Optics solution (see below) we would find that the coherent scattering coefficient is reduced by at least 43 dB over that of a smooth surface, so the Geometric Optics prediction of zero coherent scattering is not too bad. While the surface heights cannot approach a plane, the slopes of the surface can approach zero, which gives the probability distribution in (2.64) a very sharp peak at $Z_x =$

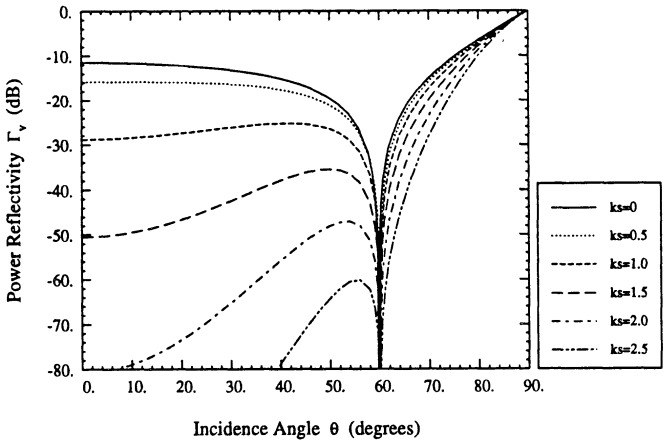

Figure 2.22: Physical Optics coherent reflectivity for v polarization vs. incidence angle for a Gaussian surface with $k\sigma$ varied from 0 to 2.5, $\varepsilon_r = 3.0 - j0.0$.

$Z_y = 0$. This in turn yields a scattering pattern which is a delta function in the specular direction, which must not be confused with a coherent scattering coefficient. The scattered waves are still incoherent.

2.4.3.4 Physical Optics

A different Kirchhoff approach is the Physical Optics solution to (2.51). The Physical Optics approach involves the integration of the Kirchhoff scattered field over all of the rough surface, not just the portions of the surface which contribute specularly in the scattered direction. Unlike the Geometric Optics solution, the Physical Optics solution predicts a coherent component. Specifically, the coherent field reflection coefficient from a surface with a Gaussian height distribution is given by

$$R_{q(PO)} = R_{q00} e^{-2k^2\sigma^2\cos^2\theta} \delta_{pq} \tag{2.67}$$

where the polarization subscripts p, q are either h or v, and $\cos\theta = -\hat{\mathbf{z}} \cdot \hat{\mathbf{k}}_i$. θ is both the angle of incidence and reflection; coherent scattering occurs only in the specular direction from the mean surface. The reflection coefficient R_{q00} for a plane surface is given by (2.75) and (2.76) below. Figure 2.22 shows $\Gamma_{v(PO)} = \left|R_{v(PO)}\right|^2$ for several values of $k\sigma$. The Brewster angle does not change with surface roughness, but the coherent scattered power decreases very rapidly with increasing roughness.

The power in the incoherent reflected field may be found by expanding the Stratton-Chu equation in a Taylor series in surface slope distributions. In Ulaby *et al.* [48] the Physical Optics solution is called the Scalar Approximation because slopes are ignored in the surface local coordinate system, leading to a decoupling of polarizations in the vector scattering equations. As a result, co-polarized scattering in the plane of incidence is quite accurate, but cross-polarized scattering is zero. With the inclusion of surface slopes transverse to the plane of incidence in the vectorial solution to the Physical Optics approximation, depolarization in the plane of incidence is predicted when the Taylor series is expanded to the second order in surface slopes. The zeroth and first order solution to the Scalar Approximation are clearly derived in Ulaby *et al.* [48] and will not be given here. Usually the Physical Optics solution is implemented by using the zeroth order term only. That is, the solution derived by neglecting all surface slopes. As will be seen in Chapter 5, this approach is incomplete even for surfaces with very small slopes.

The zeroth order term of the Physical Optics solution is given by

$$\frac{k_1^2}{4\pi A_0}\left\langle S_{mn} S_{pq}^* \right\rangle = a_{00mn} a_{00pq}^* I_0 \tag{2.68}$$

where

$$I_0 = \tfrac{1}{2}k_1^2 e^{-\kappa_z^2\sigma^2}\int_0^\infty \left(e^{\kappa_z^2\sigma^2\rho(\xi)} - 1\right)J_0(\kappa_t\xi)\xi d\xi \tag{2.69}$$

where κ_z and κ_t are given by (2.12) and (2.13), respectively, and the polarization coefficients are

$$a_{00hh} = -R_{h00}(\cos\theta_i + \cos\theta_s)\cos\phi_\Delta \tag{2.70}$$

$$a_{00vh} = -R_{h00}(1 + \cos\theta_i\cos\theta_s)\sin\phi_\Delta \tag{2.71}$$

$$a_{00hv} = R_{v00}(1 + \cos\theta_i\cos\theta_s)\sin\phi_\Delta \tag{2.72}$$

$$a_{00vv} = -R_{v00}(\cos\theta_i + \cos\theta_s)\cos\phi_\Delta \tag{2.73}$$

(2.74)

The parameters R_{v00}, R_{h00} are the zeroth order coefficients of the (field) reflectivity (2.54) and (2.55) when expanded in terms of surface slopes. That is, they are the same as (2.54) and (2.55) with the slopes set to zero, and therefore are identical to the reflection coefficients for a smooth surface:

$$R_{h00} = \frac{\eta_2\cos\theta_i - \eta_1\cos\theta_t}{\eta_2\cos\theta_i + \eta_1\cos\theta_t} \tag{2.75}$$

$$R_{v00} = \frac{\eta_1\cos\theta_i - \eta_2\cos\theta_t}{\eta_1\cos\theta_i + \eta_2\cos\theta_t} \tag{2.76}$$

where θ_t is related to θ_i by Snell's Law: $k_1\sin\theta_i = k_2\sin\theta_t$.

Some basic characteristics of the zeroth order Physical Optics solution are shown in Fig-

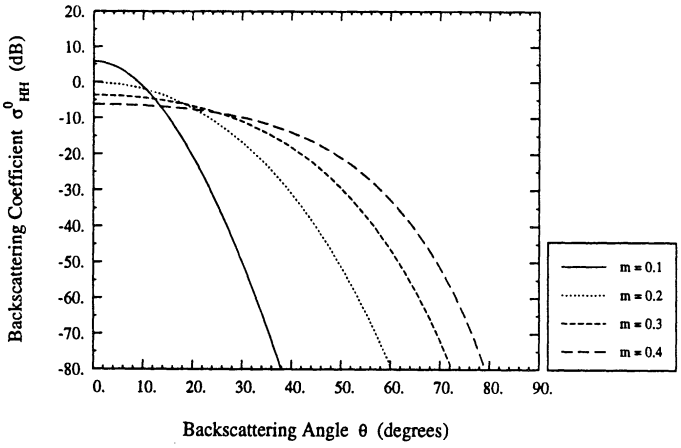

Figure 2.23: Zeroth Order Physical Optics backscattering coefficients for *hh* polarization vs. incidence angle for a Gaussian surface with rms slope m varied from 0.1 to 0.4. $\varepsilon_r = 3.0 - j0.0$, $k\sigma = 2.0$. The cross-polarized terms are zero.

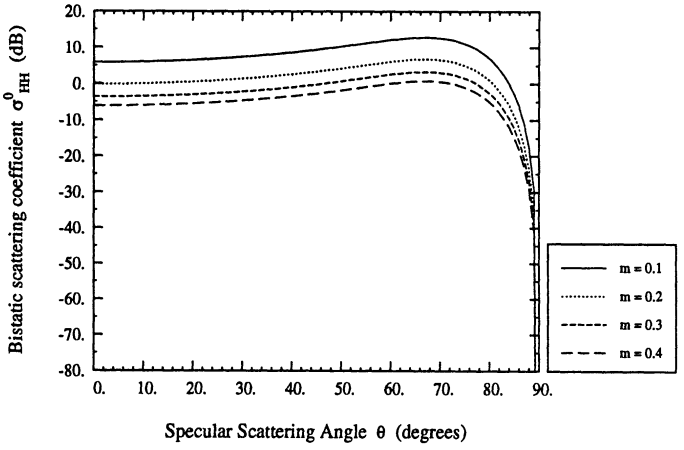

Figure 2.24: Zeroth Order Physical Optics bistatic scattering coefficients in the specular scattering direction for *hh* polarization vs. incidence angle for a Gaussian surface with rms slope m varied from 0.1 to 0.4. $\varepsilon_r = 3.0 - j0.0$, $k\sigma = 2.0$. The cross-polarized terms are zero.

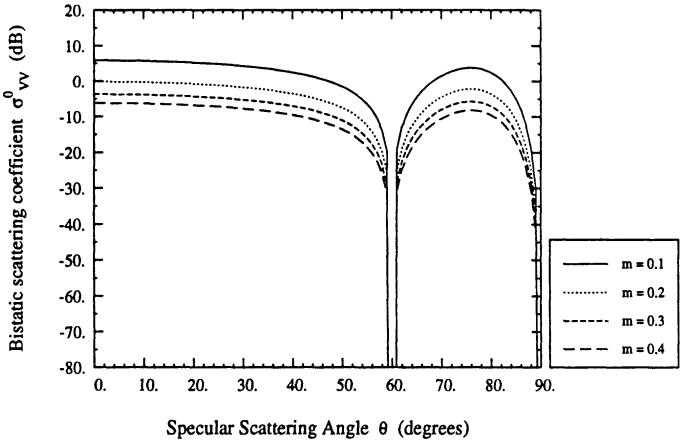

Figure 2.25: Zeroth Order Physical Optics bistatic scattering coefficients in the specular scattering direction for *vv* polarization vs. incidence angle for a Gaussian surface with rms slope m varied from 0.1 to 0.4. $\varepsilon_r = 3.0 - j0.0$, $k\sigma = 2.0$. The Brewster angle is clearly evident.

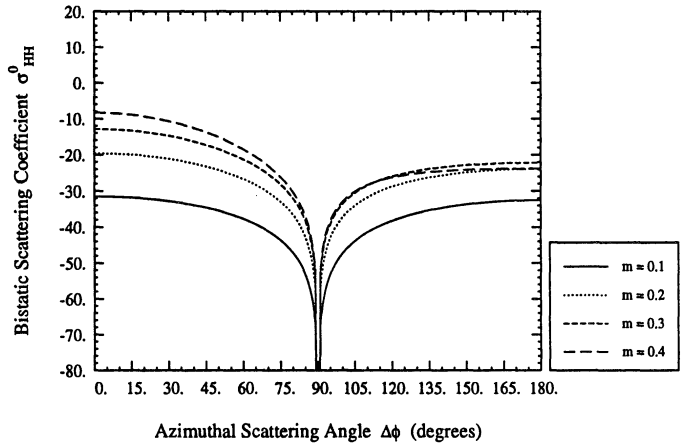

Figure 2.26: Zeroth Order Physical Optics bistatic scattering coefficients for *hh* polarization vs. azimuthal scattering angle for a Gaussian surface with rms slope m varied from 0.1 to 0.4. $\theta_i = \theta_s = 45°$, $\varepsilon_r = 3.0 - j0.0$, $k\sigma = 2.0$. Backscattering corresponds to $\phi_\Delta = 180°$ and specular scattering corresponds to $\phi_\Delta = 0°$. The null at $\phi_\Delta = 90°$ is due to the lack of surface currents generated in the $\hat{\mathbf{h}}_s$ direction for this angle.

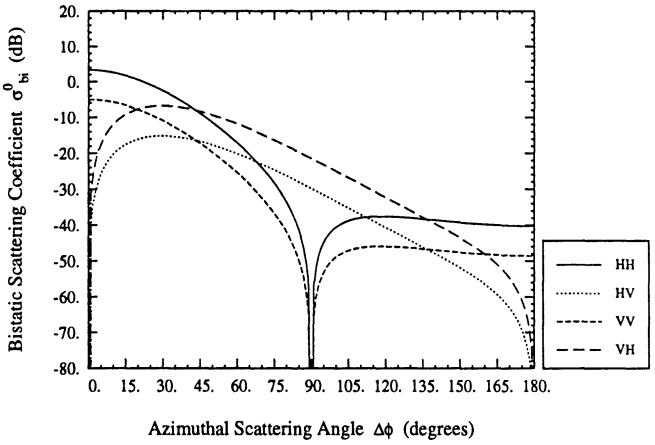

Figure 2.27: Zeroth Order Physical Optics bistatic scattering coefficients for all polarizations vs. azimuthal scattering angle for a Gaussian surface with rms slope fixed at $m = 0.1$, $\varepsilon_r = 3.0 - j0.0$, $k\sigma = 2.0$, $\theta_i = \theta_s = 45°$. Backscattering corresponds to $\phi_\Delta = 180°$ and specular scattering corresponds to $\phi_\Delta = 0°$.

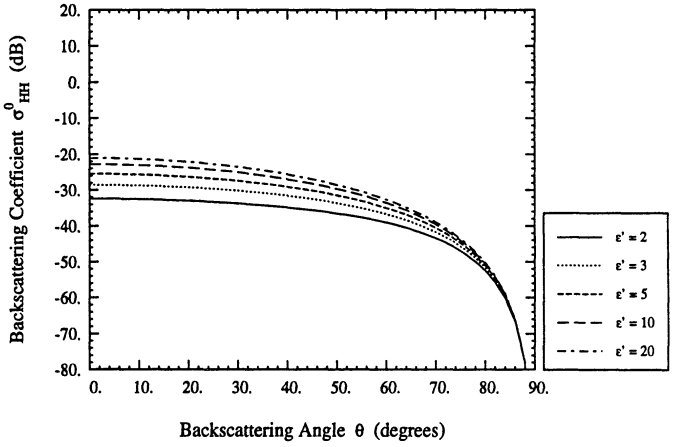

Figure 2.28: Zeroth Order Physical Optics backscattering coefficients vs. incidence angle with surface dielectric varied. The surface has Gaussian correlation with $k\sigma = 1.0$ and $m = 0.2$. The cross-polarized terms are zero.

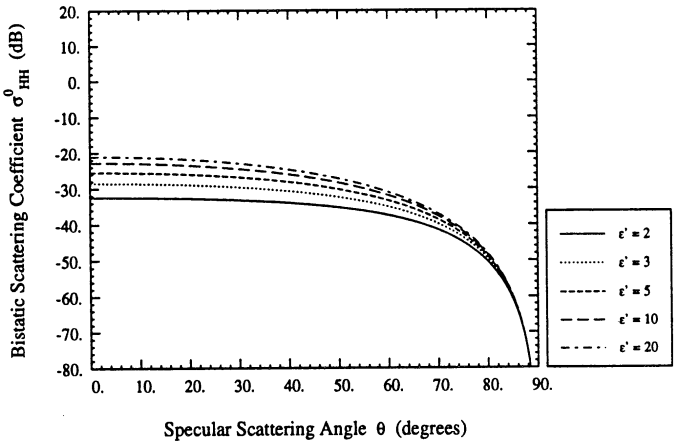

Figure 2.29: Zeroth Order Physical Optics bistatic scattering coefficients in the specular scattering direction for *hh* polarization with surface dielectric varied. The surface has Gaussian correlation with $k\sigma = 1.0$ and $m = 0.2$. The cross-polarized terms are zero.

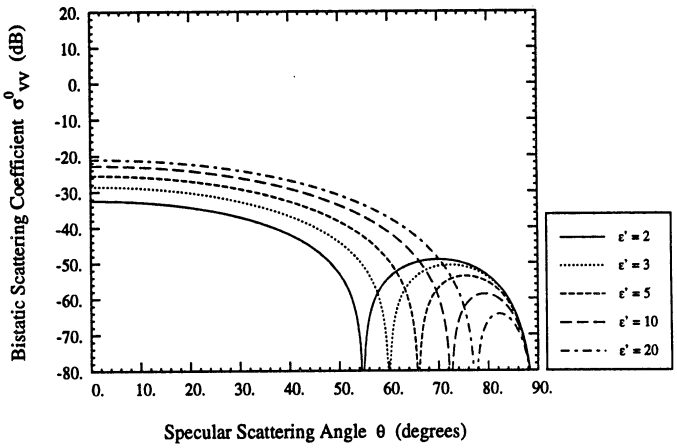

Figure 2.30: Zeroth Order Physical Optics bistatic scattering coefficients in the specular scattering direction for *vv* polarization with surface dielectric varied. The surface has Gaussian correlation with $k\sigma = 1.0$ and $m = 0.2$. The Brewster angle is clearly evident.

ure 2.23 through Figure 2.30. Figure 2.23 shows the dependence of backscattering on the rms slopes. The same basic behavior as predicted by Geometric Optics in Figure 2.13 is observed, but the drop-off is not nearly as sudden. The specular scattering coefficients as a function of rms slopes are shown in Figure 2.24 and Figure 2.25 under the same conditions as Figure 2.14 and Figure 2.15. The Brewster angle is still clearly evident in the *vv* polarized scattering. The significant difference between Geometric Optics and Physical Optics under these conditions is that the Physical Optics model predicts zero scattering at grazing, while the Geometric Optics model is strictly proportional to the reflection coefficient regardless of the closeness to grazing.

Figure 2.26 shows the Physical Optics prediction for scattering in the azimuthal cone for the same surface under the same conditions as in Figure 2.16. Unlike Geometric Optics, the scattering largely increases regardless of direction as the rms slope increases, with the exception of backscattering for the roughest surface. Also, as the zeroth order Physical Optics currents are assumed to be flowing strictly in *x*- and *y*-directions rather than on the surface itself in whatever plane that it lies in locally, as in Geometric Optics, the scattering pattern null occurs at $\phi_\Delta = 90°$. This is the point at which $\hat{\mathbf{h}}_s$ is orthogonal to $\hat{\mathbf{h}}_i$.

The polarization dependence of the azimuthal scattering is shown in Figure 2.27. Since the projections of $\hat{\mathbf{v}}_s$ and $\hat{\mathbf{v}}_i$ on the *x*-*y* plane are orthogonal at $\phi_\Delta = 90°$, the *vv* scattering pattern also exhibits a null at that angle. Since the scattering coefficients are proportional to the reflection coefficient for that angle of incidence, the ratio of σ^0_{hh} to σ^0_{vv}, as well as the ratio of σ^0_{vh} to σ^0_{hv}, is constant regardless of the azimuthal angle ϕ_Δ.

The dependence of the Physical Optics scattering coefficients with changes in dielectric, shown in Figure 2.28, Figure 2.29, and Figure 2.30, largely resembles that of Geometric Op-

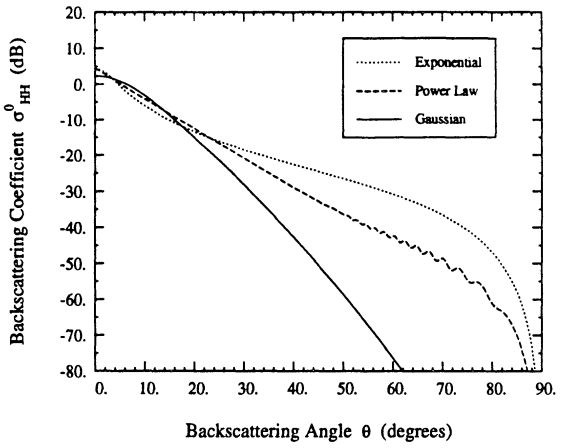

Figure 2.31: Dependence of Zeroth Order Physical Optics Backscattering on the choice of correlation function. $\varepsilon_r = 3.0 - j0.0$, $k\sigma = 0.5$, $kl = 7.0$.

tics. The angular patterns of the Physical Optics scattering is much lower due to the higher rms slopes than the corresponding Geometric Optics figures.

The importance of the choice of the appropriate correlation function is shown in Figure 2.31. The shape of the correlation function is not so important in the specular scattering direction as it is for the backscattering direction. Beyond a backscattering angle of 30°, the form of the correlation function used can make a difference on an the order of magnitude or more. The backscattering as a function of angle behaves much like the correlation function which was assumed. For example, the exponential has the highest tail in Figure 2.5 and the highest backscatter in Figure 2.31. The Gaussian, by contrast, has both the lowest tail in Figure 2.5 and the lowest backscatter in Figure 2.31.

The region of validity for the Physical Optics approach is that for the Kirchhoff Approach plus a limitation on the magnitude of the root-mean-square surface slopes, since the Physical Optics approach is essentially an expansion of the integral (2.51) into a Taylor se-

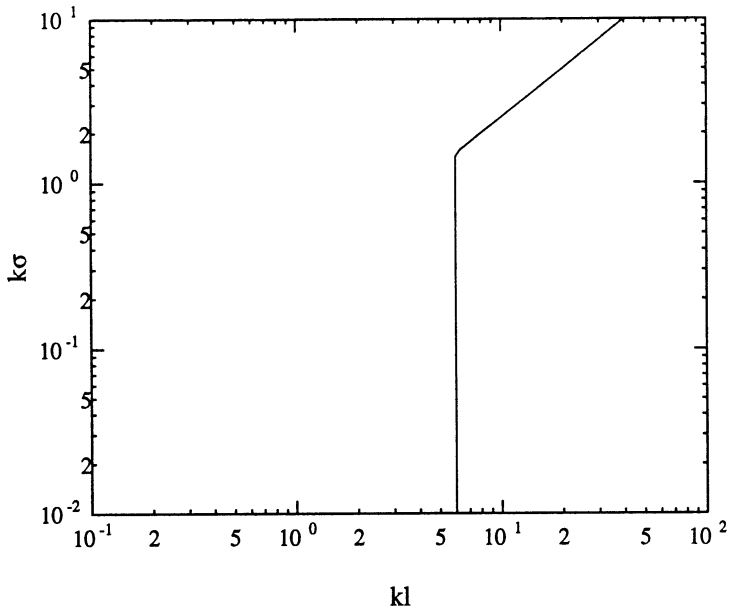

Figure 2.32: Regions of validity for the Physical Optics Approach as described by Ulaby *et al.*. The valid region is to the right of the lines.

ries in slopes. According to Ulaby *et al.* [48], this limitation for Physical Optics, including the first order terms in slopes, is

$$m < 0.25 \tag{2.77}$$

and the corresponding region of validity is shown in Figure 2.32. The region of validity for the higher order terms have not yet been determined.

2.4.4 Small Perturbation Approach

The Small Perturbation approach was originally derived by Rice [33] and later developed by many others [52, 30, 6, 24]. The Small Perturbation expressions can be derived

by two different methods, one using the Rayleigh hypothesis of only outgoing waves from the surface, and one using the Extended Boundary Condition (EBC) or extinction theorem. Using either approach, the surface currents and the scattered fields are expressed in a Taylor series in terms of the height parameter σ. The two methods differ in the integro-differential equations derived from the Stratton-Chu integral (2.47) which are used as the starting point for the perturbation series. Jackson *et al.* [24] show that the two approaches yield the same scattered field up to the fifth order in rms surface height σ, the small parameter of the perturbation series. Brown [6] gives an excellent summary of the similarities and differences in the two approaches. The zeroth order solution is the same as for a plane interface, and the first order solution gives the incoherent scattered field due to single scattering: much like the first order of Physical Optics, or Geometric Optics, the depolarization in the plane of incidence is zero. The scattering coefficients, however, are not strictly proportional to the Fresnel reflection coefficients, as they are in the Kirchhoff approaches, since in the Small Perturbation expansion the vertical components of the incident field also generate first order surface currents. As a result the Brewster angle for *vv* polarization is not evident. Also, the first order solution does not predict any contribution to the coherent scattering. The first order scattering matrix correlation product is

$$\left\langle S_{pq}^{(1)} S_{mn}^{(1)*} \right\rangle = A_0 k_1^2 \sigma^2 \cos^2\theta_s f_{pq} f_{mn}^* W(\kappa_x, \kappa_y) \tag{2.78}$$

where

$$f_{hh} = \frac{k_1}{D_h}((\mu_r-1)\cos\theta_i\cos\theta_s\cos\phi_\Delta(1-R_{h00}) - \eta_r\left(\frac{\mu_r-1}{\mu_r}\sin\theta_i\sin\theta_s+(\varepsilon_r-1)\cos\phi_\Delta\right)(1+R_{h00})\Big) \quad (2.79)$$

$$f_{hv} = \frac{-k_1}{D_h}((\mu_r-1)\cos\theta_s(1+R_{v00})-\eta_r(\varepsilon_r-1)\cos\theta_i(1-R_{v00}))\sin\phi_\Delta \quad (2.80)$$

$$f_{vh} = \frac{-k_1}{D_v}((\mu_r-1)\cos\theta_i(1-R_{h00})-\eta_r(\varepsilon_r-1)\cos\theta_s(1+R_{h00}))\sin\phi_\Delta \quad (2.81)$$

$$f_{vv} = \frac{-k_1}{D_v}\left(\left(\frac{\varepsilon_r-1}{\varepsilon_r}\sin\theta_i\sin\theta_s+(\mu_r-1)\cos\phi_\Delta\right)(1+R_{v00}) + \eta_r(\varepsilon_r-1)\cos\theta_i\cos\theta_s\cos\phi_\Delta(1-R_{v00})\right) \quad (2.82)$$

$$D_h = \eta_r\cos\theta_s+\cos\theta_{st} \quad (2.83)$$

$$D_v = \eta_r\cos\theta_{st}+\cos\theta_s \quad (2.84)$$

where θ_{st} is related to θ_s by Snell's Law: $k_1\sin\theta_s = k_2\sin\theta_{st}$ and $W(\kappa_x,\kappa_y)$ is the surface spectral density given by (2.35).

A number of characteristics of the first order Small Perturbation method are shown in Figure 2.33 through Figure 2.40. Figure 2.33 shows the *hh* backscattering as a function of incidence angle and for different values of the rms slope. Since the roughness is so slight, the backscattering coefficient reduces only slightly with increasing angle; the drop-off for the much rougher surfaces shown in Figure 2.13 and Figure 2.23 is not evident. The incoherent scattering in the specular direction is shown in Figure 2.34 for *hh* polarization and in Figure 2.35 for *vv* polarization. The specular scattering coefficients are not strictly proportional to the reflection coefficients, as evidenced by the monotonic decrease in scattering for *hh*, but the Brewster angle is still very distinct in *vv* polarization. Consistent with Geomet-

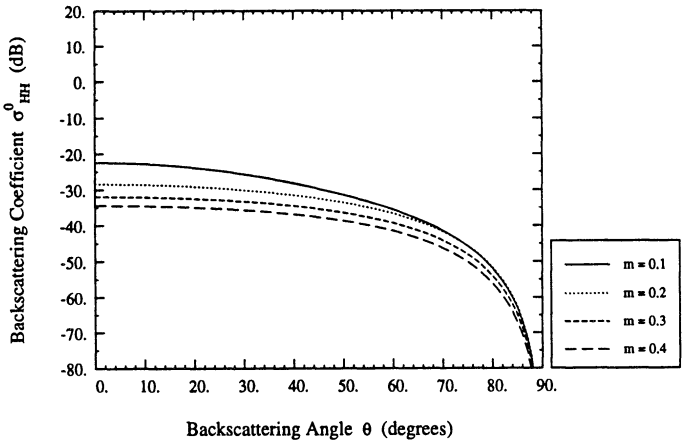

Figure 2.33: First Order Small Perturbation backscattering coefficients vs. incidence angle for a Gaussian surface with rms slope m varied from 0.1 to 0.4. $\varepsilon_r = 3.0 - j0.0, k\sigma = 0.1$. The cross-polarized terms are zero.

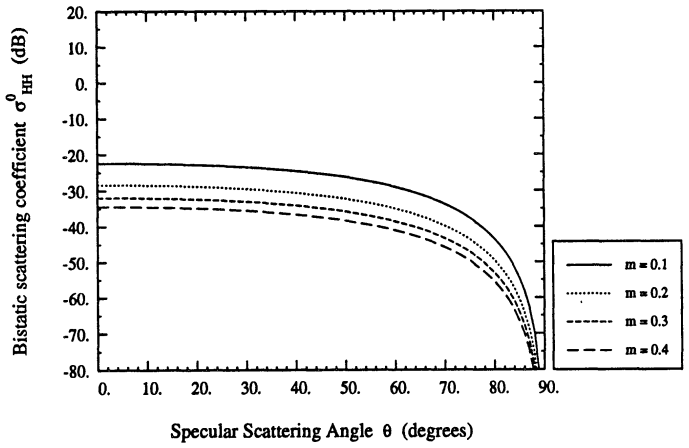

Figure 2.34: First Order Small Perturbation bistatic scattering coefficients in the specular scattering direction for *hh* polarization vs. incidence angle for a Gaussian surface with rms slope m varied from 0.1 to 0.4. $\varepsilon_r = 3.0 - j0.0, k\sigma = 0.1$. The cross-polarized terms are zero.

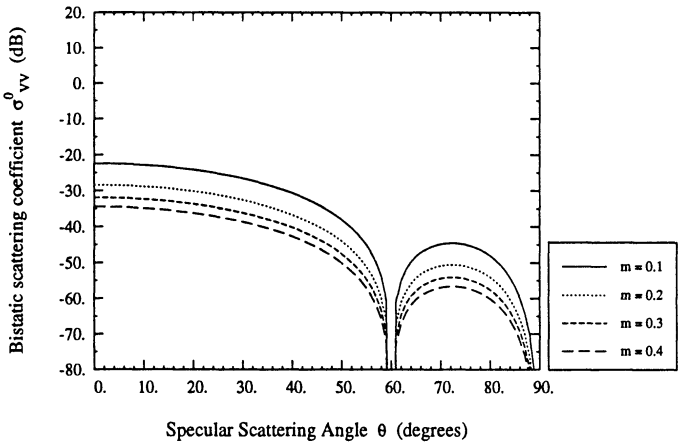

Figure 2.35: First Order Small Perturbation bistatic scattering coefficients in the specular scattering direction for *vv* polarization vs. incidence angle for a Gaussian surface with rms slope m varied from 0.1 to 0.4. $\varepsilon_r = 3.0 - j0.0$, $k\sigma = 0.1$.

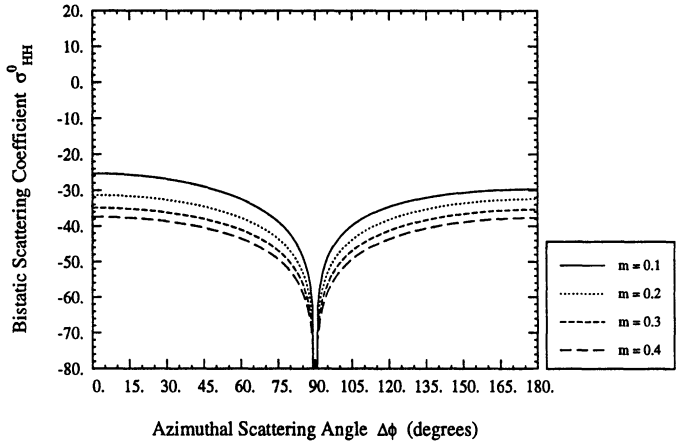

Figure 2.36: First Order Small Perturbation bistatic scattering coefficients for *hh* polarization vs. azimuthal scattering angle for a Gaussian surface with rms slope m varied from 0.1 to 0.4. $\theta_i = \theta_s = 45°$, $\varepsilon_r = 3.0 - j0.0$, $k\sigma = 0.1$. Backscattering corresponds to $\phi_\Delta = 180°$ and specular scattering corresponds to $\phi_\Delta = 0°$.

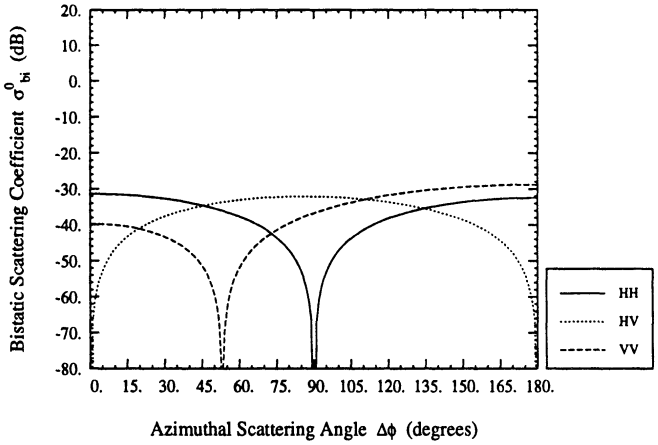

Figure 2.37: First Order Small Perturbation bistatic scattering coefficients for all polarizations vs. azimuthal scattering angle for a Gaussian surface with rms slope fixed at $m = 0.1$, $\varepsilon_r = 3.0 - j0.0$, $k\sigma = 0.1$, $\theta_i = \theta_s = 45°$. Backscattering corresponds to $\phi_\Delta = 180°$ and specular scattering corresponds to $\phi_\Delta = 0°$. $\sigma^0_{vh} = \sigma^0_{hv}$.

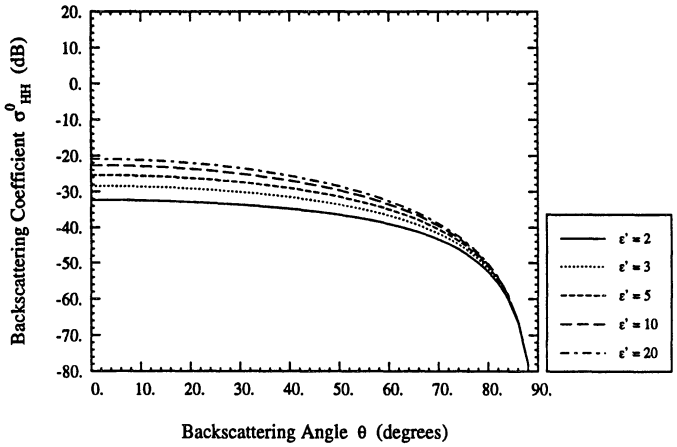

Figure 2.38: First Order Small Perturbation backscattering coefficients vs. incidence angle with surface dielectric varied. The surface has Gaussian correlation with $k\sigma = 0.1$ and $m = 0.2$. The cross-polarized terms are zero.

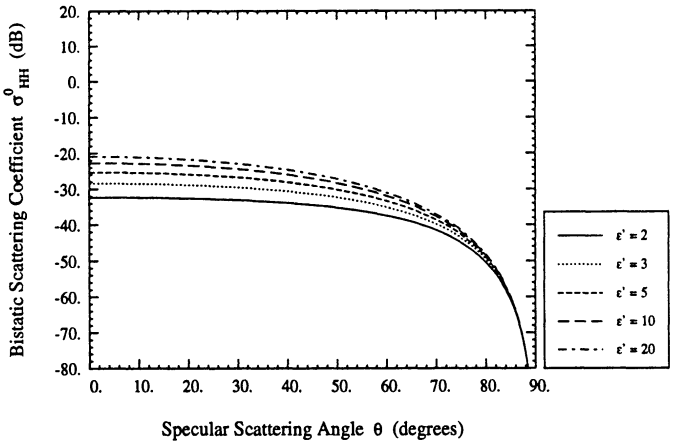

Figure 2.39: First Order Small Perturbation bistatic scattering coefficients in the specular scattering direction for *hh* polarization with surface dielectric varied. The surface has Gaussian correlation with $k\sigma = 0.1$ and $m = 0.2$. The cross-polarized terms are zero.

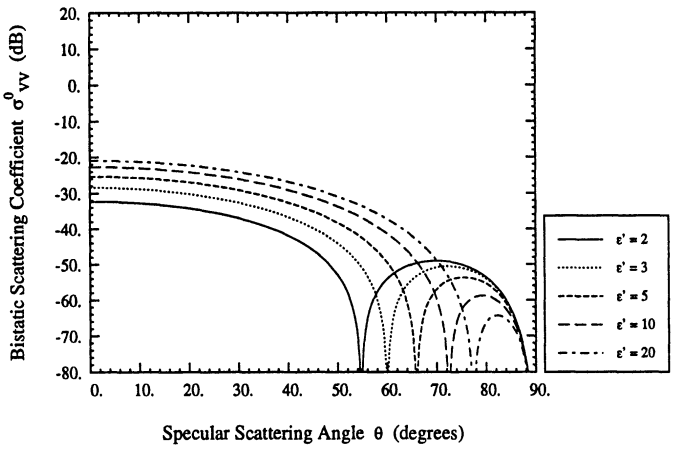

Figure 2.40: First Order Small Perturbation bistatic scattering coefficients in the specular scattering direction for *vv* polarization with surface dielectric varied. The surface has Gaussian correlation with $k\sigma = 0.1$ and $m = 0.2$. The cross-polarized terms are zero. The Brewster angle is clearly evident.

ric Optics and Physical Optics models, the scattering decreases modestly with an increase in rms slope.

The azimuthal dependence of the Small Perturbation approach is shown in Figure 2.36 and Figure 2.37. Like the Physical Optics approach, the surface currents for *hh* polarization are assumed to flow only in the *x*- and *y*- directions, resulting in a pattern null at $\phi_\Delta = 90°$ consistent with that in Figure 2.26. The surface slopes are not completely neglected in the first order Small Perturbation approach, however. The currents due to incident vertical polarization are allowed to flow in the *z*-direction, which results in a *vv* azimuthal pattern (Figure 2.37) that has a null, but its location much more resembles that of the Geometric Optics approach (Figure 2.17) than that of Physical Optics (Figure 2.27). Unlike the much rougher surfaces shown in Figure 2.16 and Figure 2.26, the level of scattering decreases in Figure 2.36 as the rms slope increases.

Figure 2.38, Figure 2.39, and Figure 2.40 show the consistent trend of increased scattering due to increased dielectric in the Small Perturbation approach, which agrees with the predictions of Geometric Optics and Physical Optics.

The second order solution, however, predicts both coherent scattering and depolarization in the plane of incidence. The Small Perturbation reflection coefficients are given by

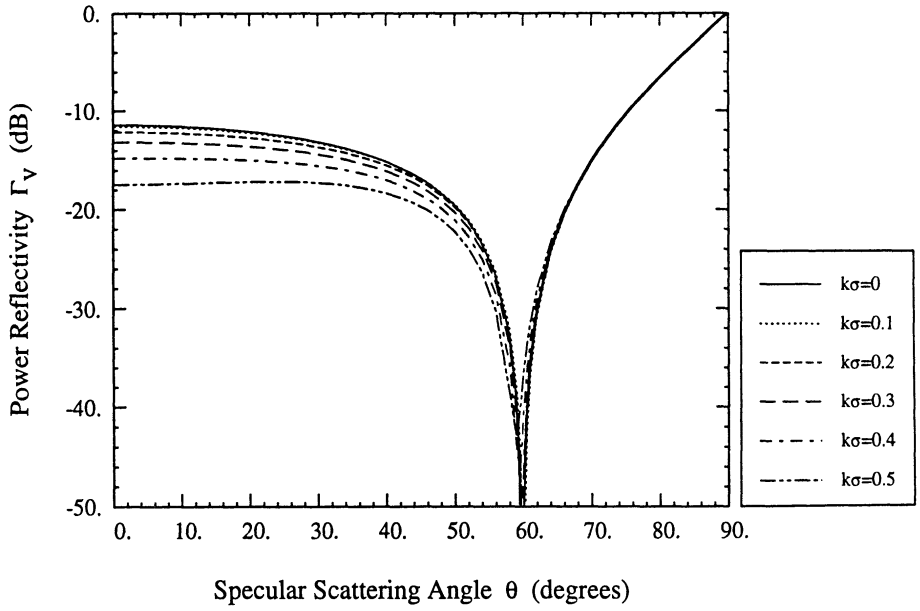

Figure 2.41: Small Perturbation coherent reflectivity for v polarization vs. incidence angle for a Gaussian surface with $k\sigma$ varied from 0 to 0.5, $\varepsilon_r = 3.0 - j0.0$, $kl = 5.0$. The Brewster angle migrates modestly toward nadir as the roughness increases.

[2, 11, 12, 45, 46]:

$$R_{h(SPM)} = R_{h00} + k_{1zi}\frac{k_2^2 - k_1^2}{(k_{1zi}+k_{2zi})^2}\sigma^2 l^2 \int_0^\infty e^{-(k_\rho^2+k_{\rho i}^2)l^2/4} \left\{ \left(k_{2zi} - \frac{k_2^2-k_1^2}{k_{1z}+k_{2z}} \right) I_0(x) + \frac{k_2^2-k_1^2}{k_{1z}+k_{2z}} \frac{k_\rho^2}{k_\rho^2 + k_{1z}k_{2z}} \frac{I_1(x)}{x} \right\} k_\rho dk_\rho \tag{2.85}$$

$$\begin{aligned} R_{v(SPM)} = R_{v00} - k_{zi}\frac{k_1^2-k^2}{(k_1^2 k_{zi} + k^2 k_{1zi})^2} k^2 k_1^2 \sigma^2 l^2 \int_0^\infty e^{-(k_\rho^2+k_{\rho i}^2)l^2/4} \\ \left\{ k_{1zi}\left(I_0(x) - 2\frac{k_\rho k_{\rho i}}{k_\rho^2 + k_z k_{1z}} I_1(x) \right) \right. \\ - \frac{k_1^2-k^2}{k_z+k_{1z}} \frac{k_{1zi}^2}{k_1^2} I_0(x) + \frac{k_1^2-k^2}{k_z+k_{1z}} \frac{k_\rho^2}{k_\rho^2+k_z k_{1z}} \frac{k_{\rho i}^2}{k^2} I_0(x) \\ \left. + \frac{k_1^2-k^2}{k_z+k_{1z}} \frac{k_{1zi}^2}{k_1^2} \frac{k_\rho^2}{k_\rho^2+k_z k_{1z}} \left(I_0(x) - \frac{I_1(x)}{x} \right) \right\} k_\rho dk_\rho \end{aligned} \tag{2.86}$$

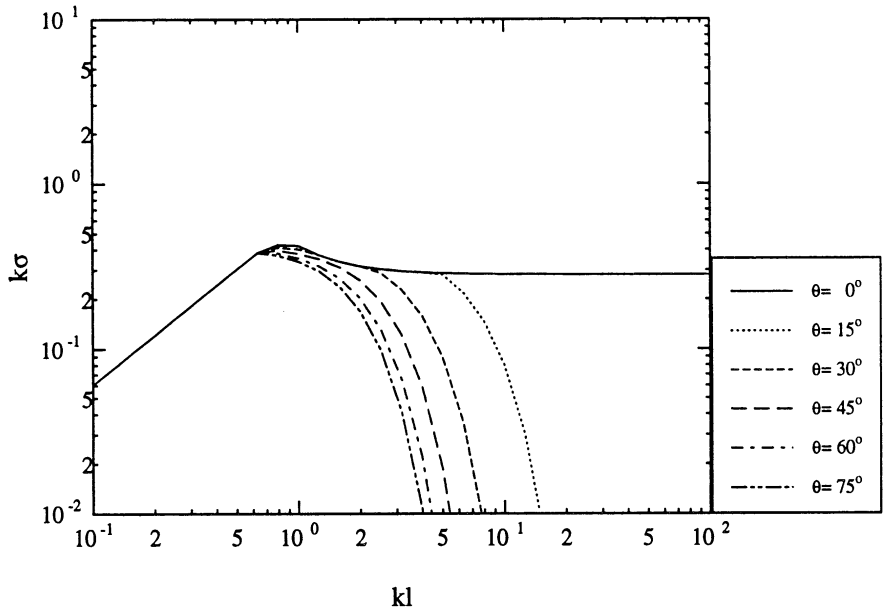

Figure 2.42: Regions of validity for the Small Perturbation Method as described by Thorsos for various backscattering angles. The valid region is below the lines.

where $x = \frac{1}{2}k_\rho k_{\rho i} l^2$, $R_{v,h(SPM)}$ are the vertical and horizontal Small Perturbation Fresnel reflection coefficients, respectively, $k_{1zi} = k_1 \cos\theta_i$, $k_{2zi} = \sqrt{k_2^2 - k_1^2 \sin^2\theta_i}$, $k_{\rho i} = k_1 \sin\theta_i$, $k_{1z}^2 = k_1^2 - k_\rho^2$ and $k_{2z}^2 = k_2^2 - k_\rho^2$ and $I_n(x)$ is the modified Bessel function of order n. The Small Perturbation reflection coefficient for vertical polariztion is shown in Figure 2.41 as a function of incidence angle and for differing rms surface heights. The level reduction at $k\sigma = 0.5$ is slightly than that for Physical Optics in Figure 2.22, but the most significant feature of the Small Perturbation model is the slight change of the location of the Brewster angle as the roughness changes.

The traditional limit of validity for the Small Perturbation Method is that the rms surface height be sufficiently small. Ulaby *et al.* [48], for example, give the region of validity for

the SPM as

$$k\sigma < 0.3 \tag{2.87}$$

$$m < 0.3 \tag{2.88}$$

Since that time numerical investigations by Chen and Fung [8] and a numerical and analytical investigation by Thorsos and Jackson [44] on a one-dimensional perfectly conducting surface with Gaussian statistics show that the SPM region of validity for first order incoherent scattering of scalar waves can be more precisely stated as

$$k\sigma < \min\left(\frac{0.428e^{-k^2l^2(\sin\theta_i-\sin\theta_s')^2/16}}{\sqrt{1-\left(\frac{\sin\theta_i+\sin\theta_s'}{2}\right)^2}}, 0.282\left(1+\frac{1}{2k^2l^2}\right)\right) \tag{2.89}$$

$$m < 0.6051 \tag{2.90}$$

to guarantee that the error does not exceed 1 dB. The numerical analyses indicate that the above inequalities are slightly conservative. The conditions evaluated in the above papers are restricted to the plane of incidence for a two dimensional problem; they are, however, likely to be indicitive of the region of validity for the general bistatic case. The scattering angle θ_s' is similar to θ_s in that it is a measure of the direction away from the $\hat{\mathbf{z}}$-axis but it may take a negative value so that the entire plane of incidence is covered by (2.89). Specular scattering occurs when $\theta_s' = \theta_i$ and backscattering occurs when $\theta_s' = -\theta_i$. Thorsos' Small Perturbation region of validity for backscattering is shown in Figure 2.42 for several values of the backscattering angle. In the specular scattering direction incoherent scattering is

dominated by coherent scattering, but the validity of the Small Perturbation prediction for coherent scattering was not analyzed in either of the above papers.

2.5 Review of Bistatic Data

While all this theoretical development is valuable, it is incomplete without experimental verification of the theories' regions of validity. Some work has been done on theory verification by means of computer simulations of rough surface scattering [8, 5], but the author is only aware of two published experimental works on bistatic rough surface scattering done at microwave frequencies.

In the optical regime, Leader and Dalton [28] investigated bistatic scattering from dielectrics and came to the conclusion that depolarization originated in volume scattering. Later, O'Donnell and Mendez [31] measured perfectly conducting rough surfaces with light in search of backscattering enhancement. While their data are not normalized to a radar cross section, they do publish both co- and cross-polarized scattering data in their correct ratio. Saillard and Maystre [35] have simulated the bistatic scattering of light from dielectric surfaces, and have observed a change in the Brewster angle as the roughness of the surface increased. Greffet [20] explained their observations using the Small Perturbation Method [33]. Phu *et al.* [32] reported millimeter-wave scattering measurements from several one-dimensional perfectly conducting Gaussian rough surfaces.

Several experimental investigations were conducted at centimeter wavelengths in the 1946-1960 period to evaluate the variation of the coherent and incoherent components of the specularly reflected energy as a function of surface roughness. The results for the coherent

component, which is represented by the reflection coefficient, are summarized in Beckmann and Spizzichino [3]. According to these results, the overall variation of the reflection coefficient with $k\sigma$, where $k = 2\pi/\lambda$, and σ is the rms height, may be explained by the coherent scattering term of the Physical Optics surface scattering model [3, 48]. The data, however, are rather lacking in several respects: (1) marginal accuracy with regard to both the measured reflected signal and the surface rms height, (2) limited dynamic range (10 dB relative to the level of the signal reflected from a perfectly smooth surface), and (3) no examination of the behavior in the angular region around the Brewster angle. Additional bistatic measurements at 1.15 GHz were reported by Cosgriff *et al.*[9] in 1960, but the data were not calibrated, nor were the surfaces characterized. Their work represented the only published experimental work in bistatic radar surface scattering for over 25 years.

More recently, Ulaby *et al.*[50] measured bistatic scattering from sand and gravel surfaces at 35 GHz in the plane of incidence and as a function of azimuth for a pair of fixed incidence and receive angles. While the data were calibrated and the surfaces were characterized, no comparison to a theoretical prediction was given.

2.5.1 Coherent Scattering

At the Brewster angle, the reflectivity for the vertical polarization is identically zero for a smooth interface. Whether it is still identically zero for a slightly rough surface is not clear. The Physical Optics approach clearly predicts that this is so, moreover, it predicts that the minimum reflectivity remains at the same incidence angle as for a smooth surface. This can be seen in Figure 2.22. However, the Small Perturbation method predicts that the angle of

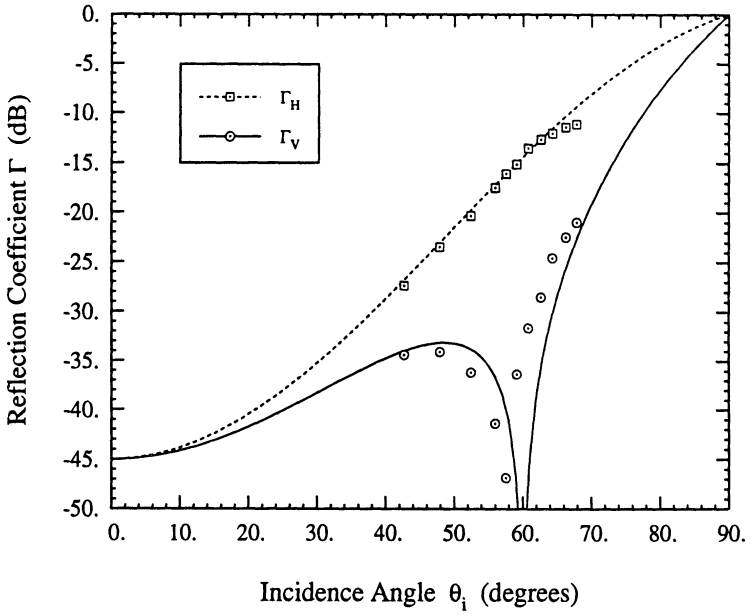

Figure 2.43: Measured coherent reflectivity of the surface shown in Figure 2.2 through Figure 2.4. Solid lines are predictions of Physical Optics for this surface, which has a relative dielectric constant $\varepsilon = 3.0$ and rms surface height $k\sigma = 1.39$. The angle of minimum reflectivity for vertical polarization is less than that for a smooth surface of the same material.

minimum vertical reflectance decreases slightly with increasing roughness of the surface, as can be seen from Figure 2.41. The fact that Physical Optics does not predict a change in angle while the Small Perturbation does is a consequence of the fact that the correction to the Fresnel coefficient is purely multiplicative for Physical Optics while it is additive for Small Perturbation. As will be seen in Chapter 5, higher order terms in Physical Optics are also additive and will move the Brewster angle much like the Small Perturbation approach does. Figure 2.43 shows the results of one of my measurements of the Brewster angle for a rough surface, indicating that the minimum reflectivity does slightly change angle with increasing roughness. The change is toward decreasing angle of incidence, in qualitative agreement with the Small Perturbation method.

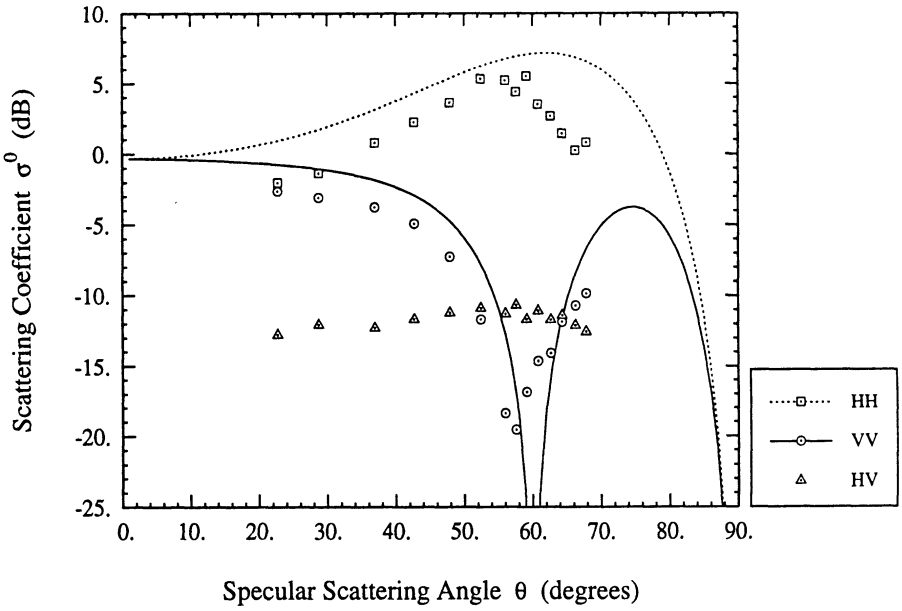

Figure 2.44: Measured incoherent scattering from the surface shown in Figure 2.2 through Figure 2.4. Solid lines are predictions of Physical Optics for this surface, which has a dielectric constant $\varepsilon = 3.0$, and a power law correlation with rms surface height $k\sigma = 1.39$ and correlation length $kl = 10.6$.

2.5.2 Incoherent Scattering

An example of incoherent scattering in the forward direction is shown in Figure 2.44. Three polarizations are shown in the figure; the fourth, *vh*, shows evidence of contamination by *hh* and is not shown. While there are serious quantitative differences between the measured data and the prediction of Physical Optics, it must be noted that several qualitative features are present which the Physical Optics model does not predict. Most important of these is the existence of cross-polarized scattering in the plane of incidence. Another is the lack of a sharp Brewster angle for σ^0_{vv}. Experimentally searching for nulls like the Brewster angle in angular patterns is an intrinsically difficult task, since a failure to discover a sharp, deep null could be due to many causes other than the non-existence of the null. In

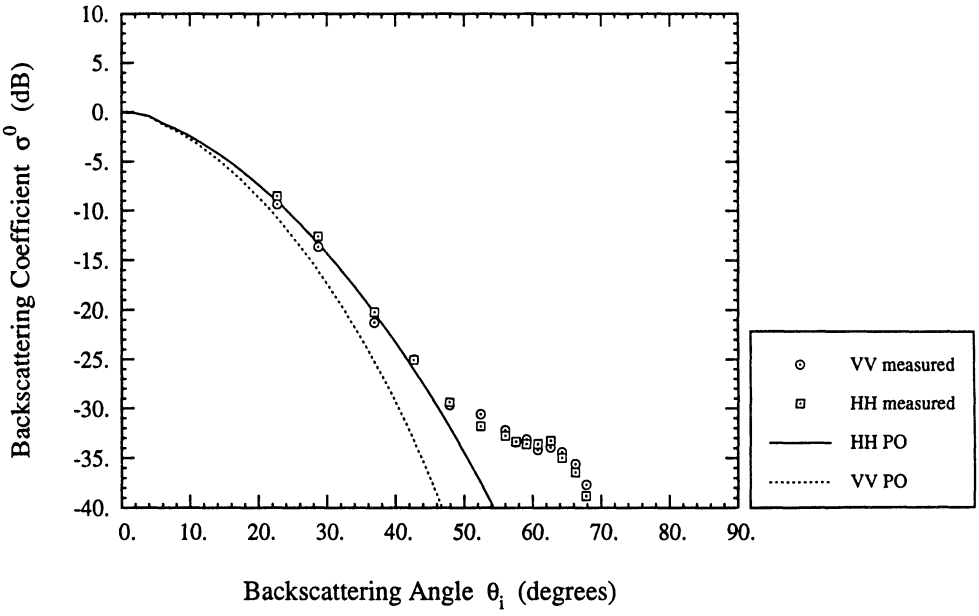

Figure 2.45: Measured incoherent backscattering from the surface shown in Figure 2.2 through Figure 2.4. Solid lines are predictions of Physical Optics for this surface, which has a dielectric constant $\varepsilon = 3.0$, and a power law correlation with rms surface height $k\sigma = 1.39$ and correlation length $kl = 10.6$. The measured cross-polarization shows evidence of contamination and is not shown.

this case, it is particularly unclear if coherent or polarization contamination has occurred since it is also possible that an important aspect of the surface has been misclassified or if the calibration is faulty.

Backscattering measurements have also been made on this surface. The results, together with the Physical Optics prediction, are shown in Figure 2.45. Much as the shape of angular pattern of coherent scattering is dependent on the surface height probability distribution, the shape of the backscattering angular pattern is a strong function of the form of the correlation function. The reasonableness of the fit, especially for σ^0_{hh}, in Figure 2.45 is strong evidence for the use of the power law form of the correlation function. While all three forms of the

correlation function yield approximately the same numerical values for the backscattering coefficient for nadir to 30°, the Gaussian underestimates the scattering by 20 dB at 50°, and the exponential overestimates scattering by 10 dB at 50°.

2.5.3 Depolarization

Electromagnetic waves, unlike scalar waves, have a polarization state which can be altered by interaction with a rough surface. How well do these theories, both single scattering and multiple scattering, predict depolarization? While Fung has shown that the Geometric Optics solution to the Kirchhoff scattering problem does not produce depolarization in the plane of incidence [16], he has also shown, however, in the same paper, how the inclusion of multiple scattering, *via* shadowing, can contribute to depolarization in the plane of incidence. Holzer and Sung [21] have derived depolarization in the plane of incidence for single scattering under a Kirchhoff solution by expanding the local surface in a Taylor series to squared terms in surface slope. They show that the depolarization is due to the local slopes transverse to the plane of incidence; numerical results, to show the magnitude of the predicted depolarization, are not given.

Rice [33] did not use his Small Perturbation approach to predict any depolarization, but since then Valenzuela [52] has shown that depolarization in the plane of incidence is a second order effect, and is due to multiple scattering.

Unfortunately, polarization changes are difficult to measure because depolarized signals can be generated by many mechanisms other than a rough surface. For the surface shown in Figure 2.2 through Figure 2.4, volume scattering has been measured at levels near $\sigma^0 =$

−50 dB and is therefore a negligible source of depolarization.

2.5.4 Polarimetry

The fact that electromagnetic waves possess polarization states gives rise to the possibility that scattering from surfaces may cause relative phase shifts for different polarization states. None of the theories developed here show any evidence that rough surfaces would cause any phase shift other than 0° or 180° between *vv* and *hh* scattered fields. My measurements indicate that this may be true for forward scattering, but for backscattering the phase shift appears to be roughly equal to the backscattering angle.

CHAPTER 3

System

3.1 System Specification

The Bistatic Measurement Facility, or its predecessors, which were functionally equivalent, was used to obtain the measurements of the rough surfaces reported in this dissertation. A photograph of the Bistatic Measurement Facility appears in Figure 3.1. It is a stepped-frequency (8.5–10 GHz) measurement system capable of measuring the scattering matrix **S** of the target contained in the area or volume formed by the intersection of the transmit and receive antenna beams. Using an HP8720 vector network analyzer with an amplifier on the transmitting antenna, the system measures a complex voltage for any pair of *v* or *h* receive and transmit polarization states. With proper calibration, it is capable of measuring all four complex elements of the scattering matrix of the target surface. The hardware allows the transmitter and receiver to be located independently at any point on a hemispherical shell 2.1 m from the center of the target. In practice, however, measurements are accurate only when both antennas are within 70° of nadir.

The receive antenna is a dual-polarized horn antenna with a beamwidth of 12°, and the transmit antenna is a dual-polarized parabolic dish whose feed was designed such that the

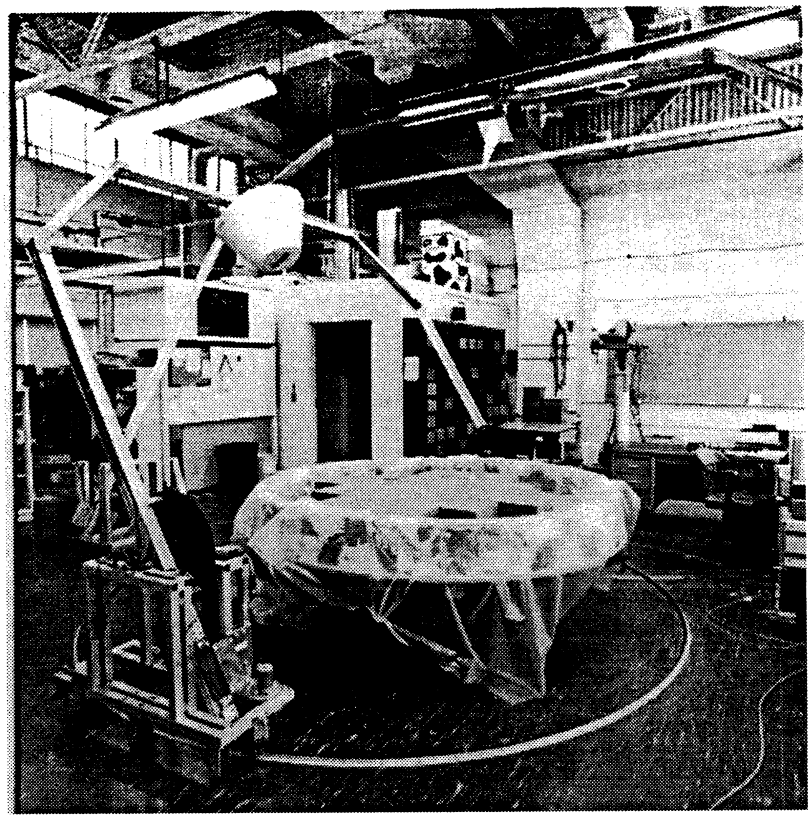

Figure 3.1: The Bistatic Measurement Facility. On the left is a dual polarized transmitter mounted on an arch which can go from 0° to 90° in elevation and 0° to 360° in azimuth. Above and to the right is a dual polarized transmitter/receiver, which ranges from 0° to 90° in elevation. The target holder consists of a wading pool mounted on a turntable; the target is a set of water–absorbing foam bricks.

main beam of the parabolic dish is focused at a range equal to the distance to the target surface, which is held constant for all measurements. Because of the larger aperture (30 cm diameter), the transmit antenna has a narrow beam of 5°, which dictates the extent of the surface area responsible for the scattered energy. By using a focused beam antenna, we achieve a narrow-beam configuration without having to satisfy the usual far-field criterion. A baffle made of radar absorbing material was placed in the direct path between the transmitter and receiver to insure proper isolation of the two antennas.

The Bistatic Measurement Facility (BMF) uses an X-band bistatic radar system mounted on rotatable arches in order to measure the RCS of point targets or the bistatic scattering

coefficient of distributed targets over a wide range of incident and scattering directions. Table 3.1 provides a summary of the system specifications. The sweet spot refers to the region near the center of the Bistatic Measurement Facility where the incident field is sufficiently planar to accurately measure a radar cross section. Refer to Section A.1.1 of Appendix A for more details on using the sweet spot. The noise equivalent measurements refer to the values that the BMF reports when there is no scattering target observed, and represent the minimum values which are obtainable. The bistatic noise equivalents are measured in the specular direction, and the incidence angle is given. The noise equivalent measurements in the specular direction with the angle of incidence at 70° exhibits a higher value than does the similar measurement at 30° because some power leaks directly from the transmitter to the receiver. The noise equivalent measurements at 30° should be indicative of typical noise equivalents at most combinations of the bistatic angles where the antennas are not nearly pointed directly at each other.

A block diagram of the microwave components of the Bistatic Measurement Facility is shown in Figure 3.2. The horn serves as both the bistatic receiver and the backscatter antenna, and is mounted on the outer arch. The dish, mounted on the inner arch, is the transmitter when the BMF is in bistatic mode. Details of the microwave components, including the antenna patterns for horn and dish, are given in the next section.

3.2 Antennas

The antenna patterns, measured at the operating ranges given in Table 3.1, are given in Figures 3.3 thru 3.6. The patterns for the Dish are measured with the dish as the transmitter;

User supplied Network Analyzer	NWA	Hewlett-Packard 8510 or 8720
Network Analyzer Measurement Response		S21
Frequency Bandwidth	B	1.52 GHz
Center Frequency	f_c	9.25 GHz
Frequency Sweep Type		linear, 201 freq. pts.
Calibration Accuracy		±1 dB
Positional Accuracy (all axes)		±0.1°
Bistatic Transmitter:		
Antenna Type		Dish reflector
Polarizations	q	v and h
v-pol. Elevation One Way FWHP Beamwidth	β_{tv}^{el}	5.0°
v-pol. Azimuth One Way FWHP Beamwidth	β_{tv}^{az}	4.7°
h-pol. Elevation One Way FWHP Beamwidth	β_{th}^{el}	4.6°
h-pol. Azimuth One Way FWHP Beamwidth	β_{th}^{az}	4.6°
Range, aperture to BMF center	R_{t0}	2.11 m
Raw Polarization Isolation		>30 dB
Bistatic Receiver / Backscatter Antenna:		
Antenna Type		Horn with lens
Polarizations	p	v and h
v-pol. Elevation One Way FWHP Beamwidth	β_{rv}^{el}	9.8°
v-pol. Azimuth One Way FWHP Beamwidth	β_{rv}^{az}	11.3°
h-pol. Elevation One Way FWHP Beamwidth	β_{rh}^{el}	11.1°
h-pol. Azimuth One Way FWHP Beamwidth	β_{rh}^{az}	9.7°
Range, aperture to BMF center	R_{r0}	3.36 m
Raw Polarization Isolation		>30 dB
Bistatic Mode:		
Maximum Transmit Power Level	P^t	20 dBm
Approximate Diameter of "Sweet Spot"		9 cm
Noise Equivalent RCS at 30°	σ_{min}	<-50 dBsm
Noise Equivalent RCS at 70°	σ_{min}	<-30 dBsm
Approximate Effective Illuminated Area	A_{ill}	266 $cm^2 \sec\theta_t$
Noise Equivalent Scattering Coefficient at 30°	σ^0_{min}	<-45 dB
Noise Equivalent Scattering Coefficient at 70°	σ^0_{min}	<-30 dB
Backscatter Mode:		
Maximum Transmit Power Level	P^t	10 dBm
Approximate Diameter of "Sweet Spot"		>15 cm
Noise Equivalent RCS	σ_{min}	<-40 dBsm
Approximate Effective Illuminated Area	A_{ill}	2720 $cm^2 \sec\theta_r$
Noise Equivalent Scattering Coefficient	σ^0_{min}	<-30 dB

Table 3.1: Bistatic Measurement Facility system specifications

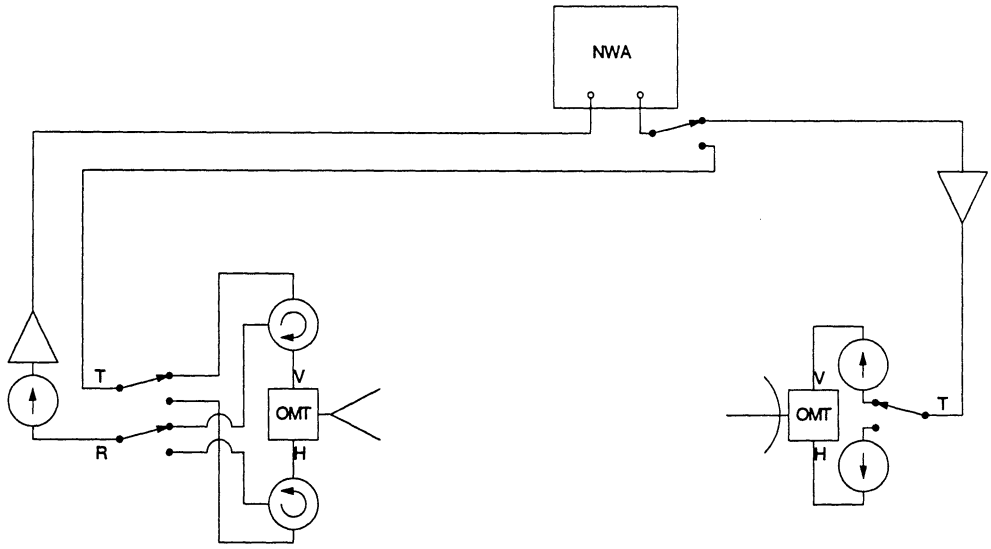

Figure 3.2: Bistatic System Microwave Block Diagram

the patterns for the Horn are measured with the horn as the receiver. The patterns for the Horn as transmitter are the same as for the Horn as receiver.

3.2.1 Dish Antenna

The construction of the Dish Antenna, which is used as the bistatic transmitter, is such that the most important element, namely the dish, is not visible. The polystyrene which conceals most of the elements of the dish comprises a rigid and strong support which holds the active components precisely in their correct locations, yet is practically invisible to microwaves. The dish feed, of which the orthomode and waveguide-to-coax transitions are visible in front, is held in its location relative to the dish by the polystyrene block. The dish and feed are attached to the polystyrene block with foam polyurethane. The polystyrene block is in turn permanently attached to the back plate by wood screws.

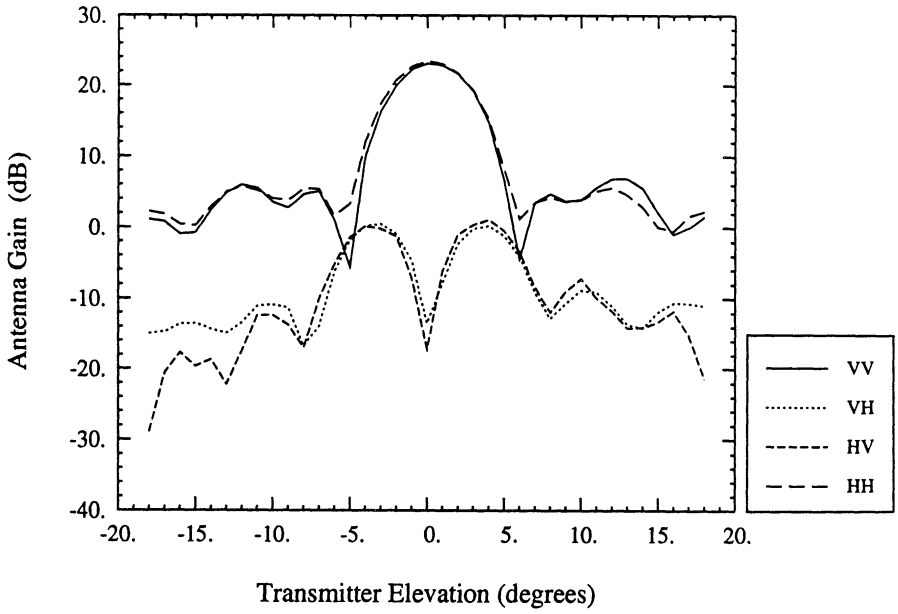

Figure 3.3: Dish Elevation One-Way Patterns.

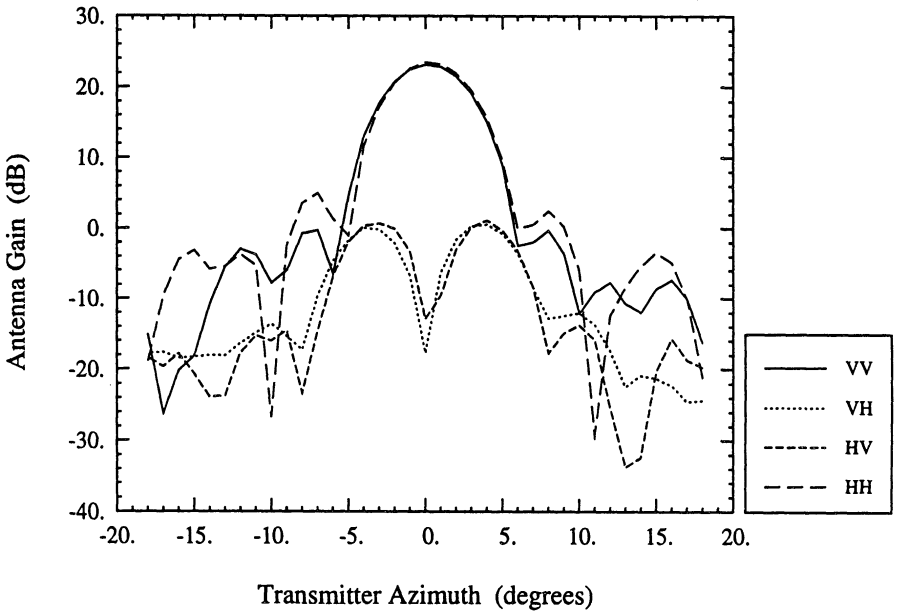

Figure 3.4: Dish Azimuth One-Way Patterns.

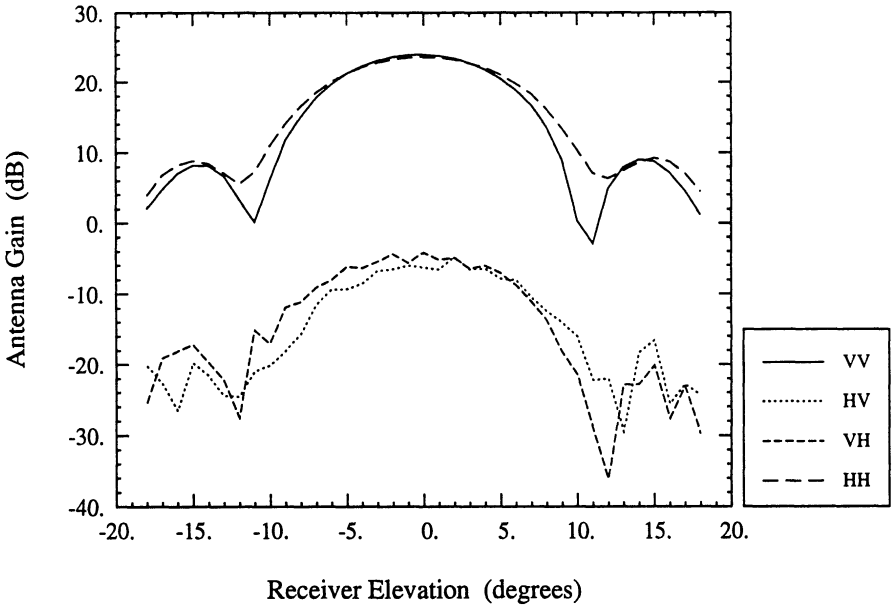

Figure 3.5: Horn Elevation One-Way Patterns.

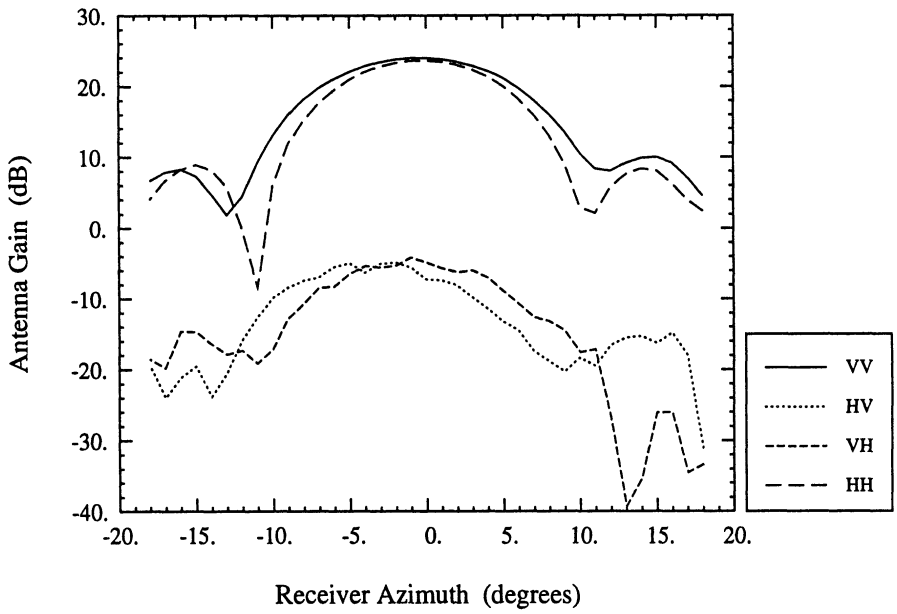

Figure 3.6: Horn Azimuth One-Way Patterns.

3.2.2 Horn Antenna

The most impressive feature of the Horn antenna is the polystyrene lens placed in the aperture. It narrows the horn antenna one-way beamwidth from approximately 17° without a lens to about 10° with the lens. The lens itself is very simple. It is made from two polystyrene cones, one extending outside the horn and one inside it, and a piece of 1 inch thick polystyrene sheet cut to the size of the aperture. The pieces are held together with epoxy cement. The horn has multiple flares, each no greater than 5°, designed to reduce internal reflections within the antenna and supporting circuitry.

3.3 Laser Profiler

The surfaces were characterized by a Laser Profiler, a device engineered at the University of Michigan to measure 2 meter linear or 1 meter by 1 meter square sections of surface profiles. The Profiler is shown in 2 meter linear mode in Figure 3.7. Using a Pulsar 50 Electronic Distancemeter manufactured by GEO Fennel, it can measure profiles of surfaces without direct contact. The profiler has a horizontal resolution of 1 mm and a vertical resolution of 2 mm. Figure 2.3 is an example of the height histogram generated from the profile measured for one of the surfaces, and Figure 2.4 shows the corresponding correlation function.

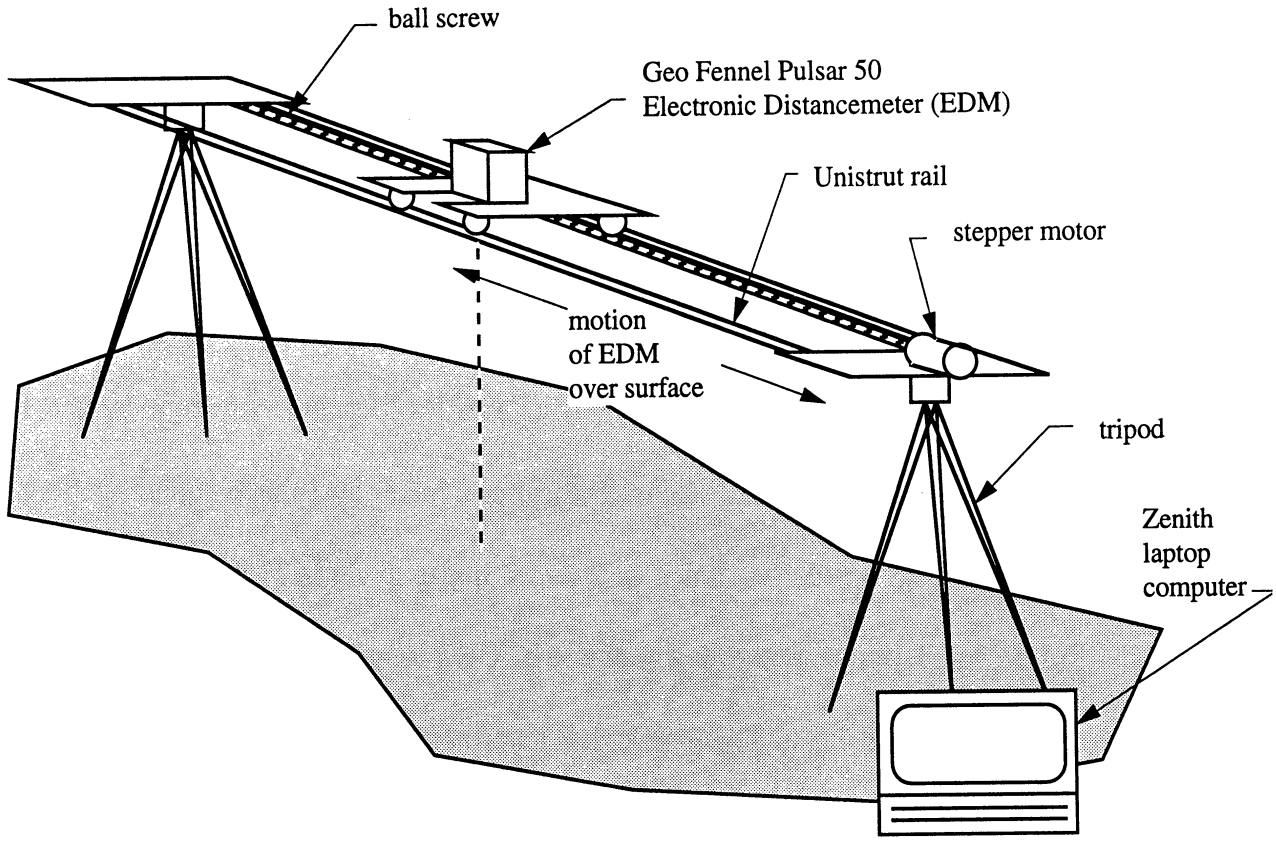

Figure 3.7: Diagram of Laser Profiler

CHAPTER 4

Calibration

The network analyzer measures only the the ratio of received to transmitted power. This ratio is dependent on the polarization state, the geometry of the Bistatic Measurement Facility, and, of course, the target. This ratio can be converted into a useful quantity, such as the bistatic radar cross section σ or the scattering coefficient σ^0, only after calibration. The calibration procedures are described in Section A.3.6 and Section A.3.7. But first, a brief introduction is presented to acquaint the reader with the general concept of distortion matrices and associated terminology.

4.1 Distortion Matrix Model

The distortion matrix model [53] was developed to analyze the relationships between the ideal scattering characteristics of a point target and the actual signals measured by a NWA. The method is very similar to the S-parameter analysis method used in conjunction with microwave networks. A review of the calibration documentation for a typical NWA is very instructive towards the general approaches that are described in this chapter.

The Bistatic Facility, regardless of whether it is in bistatic or in backscatter mode, can

measure four quantities for each target position. These are four complex voltage ratios corresponding to four combinations of the transmit and receive polarizations. The transmitter is equipped with a polarization switch which can be actuated to cause the antenna to transmit a nominally horizontally polarized or nominally vertically polarized wave. Similarly, the receiver is equipped with a similar polarization switch that causes the receive antenna to accept a nominally vertically or nominally horizontally polarized wave. Deviations from the perfect polarization state are called distortions, and the purpose of the calibration procedure is to correct them.

The four measurements constitute a 2×2 scattering matrix, denoted **M** (for the *measured* scattering matrix), with elements denoted M_{rt}, where r represents the nominal receive polarization (either v or h), and t represents the nominal transmit polarization (again, either v or h). **M** can be considered to consist of two terms, an undesired signal **B** due to *background* effects, and a desired signal due to the target **S** distorted by an imperfect transmitter **T** and an imperfect receiver **R**, and scaled by a constant:

$$\mathbf{M} = \mathbf{B} + k_{cal}\mathbf{RST} \tag{4.1}$$

or,

$$\begin{bmatrix} M_{vv} & M_{vh} \\ M_{hv} & M_{hh} \end{bmatrix} = \begin{bmatrix} B_{vv} & B_{vh} \\ B_{hv} & B_{hh} \end{bmatrix} + k_{cal} \begin{bmatrix} R_{vv} & R_{vh} \\ R_{hv} & R_{hh} \end{bmatrix} \begin{bmatrix} S_{vv} & S_{vh} \\ S_{hv} & S_{hh} \end{bmatrix} \begin{bmatrix} T_{vv} & T_{vh} \\ T_{hv} & T_{hh} \end{bmatrix} \tag{4.2}$$

where all the matrix elements are complex. Thermal noise is assumed to be negligibly small.

The background term **B** can be directly measured in the absence of a target (i.e., when $\mathbf{S} = 0$) and then, if not already negligibly small, subtracted from the measured scattering matrix to give the distorted signal from the desired target:

$$\mathbf{N} = \mathbf{M} - \mathbf{B} \;=\; k_{cal}\mathbf{RST} \tag{4.3}$$

If a measurement of **B** results in the measurement of noise (i.e., the measurements of **B** are not repeatable), then the background should be ignored by assigning all the elements of **B** to zero.

S is the 2×2 polarimetric scattering matrix of the target under examination. Its complex elements are functions of the bistatic angles $(\theta_t, \theta_r, \phi_t)$ as well as the target's orientation (θ_j, ϕ_j). When **S** is theoretically known, as for calibration targets, it will be denoted **P**.

R is the 2×2 distortion matrix for the receive antenna, and represents the effects (gain, loss, phase delay, etc) of the horn, orthomode, circulators, transitions, and plumbing up to and including the microwave switch. For example, R_{pq} is the signal measured at the common terminal of the microwave switch while it is in the p-polarized position and the antenna is illuminated with a perfect unit amplitude q-polarized plane wave. Since the target is designed to always reside in the receive antenna's far field, the R_{pq} elements incorporate the $\frac{e^{ikR_r}}{R_r}$ range dependence. The matrix elements also incorporate the antenna gain by being functions of the directions from the antenna (as measured from boresight). Within the main beam, $|R_{pq}| \ll |R_{qq}|$. **R** is the same regardless of whether the system is in backscatter or bistatic mode, since the same hardware is used to receive in both modes.

T is the 2×2 distortion matrix for the transmit antenna, and represents the effects (gain, loss, phase delay, etc) of the feed horn, dish and supports, orthomode, transitions, isolators, and plumbing up to and including the microwave switch. T_{pq} is the amplitude and phase of the p-polarized component of the transmitted wave when the microwave switch is in the q-polarized position and a unit amplitude signal applied to the common terminal of the switch. Unlike **R**, **T** depends on measurement mode of the system. For backscattering, **T** has very similar range and direction characteristics as does **R**. The bistatic transmit module, however, is not designed to operate with the target in its far field, and thus the T_{pq} elements are more complicated functions of direction (as measured from boresight) and range from the antenna. Within the main beam, $|T_{pq}| \ll |T_{qq}|$.

k_{cal} is a complex constant accounting for the change in amplitude and phase of the signal due to elements in common for all measurement polarizations. This includes all the active elements (amplifiers and the NWA), as well as the microwave plumbing up to the antenna modules. If some of the plumbing has been damaged or if plumbing connections have come loose, it may change with respect to the bistatic angles, but the system was designed such that this constant remains unchanged over long periods of time, regardless of the measurements made.

Calibration then is the measuring of a set of targets with theoretically known $\mathbf{P}^{cal}$ and using the corresponding $\mathbf{N}^{cal}$ to determine an unknown $\mathbf{S}^{unk}$ from a measurement $\mathbf{N}^{unk}$. The resulting $\mathbf{S}^{unk}$ has the same units as $\mathbf{P}^{cal}$. In other words, if a sphere is used as a calibration target, then $\mathbf{S}^{unk}$ will be reported as a radar cross section, whereas if a large conducting plate is used as a calibration target the unknown targets will be reported in units of reflectivity. No reliable distributed targets have been developed for the purpose of calibration, so if the

unknown targets are distributed the measurements must be translated into a differential radar cross section σ^0.

4.2 General Calibration Technique

Whitt and Ulaby [53] developed a calibration technique, known as the General Calibration Technique, with which the matrices **R** and **T** can be determined by using three calibration targets with known characteristics $\mathbf{P}_1, \mathbf{P}_2, \mathbf{P}_3$ and the following conditions:

(1) $\mathbf{P}_1$ (at least) is an invertible matrix.

(2) Both $\mathbf{P}_1^{-1}\mathbf{P}_2$ and $\mathbf{P}_1^{-1}\mathbf{P}_3$ must have distinct eigenvalues; i.e., $\lambda_1 \neq \lambda_2$.

(3) $\mathbf{P}_1^{-1}\mathbf{P}_2$ and $\mathbf{P}_1^{-1}\mathbf{P}_3$ must have no more than one common eigenvector.

(4) Both $\mathbf{P}_1^{-1}\mathbf{P}_2$ and $\mathbf{P}_1^{-1}\mathbf{P}_3$ must have eigenvalues which are not negatives of each other; i.e., $\lambda_1 \neq -\lambda_2$.

If the first 3 conditions are not met, the calibration targets are not sufficiently different to determine **R** and **T**. The last condition is not described in [53] and if it is not met the solutions for **R** and **T** are not unique. The incorrect solutions may or may not be obvious.

Examples of a set of targets which fulfill these criteria for backscatter are: a sphere, a 45° oriented metallic cylinder, and a horizontally oriented metallic cylinder. The corresponding theoretical scattering matrices of these targets are (in the limit as the cylinder diameter be-

comes very small):

$$\mathbf{P}_1 = \mathbf{P}_{sphere} = c_1 \begin{bmatrix} 1 & 0 \\ 0 & 1 \end{bmatrix} \tag{4.4}$$

$$\mathbf{P}_2 = \mathbf{P}_{45^\circ\ cyl} = c_2 \begin{bmatrix} 1 & 1 \\ 1 & 1 \end{bmatrix} \tag{4.5}$$

$$\mathbf{P}_3 = \mathbf{P}_{horiz\ cyl} = c_3 \begin{bmatrix} 0 & 0 \\ 0 & 1 \end{bmatrix} \tag{4.6}$$

where c_1,c_2, and c_3 are constants which depend on the size and wavelength.

Kähny *et al.* [25] uses a fixed set of calibration targets to solve the calibration problem in a similar fashion. However, he employs a unique "twist": He measures two physically different targets, but obtains a third by rotating one of the bistatic antennas 90° about its boresight direction. For this purpose, the Bistatic Facility Transmitter Module has been designed to rotate about its boresight direction. When the transmitter is rotated by θ about its boresight, the target's scattering matrix gets modified from $\mathbf{P}$ to $\mathbf{P}' = \mathbf{P}\theta$ where

$$\theta = \begin{bmatrix} \cos\theta & \sin\theta \\ -\sin\theta & \cos\theta \end{bmatrix} \tag{4.7}$$

(If the Receiver Module were capable of such rotations, the new target scattering matrix would be $\theta^{-1}\mathbf{P}$). The reader is referred to [53] for details of the General Calibration Technique.

The improvement in a backscattering antenna's cross-polarized isolation (the minimum

value of *measured* $\left|\frac{S_{vv}}{S_{vh}}\right|^2$, $\left|\frac{S_{vv}}{S_{hv}}\right|^2$, $\left|\frac{S_{hh}}{S_{vh}}\right|^2$ and $\left|\frac{S_{hh}}{S_{hv}}\right|^2$ for a target whose *theoretical* $P_{vh} = P_{hv} = 0$) is a good indicator of the quality of a calibration technique. The GCT improves the isolation from a raw value of 20 dB (i.e., assuming $R_{vh} = R_{hv} = T_{vh} = T_{hv} = 0$) to a corrected value of 50 dB. A perfect calibration technique would make the isolation infinite.

While the technique is exact, its application is somewhat cumbersome. The targets require very accurate positioning and orientations to prevent small errors from overwhelming the minute corrections that the technique provides. The General Calibration Technique is therefore reserved for situations requiring very accurate polarimetric measurements. Other more convenient approaches are discussed in the following sections, first for the backscatter case and next for the bistatic case.

4.3 Backscatter Calibration Theory: Single Target Calibration Technique

The Single Target Calibration Technique (STCT) was developed by Sarabandi and Ulaby [37] for a backscatter antenna for which the distortion was small, but not negligible. It starts by taking the distortion model and further separating some of the physical processes contained in the distortion elements, in particular the electrical differences in plumbing (length of coaxial tubing, different circuit elements, etc.) for the different polarizations as separated from the depolarizations caused by geometrical imperfections (in the dish, feed, horn, etc.).

Mathematically, these are represented as:

$$\mathbf{R} = \mathbf{R}_p\mathbf{C}_r \tag{4.8}$$

$$\mathbf{T} = \mathbf{C}_t\mathbf{T}_p \tag{4.9}$$

where

$$\mathbf{R}_p = \begin{bmatrix} R_v & 0 \\ 0 & R_h \end{bmatrix} \tag{4.10}$$

$$\mathbf{T}_p = \begin{bmatrix} T_v & 0 \\ 0 & T_h \end{bmatrix} \tag{4.11}$$

$$\mathbf{C}_r = \begin{bmatrix} 1 & C_{rv} \\ C_{rh} & 1 \end{bmatrix} \tag{4.12}$$

$$\mathbf{C}_t = \begin{bmatrix} 1 & C_{th} \\ C_{tv} & 1 \end{bmatrix} \tag{4.13}$$

Since the same physical antenna is used for transmitting and receiving, the geometric distortions for transmit and receive are identical. Thus, $C_{th} = C_{rh}$ and $C_{tv} = C_{rv}$ (let us denote them as C_h and C_v respectively). Then, this technique assumes that all these crosstalk terms are identical; i.e., $C_h = C_v$, which is then denoted as C. The justification for this assumption is described in [37], and requires that $|C_h| \ll 1$ and $|C_v| \ll 1$. Most dual-polarized antennas are built such that both $|C_h|$ and $|C_v|$ are approximately on the order of -20 dB.

The calibration is achieved by measuring a single target with a theoretical scattering ma-

trix proportional to the identity matrix:

$$\mathbf{S}_{cal} = s_{cal}\begin{bmatrix} 1 & 0 \\ 0 & 1 \end{bmatrix} \tag{4.14}$$

Such targets include a sphere in freespace, and a large conducting plate. If a sphere is used, the calibration results in measurements reported in radar cross section; if the plate is used the measurements are reported in term of reflectivity. These units can be converted into each other or into differential radar cross sections with the appropriate knowledge of the antenna pattern, as discussed in Section 4.5.

After background subtraction (if necessary), we achieve a set of four complex values: $\mathbf{N}^{cal}$. From this single set of measurements we generate a complex parameter a:

$$a = \frac{N_{vh}^{cal} N_{hv}^{cal}}{N_{vv}^{cal} N_{hh}^{cal}} \tag{4.15}$$

Since we assume that the crosstalk is small to begin with, and the measured target has no cross-polarized scattering, we can expect $|a| \ll 1$. In fact, it can be shown that a and C are related by

$$C = \pm\frac{1}{\sqrt{a}}\left(1 \pm \sqrt{1-a}\right) \tag{4.16}$$

which has four solutions. Fortunately, two of the solutions result in a value of C which is not small, and can be discarded. These large incorrect values are a consequence of the fact that $P_{vv}^{cal} = P_{hh}^{cal}$ and therefore the calibration cannot, by itself, tell the difference between $\hat{\mathbf{v}}$

and $\hat{\mathbf{h}}$ at the target. Then, since a is small, we can expand the expression for C in a Taylor series to avoid division by a small number:

$$C = \frac{b}{2}\left(1+\frac{a}{4}+\frac{a^2}{8}+\cdots\right) \tag{4.17}$$

where $b = \pm\sqrt{a}$.

We cannot solve directly for R_h, R_v, T_h or T_v. However, given a measurement of an unknown target $\mathbf{N}^{unk}$, we can solve for the scattering matrix $\mathbf{S}^{unk}$ that would result in such a measurement for this antenna under this set of (reasonable) assumptions:

$$\begin{aligned}\mathbf{S}^{unk} &= \begin{bmatrix} S_{vv}^{unk} & S_{vh}^{unk} \\ S_{hv}^{unk} & S_{hh}^{unk} \end{bmatrix} \\ &= s_{cal}\frac{1+C^2}{(1-C^2)^2}\begin{bmatrix} 1 & -C \\ -C & 1 \end{bmatrix}\begin{bmatrix} \frac{N_{vv}^{unk}}{N_{vv}^{cal}} & b\frac{N_{vh}^{unk}}{N_{vh}^{cal}} \\ b\frac{N_{hv}^{unk}}{N_{hv}^{cal}} & \frac{N_{hh}^{unk}}{N_{hh}^{cal}} \end{bmatrix}\begin{bmatrix} 1 & -C \\ -C & 1 \end{bmatrix}\end{aligned} \tag{4.18}$$

The result is unambiguous in S_{vv} and S_{hh}, but there is a 180° ambiguity in the phase of S_{hv} and S_{vh}, as evidenced by the choice of sign in the calculation of b. Another measurement is required to determine the sign, but is unnecessary if magnitudes of the scattering matrix are all that is desired.

4.4 Bistatic Calibration Theory

The basic bistatic calibration procedure is based on the Isolated Antenna Calibration Technique (IACT) developed for backscattering by Sarabandi *et al.*[38]. The IACT is a pre-

cursor to the STCT described in Section 4.3, and it does not account for antenna cross-talk. In other words, C is assumed to be not just small, but to be zero.

In addition, the transmitter is made to rotate about its boresight direction. For a rotation of θ degrees, the transmit distortion matrix for a distortionless antenna becomes:

$$\mathbf{T} = T_v \begin{bmatrix} \cos\theta & \sin\theta \\ -\sin\theta & \cos\theta \end{bmatrix} \begin{bmatrix} 1 & 0 \\ 0 & T_h' \end{bmatrix} \tag{4.19}$$

where $T_h' = \frac{T_h}{T_v}$. The receiver distortion matrix becomes

$$\mathbf{R} = R_v \begin{bmatrix} 1 & 0 \\ 0 & R_h' \end{bmatrix} \tag{4.20}$$

where $R_h' = \frac{R_h}{R_v}$.

Up to two measurements of the same target are required with this technique, one with the transmitter module in the normal position, and an optional one with the transmitter module rotated by approximately 45°. The calibration target must be diagonal, ie. in the bistatic measurement configuration

$$\mathbf{P}^{cal} = \begin{bmatrix} P_{vv}^{cal} & 0 \\ 0 & P_{hh}^{cal} \end{bmatrix} \tag{4.21}$$

For the usual calibration targets, namely a sphere and conducting plate, this condition can be made true. For the sphere, the bistatic system must have the receiver in the the plane of incidence, ie. $\phi_t = 0°$ or $\phi_t = 180°$. For the plate, the specular position, where $\theta_r = \theta_t$ and

$\phi_t = 0°$, must be used, in which case the theoretical scattering matrix is not just diagonal, but $P_{vv}^{cal} = P_{hh}^{cal}$.

Then, for a measurement of arbitrary θ,

$$\begin{aligned} \mathbf{N} &= \begin{bmatrix} N_{vv} & N_{vh} \\ N_{hv} & N_{hh} \end{bmatrix} \\ &= k\mathbf{RP\theta T} \\ &= k' \begin{bmatrix} P_{vv}\cos\theta & P_{vv}T_h'\sin\theta \\ -R_h'P_{hh}\sin\theta & R_h'P_{hh}T_h'\cos\theta \end{bmatrix} \end{aligned} \tag{4.22}$$

where $k' = kR_vT_v$. Then the following relations are easily shown:

$$\frac{R_h'P_{hh}T_h'}{P_{vv}} = \frac{N_{hh}}{N_{vv}} \tag{4.23}$$

$$\frac{R_h'P_{hh}}{P_{vv}T_h'} = \frac{-N_{hv}}{N_{vh}} \tag{4.24}$$

$$k'^2P_{vv}R_h'P_{hh}T_h' = N_{vv}N_{hh} - N_{vh}N_{hv} \tag{4.25}$$

$$k'^2P_{vv}R_h'P_{hh}T_h'\cos 2\theta = N_{vv}N_{hh} + N_{vh}N_{hv} \tag{4.26}$$

$$T_h'\tan\theta = \frac{N_{vh}}{N_{vv}} \tag{4.27}$$

$$\frac{-\tan\theta}{T_h'} = \frac{N_{hv}}{N_{hh}} \tag{4.28}$$

and, for the measurement at 45°,

$$\tan\theta_{45} = +\sqrt{\frac{-N_{vh}(45°)N_{hv}(45°)}{N_{vv}(45°)N_{hh}(45°)}} \tag{4.29}$$

From these relations the quantities of interest can be derived:

$$T_h' = \frac{N_{vh}(45°)}{N_{vv}(45°)\tan\theta_{45}} \tag{4.30}$$

$$R_h' = -T_h'\frac{P_{vv}}{P_{hh}}\frac{N_{hv}(45°)}{N_{vh}(45°)} = \frac{1}{T_h'}\frac{P_{vv}}{P_{hh}}\frac{N_{hh}}{N_{vv}} \tag{4.31}$$

$$k'^2 = \frac{N_{vv}N_{hh} - N_{vh}N_{hv}}{R_h'T_h'P_{vv}P_{hh}} \tag{4.32}$$

$$\cos\theta_0 = +\sqrt{\frac{N_{vv}(0°)N_{hh}(0°)}{N_{vv}(0°)N_{hh}(0°) - N_{vh}(0°)N_{hv}(0°)}} \tag{4.33}$$

$$\sin\theta_0 = -T_h'\cos\theta_0\frac{N_{hv}(0°)}{N_{hh}(0°)} \tag{4.34}$$

The positive sign in (4.29) and (4.33) indicates that the square root which yields a positive real part for the complex quantities $\tan\theta_{45}$ and $\cos\theta_0$ should be used.

It can be seen from this development that the need for calibration with the antenna rotated is only necessary to prevent a multiplication and division by small numbers in the calculation of T_h'. A rotation by 45° is best to eliminate such difficulties, but it may be that using a lesser or greater rotation, or even using no rotation at all, may be satisfactory.

Then, the scattering matrix $\mathbf{S}^{unk}$ can be determined from a measurement $\mathbf{N}^{unk}$ as follows:

$$\mathbf{S}^{unk} = \mathbf{R}^{-1}\mathbf{N}^{unk}\mathbf{T}^{-1}\theta^{-1}/k' \tag{4.35}$$

where

$$\mathbf{R}^{-1} = \begin{bmatrix} 1 & 0 \\ 0 & 1/R'_h \end{bmatrix} \tag{4.36}$$

$$\mathbf{T}^{-1} = \begin{bmatrix} 1 & 0 \\ 0 & 1/T'_h \end{bmatrix} \tag{4.37}$$

$$\theta^{-1} = \begin{bmatrix} \cos\theta_0 & -\sin\theta_0 \\ \sin\theta_0 & \cos\theta_0 \end{bmatrix} \tag{4.38}$$

and k' is the square root of (4.32) that is closest to $N_{vv}(0°)/(P_{vv}\cos\theta_0)$.

4.5 Target Types

The Bistatic Facility can characterize three classes of objects: point targets, distributed targets, and reflectors. Point targets are small objects (when compared to the cross section of the radar beam) and scatter energy coherently in many directions. They are characterized by a radar cross section σ, which has the units of area and is usually measured in dBsm (sometimes written as dBm^2), which is an area expressed in decibels relative to 1 square meter.

Distributed targets are large (when compared to the cross section of the radar beam) random objects and scatter energy incoherently in many directions. They are characterized by a differential radar cross section σ^0, which is defined as the ratio of the surface's radar cross section to its physical area, and is thus dimensionless. It is usually expressed in dB. Reflectors are large (when compared to the cross section of the radar beam) objects which scatter

energy into a finite set of directions. They are characterized by the reflection coefficient R_{pq}, which is dimensionless complex ratio of the p-polarized coherent field amplitude scattered from the reflector to the q-polarized field amplitude incident upon it. It is also often characterized by the reflectivity Γ_{pq}, which simply the magnitude squared of the reflection coefficient. This quantity is also dimensionless and is expressed in dB.

The conversion of a calibration using one target into a measurement of another target starts with the radar equation for each target:

$$P_p^{pt} = P_q^t \frac{G_r G_t \lambda^2}{(4\pi)^3 R_r^2 R_t^2} \sigma_{pq} \tag{4.39}$$

$$P_p^{inc} = P_q^t \frac{\lambda^2}{(4\pi)^3} \int_{A_{ill}} \frac{G_r G_t}{R_r^2 R_t^2} \sigma_{pq}^0 dA_{ill} \tag{4.40}$$

$$P_p^{coh} = P_q^t \frac{G_r G_t \lambda^2}{(4\pi)^2 (R_r + R_t)^2} \Gamma_{pq} \tag{4.41}$$

where P^{pt} is the received coherent power scattered by a point target, P^{inc} is the received incoherent power scattered by a distributed target, and P^{coh} is the received coherent power scattered by a distributed target. In addition, λ is the radar wavelength in a vacuum, G_r and G_t are the antenna gains of the receiver and transmitter in the direction to the target, R_r and R_t are the ranges from the receiver and transmitter to the target, P^t is the transmitted power, the subscripts p and q indicate the received and transmitted polarizations, respectively, and A_{ill} is the area of illumination on the distributed target.

Point targets are deterministic, so only one measurement need be made for every combination of bistatic angles $(\theta_t, \theta_r, \phi_t)$ and target orientation angles (θ_j, ϕ_j).

Distributed targets, however, are statistical. Therefore, accurate determination of the

coherent and incoherent power, and thus the reflectivity Γ and the scattering coefficient σ^0, require the measurement of many independent realizations of statistically identical targets. There are numerous ways to do this, but the easiest is to make a distributed target which is much larger than illuminated area A_{ill}, and to move the target between measurements so that different portions of the target correspond to the radar's illuminated area during a measurement. For this reason the Bistatic Measurement Facility is equipped with the capacity to include a turntable and 215 cm diameter sample holder. (It is important that the turntable be positioned with its axis of rotation offset from the center of the BMF by at least the diameter of the area of illumination, so that different portions of the distributed target can be rotated into and out of the illuminated area. This is in contrast to a turntable which might be used to control ϕ_j for point targets, which should be located at the center of the BMF so that the point target stays at the same location within the sweet spot.)

The separation of the coherent and incoherent powers measured by the radar can be achieved by applying complex statistics on the calibrated scatter matrices $\mathbf{S}$. The calibrated scatter matrix elements S_{pq} represent a complex voltage ratio which is proportional to the scattered electric field for each polarization state at each spatially independent sample of the surface. Because the scattered electric field is composed of a coherent component from the mean surface and an incoherent component from the distributed target, the measured voltage ratio will also have a coherent and incoherent component: $S_{pq} = S_{pq}^{coh} + S_{pq}^{inc}$. These two components can be separated because the incoherent component has a zero mean: $\overline{S_{pq}^{inc}} = 0$ (where $\bar{x}$ indicates the mean of x). Provided a large number of independent samples are measured, the coherent power P_{coh} is proportional to the square of the complex average of the

measured voltages:

$$P^{coh} = \left|S_{pq}^{coh}\right|^2 = \left|\overline{S_{pq}}\right|^2 \tag{4.42}$$

The incoherent power P_{inc} is then proportional to the variance of the fluctuating component of the measured voltage:

$$P^{inc} = \overline{\left|S_{pq}^{inc}\right|^2} = \overline{\left|S_{pq} - \overline{S_{pq}}\right|^2} = \mathrm{Var}(S_{pq}) \tag{4.43}$$

These averages and variances are calculated on the fly by means of the following equations. For the first independent spatial sample, $\left(\overline{S_{pq}}\right)_1 = S_{pq}$ and $\mathrm{Var}(S_{pq})_1 = 0$ and for the nth spatial independent sample,

$$\left(\overline{S_{pq}}\right)_n = \frac{n-1}{n}\left(\overline{S_{pq}}\right)_{n-1} + \frac{1}{n}S_{pq} \tag{4.44}$$

$$\mathrm{Var}(S_{pq})_n = \frac{n-2}{n-1}\mathrm{Var}(S_{pq})_{n-1} + \frac{1}{n}\left(S_{pq} - \left(\overline{S_{pq}}\right)_{n-1}\right)^2 \tag{4.45}$$

Provided that calibration is achieved with a large flat metal plate, for which

$$\mathbf{P}^{cal} = \begin{bmatrix} 1 & 0 \\ 0 & 1 \end{bmatrix}, \tag{4.46}$$

it can be readily shown that

$$\sigma_{pq} = \frac{4\pi R_{r0}^2 R_{t0}^2}{(R_{r0}+R_{t0})^2}|S_{pq}|^2 \tag{4.47}$$

$$\Gamma_{pq} = \left|\overline{S_{pq}}\right|^2 \tag{4.48}$$

$$\sigma_{pq}^0 = \frac{4\pi}{(R_{r0}+R_{t0})^2 I_{ill}}\mathrm{Var}(S_{pq}) \tag{4.49}$$

where R_{t0} and R_{r0} are the boresight ranges from the transmitter and receiver, respectively, to the center of the Bistatic Measurement Facility and the illumination integral I_{ill} is given by

$$I_{ill} = \int_{A_{ill}} \frac{G_r G_t}{R_r^2 R_t^2} dA_{ill}. \tag{4.50}$$

and has been implemented with the following approximation:

$$I_{ill} \approx \frac{\pi \tan\frac{1}{2}\beta_t^{az} \tan\frac{1}{2}\beta_t^{el}}{R_{r0}^2 \cos\theta_t} \tag{4.51}$$

The values of some of these parameters in equations 4.47 thru 4.51 depend on whether the BMF is in bistatic or backscatter modes. Technically, some of the variables in equation 4.51 also depend on the polarization state, but that dependence is sufficiently weak that it has been neglected.

4.6 Independent Samples

The total number of independent samples is an indicator of the quality of the measurement of Γ or σ^0. Generally, 20 to 30 independent samples should be considered a minimum for a valid measurement; 50 to 100 independent samples would constitute a good measurement.

4.6.1 Frequency Averaging

The total number of independent samples for σ^0 is not always the same as the number of spatial independent samples. A single spatial independent sample may have more than one independent sample due to a phenomenon known as "frequency averaging." We can consider a radar with bandwidth B to be equivalent to a pulse radar operating at a single frequency but with a pulse duration of $\tau = 1/B$. For each point in the illuminated area there is a path r going directly from the transmitter to that point, then continuing from that point directly to the receiver. The propagation time associated with these paths is $t = r/c$, where c is the speed of light. One of the points has the longest such path r_{max}, and one has the shortest such path r_{min}. Therefore, for each instant that the radar transmits power, it is receiving energy from the distributed target for a total duration $\Delta t = \Delta r/c$ where $\Delta r = r_{max} - r_{min}$. If $\Delta t > \tau$, then different portions of the illuminated area are distinct, that is, they are independent samples. Thus, the number of independent samples per spatial sample, denoted N_f, is

$$N_f = \frac{\Delta t}{\tau} = \frac{B\Delta r}{c} \tag{4.52}$$

The number of independent samples per spatial sample is never less than one, nor is it greater than the number of frequencies sampled (for the BMF, while 201 frequency points are measured by the network analyzer, only 21 equally spaced frequency points are used by the software). For the backscatter mode,

$$\Delta r = 4R_{r0}\frac{\sin 2\theta_r \sin \frac{1}{2}\beta_r^{el}}{\cos 2\theta_r + \cos \beta_r^{el}} \tag{4.53}$$

and for bistatic mode

$$\Delta r = 2R_{t0}\left|\sin \tfrac{1}{2}\phi_t\right| \times \left(\frac{\tan \frac{1}{2}\beta_t^{el}}{\cos \theta_t}(\sin \theta_t - \sin \theta_r \cos \phi_t) + \tan \tfrac{1}{2}\beta_t^{az}(1 + \cos \phi_t)\sin \theta_t\right) \tag{4.54}$$

Generally, for a given θ_r, the backscattering direction provides the greatest Δr. Also, $N_f = 1$ for the specular direction.

The reported scattering coefficient is the average scattering coefficient over all 21 frequency points used by the software. Reflectivities do not average well over frequencies, so the reported reflectivity is just that at the center frequency and the total number of independent samples for the reported reflectivity is the same as total number of spatial samples. The reported radar cross section, of course, involves neither spatial nor frequency averaging.

4.6.2 Measuring Sample Independence

The maximum number of spatial independent samples, and thus the amount of rotation required between measurements, can be determined by the finding the angle of rotation of

the turntable necessary for decorrelating the measured power. This is achieved by measuring the RCS of a distributed target, preferably a relatively strong scattering target which has many random variations within each possible illuminated area, at many close but equally spaced rotations of the turntable. Let N_ρ be the number these close but equally spaced samples. Then the amount of turntable rotation per (non-independent) sample ϕ_{rot} would be $\phi_{rot} = 360°/N_\rho$. N_ρ should be on the order of 100 or more. Then the resultant measurements at position n, namely $\sigma_{pq}(n\phi_{rot})$ for the pq polarization, are used to find the autocorrelation of the measured signal ρ:

$$\rho(n\phi_{rot}) = \sum_{m=0}^{N_\rho - 1} 10^{\sigma_{pq}(m\phi_{rot})/10} 10^{\sigma_{pq}((m+n)\phi_{rot})/10} \tag{4.55}$$

where it is recognized that angles greater than 360° are equivalent to an angle between 0° and 360°. The smallest angle ϕ_s at which $\rho(\phi_s)/\rho(0°) < e^{-1}$ is the decorrelation angle. The total number of spatial independent samples N_s to be used per rotation of the sample holder is then $N_s = 360°/\phi_s$.

The value for ϕ_s should be a weak function of the bistatic angles, since it will change only with the extent of the illuminated area. Formula 4.55 will only work, however, if the target measured produces much more incoherent power than coherent power for the bistatic angles chosen. Therefore, care must be taken to use a scattering target with sufficient randomness and physical fluctuations, especially if this is to be measured at or near the specular direction.

To separate the measured signal into its coherent and incoherent components, it is necessary to measure many statistically independent samples of the random surface characterizing the target surface. This is achieved by rotating the sample holder in increments of 10°,

thereby realizing 36 spatial samples per full rotation. The spatial correlation of the measured incoherent power indicates that measurements decorrelated every 15°, resulting in 24 independent samples per surface. Measurements of smooth surfaces indicate that phase coherence is maintained between independent samples. The total path length, from transmitter to target to receiver, has a standard deviation less than 4 mm (7° at 9.25 GHz) for the set of independent samples.

4.7 Validation

Validation is the process of quantifying the accuracy of a particular calibration or of a calibration technique. Validation is achieved by measuring a target with a known scattering matrix and comparing it to the calibrated measurement of that scattering matrix. For an effective validation, the validation target should have a scattering matrix which is sufficiently different from those known targets used for calibration, since an otherwise faulty calibration could still give correct results for a small class of targets which are very similar or identical to the calibration targets.

One possible target for validation is a metal sphere located at the center of the bistatic facility. Such a validation target has a known scattering matrix which can be calculated via Mie theory [4]. The scattering matrix of a sphere is diagonal when the fields are oriented within and orthogonal to the plane of scattering of the sphere, which is the plane containing the transmitter, the sphere and the receiver. For a perfectly conducting sphere, the two scattering amplitudes themselves are functions only of the sphere radius a, normalized to the wavelength of the incident radiation, and the cosine of the angle between the incident

and scattered directions (ie. the supplement of the transmitter-sphere-receiver angle), represented by μ:

$$\mathbf{P}'_{\text{sphere}}(ka,\mu) = \begin{bmatrix} P'_{\perp}(ka,\mu) & 0 \\ 0 & P'_{\parallel}(ka,\mu) \end{bmatrix} \tag{4.56}$$

where $\perp$ and $\parallel$ indicate directions perpendicular to the scattering plane and within the scattering plane, respectively, and the prime indicates that the scattering matrix is represented in that coordinate system. A FORTRAN subroutine which can be used to calculate $P'_{\perp}$ and $P'_{\parallel}$ is listed in Bohren and Huffman [4]. The orientation of the scattering plane is undefined for two cases: forward scattering and backscattering. For forward scattering, where $\mu = 1$, $P'_{\perp} = P'_{\parallel}$, while for backscattering, where $\mu = -1$, $P'_{\perp} = -P'_{\parallel}$.

In order for (4.56) to be useful, the value of μ must be found and the bistatic coordinate system of Figure 2.1 must be reconciled with that the previous paragraph. From Figure 4.1, it is evident that the latter is accomplished by rotating the incident field coordinate system by an angle α_i about the incident direction, and the scattered field coordinate system by an angle α_s about the scattering direction, so that the scattering matrix of the sphere in the bistatic coordinate system is

$$\mathbf{P}_{\text{sphere}}(ka,\theta_i,\theta_s,\phi_\Delta) = \begin{bmatrix} \sin\alpha_s & -\cos\alpha_s \\ \cos\alpha_s & \sin\alpha_s \end{bmatrix} \begin{bmatrix} P'_{\perp}(ka,\mu) & 0 \\ 0 & P'_{\parallel}(ka,\mu) \end{bmatrix} \begin{bmatrix} \sin\alpha_i & \cos\alpha_i \\ -\cos\alpha_i & \sin\alpha_i \end{bmatrix} \tag{4.57}$$

where the rotation angles α_i and α_s can be found from the Sine Law for spherical trigonom-

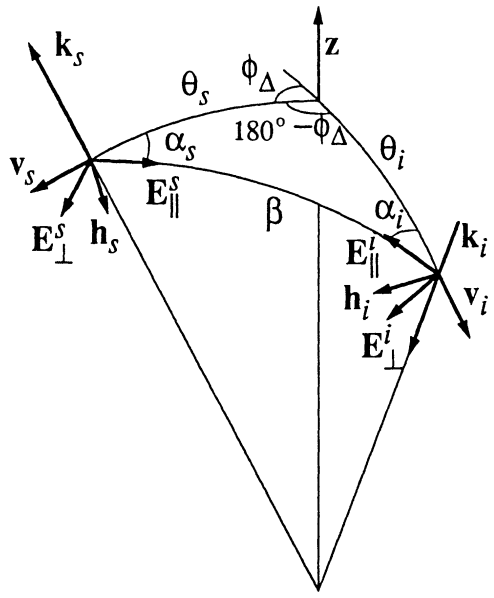

Figure 4.1: A triangular section of a unit sphere centered at the target is used to convert from the $\perp$-$\|$ coordinate system of Bohren and Huffman to the bistatic coordinate system. The target is located at the junction of the **z**, $\mathbf{k}_i$, and $\mathbf{k}_s$ vectors at the bottom of the figure. For both the incident and scattered directions, **k** is in the $\mathbf{v} \times \mathbf{h}$ direction as well as the $\mathbf{E}_\perp \times \mathbf{E}_\|$ direction

etry:

$$\frac{\sin\alpha_i}{\sin\theta_s} = \frac{\sin\alpha_s}{\sin\theta_i} = \frac{\sin(180° - \phi_\Delta)}{\sin\beta} \tag{4.58}$$

and the cosine of the scattering angle, μ, can be found from the Cosine Law for spherical trigonometry:

$$\mu = \cos(180° - \beta) = -(\cos\theta_i \cos\theta_s + \sin\theta_i \sin\theta_s \cos\phi_\Delta) \tag{4.59}$$

Two problems exist with using the sphere for a validation target, one practical and one theoretical. The practical problem is that the sphere requires an absence of other scattering

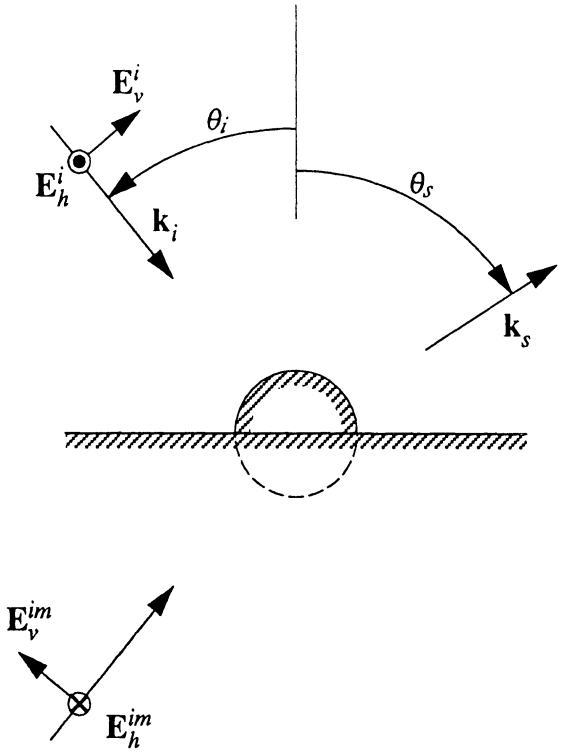

Figure 4.2: A hemisphere on a ground plane is used as the target for validation of calibration of the Bistatic Measurement Facility. Image theory is used to make the hemisphere appear as a complete sphere illuminated simultaneously with the incident wave and its image, with the polarizations as shown.

objects in the vicinity of the center of the bistatic facility. The surfaces measured in the Bistatic Measurement Facility are heavy, bulky and fragile, and removing and replacing them at the center of the facility ranges from difficult to impossible. The large planar metal sheet used for calibration can be used simultaneously to calibrate the system and shield the system from the unknown target directly underneath it. The verification target should have similar shielding properties.

The theoretical problem is that a sphere has a diagonal scattering matrix in the appropriate coordinate system. This scattering matrix is not all that different from that of the calibration target, limiting the value of its use for validation.

Both of these problems can be solved by using a hemisphere placed on the calibration ground plane as the validation target. The calibration ground plane solves the practical problem of shielding the unknown target beneath; the ground plane affects the target scattering matrix such that, for a large number of bistatic angles, the scattering matrix is not diagonal in any coordinate system. Figure 4.2 shows a schematic of this validation measurement configuration. Image theory manifests itself in this geometry in two ways. The receiver sees not just the hemisphere itself, but also its image under the ground plane, so that the receiver sees a complete sphere. As a result, the Mie theory developed above is useful for characterizing the scattering from this geometry. Image theory also effects the transmitter: the hemisphere is illuminated not just by the transmitter but also by the image of the transmitter. As as result, the scattering from the hemisphere on a ground plane appears as an interference pattern of a single sphere illuminated by two sources, one at an incidence angle of θ_i and an image source with an incidence angle of $180° - \theta_i$. Also, image theory for the perfect electric conductor states that the vertical components of the incident field and the image field are in-phase, while the horizontal components are 180° out-of-phase, as shown in Figure 4.2. Thus, the scattering matrix of the hemisphere on the ground plane is

$$\begin{aligned}\mathbf{P}_{\text{hemisphere}}(ka, \theta_i, \theta_s, \phi_\Delta) &= \mathbf{P}_{\text{sphere}}(ka, \theta_i, \theta_s, \phi_\Delta) \\ &\quad + \mathbf{P}_{\text{sphere}}(ka, 180° - \theta_i, \theta_s, \phi_\Delta) \begin{bmatrix} 1 & 0 \\ 0 & -1 \end{bmatrix}\end{aligned} \tag{4.60}$$

This matrix, unlike that for a sphere $\mathbf{P}_{\text{sphere}}$, typically varies dramatically with a change in

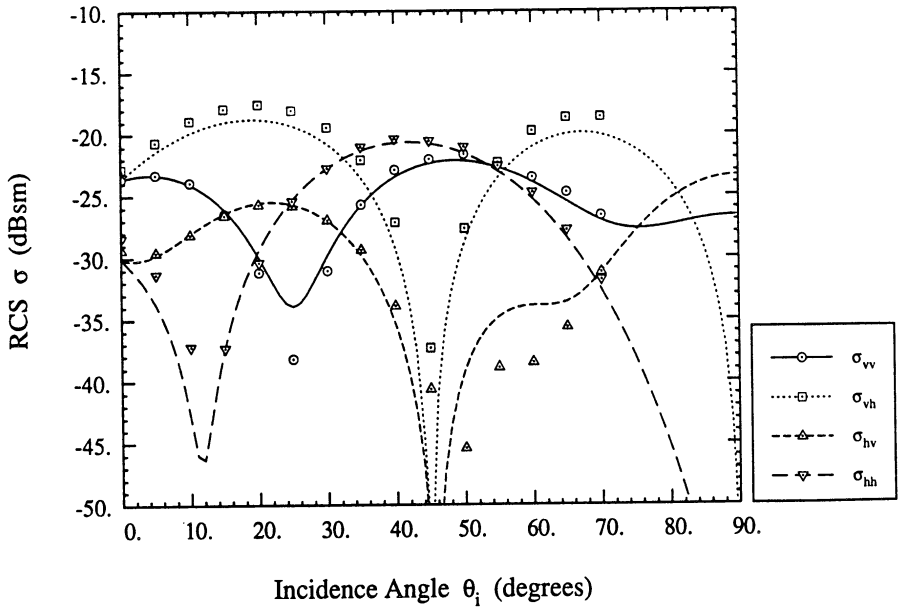

Figure 4.3: Radar cross section of a hemisphere on a conducting ground plane. The curves represent the theoretical development in this section and the dots are calibrated measurements made in the Bistatic Measurement Facility at 9.25 GHz. The hemisphere has a 2" diameter and the other bistatic angles are $\phi_\Delta = 45°$ and $\theta_s = 45°$.

the bistatic angles. Out of the plane of incidence, it is rarely, if ever, diagonal in any coordinate system, because the plane of scattering for the incident wave and its image do not coincide.

A comparison of measurements of the hemisphere calibration target with the theoretical radar cross section which is described in this section is shown in Figure 4.3.

A serious weakness of this theoretical description is that it does not account for the specular flash from the ground plane. As a result, the calibration cannot be verified with this target in the specular direction, or within one system beamwidth of the specular direction. If the calibration is validated away from the specular direction, it should be valid also in the direction that the calibration was performed. A limited confirmation in the specular direction was performed by measuring the reflectivity of a pool of tap water and is shown in

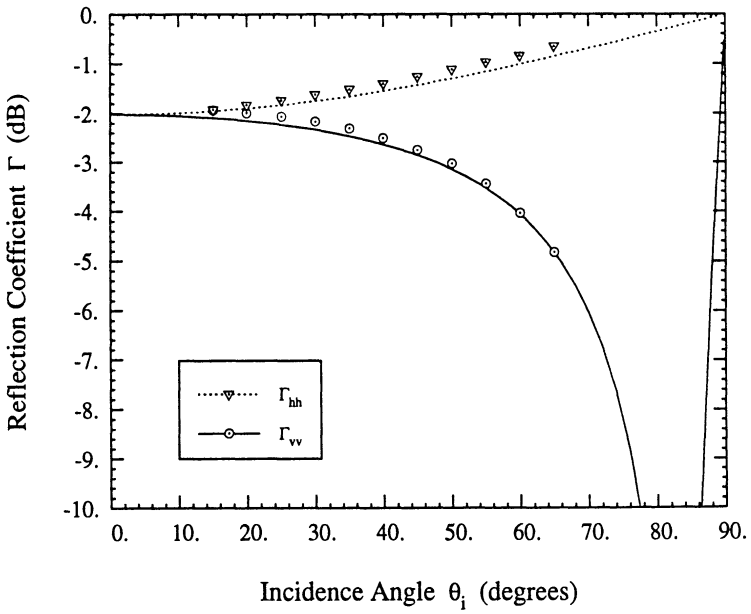

Figure 4.4: Reflectivity of water. Curves represent the theoretical reflectivity of fresh water at 9.25 GHz ($\varepsilon_r = 63.2 - j31.4$) and the dots are single measurements of still water in the specular direction. The error in the measured data does not exceed 0.2 dB. All cross-polarized data lie between -28 dB and -30 dB.

Figure 4.4. Ulaby *et al.* [49] gives the dielectric constant of 0 parts per thousand salinity water as $\varepsilon_r = 63.2 - j31.4$ at 9.25 GHz and 20°C.

CHAPTER 5

Modified Physical Optics Model

In this chapter, an extension to the traditional Physical Optics expression for the scattered field is developed. While higher orders to Physical Optics have been attempted before (see, for example, Ulaby *et al.* [48] and Leader [27]), this development is unique in several aspects: it is generalized for full polarimetry, in that the expressions are amenable to creating Mueller matrices, and, after the tangent-plane approximation, the Taylor series in slopes are expanded without further approximations. In the derivation of this modified Physical Optics approach a recipe is given to extend it to arbitrary orders.

Some fundamental assumptions about the scattering problem are: the surface height must be single-valued; the surface height probability density must be Gaussianly distributed; the two regions, that is, above and below the surface, must have isotropic, linear, homogeneous electrical and magnetic characteristics; the surface can be described by a stationary random process; the surface has a well-characterized correlation function; and that correlation function is isotropic.

5.1 Stratton-Chu Integral Equation

In Ulaby *et al.* [48], the Physical Optics solution for scattering from a dielectric rough surface is presented under the scalar approximation. This approximation leaves out many terms, some of which change the results of the calculations significantly. In particular, cross-polarized scattering is neglected in the plane of incidence under the scalar approximation. What follows is a full vector solution to the Physical Optics problem, including vector terms which are neglected *via* the scalar approximation and some higher order terms in the expansion of the solution with respect to surface slope, with the rest of the assumptions remaining the same as in Ulaby *et al.* [48].

The solution starts with the exact Stratton-Chu integral equation for the p-polarized scattered far field due to a q-polarized wave ($\hat{\mathbf{q}}E_0 e^{-jk\hat{\mathbf{k}}_i\cdot\mathbf{r}}$) incident upon a rough surface:

$$E^s_{pq} = \frac{-jk_s e^{-jk_s R_0}}{4\pi R_0} E_0 \int \frac{U_{pq}}{D_n} e^{jk_s(\hat{\mathbf{k}}_s-\hat{\mathbf{k}}_i)\cdot\mathbf{r}} dS \tag{5.1}$$

$$U_{pq} = \frac{D_n}{E_0}\hat{\mathbf{p}}\cdot\left(\hat{\mathbf{k}}_s\times\left[(\hat{\mathbf{n}}\times\mathbf{E})-\eta_s\hat{\mathbf{k}}_s\times(\hat{\mathbf{n}}\times\mathbf{H})\right]\right)e^{jk_s\hat{\mathbf{k}}_i\cdot\mathbf{r}} \tag{5.2}$$

where $\hat{\mathbf{k}}_i$ is the direction of propagation of the incident field, $\hat{\mathbf{k}}_s$ is the direction of propagation of the scattered field (in either medium), $\hat{\mathbf{p}}$ is the polarization of the receiver, and $\hat{\mathbf{n}}$ is the unit surface normal $\hat{\mathbf{n}}_1$ or $\hat{\mathbf{n}}_2$, depending upon in which medium the scattered field is observed. The vector $\mathbf{r}$ describes any point on the surface, and, for the purposes of calculating rough surface scattering, is considered to be of the form $\mathbf{r} = \hat{\mathbf{x}}x+\hat{\mathbf{y}}y+\hat{\mathbf{z}}f(x,y)$, where $f(x,y)$ is differentiable everywhere with $Z_x = \frac{\partial}{\partial x}f(x,y)$ and $Z_y = \frac{\partial}{\partial y}f(x,y)$. Under these

circumstances, the unit normal exists for all points on the surface and is given by

$$\hat{\mathbf{n}}_1 = \frac{\hat{\mathbf{z}} - Z_x\hat{\mathbf{x}} - Z_y\hat{\mathbf{y}}}{D_n} \tag{5.3}$$

$$\hat{\mathbf{n}}_2 = -\hat{\mathbf{n}}_1 \tag{5.4}$$

$$D_n = \sqrt{1 + Z_x^2 + Z_y^2} \tag{5.5}$$

The polarization amplitude U_{pq}, given by (5.2), is the same as that given by Ulaby *et al.* [48] except for the factor of D_n, which makes a number of the expressions which follow slightly simpler.

For scattering in the "upper" medium (ie. medium 1, the medium in which the source of the incident field exists), the singly scattered fields on the surface calculated with the tangent plane approximation have been given by Holzer and Sung [21] and Tsang *et al.* [46]. Leader [27] gave the equivalent expressions for the total fields on the surface. These singly scattered fields are given by:

$$\hat{\mathbf{n}}_1 \times \mathbf{E} = \left[R_h(\hat{\mathbf{q}}\cdot\hat{\mathbf{t}})(\hat{\mathbf{n}}_1\times\hat{\mathbf{t}}) + R_v(\hat{\mathbf{n}}_1\cdot\hat{\mathbf{k}}_i)(\hat{\mathbf{q}}\cdot\hat{\mathbf{d}})\hat{\mathbf{t}}\right]E_0 e^{-jk_s\hat{\mathbf{k}}_i\cdot\mathbf{r}} \tag{5.6}$$

$$\eta_1\hat{\mathbf{n}}_1 \times \mathbf{H} = \left[R_h(\hat{\mathbf{n}}_1\cdot\hat{\mathbf{k}}_i)(\hat{\mathbf{q}}\cdot\hat{\mathbf{t}})\hat{\mathbf{t}} - R_v(\hat{\mathbf{q}}\cdot\hat{\mathbf{d}})(\hat{\mathbf{n}}_1\times\hat{\mathbf{t}})\right]E_0 e^{-jk_s\hat{\mathbf{k}}_i\cdot\mathbf{r}} \tag{5.7}$$

where $\hat{\mathbf{k}}_i$ is the incident wave direction, $\hat{\mathbf{q}}$ is the incident wave polarization direction, $\hat{\mathbf{n}}_1$ is the unit normal to the surface, $\hat{\mathbf{t}} = \hat{\mathbf{k}}_i \times \hat{\mathbf{n}}_1 / \left|\hat{\mathbf{k}}_i \times \hat{\mathbf{n}}_1\right|$ is the unit vector simultaneously tangential to the surface and normal to direction of propagation of the incident wave, and $\hat{\mathbf{d}} = \hat{\mathbf{k}}_i \times \hat{\mathbf{t}}$ completes the right handed coordinate system $(\hat{\mathbf{k}}_i, \hat{\mathbf{t}}, \hat{\mathbf{d}})$ located at the surface. This coordinate system local to the surface is shown in Figure 2.11. Also, R_v and R_h are the *v*- and *h*-

polarized Fresnel Reflection coefficients local to a point on the surface.

5.2 Evaluation of Vector Products

Regardless of the form used for the local reflection coefficients R_v and R_h, all the unit vectors are known that appear in the polarization amplitude given by (5.2) through (5.6) and (5.7). The local unit coordinate system $(\hat{\mathbf{k}}_i, \hat{\mathbf{t}}, \hat{\mathbf{d}})$ is given by (2.40), (2.45), and (2.46). The incident and scattered wave directions are given by (2.1) and (2.2), respectively. The scattered wave polarization vectors, $\hat{\mathbf{h}}_s$ and $\hat{\mathbf{v}}_s$, which are used in the unit vector $\hat{\mathbf{p}}$ to pick the polarization, are given by (2.8) and (2.9), respectively. The incident wave polarization vectors, $\hat{\mathbf{h}}_i$ and $\hat{\mathbf{v}}_i$, which are used in the unit vector $\hat{\mathbf{q}}$ to pick the polarization, are given by (2.3) and (2.4), respectively.

Carrying out all the vector products without employing any approximations, one can derive the following expressions for the polarization amplitudes in terms of the local reflection coefficient, the local surface slopes, and the bistatic angles:

$$U_{hh} = D_n \left(R_h \left((\hat{\mathbf{n}}_1 \cdot \hat{\mathbf{k}}_i)(\hat{\mathbf{h}}_i \cdot \hat{\mathbf{t}})(\hat{\mathbf{h}}_s \cdot \hat{\mathbf{t}}) + (\hat{\mathbf{h}}_i \cdot \hat{\mathbf{t}})\hat{\mathbf{v}}_s \cdot (\hat{\mathbf{n}}_1 \times \hat{\mathbf{t}}) \right) \right.$$

$$\left. + R_v \left((\hat{\mathbf{n}}_1 \cdot \hat{\mathbf{k}}_i)(\hat{\mathbf{h}}_i \cdot \hat{\mathbf{d}})(\hat{\mathbf{v}}_s \cdot \hat{\mathbf{t}}) - (\hat{\mathbf{h}}_i \cdot \hat{\mathbf{d}})\hat{\mathbf{h}}_s \cdot (\hat{\mathbf{n}}_1 \times \hat{\mathbf{t}}) \right) \right) \tag{5.8}$$

$$= \frac{1}{D_1^2} \left[R_v Z_t \left((\cos\theta_i + Z_l \sin\theta_i) \right. \right.$$

$$\left((\sin\theta_i - Z_l \cos\theta_i)\cos\theta_s \sin\phi_\Delta - Z_t (\sin\theta_i \sin\theta_s - \cos\theta_i \cos\theta_s \cos\phi_\Delta) \right)$$

$$+ \left(\left(1 + Z_t^2\right) \sin\theta_i - Z_l \cos\theta_i \right) \sin\phi_\Delta + Z_t (\cos\theta_i + Z_l \sin\theta_i) \cos\phi_\Delta \Big)$$

$$- R_h (\sin\theta_i - Z_l \cos\theta_i) \left(\left(\left(\left(1 + Z_t^2\right) \sin\theta_i - Z_l \cos\theta_i \right) \cos\theta_s \cos\phi_\Delta \right. \right.$$

$$- Z_t (\cos\theta_i + Z_l \sin\theta_i) \cos\theta_s \sin\phi_\Delta + \left(Z_t^2 \cos\theta_i - Z_l (\sin\theta_i - Z_l \cos\theta_i) \right) \sin\theta_s \Big)$$

$$\left. \left. + (\cos\theta_i + Z_l \sin\theta_i) \left((\sin\theta_i - Z_l \cos\theta_i) \cos\phi_\Delta - Z_t \cos\theta_i \sin\phi_\Delta \right) \right) \right] \tag{5.9}$$

$$U_{vh} = D_n \left(R_h \left((\hat{\mathbf{n}}_1 \cdot \hat{\mathbf{k}}_i)(\hat{\mathbf{h}}_i \cdot \hat{\mathbf{t}})(\hat{\mathbf{v}}_s \cdot \hat{\mathbf{t}}) - (\hat{\mathbf{h}}_i \cdot \hat{\mathbf{t}})\hat{\mathbf{h}}_s \cdot (\hat{\mathbf{n}}_1 \times \hat{\mathbf{t}}) \right) \right.$$

$$\left. - R_v \left((\hat{\mathbf{h}}_i \cdot \hat{\mathbf{d}})\hat{\mathbf{v}}_s \cdot (\hat{\mathbf{n}}_1 \times \hat{\mathbf{t}}) + (\hat{\mathbf{n}}_1 \cdot \hat{\mathbf{k}}_i)(\hat{\mathbf{h}}_i \cdot \hat{\mathbf{d}})(\hat{\mathbf{h}}_s \cdot \hat{\mathbf{t}}) \right) \right) \tag{5.10}$$

$$= \frac{1}{D_1^2} \left[-R_h (\sin\theta_i - Z_l \cos\theta_i) \left((\cos\theta_i + Z_l \sin\theta_i) \right. \right.$$

$$\left((\sin\theta_i - Z_l \cos\theta_i)\cos\theta_s \sin\phi_\Delta - Z_t (\sin\theta_i \sin\theta_s - \cos\theta_i \cos\theta_s \cos\phi_\Delta) \right)$$

$$+ \left(\left(1 + Z_t^2\right) \sin\theta_i - Z_l \cos\theta_i \right) \sin\phi_\Delta + Z_t (\cos\theta_i + Z_l \sin\theta_i) \cos\phi_\Delta \Big)$$

$$- R_v Z_t \left(\left(\left(1 + Z_t^2\right) \sin\theta_i - Z_l \cos\theta_i \right) \cos\theta_s \cos\phi_\Delta \right.$$

$$- Z_t (\cos\theta_i + Z_l \sin\theta_i) \cos\theta_s \sin\phi_\Delta + \left(Z_t^2 \cos\theta_i - Z_l (\sin\theta_i - Z_l \cos\theta_i) \right) \sin\theta_s$$

$$\left. \left. + (\cos\theta_i + Z_l \sin\theta_i) \left((\sin\theta_i - Z_l \cos\theta_i) \cos\phi_\Delta - Z_t \cos\theta_i \sin\phi_\Delta \right) \right) \right] \tag{5.11}$$

$$U_{hv} = D_n \left(R_h \left((\hat{\mathbf{n}}_1 \cdot \hat{\mathbf{k}}_i)(\hat{\mathbf{v}}_i \cdot \hat{\mathbf{t}})(\hat{\mathbf{h}}_s \cdot \hat{\mathbf{t}}) + (\hat{\mathbf{v}}_i \cdot \hat{\mathbf{t}})\hat{\mathbf{v}}_s \cdot (\hat{\mathbf{n}}_1 \times \hat{\mathbf{t}}) \right) \right.$$

$$\left. -R_v \left((\hat{\mathbf{v}}_i \cdot \hat{\mathbf{d}})\hat{\mathbf{h}}_s \cdot (\hat{\mathbf{n}}_1 \times \hat{\mathbf{t}}) - (\hat{\mathbf{n}}_1 \cdot \hat{\mathbf{k}}_i)(\hat{\mathbf{v}}_i \cdot \hat{\mathbf{d}})(\hat{\mathbf{v}}_s \cdot \hat{\mathbf{t}}) \right) \right) \tag{5.12}$$

$$= \frac{1}{D_1^2} \left[R_h Z_t \left((\cos\theta_i + Z_l \sin\theta_i) \left((\sin\theta_i - Z_l \cos\theta_i) \cos\phi_\Delta - Z_t \cos\theta_i \sin\phi_\Delta \right) \right. \right.$$

$$+ \left(\left(1 + Z_t^2 \right) \sin\theta_i - Z_l \cos\theta_i \right) \cos\theta_s \cos\phi_\Delta$$

$$- Z_t (\cos\theta_i + Z_l \sin\theta_i) \cos\theta_s \sin\phi_\Delta + \left(Z_t^2 \cos\theta_i - Z_l (\sin\theta_i - Z_l \cos\theta_i) \right) \sin\theta_s \Big)$$

$$+ R_v (\sin\theta_i - Z_l \cos\theta_i) \left((\cos\theta_i + Z_l \sin\theta_i) \right.$$

$$\left((\sin\theta_i - Z_l \cos\theta_i) \cos\theta_s \sin\phi_\Delta - Z_t (\sin\theta_i \sin\theta_s - \cos\theta_i \cos\theta_s \cos\phi_\Delta) \right)$$

$$\left. \left. + \left(\left(1 + Z_t^2 \right) \sin\theta_i - Z_l \cos\theta_i \right) \sin\phi_\Delta + Z_t (\cos\theta_i + Z_l \sin\theta_i) \cos\phi_\Delta \right) \right] \tag{5.13}$$

$$U_{vv} = D_n \left(R_h \left((\hat{\mathbf{n}}_1 \cdot \hat{\mathbf{k}}_i)(\hat{\mathbf{v}}_i \cdot \hat{\mathbf{t}})(\hat{\mathbf{v}}_s \cdot \hat{\mathbf{t}}) - (\hat{\mathbf{v}}_i \cdot \hat{\mathbf{t}})\hat{\mathbf{h}}_s \cdot (\hat{\mathbf{n}}_1 \times \hat{\mathbf{t}}) \right) \right.$$

$$\left. -R_v \left((\hat{\mathbf{v}}_i \cdot \hat{\mathbf{d}})\hat{\mathbf{v}}_s \cdot (\hat{\mathbf{n}}_1 \times \hat{\mathbf{t}}) + (\hat{\mathbf{n}}_1 \cdot \hat{\mathbf{k}}_i)(\hat{\mathbf{v}}_i \cdot \hat{\mathbf{d}})(\hat{\mathbf{h}}_s \cdot \hat{\mathbf{t}}) \right) \right) \tag{5.14}$$

$$= \frac{1}{D_1^2} \left[R_h Z_t \left((\cos\theta_i + Z_l \sin\theta_i) \right. \right.$$

$$\left((\sin\theta_i - Z_l \cos\theta_i) \cos\theta_s \sin\phi_\Delta - Z_t (\sin\theta_i \sin\theta_s - \cos\theta_i \cos\theta_s \cos\phi_\Delta) \right)$$

$$+ \left(\left(1 + Z_t^2 \right) \sin\theta_i - Z_l \cos\theta_i \right) \sin\phi_\Delta + Z_t (\cos\theta_i + Z_l \sin\theta_i) \cos\phi_\Delta \Big)$$

$$- R_v (\sin\theta_i - Z_l \cos\theta_i) \left(\left(\left(1 + Z_t^2 \right) \sin\theta_i - Z_l \cos\theta_i \right) \cos\theta_s \cos\phi_\Delta \right.$$

$$- Z_t (\cos\theta_i + Z_l \sin\theta_i) \cos\theta_s \sin\phi_\Delta + \left(Z_t^2 \cos\theta_i - Z_l (\sin\theta_i - Z_l \cos\theta_i) \right) \sin\theta_s$$

$$\left. \left. + (\cos\theta_i + Z_l \sin\theta_i) \left((\sin\theta_i - Z_l \cos\theta_i) \cos\phi_\Delta - Z_t \cos\theta_i \sin\phi_\Delta \right) \right) \right] \tag{5.15}$$

where

$$D_1 = \left|\hat{\mathbf{k}}_i \times \hat{\mathbf{n}}_1\right| = \sqrt{(\sin\theta_i - Z_l \cos\theta_i)^2 + Z_t^2} \tag{5.16}$$

The literature (see, for example, [14, 27, 48, 15]) abounds with exact expressions for the polarization amplitudes U_{pq} in terms of the unit vectors, that is, in the forms provided by (5.8) (5.10) (5.12), and (5.14), or their equivalents. However, the exact expressions for U_{pq} in terms of the general bistatic angles do not appear elsewhere. Fung [14] has these expressions, but they are specialized to the backscattering case only, for example, and Ulaby *et al.* [48] employ multiple approximations to the vector products in deriving the polarization amplitudes in terms of the bistatic angles, in the process losing terms which contribute to scattering comparably with the lowest order term of the expansion to follow.

Since the coordinate system $(\hat{\mathbf{x}}, \hat{\mathbf{y}}, \hat{\mathbf{z}})$ is attached to the surface, and the surface is allowed to rotate under a fixed transmitter and receiver, explicit dependence of the solution on the azimuthal incident direction ϕ_i and the azimuthal scattering direction ϕ_s will be maintained, rather than aligning the global coordinate system with either the transmitter or receiver azimuth direction. The directions of incidence and scattering will then be uniquely determined by $(\theta_i, \theta_s, \phi_\Delta)$. While the surfaces in this dissertation are assumed to be azimuthally symmetric, the polarization amplitudes above do not yet incorporate that assumption and need not be rederived for the case of a non-azimuthally symmetric rough surface or a periodic surface.

5.3 Field Expansions

Unfortunately, the exact expressions for the polarization amplitudes U are not mathematically tractable in the Stratton-Chu integral, as the surface slopes are random functions of the location on the surface. Sung and Holzer [41] provide an exact solution to the two dimensional rough surface problem by employing a spectral representation for the surface slopes, yielding a deterministic, rather than ensemble average, 3-fold integral for the incoherent field. Further approximations reduce the dimensionality of the solution, but their effects are difficult to measure. An exact solution, under the tangent plane approximation, for the corresponding three dimensional incoherent scattering problem would reduce to a 6-fold integral.

An approximate solution which is much easier to evaluate, both for the solution and for the effect of the approximation, can be obtained by expanding U in a Taylor series in slopes and retaining only the first terms:

$$U_{pq}(x,y) = U_{pq}^{(0)} + U_{pq}^{(1)} + U_{pq}^{(2)} + \ldots \tag{5.17}$$

$$U_{pq}^{(0)} = a_{00pq} \tag{5.18}$$

$$U_{pq}^{(1)} = \frac{1}{\sin\theta_i}\left(a_{10pq}Z_l(x,y) + a_{01pq}Z_t(x,y)\right) \tag{5.19}$$

$$U_{pq}^{(2)} = \frac{1}{\sin^2\theta_i}\left(a_{20pq}Z_l^2(x,y) + a_{11pq}Z_l(x,y)Z_t(x,y) + a_{02pq}Z_t^2(x,y)\right) \tag{5.20}$$

where the coefficient $a_{k'l'pq}$ is for the term of U_{pq} proportional to $\frac{Z_l^{k'}}{\sin^{k'}\theta_i}\frac{Z_t^{l'}}{\sin^{l'}\theta_i}$. Except for the local reflection coefficients, the Taylor expansion of the algebraic expressions that constitute the numerators of U_{pq} is straightforward. The variable in the denominator, D_1, is Taylor

expanded as follows:

$$\frac{1}{D_1^2} = \frac{1}{(\sin\theta_i - Z_l\cos\theta_i)^2 + Z_t^2} \tag{5.21}$$

$$= \frac{1}{\sin^2\theta_i}\sum_{m=0}^{\infty}\sum_{n=0}^{\infty}(-1)^n\frac{(2n+m+1)!}{m!(2n+1)!}\frac{Z_t^{2n}}{\sin^{2n}\theta_i}\frac{Z_l^m}{\tan^m\theta_i} \tag{5.22}$$

$$= \frac{1}{\sin^2\theta_i}\left(1 - \frac{Z_t^2}{\sin^2\theta_i} + 2\frac{Z_l}{\tan\theta_i} + 3\frac{Z_l^2}{\tan^2\theta_i} + \ldots\right) \tag{5.23}$$

The local reflection coefficients are functions of the position on the surface, and, under the tangent-plane approximation, the Fresnel reflection coefficients are given by

$$R_h = \frac{\eta_2\cos\theta_{il} - \eta_1\cos\theta_{tl}}{\eta_2\cos\theta_{il} + \eta_1\cos\theta_{tl}} \tag{5.24}$$

$$R_v = \frac{\eta_1\cos\theta_{il} - \eta_2\cos\theta_{tl}}{\eta_1\cos\theta_{il} + \eta_2\cos\theta_{tl}} \tag{5.25}$$

where θ_{il} and θ_{tl} are the local angles of incidence and transmission, respectively. From Figure 2.11, it is apparent that

$$\cos\theta_{il} = -\hat{\mathbf{k}}_i\cdot\hat{\mathbf{n}}_1 = (\cos\theta_i + Z_l\sin\theta_i)/D_n \tag{5.26}$$

From Snell's Law, namely, $k_1\sin\theta_{il} = k_2\sin\theta_{tl}$,

$$\cos\theta_{tl} = \sqrt{1 - \frac{k_1^2}{k_2^2}\sin^2\theta_{il}}$$

$$= \sqrt{1 - \frac{k_1^2}{k_2^2} + \frac{k_1^2}{k_2^2}(\cos\theta_i + Z_l\sin\theta_i)^2/D_n^2} \tag{5.27}$$

The local reflection coefficients, expanded in a Taylor series around zero slopes, are:

$$\begin{aligned} R_v(x,y) &= \sum_{m=0}^{\infty}\sum_{n=0}^{\infty} R_{vmn} Z_l^m(x,y) Z_t^n(x,y) \\ &= R_{v00} + R_{v10} Z_l(x,y) + R_{v20} Z_l^2(x,y) + R_{v02} Z_t^2(x,y) + \ldots \end{aligned} \tag{5.28}$$

$$\begin{aligned} R_h(x,y) &= \sum_{m=0}^{\infty}\sum_{n=0}^{\infty} R_{hmn} Z_l^m(x,y) Z_t^n(x,y) \\ &= R_{h00} + R_{h10} Z_l(x,y) + R_{h20} Z_l^2(x,y) + R_{h02} Z_t^2(x,y) + \ldots \end{aligned} \tag{5.29}$$

The local reflection coefficients depend on even powers only of Z_t.

The Taylor series coefficients are found from the standard formula for a two-variable Taylor series:

$$R_{pmn} = \frac{1}{m!n!}\left(\frac{\partial^{m+n}}{\partial^m Z_l \partial^n Z_t} R_p\right)\Bigg|_{Z_l=Z_t=0} \tag{5.30}$$

and will be referred to as the local field reflectivity expansion coefficients, or expansion co-

efficients, to avoid confusion. The first few expansion coefficients evaluated this way are

$$R_{h00} = \frac{\eta_2 \cos\theta_i - \eta_1 \cos\theta_t}{\eta_2 \cos\theta_i + \eta_1 \cos\theta_t} \tag{5.31}$$

$$R_{v00} = \frac{\eta_1 \cos\theta_i - \eta_2 \cos\theta_t}{\eta_1 \cos\theta_i + \eta_2 \cos\theta_t} \tag{5.32}$$

$$R_{h10} = \frac{\eta_2 \sin\theta_i (1 - R_{h00}) - \eta_1 \frac{k_1 \cos\theta_i}{k_2 \cos\theta_t} \sin\theta_t (1 + R_{h00})}{\eta_2 \cos\theta_i + \eta_1 \cos\theta_t} \tag{5.33}$$

$$R_{v10} = \frac{\eta_1 \sin\theta_i (1 - R_{v00}) - \eta_2 \frac{k_1 \cos\theta_i}{k_2 \cos\theta_t} \sin\theta_t (1 + R_{v00})}{\eta_1 \cos\theta_i + \eta_2 \cos\theta_t} \tag{5.34}$$

$$R_{h02} = \frac{-\eta_1 (1 - k_1^2/k_2^2)(1 + R_{h00})}{2(\eta_2 \cos\theta_i + \eta_1 \cos\theta_t)\cos\theta_t} \tag{5.35}$$

$$R_{h20} = \frac{R_{h02}}{\cos^2\theta_t} - R_{h10} \frac{\eta_2 \sin\theta_i + \eta_1 \frac{k_1 \cos\theta_i}{k_2 \cos\theta_t} \sin\theta_t}{\eta_2 \cos\theta_i + \eta_1 \cos\theta_t} \tag{5.36}$$

$$R_{v02} = \frac{-\eta_2 (1 - k_1^2/k_2^2)(1 + R_{v00})}{2(\eta_1 \cos\theta_i + \eta_2 \cos\theta_t)\cos\theta_t} \tag{5.37}$$

$$R_{v20} = \frac{R_{v02}}{\cos^2\theta_t} - R_{v10} \frac{\eta_1 \sin\theta_i + \eta_2 \frac{k_1 \cos\theta_i}{k_2 \cos\theta_t} \sin\theta_t}{\eta_1 \cos\theta_i + \eta_2 \cos\theta_t} \tag{5.38}$$

where θ_t is related to θ_i by Snell's Law: $k_1 \sin\theta_i = k_2 \sin\theta_t$. The expansion coefficients have been confirmed numerically with the aid of modern symbolic mathematical analysis software.

The zeroth order expansion coefficients are identical to the reflection coefficients for a smooth surface. Leader [27] solves the scattering problem with this sort of expansion, but explicit expressions for the neither local reflection coefficients nor their derivatives are given. Holzer and Sung [21] propose expanding the reflection coefficients up to second order in this manner, but the factorals in (5.30) were neglected, resulting in errors for all second order expansion coefficients. Their terms for R_{h20} and R_{v20} do not agree to two digits of precision with the expressions above even with the factor of two correction.

These first order expansion coefficients, R_{v10} and R_{h10}, are different from those found in Ulaby *et al.* [48] and Ulaby and Elachi [47] due to the incorporation of a more precise method for expanding the local angle of transmission, in which the local angle of transmission is related to the local angle of incidence *via* Snell's law (5.27). In [48], the expansion coefficients are calculated only after simplifying approximations have been applied to the expressions for the local reflection coefficients. These approximation do not change the zeroth order expansion coefficients from those presented here, but they do change the first order expansion coefficients.

For v polarization, some higher order reflection coefficients are

$$\begin{aligned} R_{v12} &= -R_{v02}\left(\frac{\eta_1 \sin\theta_i + \eta_2 \frac{k_1 \cos\theta_i}{k_2 \cos\theta_t} \sin\theta_t}{\eta_1 \cos\theta_i + \eta_2 \cos\theta_t} + \frac{k_1 \cos\theta_i}{k_2 \cos\theta_t} \tan\theta_t\right) \\ &\quad - \frac{\eta_2 R_{v10}\left(1 - \frac{k_1^2}{k_2^2}\right)}{2(\eta_1 \cos\theta_i + \eta_2 \cos\theta_t)\cos\theta_t} \end{aligned} \tag{5.39}$$

$$R_{v30} = \frac{R_{v12}}{\cos^2\theta_t} + R_{v10}\left(\frac{\eta_1 \sin\theta_i + \eta_2 \frac{k_1 \cos\theta_i}{k_2 \cos\theta_t} \sin\theta_t}{\eta_1 \cos\theta_i + \eta_2 \cos\theta_t}\right)^2 \tag{5.40}$$

$$R_{v04} = -R_{v02}(2 - R_{v00}) \frac{1}{4\cos^2\theta_t}\left(1 - \frac{k_1^2}{k_2^2}\right) \tag{5.41}$$

$$\begin{aligned} R_{v22} &= R_{v02}\left(\left(\frac{\eta_1 \sin\theta_i + \eta_2 \frac{k_1 \cos\theta_i}{k_2 \cos\theta_t} \sin\theta_t}{\eta_1 \cos\theta_i + \eta_2 \cos\theta_t}\right)^2 - \frac{1}{2\cos^4\theta_t}\left(1 - \frac{k_1^2}{k_2^2}\right)\right) \\ &\quad - R_{v12}\frac{k_1 \cos\theta_i}{k_2 \cos\theta_t}\tan\theta_t - R_{v20}\frac{\eta_2\left(1 - \frac{k_1^2}{k_2^2}\right)}{(\eta_1 \cos\theta_i + \eta_2 \cos\theta_t)\cos\theta_t} \end{aligned} \tag{5.42}$$

$$R_{v40} = \frac{R_{v22}}{\cos^2\theta_t} - \frac{R_{v04}}{\cos^4\theta_t} - R_{v10}\left(\frac{\eta_1 \sin\theta_i + \eta_2 \frac{k_1 \cos\theta_i}{k_2 \cos\theta_t} \sin\theta_t}{\eta_1 \cos\theta_i + \eta_2 \cos\theta_t}\right)^3 \tag{5.43}$$

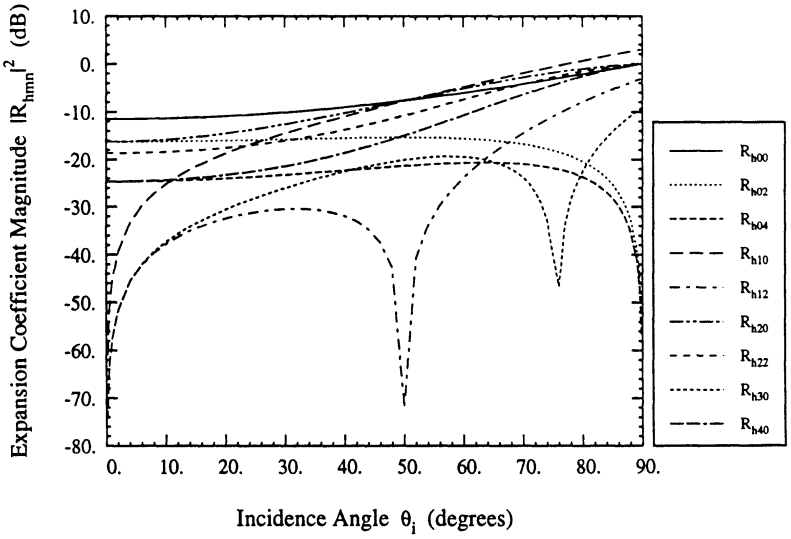

Figure 5.1: h-polarized field reflectivity expansion coefficients for a nonmagnetic surface with a relative dielectric $\varepsilon_r = 3.0 - j0.0$.

The corresponding h coefficients are found by applying the duality principle; in particular, replace R_{vmn} with R_{hmn}, and exchange η_1 and η_2.

For a perfectly conducting surface, $\eta_2 = 0$ and all the expansion coefficients are zero, except for the zeroth order expansion coefficients, which evaluate to $R_{h00} = -1$ and $R_{v00} = 1$. For dielectric surfaces, the relative magnitudes of the expansion coefficients are shown in Figure 5.1 through Figure 5.4. While the figures show the magnitudes of the expansion coefficients for lossless dielectrics only, the same trends exist for lossy dielectrics. As can be seen in the figures, the lowest order expansion coefficients, R_{v00} and R_{h00}, are always larger than the others at nadir. As the incidence angle θ_i increases, however, the lowest order expansion coefficients may not be the largest. For h-polarization, an increase in the dielectric, from $\varepsilon_r = 3$ in Figure 5.1 to $\varepsilon_r = 30$ in Figure 5.3, results in a decrease in the higher order expansion coefficients relative to the zeroth order expansion coefficient. This trend is in agreement with our expectation for the perfectly conducting surface. The v-polarized expansion

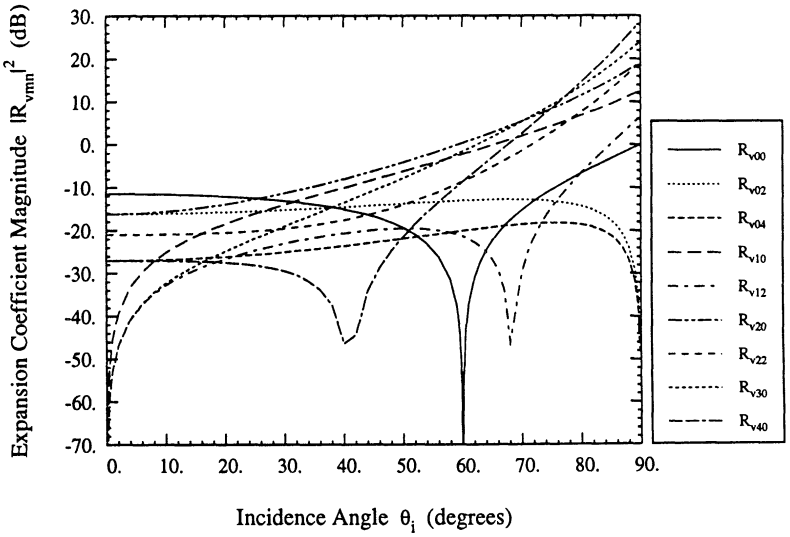

Figure 5.2: *v*-polarized field reflectivity expansion coefficients for a nonmagnetic surface with a relative dielectric $\varepsilon_r = 3.0 - j0.0$.

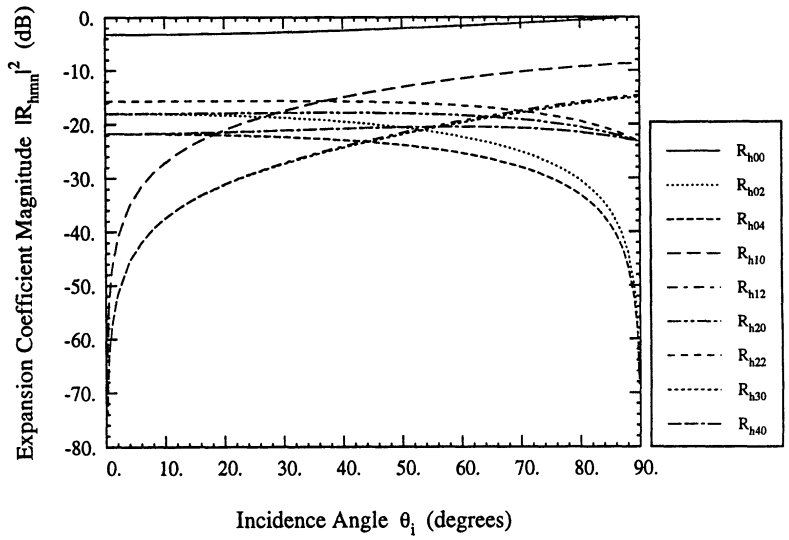

Figure 5.3: *h*-polarized field reflectivity expansion coefficients for a nonmagnetic surface with a relative dielectric $\varepsilon_r = 30.0 - j0.0$.

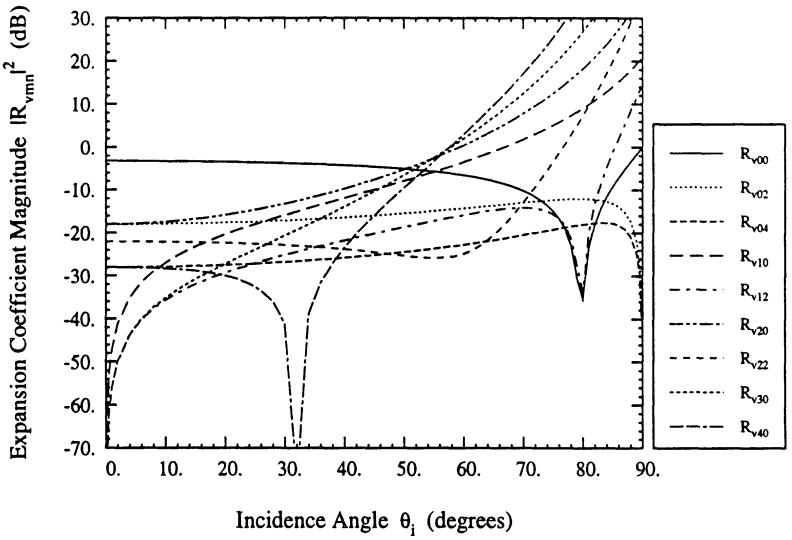

Figure 5.4: v-polarized field reflectivity expansion coefficients for a nonmagnetic surface with a relative dielectric $\varepsilon_r = 30.0 - j0.0$.

coefficients in Figure 5.2 and Figure 5.4 show a dramatically different trend, however. At nadir, the zeroth order expansion coefficient becomes more dominant as the dielectric increases, and the range of incidence angles for which it is the largest expansion coefficient gets larger. But the higher order expansion coefficients are growing larger near grazing, indicating that the perfectly conducting case is not uniformly arrived at as the dielectric increases for v-polarization. One cannot automatically conclude that as the dielectric of the surface increases that higher order scattering terms can be neglected for v-polarized scattering involving near–grazing incidence.

While the different expansion coefficients can be compared on the basis of their magnitudes, their effect on the coherent and incoherent scattering terms is through the coefficients a, which also depend heavily on the bistatic angles. In other words, comparisons such as those shown in Figure 5.1 through Figure 5.4 should not be used solely to determine if a particular expansion coefficient is negligible or not.

The coefficients a, from (5.18) through (5.20), in the expansion of U_{hh} are given by:

$$a_{00hh} = -R_{h00}(\cos\theta_i + \cos\theta_s)\cos\phi_\Delta \tag{5.44}$$

$$a_{10hh} = (R_{h00}(\sin\theta_s - \sin\theta_i\cos\phi_\Delta) - R_{h10}(\cos\theta_i + \cos\theta_s)\cos\phi_\Delta)\sin\theta_i \tag{5.45}$$

$$a_{01hh} = R_{v00}(1 + \cos\theta_i\cos\theta_s)\sin\phi_\Delta + R_{h00}\cos\theta_i(\cos\theta_i + \cos\theta_s)\sin\phi_\Delta \tag{5.46}$$

$$a_{20hh} = (R_{h10}(\sin\theta_s - \sin\theta_i\cos\phi_\Delta) - R_{h20}(\cos\theta_i + \cos\theta_s)\cos\phi_\Delta)\sin^2\theta_i \tag{5.47}$$

$$\begin{aligned} a_{11hh} = {} & (R_{v00} + R_{h00})(\cos\theta_i + \cos\theta_s)\sin\phi_\Delta + R_{v10}\sin\theta_i(1 + \cos\theta_i\cos\theta_s)\sin\phi_\Delta \\ & + R_{h10}\sin\theta_i\cos\theta_i(\cos\theta_i + \cos\theta_s)\sin\phi_\Delta \end{aligned} \tag{5.48}$$

$$\begin{aligned} a_{02hh} = {} & -(R_{h00} + R_{v00})\cos\theta_i(\sin\theta_i\sin\theta_s - (1 + \cos\theta_i\cos\theta_s)\cos\phi_\Delta) \\ & - R_{h02}\sin^2\theta_i(\cos\theta_i + \cos\theta_s)\cos\phi_\Delta \end{aligned} \tag{5.49}$$

The third order coefficients a are given by

$$a_{30hh} = (R_{h20}(\sin\theta_s - \sin\theta_i\cos\phi_\Delta) - R_{h30}(\cos\theta_i + \cos\theta_s)\cos\phi_\Delta)\sin^3\theta_i \tag{5.50}$$

$$\begin{aligned} a_{21hh} = {} & ((R_{h00} + R_{v00})\cos\theta_i + (R_{h10} + R_{v10})\sin\theta_i)(\cos\theta_i + \cos\theta_s)\sin\phi_\Delta \\ & + (R_{h20}\cos\theta_i(\cos\theta_i + \cos\theta_s) + R_{v20}(1 + \cos\theta_i\cos\theta_s))\sin^2\theta_i\sin\phi_\Delta \end{aligned} \tag{5.51}$$

$$\begin{aligned} a_{12hh} = {} & -(R_{h00} + R_{v00})\left(1 + \cos^2\theta_i\right)(\sin\theta_i\sin\theta_s - (1 + \cos\theta_i\cos\theta_s)\cos\phi_\Delta) \\ & + (R_{h10} + R_{v10})\sin\theta_i\cos\theta_i(\sin\theta_i\sin\theta_s - (1 + \cos\theta_i\cos\theta_s)\cos\phi_\Delta) \\ & + (R_{h02}(\sin\theta_s - \sin\theta_i\cos\phi_\Delta) - R_{h12}(\cos\theta_i + \cos\theta_s)\cos\phi_\Delta)\sin^3\theta_i \end{aligned} \tag{5.52}$$

$$\begin{aligned} a_{03hh} = {} & -(R_{h00} + R_{v00})\cos\theta_i(\cos\theta_i + \cos\theta_s)\sin\phi_\Delta \\ & + (R_{h02}\cos\theta_i(\cos\theta_i + \cos\theta_s) + R_{v02}(1 + \cos\theta_i\cos\theta_s))\sin^2\theta_i\sin\phi_\Delta \end{aligned} \tag{5.53}$$

The fourth order coefficients a are given by

$$a_{40hh} = (R_{h30}(\sin\theta_s - \sin\theta_i\cos\phi_\Delta) - R_{h40}(\cos\theta_i + \cos\theta_s)\cos\phi_\Delta)\sin^4\theta_i \quad (5.54)$$

$$\begin{aligned} a_{31hh} = {} & (R_{h00} + R_{v00})\cos^2\theta_i(\cos\theta_i + \cos\theta_s)\sin\phi_\Delta \\ & + (R_{h10} + R_{v10})\sin\theta_i\cos\theta_i(\cos\theta_i + \cos\theta_s)\sin\phi_\Delta \\ & + (R_{h20} + R_{v20})\sin^2\theta_i(\cos\theta_i + \cos\theta_s)\sin\phi_\Delta \\ & + R_{h30}\sin^3\theta_i\cos\theta_i(\cos\theta_i + \cos\theta_s)\sin\phi_\Delta \\ & + R_{v30}\sin^3\theta_i(1 + \cos\theta_i\cos\theta_s)\sin\phi_\Delta \end{aligned} \quad (5.55)$$

$$\begin{aligned} a_{22hh} = {} & (R_{h00} + R_{v00})\left(2 + \cos^2\theta_i\right)\cos\theta_i(\sin\theta_i\sin\theta_s - (1 + \cos\theta_i\cos\theta_s)\cos\phi_\Delta) \\ & + (R_{h10} + R_{v10})\left(1 + \cos^2\theta_i\right)\sin\theta_i(\sin\theta_i\sin\theta_s - (1 + \cos\theta_i\cos\theta_s)\cos\phi_\Delta) \\ & + (R_{h20} + R_{v20})\sin^2\theta_i\cos\theta_i(\sin\theta_i\sin\theta_s - (1 + \cos\theta_i\cos\theta_s)\cos\phi_\Delta) \\ & + (R_{h12}(\sin\theta_s - \sin\theta_i\cos\phi_\Delta) + R_{h22}(\cos\theta_i + \cos\theta_s)\cos\phi_\Delta)\sin^4\theta_i \end{aligned} \quad (5.56)$$

$$\begin{aligned} a_{13hh} = {} & -(R_{h00} + R_{v00})\left(1 + 2\cos^2\theta_i\right)(\cos\theta_i + \cos\theta_s)\sin\phi_\Delta \\ & - (R_{h10} + R_{v10})\sin\theta_i\cos\theta_i(\cos\theta_i + \cos\theta_s)\sin\phi_\Delta \\ & + (R_{h02} + R_{v02})\sin^2\theta_i(\cos\theta_i + \cos\theta_s)\sin\phi_\Delta \\ & + (R_{h12}\cos\theta_i(\cos\theta_i + \cos\theta_s) + R_{v12}(1 + \cos\theta_i\cos\theta_s))\sin^3\theta_i\sin\phi_\Delta \end{aligned} \quad (5.57)$$

$$\begin{aligned} a_{04hh} = {} & (R_{h00} + R_{v00})\cos\theta_i(\sin\theta_i\sin\theta_s - (1 + \cos\theta_i\cos\theta_s)\cos\phi_\Delta) \\ & - (R_{h02} + R_{v02})\sin^2\theta_i\cos\theta_i(\sin\theta_i\sin\theta_s - (1 + \cos\theta_i\cos\theta_s)\cos\phi_\Delta) \\ & - R_{h04}\sin^4\theta_i(\cos\theta_i + \cos\theta_s)\cos\phi_\Delta \end{aligned} \quad (5.58)$$

The coefficients for U_{vv} can be found from those for U_{hh} by replacing R_h with R_v and *vice*

versa.

The coefficients a in the expansion of U_{vh} are given by:

$$a_{00vh} = -R_{h00}(1+\cos\theta_i\cos\theta_s)\sin\phi_\Delta \tag{5.59}$$

$$a_{10vh} = -R_{h00}\sin^2\theta_i\cos\theta_s\sin\phi_\Delta - R_{h10}\sin\theta_i(1+\cos\theta_i\cos\theta_s)\sin\phi_\Delta \tag{5.60}$$

$$a_{01vh} = R_{h00}\cos\theta_i(\sin\theta_i\sin\theta_s - (1+\cos\theta_i\cos\theta_s)\cos\phi_\Delta) - R_{v00}(\cos\theta_i+\cos\theta_s)\cos\phi_\Delta \tag{5.61}$$

$$a_{20vh} = -R_{h10}\sin^3\theta_i\cos\theta_s\sin\phi_\Delta - R_{h20}\sin^2\theta_i(1+\cos\theta_i\cos\theta_s)\sin\phi_\Delta \tag{5.62}$$

$$\begin{aligned} a_{11vh} = {} & (R_{h00}+R_{v00}+R_{h10}\sin\theta_i\cos\theta_i)(\sin\theta_i\sin\theta_s-(1+\cos\theta_i\cos\theta_s)\cos\phi_\Delta) \\ & -R_{v10}\sin\theta_i(\cos\theta_i+\cos\theta_s)\cos\phi_\Delta \end{aligned} \tag{5.63}$$

$$a_{02vh} = \Big((R_{h00}+R_{v00})\cos\theta_i(\cos\theta_i+\cos\theta_s) - R_{h02}\sin^2\theta_i(1+\cos\theta_i\cos\theta_s)\Big)\sin\phi_\Delta \tag{5.64}$$

The coefficients for U_{hv} can be found from those for U_{vh} by replacing the expansion coefficients for R_h with those for $-R_v$ and *vice versa.*

5.4 Rough Surface Reflection Coefficient

With the exact expressions for the tangent-plane polarization amplitudes U, and their Taylor series coefficients a in surface slopes, the mean field from the surface can be calcu-

lated directly from the far-field expression for the Stratton-Chu integral equation (5.1):

$$\langle E^s_{pq} \rangle = \frac{-jk_s e^{-jk_s R_0}}{4\pi R_0} E_0 \left\langle \int \frac{U_{pq}}{D_n} e^{jk_s(\hat{\mathbf{k}}_s - \hat{\mathbf{k}}_i)\cdot \mathbf{r}} dS \right\rangle \tag{5.65}$$

$$= \frac{-jk_s e^{-jk_s R_0}}{4\pi R_0} E_0 \left\langle \int \frac{U_{pq}}{D_n} e^{j\kappa_z z(x,y)} e^{j(\kappa_x x + \kappa_y y)} D_n dxdy \right\rangle \tag{5.66}$$

$$= \frac{-jk_s e^{-jk_s R_0}}{4\pi R_0} E_0 \int \left\langle U_{pq} e^{j\kappa_z z(x,y)} \right\rangle e^{j(\kappa_x x + \kappa_y y)} dxdy \tag{5.67}$$

where κ_x, κ_y, and κ_z denote the x, y and z components of the change in k-vector due to scattering and are defined by (2.10) through (2.12).

Upon applying the expansion in (5.17), the scattered field can be expressed as a sum of scattered fields each of a particular order:

$$\langle E^s_{pq} \rangle = \left\langle E^{(0)}_{pq} \right\rangle + \left\langle E^{(1)}_{pq} \right\rangle + \left\langle E^{(2)}_{pq} \right\rangle + \ldots \tag{5.68}$$

$$\left\langle E^{(n)}_{pq} \right\rangle = \frac{-jk_s e^{-jk_s R_0}}{4\pi R_0} E_0 \iint \left\langle U^{(n)}_{pq} e^{j\kappa_z z} \right\rangle e^{j(\kappa_x x + \kappa_y y)} dxdy \tag{5.69}$$

The nth term of $\langle E^s_{pq} \rangle$ is proportional to $U^{(n)}_{pq}$, which, in turn, is proportional to the nth power of the slopes of the surface. When the surface is flat, the slopes are zero, so for a flat surface, $\left\langle E^{(n)}_{pq} \right\rangle = 0$ for all $n > 0$. Therefore, the scattered field for a flat surface (defined

by $z = 0$) is given by

$$\langle E^s_{pq} \rangle_{flat} = \frac{-jk_s e^{-jk_s R_0}}{4\pi R_0} E_0 \iint \left\langle U^{(0)}_{pq} e^{j\kappa_z 0} \right\rangle e^{j(\kappa_x x + \kappa_y y)} dxdy \tag{5.70}$$

$$= \frac{-jk_s e^{-jk_s R_0}}{4\pi R_0} E_0 a_{00pq} \iint e^{j(\kappa_x x + \kappa_y y)} dxdy \tag{5.71}$$

$$= \frac{-jk_s e^{-jk_s R_0}}{4\pi R_0} E_0 a_{00pq} (2\pi)^2 \delta(\kappa_x)\delta(\kappa_y) \tag{5.72}$$

$$= \frac{jk_s e^{-jk_s R_0}}{4\pi R_0} E_0 (2\pi)^2 R_{q00}(\cos\theta_i + \cos\theta_s)\delta(\kappa_x)\delta(\kappa_y)\delta_{pq} \tag{5.73}$$

The Dirac delta functions, $\delta(\kappa_x)$ and $\delta(\kappa_y)$, together indicate that the coherent field exists only in the specular scattering direction ($\kappa_x = \kappa_y = 0$). In the specular scattering direction, $\phi_\Delta = 0$ and $\theta_i = \theta_s$. The Kronecker delta function, δ_{pq}, reflects the fact that the coherent field does not exist for cross-polarization.

From our knowledge of scattering of plane waves by plane interfaces, the p-polarized scattered field due to a q-polarized wave ($\hat{\mathbf{q}} E_0 e^{-jk\hat{\mathbf{k}}_i \cdot \mathbf{r}}$) is

$$E^s_{pq} = R_{q00} E_0 e^{-jk\hat{\mathbf{k}}_s \cdot \mathbf{r}} \delta_{pq} \tag{5.74}$$

and this expression must be equivalent to (5.73).

5.4.1 Evaluation of Expected Values: Coherent Case

The calculation of expected scattered field from a rough surface requires the evaluation of the expected value within (5.69). This translates into an evaluation of an expected value

of the form

$$\left\langle Z_l^{n_l} Z_t^{n_t} e^{j\kappa_z z} \right\rangle \tag{5.75}$$

where n_l and n_t are arbitrary non-negative integers, since the polarization amplitudes U have been expanded into a power series in slopes.

The analysis of (5.75) starts with the expression for the characteristic function of N Gaussian distributed random variables [10]:

$$\left\langle e^{j\sum_{n=1}^{N} \nu_n z_n} \right\rangle = e^{j\sum_{n=1}^{N} \nu_n \mu_n - \frac{1}{2}\sum_{n=1}^{N}\sum_{m=1}^{N} \nu_n \nu_m \sigma_n \sigma_m \rho_{nm}} \tag{5.76}$$

where z_n is a Gaussian random variable with mean μ_n and variance σ_n^2, and ρ_{nm} is the normalized correlation function of z_n and z_m:

$$\rho_{nm} = \left\langle \left(\frac{z_n - \mu_n}{\sigma_n} \right) \left(\frac{z_m - \mu_m}{\sigma_m} \right) \right\rangle \tag{5.77}$$

$\rho_{nm} = \rho_{mn}$ for all n, m, and $\rho_{nn} = 1$.

If we are to interpret z_n as the height of a zero mean surface at point (x_n, y_n), then (5.76) becomes:

$$\left\langle e^{j\sum_{n=1}^{N} \nu_n z_n(x_n, y_n)} \right\rangle = e^{-\frac{1}{2}\sum_{n=1}^{N}\sum_{m=1}^{N} \nu_n \nu_m \sigma^2 \rho(x_n - x_m, y_n - y_m)} \tag{5.78}$$

where it is recognized that the variance σ^2 of the surface is independent of where it is evaluated, and the explicit relationship of z_n and ρ on the surface points is given.

For evaluating (5.75), set $N = \max(1, n_x + n_y)$ in (5.78) and differentiate both sides $n_x + n_y$ times, once with respect to each of $x_1, x_2, \cdots, x_{n_x}, y_{n_x+1}, \cdots, y_{n_x+n_y}$, then evaluate the result at the same point (x, y) on the surface for all N. For example, to find

$$\left\langle Z_x^2 e^{j\kappa_z z} \right\rangle \tag{5.79}$$

we evaluate

$$\frac{\partial}{\partial x_1}\frac{\partial}{\partial x_2}\left\langle e^{j\nu_1 z_1 + j\nu_2 z_2}\right\rangle = \frac{\partial}{\partial x_1}\frac{\partial}{\partial x_2} e^{-\frac{1}{2}\sigma^2(\nu_1^2+\nu_2^2+2\nu_1\nu_2\rho_{12})} \tag{5.80}$$

$$\left\langle \left(j\nu_1\frac{\partial}{\partial x_1}z_1\right)\left(j\nu_2\frac{\partial}{\partial x_2}z_2\right) e^{j\nu_1 z_1 + j\nu_2 z_2}\right\rangle = \left(\left(\sigma^2\nu_1\nu_2\frac{\partial}{\partial x_1}\rho_{12}\right)\left(\sigma^2\nu_1\nu_2\frac{\partial}{\partial x_2}\rho_{12}\right) - \sigma^2\nu_1\nu_2\frac{\partial^2}{\partial x_1 \partial x_2}\rho_{12}\right) e^{-\frac{1}{2}\sigma^2(\nu_1^2+\nu_2^2+2\nu_1\nu_2\rho_{12})} \tag{5.81}$$

where the shorthand notation $\rho_{nm} = \rho(x_n - x_m, y_n - y_m)$ is used.

If we can guarantee that $\nu_1\nu_2 \neq 0$ we can divide both sides by $-\nu_1\nu_2$. Also, $\frac{\partial}{\partial x_2}\rho_{12} = -\frac{\partial}{\partial x_1}\rho_{12}$, so

$$\left\langle \left(\frac{\partial}{\partial x_1}z_1\right)\left(\frac{\partial}{\partial x_2}z_2\right) e^{j\nu_1 z_1 + j\nu_2 z_2}\right\rangle = -\sigma^2\left(\frac{\partial^2}{\partial {x_1}^2}\rho_{12} - \sigma^2\nu_1\nu_2\left(\frac{\partial}{\partial x_1}\rho_{12}\right)^2\right) e^{-\frac{1}{2}\sigma^2(\nu_1^2+\nu_2^2+2\nu_1\nu_2\rho_{12})} \tag{5.82}$$

At this point, we specialize to the more specific case where $x = x_1 = x_2$ and $y = y_1 = y_2$.

Under these circumstances, $z = z_1 = z_2$ as well:

$$\left\langle \left(\frac{\partial}{\partial x} z\right)^2 e^{j(\nu_1+\nu_2)z} \right\rangle = -\sigma^2 \left(\frac{\partial^2}{\partial x^2}\rho(0,0)\right) e^{-\frac{1}{2}\sigma^2(\nu_1+\nu_2)^2} \tag{5.83}$$

where it has been recognized that $\rho(0,0) = 1$ and $\frac{\partial}{\partial x}\rho(0,0) = 0$. By setting $\nu_1 + \nu_2 = \kappa_z$,

$$\left\langle Z_x^2 e^{j\kappa_z z} \right\rangle = \left(-\sigma^2 \frac{\partial^2}{\partial x^2}\rho(x,y)\right)\Big|_{x=y=0} e^{-\frac{1}{2}\kappa_z^2\sigma^2} \tag{5.84}$$

$$= m^2 e^{-\frac{1}{2}\kappa_z^2\sigma^2} \tag{5.85}$$

where the mean squared slope $m^2 = \left(-\sigma^2 \frac{\partial^2}{\partial x^2}\rho(x,y)\right)\Big|_{x=y=0}$.

Since the surface is azimuthally symmetric, $m^2 = \left(-\sigma^2 \frac{\partial^2}{\partial y^2}\rho(x,y)\right)\Big|_{x=y=0}$ as well.

Upon carrying this process out for arbitrary powers of the surface slopes in the x- and y-directions, it appears that the general solution is of the form

$$\begin{aligned}\left\langle Z_x^{2n_x} Z_y^{2n_y} e^{j\kappa_z z} \right\rangle &= (1\cdot 3\cdot 5\ldots(2n_x-1)) m^{2n_x} \left(1\cdot 3\cdot 5\ldots(2n_y-1)\right) m^{2n_y} e^{-\frac{1}{2}\kappa_z^2\sigma^2} \\ &= \frac{(2n_x)!(2n_y)!}{2^{n_x+n_y} n_x! n_y!} m^{2(n_x+n_y)} e^{-\frac{1}{2}\kappa_z^2\sigma^2}\end{aligned} \tag{5.86}$$

$$\left\langle Z_x^{2n_x+1} Z_y^{2n_y} e^{j\kappa_z z} \right\rangle = \left\langle Z_x^{2n_x+1} Z_y^{2n_y+1} e^{j\kappa_z z} \right\rangle = \left\langle Z_x^{2n_x} Z_y^{2n_y+1} e^{j\kappa_z z} \right\rangle = 0 \tag{5.87}$$

which can be used with (2.41) and (2.42) to show that (5.75) has these solutions:

$$\left\langle Z_l^{2n_l} Z_t^{2n_t} e^{j\kappa_z z} \right\rangle = \frac{(2n_l)!(2n_t)!}{2^{n_l+n_t} n_l! n_t!} m^{2(n_l+n_t)} e^{-\frac{1}{2}\kappa_z^2\sigma^2} \tag{5.88}$$

$$\left\langle Z_l^{2n_l+1} Z_t^{2n_t} e^{j\kappa_z z} \right\rangle = \left\langle Z_l^{2n_l+1} Z_t^{2n_t+1} e^{j\kappa_z z} \right\rangle = \left\langle Z_l^{2n_l} Z_t^{2n_t+1} e^{j\kappa_z z} \right\rangle = 0 \tag{5.89}$$

Since the evaluations of the expected value within (5.69) are independent of x and y, they may be pulled outside the integral:

$$\left\langle E_{pq}^{(n)} \right\rangle = \frac{-jk_s e^{-jk_s R_0}}{4\pi R_0} E_0 \left\langle U_{pq}^{(n)} e^{j\kappa_z z} \right\rangle \iint e^{j(\kappa_x x + \kappa_y y)} dxdy \tag{5.90}$$

$$= \frac{-jk_s e^{-jk_s R_0}}{4\pi R_0} E_0 \left\langle U_{pq}^{(n)} e^{j\kappa_z z} \right\rangle (2\pi)^2 \delta(\kappa_x)\delta(\kappa_y) \tag{5.91}$$

Thus, like the scattered field from the smooth surface, the coherent field scattered from a rough surface exists only in the specular direction. By comparing (5.91) to (5.73), it is apparent that an alternative description of the scattered field may be provided by defining an nth order rough surface reflection coefficient, such that

$$\left\langle E_{pq}^{(n)} \right\rangle = R_{pq}^{(n)} E_0 e^{-jk\hat{\mathbf{k}}_s \cdot \mathbf{r}} \tag{5.92}$$

similar to (5.74), where

$$R_{pq}^{(n)} = -\left(\frac{\left\langle U_{pq}^{(n)} e^{j\kappa_z z} \right\rangle}{\cos\theta_i + \cos\theta_s} \right) \Bigg|_{\theta_s = \theta_i, \phi_\Delta = 0^\circ} \tag{5.93}$$

5.4.2 Zeroth Order Reflection Coefficient

The expected value in (5.69) for the zeroth order field scattered from a rough surface is given by

$$\left\langle U_{pq}^{(0)} e^{j\kappa_z z} \right\rangle = a_{00pq} \left\langle e^{j\kappa_z z} \right\rangle = a_{00pq} e^{-\frac{1}{2}\kappa_z^2 \sigma^2} \tag{5.94}$$

so that

$$R_{pq}^{(0)} = R_{q00} e^{-\frac{1}{2}\kappa_z^2 \sigma^2} \delta_{pq} \tag{5.95}$$

This is the reflection coefficient for the Physical Optics rough surface that appears in Chapter 2.

5.4.3 First Order Reflection Coefficient

From the general expression for the expected values for odd powers of the slopes given by (5.89), the expected value for the first order reflection coefficient is zero:

$$\left\langle U_{pq}^{(1)} e^{j\kappa_z z} \right\rangle = \frac{\left\langle \left(a_{10pq} Z_l + a_{01pq} Z_t \right) e^{j\kappa_z z} \right\rangle}{\sin\theta_i} = 0 \tag{5.96}$$

Therefore, the first order rough surface reflection coefficient is zero:

$$R_{pq}^{(1)} = 0 \tag{5.97}$$

From the form of (5.89), all odd orders of the rough surface scattering coefficients are zero. That is,

$$R_{pq}^{(n)} = 0 \tag{5.98}$$

for all odd integers n.

5.4.4 Second Order Reflection Coefficient

Using (5.88) and (5.89), the expected value for the second order rough surface reflection coefficient is

$$\left\langle U_{pq}^{(2)} e^{j\kappa_z z} \right\rangle = \frac{\left\langle \left(a_{20pq} Z_l^2 + a_{11pq} Z_l Z_t + a_{02pq} Z_t^2 \right) e^{j\kappa_z z} \right\rangle}{\sin^2 \theta_i} \tag{5.99}$$

$$= \frac{\left(a_{20pq} + a_{02pq} \right) m^2 e^{-\frac{1}{2}\kappa_z^2 \sigma^2}}{\sin^2 \theta_i} \tag{5.100}$$

so that

$$R_{pq}^{(2)} = m^2 e^{-\frac{1}{2}\kappa_z^2 \sigma^2} \frac{\left(a_{20pq} + a_{02pq} \right)\big|_{\theta_s = \theta_i, \phi_\Delta = 0}}{-2 \sin^2 \theta_i \cos \theta_i} \tag{5.101}$$

For h-polarization, this becomes

$$R_{hh}^{(2)} = -m^2 e^{-2k^2 \sigma^2 \cos^2 \theta_i} \left(\left(R_{h00} + R_{v00} \right) \frac{\cos^2 \theta_i}{\sin^2 \theta_i} - \left(R_{h20} + R_{h02} \right) \right) \tag{5.102}$$

while for v-polarization,

$$R_{vv}^{(2)} = -m^2 e^{-2k^2 \sigma^2 \cos^2 \theta_i} \left(\left(R_{v00} + R_{h00} \right) \frac{\cos^2 \theta_i}{\sin^2 \theta_i} - \left(R_{v20} + R_{v02} \right) \right) \tag{5.103}$$

These expressions appears to be indeterminate at nadir, but, from (5.31) and (5.32), it is possible to show that

$$R_{v00} + R_{h00} = \frac{2\eta_1 \eta_2 \left(k_2^2 / k_1^2 - 1 \right) \sin^2 \theta_i}{\left(\eta_2 \cos \theta_i + \eta_1 \cos \theta_t \right) \left(\eta_1 \cos \theta_i + \eta_2 \cos \theta_t \right)} \tag{5.104}$$

which demonstrates that the second order rough surface reflection coefficient expressions can be evaluated at nadir.

The second order reflection coefficients are zero for cross-polarization.

5.4.5 Fourth Order Reflection Coefficient

The third order reflection coefficients, like the first order, and all odd order coefficients, are zero. This is a consequence of (5.89). The fourth order reflection coefficients begin with the expected value:

$$\left\langle U_{pq}^{(4)} e^{j\kappa_z z} \right\rangle = \left\langle \frac{a_{40pq}Z_l^4 + a_{31pq}Z_l^3 Z_t + a_{22pq}Z_l^2 Z_t^2 + a_{13pq}Z_l Z_t^3 + a_{04pq}Z_t^4}{\sin^4\theta_i} e^{j\kappa_z z} \right\rangle \tag{5.105}$$

$$= \frac{\left(3\left(a_{40pq}+a_{04pq}\right)+a_{22pq}\right)m^4 e^{-\frac{1}{2}\kappa_z^2\sigma^2}}{\sin^4\theta_i} \tag{5.106}$$

so that

$$R_{pq}^{(4)} = m^4 e^{-\frac{1}{2}\kappa_z^2\sigma^2} \frac{\left(3\left(a_{40pq}+a_{04pq}\right)+a_{22pq}\right)\big|_{\theta_s=\theta_i,\phi_\Delta=0}}{-2\sin^4\theta_i\cos\theta_i} \tag{5.107}$$

For v-polarization,

$$R_{vv}^{(4)} = m^4 e^{-\frac{1}{2}\kappa_z^2\sigma^2}\left(\left((R_{v00}+R_{h00})-(R_{v20}+R_{h20}) -3(R_{v02}+R_{h02})\right)\frac{\cos^2\theta_i}{\sin^2\theta_i} -(R_{v10}+R_{h10})\frac{\left(1+\cos^2\theta_i\right)\cos\theta_i}{\sin^3\theta_i}+3R_{v40}+R_{v22}+3R_{v04}\right) \tag{5.108}$$

5.5 Differential Radar Cross Section

Ulaby *et al.* [47] gives the elements of the covariance matrix as:

$$\langle S_{mn} S_{pq}^{*} \rangle = \left\langle \iint \frac{U_{mn} U_{pq}^{*}}{D_n D_n'} e^{jk(\hat{\mathbf{k}}_s - \hat{\mathbf{k}}_i)\cdot(\mathbf{r}-\mathbf{r}')} dS dS' \right\rangle \tag{5.109}$$

This definition includes both the incoherent scattered fields and the coherent scattered fields. Since the coherent scattered fields are completely described by the reflection coefficients above, there is no advantage to including them in the covariance matrix. In fact, there is a disadvantage to including both coherent and incoherent fields: the coherent field is a plane wave propagating away from the surface while the incoherent field is composed of spherical waves propagating away from the surface. As a result, the usual quantities which are used to describe scattering, such as the differential radar cross section or the elements of the Mueller matrix, become dependent on radar parameters (such as the range to target and the radar beamwidth) instead of depending solely on characteristics of the target.

If the covariance matrix is made only of the incoherent fields, these difficulties are eliminated. No information is lost: Total power received (for example) can then be composed of the sum of the power in the coherent field (described by the reflection coefficient, which is independent of radar parameters) and the power in the incoherent field (described by the scattering coefficient, also independent of the radar parameters).

The incoherent elements of the covariance matrix are given by:

$$\begin{aligned}\left\langle S^i_{mn} S^{i*}_{pq} \right\rangle &= \iiiint \left\langle \left(U_{mn} e^{jk\left(\hat{\mathbf{k}}_s - \hat{\mathbf{k}}_i\right)\cdot \mathbf{r}} - \left\langle U_{mn} e^{jk\left(\hat{\mathbf{k}}_s - \hat{\mathbf{k}}_i\right)\cdot \mathbf{r}} \right\rangle \right) \right. \\ &\quad \left. \left(U^*_{pq} e^{-jk\left(\hat{\mathbf{k}}_s - \hat{\mathbf{k}}_i\right)\cdot \mathbf{r}'} - \left\langle U^*_{pq} e^{-jk\left(\hat{\mathbf{k}}_s - \hat{\mathbf{k}}_i\right)\cdot \mathbf{r}'} \right\rangle \right) \right\rangle dx dy dx' dy' \qquad (5.110) \\ &= \iiiint \left\langle \left(U_{mn} e^{j\kappa_z z} - \left\langle U_{mn} e^{j\kappa_z z} \right\rangle \right) \left(U^*_{pq} e^{-j\kappa_z z'} - \left\langle U^*_{pq} e^{-j\kappa_z z'} \right\rangle \right) \right\rangle \\ &\quad e^{j\left(\kappa_x (x - x') + \kappa_y (y - y')\right)} dx dy dx' dy' \qquad (5.111)\end{aligned}$$

from which the differential radar cross section can be derived:

$$\sigma^0_{pq} = \frac{k^2}{4\pi A_0} \left\langle S^i_{pq} S^{i*}_{pq} \right\rangle \qquad (5.112)$$

Using (5.17):

$$\begin{aligned}&\left\langle \left(U_{mn} e^{j\kappa_z z} - \left\langle U_{mn} e^{j\kappa_z z} \right\rangle \right) \left(U^*_{pq} e^{-j\kappa_z z'} - \left\langle U^*_{pq} e^{-j\kappa_z z'} \right\rangle \right) \right\rangle \\ &= \left\langle U_{mn} U^*_{pq} e^{j\kappa_z (z - z')} \right\rangle - \left\langle U_{mn} e^{j\kappa_z z} \right\rangle \left\langle U^*_{pq} e^{-j\kappa_z z'} \right\rangle \\ &= \left\langle U^{(0)}_{mn} U^{(0)*}_{pq} e^{j\kappa_z (z - z')} \right\rangle - \left\langle U^{(0)}_{mn} e^{j\kappa_z z} \right\rangle \left\langle U^{(0)*}_{pq} e^{-j\kappa_z z'} \right\rangle \\ &\quad + \left\langle U^{(0)}_{mn} U^{(1)*}_{pq} e^{j\kappa_z (z - z')} \right\rangle - \left\langle U^{(0)}_{mn} e^{j\kappa_z z} \right\rangle \left\langle U^{(1)*}_{pq} e^{-j\kappa_z z'} \right\rangle \\ &\quad + \left\langle U^{(1)}_{mn} U^{(0)*}_{pq} e^{j\kappa_z (z - z')} \right\rangle - \left\langle U^{(1)}_{mn} e^{j\kappa_z z} \right\rangle \left\langle U^{(0)*}_{pq} e^{-j\kappa_z z'} \right\rangle \\ &\quad + \left\langle U^{(1)}_{mn} U^{(1)*}_{pq} e^{j\kappa_z (z - z')} \right\rangle - \left\langle U^{(1)}_{mn} e^{j\kappa_z z} \right\rangle \left\langle U^{(1)*}_{pq} e^{-j\kappa_z z'} \right\rangle \\ &\quad + \left\langle U^{(0)}_{mn} U^{(2)*}_{pq} e^{j\kappa_z (z - z')} \right\rangle - \left\langle U^{(0)}_{mn} e^{j\kappa_z z} \right\rangle \left\langle U^{(2)*}_{pq} e^{-j\kappa_z z'} \right\rangle \\ &\quad + \left\langle U^{(2)}_{mn} U^{(0)*}_{pq} e^{j\kappa_z (z - z')} \right\rangle - \left\langle U^{(2)}_{mn} e^{j\kappa_z z} \right\rangle \left\langle U^{(0)*}_{pq} e^{-j\kappa_z z'} \right\rangle + \cdots \qquad (5.113)\end{aligned}$$

Employing the relations (5.94) (5.96) and (5.100),

$$\begin{aligned}
&\left\langle \left(U_{mn}e^{j\kappa_z z} - \left\langle U_{mn}e^{j\kappa_z z}\right\rangle\right)\left(U_{pq}^{*}e^{-j\kappa_z z'} - \left\langle U_{pq}^{*}e^{-j\kappa_z z'}\right\rangle\right)\right\rangle \\
&= \left\langle U_{mn}^{(0)}U_{pq}^{(0)*}e^{j\kappa_z(z-z')}\right\rangle - a_{00mn}a_{00pq}^{*}e^{-\kappa_z^2\sigma^2} \\
&\quad + \left\langle \left(U_{mn}^{(0)}U_{pq}^{(1)*} + U_{mn}^{(1)}U_{pq}^{(0)*}\right)e^{j\kappa_z(z-z')}\right\rangle \\
&\quad + \left\langle U_{mn}^{(1)}U_{pq}^{(1)*}e^{j\kappa_z(z-z')}\right\rangle \\
&\quad + \left\langle \left(U_{mn}^{(0)}U_{pq}^{(2)*} + U_{mn}^{(2)}U_{pq}^{(0)*}\right)e^{j\kappa_z(z-z')}\right\rangle \\
&\quad - \left(a_{00mn}\left(a_{20pq}^{*} + a_{02pq}^{*}\right) + \left(a_{20mn} + a_{02mn}\right)a_{00pq}^{*}\right)\frac{m^2}{\sin^2\theta_i}e^{-\kappa_z^2\sigma^2} + \cdots
\end{aligned} \tag{5.114}$$

and evaluating these separately, we can express σ^0 as:

$$\sigma_{pq}^{0} \approx \frac{k^2}{4\pi A_0}\left(\left\langle S_{pq}^{i}S_{pq}^{i*}\right\rangle_{s^0} + \left\langle S_{pq}^{i}S_{pq}^{i*}\right\rangle_{s^1} + \left\langle S_{pq}^{i}S_{pq}^{i*}\right\rangle_{s_1^2} + \left\langle S_{pq}^{i}S_{pq}^{i*}\right\rangle_{s_2^2}\right) \tag{5.115}$$

$$\begin{aligned}
\left\langle S_{mn}^{i}S_{pq}^{i*}\right\rangle_{s^0} = \iiiint &\left(\left\langle U_{mn}^{(0)}U_{pq}^{(0)*}e^{j\kappa_z(z-z')}\right\rangle - a_{00mn}a_{00pq}^{*}e^{-\kappa_z^2\sigma^2}\right) \\
&e^{j\left(\kappa_x(x-x')+\kappa_y(y-y')\right)}dxdydx'dy'
\end{aligned} \tag{5.116}$$

$$\left\langle S_{mn}^{i}S_{pq}^{i*}\right\rangle_{s^1} = \iiiint \left\langle \left(U_{mn}^{(0)}U_{pq}^{(1)*} + U_{mn}^{(1)}U_{pq}^{(0)*}\right)e^{j\kappa_z(z-z')}\right\rangle e^{j\left(\kappa_x(x-x')+\kappa_y(y-y')\right)}dxdydx'dy' \tag{5.117}$$

$$\left\langle S_{mn}^{i}S_{pq}^{i*}\right\rangle_{s_1^2} = \iiiint \left\langle U_{mn}^{(1)}U_{pq}^{(1)*}e^{j\kappa_z(z-z')}\right\rangle e^{j\left(\kappa_x(x-x')+\kappa_y(y-y')\right)}dxdydx'dy' \tag{5.118}$$

$$\begin{aligned}
\left\langle S_{mn}^{i}S_{pq}^{i*}\right\rangle_{s_2^2} = \iiiint &\left(\left\langle \left(U_{mn}^{(2)}U_{pq}^{(0)*} + U_{mn}^{(0)}U_{pq}^{(2)*}\right)e^{j\kappa_z(z-z')}\right\rangle \right. \\
&\left. -\frac{m^2e^{-\kappa_z^2\sigma^2}}{\sin^2\theta_i}\left(a_{00mn}\left(a_{20pq}^{*} + a_{02pq}^{*}\right) + \left(a_{20mn} + a_{02mn}\right)a_{00pq}^{*}\right)\right) \\
&e^{j\left(\kappa_x(x-x')+\kappa_y(y-y')\right)}dxdydx'dy'
\end{aligned} \tag{5.119}$$

5.5.1 Evaluation of Expected Values: Incoherent Case

When the remaining polarization amplitudes, U, are expressed in terms of the coefficients a and the surface slopes, the expected values in (5.116) through (5.119) are of the form

$$\left\langle Z_l^{n_l} Z_t^{n_t} Z_l'^{n_{l'}} Z_t'^{n_{t'}} e^{j\kappa_z(z-z')} \right\rangle \tag{5.120}$$

where n_l,n_t,$n_{l'}$ and $n_{t'}$ are arbitrary non-negative integers.

Similar to the technique described for evaluating for evaluating (5.75), the solution to (5.120), starts by setting $N = \max(1, n_x + n_y) + \max(1, n_{x'} + n_{y'})$ in (5.78) and differentiating both sides $n_x + n_y + n_{x'} + n_{y'}$ times, once with respect to each of $x_1, x_2, \cdots, x_{n_x}$, and $y_{n_x+1}, \cdots, y_{n_x+n_y}$, and $x_{n_x+n_y+1}, \cdots, x_{n_x+n_y+n_{x'}}$, and $y_{n_x+n_y+n_{x'}+1}, \cdots, y_{n_x+n_y+n_{x'}+n_{y'}}$. The result of this differentiation is then evaluated at $x_1 = x_2 = \cdots = x_{n_x+n_y} = x$, and $y_1 = y_2 = \cdots = y_{n_x+n_y} = y$, and $x_{n_x+n_y+1} = \cdots = x_{n_x+n_y+n_{x'}+n_{y'}} = x'$, and $y_{n_x+n_y+1} = \cdots = y_{n_x+n_y+n_{x'}+n_{y'}} = y'$.

For example, to find

$$\left\langle Z_y^2 e^{j\kappa_z(z-z')} \right\rangle \tag{5.121}$$

it is observed that $N = 3$, and the following diffentiations are performed:

$$\frac{\partial}{\partial y_1}\frac{\partial}{\partial y_2}\left\langle e^{j\nu_1 z_1 + j\nu_2 z_2 + j\nu_3 z_3} \right\rangle = \frac{\partial}{\partial y_1}\frac{\partial}{\partial y_2} e^{-\frac{1}{2}\sigma^2(\nu_1^2+\nu_2^2+\nu_3^2+2\nu_1\nu_2\rho_{12}+2\nu_1\nu_3\rho_{13}+2\nu_2\nu_3\rho_{23})} \tag{5.122}$$

This results in

$$\begin{aligned}
&\left\langle \left(j\nu_1\frac{\partial}{\partial y_1}z_1\right)\left(j\nu_2\frac{\partial}{\partial y_2}z_2\right)e^{j\nu_1 z_1+j\nu_2 z_2+j\nu_3 z_3}\right\rangle \\
= &\left(\left(\sigma^2\nu_1\nu_2\frac{\partial}{\partial y_1}\rho_{12}+\sigma^2\nu_1\nu_3\frac{\partial}{\partial y_1}\rho_{13}\right)\left(\sigma^2\nu_1\nu_2\frac{\partial}{\partial y_2}\rho_{12}+\sigma^2\nu_2\nu_3\frac{\partial}{\partial y_2}\rho_{23}\right)\right. \\
&\left.-\sigma^2\nu_1\nu_2\frac{\partial^2}{\partial y_1\partial y_2}\rho_{12}\right)e^{-\frac{1}{2}\sigma^2\left(\nu_1^2+\nu_2^2+\nu_3^3+2\nu_1\nu_2\rho_{12}+2\nu_1\nu_3\rho_{13}+2\nu_2\nu_3\rho_{23}\right)} \qquad (5.123)
\end{aligned}$$

Let $x_2 \to x_1$ and $y_2 \to y_1$. Then $z_2 \to z_1$ as well. Also, $\frac{\partial}{\partial y_2}\rho_{12} = -\frac{\partial}{\partial y_1}\rho_{12}$, so

$$\begin{aligned}
&\left\langle -\nu_1\nu_2 Z_y^2 e^{j(\nu_1+\nu_2)z_1+j\nu_3 z_3}\right\rangle \\
= &\left(\left(\sigma^2\nu_1\nu_2\frac{\partial}{\partial y}\rho(0,0)+\sigma^2\nu_1\nu_3\frac{\partial}{\partial y}\rho_{13}\right)\left(-\sigma^2\nu_1\nu_2\frac{\partial}{\partial y}\rho(0,0)+\sigma^2\nu_2\nu_3\frac{\partial}{\partial y}\rho_{13}\right)\right. \\
&\left.+\sigma^2\nu_1\nu_2\frac{\partial^2}{\partial y^2}\rho(0,0)\right)e^{-\frac{1}{2}\sigma^2\left(\nu_1^2+\nu_2^2+\nu_3^3+2\nu_1\nu_2\rho(0,0)+2(\nu_1+\nu_2)\nu_3\rho_{13}\right)} \qquad (5.124) \\
= &\left(\sigma^4\nu_1\nu_2\nu_3^2\left(\frac{\partial}{\partial y}\rho_{13}\right)^2-\nu_1\nu_2 m^2\right)e^{-\frac{1}{2}\sigma^2\left((\nu_1+\nu_2)^2+\nu_3^3+2(\nu_1+\nu_2)\nu_3\rho_{13}\right)} \qquad (5.125)
\end{aligned}$$

At this point, letting $x = x_1, y = y_1, z = z_1$, $x' = x_3, y' = y_3, z' = z_3$ and $\kappa_z = \nu_1 + \nu_2 = -\nu_3$, we can reduce the identity farther. From the last substitution, we can also guarantee that $-\nu_1\nu_2 \neq 0$ and therefore we will also divide both sides by it.

$$\left\langle Z_y^2 e^{j\kappa_z(z-z')}\right\rangle = \left(m^2-\sigma^4\kappa_z^2\left(\frac{\partial}{\partial y}\rho\left(x-x',y-y'\right)\right)^2\right)e^{-\kappa_z^2\sigma^2(1-\rho(x-x',y-y'))} \qquad (5.126)$$

Finally, the identity is converted from the rectangular difference coordinates given by $(x-x', y-y')$ to the polar difference coordinates (ξ, α), where $x - x' = \xi\cos\alpha$ and $y - y' =$

$\xi \sin\alpha$.

$$\left\langle Z_y^2 e^{j\kappa_z(z-z')} \right\rangle = \left(m^2 - \sigma^4 \kappa_z^2 \left(\frac{\partial}{\partial \xi} \rho(\xi) \sin\alpha \right)^2 \right) e^{-\kappa_z^2 \sigma^2 (1-\rho(\xi))} \tag{5.127}$$

Similar analysis for other second-order combinations of two slopes Z_x and Z_y result in:

$$\left\langle Z_x^2 e^{j\kappa_z(z-z')} \right\rangle = \left(m^2 - \sigma^4 \kappa_z^2 \left(\frac{\partial}{\partial \xi} \rho(\xi) \cos\alpha \right)^2 \right) e^{-\kappa_z^2 \sigma^2 (1-\rho(\xi))} \tag{5.128}$$

$$\left\langle Z_x Z_y e^{j\kappa_z(z-z')} \right\rangle = \sigma^4 \kappa_z^2 \left(\frac{\partial}{\partial \xi} \rho(\xi) \right)^2 \sin\alpha \cos\alpha e^{-\kappa_z^2 \sigma^2 (1-\rho(x-x', y-y'))} \tag{5.129}$$

Unfortunately, the resultant expressions for arbitrary orders of (5.120) are considerably more complicated than that of (5.75), so that no general expression has been derived.

One identity, used to derive the zeroth order scattering coefficients, can be found directly from (5.78) when $N = 2$:

$$\left\langle e^{j\kappa_z(z-z')} \right\rangle = e^{-\kappa_z^2 \sigma^2 (1-\rho(\xi))} \tag{5.130}$$

These two identities, used to derive the first order scattering coefficient, can be derived with this analysis but have also appeared in Ulaby *et al.* [48]:

$$\left\langle Z_x e^{j\kappa_z(z-z')} \right\rangle = \left\langle Z_x' e^{j\kappa_z(z-z')} \right\rangle = -j\kappa_z \sigma^2 \cos\alpha \frac{\partial \rho(\xi)}{\partial \xi} e^{-\kappa_z^2 \sigma^2 (1-\rho(\xi))} \tag{5.131}$$

$$\left\langle Z_y e^{j\kappa_z(z-z')} \right\rangle = \left\langle Z_y' e^{j\kappa_z(z-z')} \right\rangle = -j\kappa_z \sigma^2 \sin\alpha \frac{\partial \rho(\xi)}{\partial \xi} e^{-\kappa_z^2 \sigma^2 (1-\rho(\xi))} \tag{5.132}$$

Other identities which result from this analysis and which will be used to derive higher order scattering coefficients are:

$$\left\langle Z_x Z'_x e^{j\kappa_z(z-z')} \right\rangle = -\sigma^2 \left(\frac{\partial^2}{\partial \xi^2}\rho(\xi)\cos^2\alpha + \frac{1}{\xi}\frac{\partial}{\partial \xi}\rho(\xi)\sin^2\alpha + \kappa_z^2\sigma^2\left(\frac{\partial}{\partial \xi}\rho(\xi)\right)^2 \cos^2\alpha \right) e^{-\kappa_z^2\sigma^2(1-\rho(\xi))} \tag{5.133}$$

$$\left\langle Z_y Z'_y e^{j\kappa_z(z-z')} \right\rangle = -\sigma^2 \left(\frac{\partial^2}{\partial \xi^2}\rho(\xi)\sin^2\alpha + \frac{1}{\xi}\frac{\partial}{\partial \xi}\rho(\xi)\cos^2\alpha + \kappa_z^2\sigma^2\left(\frac{\partial}{\partial \xi}\rho(\xi)\right)^2 \sin^2\alpha \right) e^{-\kappa_z^2\sigma^2(1-\rho(\xi))} \tag{5.134}$$

$$\left\langle Z_x Z'_y e^{j\kappa_z(z-z')} \right\rangle = \left\langle Z_y Z'_x e^{j\kappa_z(z-z')} \right\rangle = -\sigma^2 \sin\alpha\cos\alpha \left(\frac{\partial^2}{\partial \xi^2}\rho(\xi) - \frac{1}{\xi}\frac{\partial}{\partial \xi}\rho(\xi) + \kappa_z^2\sigma^2\left(\frac{\partial}{\partial \xi}\rho(\xi)\right)^2 \right) e^{-\kappa_z^2\sigma^2(1-\rho(\xi))} \tag{5.135}$$

5.5.2 Zeroth Order Scattering Coefficient

The analysis of the zeroth order term is straightforward and yields the traditional coefficients for Physical Optics. For completeness, the zeroth order term, which is derived in many other places, is rederived here.

The double integration over the primed coordinates (x', y') and unprimed coordinates (x, y) in (5.116) is converted into a double integration over the average coordinates ($x_a =$

$\frac{1}{2}(x+x'), y_a = \frac{1}{2}(y+y'))$ and difference coordinates $(u = x-x', v = y-y')$:

$$\frac{k^2}{4\pi A_0}\left\langle S_{mn}S^*_{pq}\right\rangle_{s^0} = \frac{k^2}{4\pi A_0}\iiiint_{-\infty}^{\infty} a_{00mn}a^*_{00pq}\left(\left\langle e^{j\kappa_z(z-z')}\right\rangle - e^{-\kappa_z^2\sigma^2}\right) e^{j\kappa_x u + j\kappa_y v}\,du\,dv\,dx_a\,dy_a \tag{5.136}$$

The integration over the average coordinates yields the illuminated area A_0; a mathematically precise approach, showing such infinite integration as a limiting process of a finite integral, is found in [48].

$$\frac{k^2}{4\pi A_0}\left\langle S_{mn}S^*_{pq}\right\rangle_{s^0} = \frac{k^2}{4\pi}a_{00mn}a^*_{00pq}\iint_{-\infty}^{\infty} e^{j\kappa_x u + j\kappa_y v}\left(\left\langle e^{j\kappa_z(z-z')}\right\rangle - e^{-\kappa_z^2\sigma^2}\right)du\,dv \tag{5.137}$$

At this point, the Cartesian difference coordinates (u, v) are converted to polar form (ξ, α) and (5.130) is employed, resulting in

$$\frac{k^2}{4\pi A_0}\left\langle S_{mn}S^*_{pq}\right\rangle_{s^0} = \frac{k^2}{4\pi}a_{00mn}a^*_{00pq}\int_0^{\infty}\int_{2\pi} e^{j\kappa_x\xi\cos\alpha + j\kappa_y\xi\sin\alpha}\left(e^{-\kappa_z^2\sigma^2(1-\rho(\xi))} - e^{-\kappa_z^2\sigma^2}\right)d\alpha\,\xi\,d\xi \tag{5.138}$$

The integral over α is evaluated with the aid of this Bessel function integral identity:

$$\int_{2\pi}\cos(n\alpha+\beta)e^{jx\cos\alpha}d\alpha = 2\pi j^n\cos\beta J_n(x) \tag{5.139}$$

which yields

$$\frac{k^2}{4\pi A_0}\left\langle S_{mn}S^*_{pq}\right\rangle_{s^0} = a_{00mn}a^*_{00pq}I_0 \tag{5.140}$$

where

$$I_0 = \tfrac{1}{2}k^2 e^{-\kappa_z^2\sigma^2}\int_0^\infty \left(e^{\kappa_z^2\sigma^2\rho(\xi)} - 1\right)J_0(\kappa_t\xi)\xi d\xi \tag{5.141}$$

and κ_t is given by (2.13). A necessary condition for the integral in I_0 to converge is that, for large ξ, the surface autocorrelation function $\rho(\xi)$ must tend toward zero at least as fast as $\xi^{-\frac{1}{2}}$. This is not a very stringent requirement; most models of surface correlation functions assume a much more rapid decay.

This zeroth order scattering term represents the expected power in a particular direction due to the correlation of the height of the surface at one point to the height at another point. For most combinations of bistatic angles, particularly for incidence angles near nadir, this term is the largest contribution to σ^0.

5.5.3 First Order Scattering Coefficient

The first order term in Ulaby *et al.* [48] is that of the scalar approximation. Below is the full vector solution under the tangent-plane approximation, the difference being that the coefficients a for first order have been calculated from the tangent-plane polarization amplitudes U without further approximations. Using the expansions for the zeroth and first order polarization amplitudes provided by (5.18) and (5.19) in (5.117) and employing the

expected value identities provided by (5.131) and (5.132) the following expression is obtained:

$$\frac{k^2}{4\pi A_0}\langle S_{mn}S^*_{pq}\rangle_{s^1} = \frac{k^2}{4\pi\sin\theta_i}\int_0^\infty\int_{2\pi} -j\kappa_z\sigma^2\frac{\partial\rho(\xi)}{\partial\xi}$$
$$[(a_{00mn}a^*_{10pq}+a_{10mn}a^*_{00pq})(\cos\alpha\cos\phi_i+\sin\alpha\sin\phi_i)$$
$$+(a_{00mn}a^*_{01pq}+a_{01mn}a^*_{00pq})(\sin\alpha\cos\phi_i-\cos\alpha\sin\phi_i)]$$
$$e^{j\kappa_x\xi\cos\alpha+j\kappa_y\xi\sin\alpha-\kappa_z^2\sigma^2(1-\rho(\xi))}d\alpha\xi d\xi \qquad (5.142)$$

The integration over the variable α is again evaluated with the aid of the Bessel function identity (5.139) resulting in

$$\frac{k^2}{4\pi A_0}\langle S_{mn}S^*_{pq}\rangle_{s^1} = \frac{k^2\sigma^2}{2\sin\theta_i}\frac{\kappa_z}{\kappa_t}$$
$$[(a_{00mn}a^*_{10pq}+a_{10mn}a^*_{00pq})(\kappa_x\cos\phi_i+\kappa_y\sin\phi_i)$$
$$+(a_{00mn}a^*_{01pq}+a_{01mn}a^*_{00pq})(\kappa_y\cos\phi_i-\kappa_x\sin\phi_i)]$$
$$\int_0^\infty\frac{\partial\rho(\xi)}{\partial\xi}e^{-\kappa_z^2\sigma^2(1-\rho(\xi))}J_1(\kappa_t\xi)\xi d\xi \qquad (5.143)$$

The following notation for the components of the k vector change due to scattering is similar to that for the surface slopes given by (2.41) and (2.42).

$$\kappa_{li} = \kappa_x\cos\phi_i+\kappa_y\sin\phi_i = k(\sin\theta_s\cos\phi_\Delta-\sin\theta_i) \qquad (5.144)$$

$$\kappa_{ti} = \kappa_y\cos\phi_i-\kappa_x\sin\phi_i = k\sin\theta_s\sin\phi_\Delta \qquad (5.145)$$

Therefore,

$$\frac{k^2}{4\pi A_0}\langle S_{mn}S^*_{pq}\rangle_{s^1} = [(a_{00mn}a^*_{10pq}+a_{10mn}a^*_{00pq})\kappa_{li} + (a_{00mn}a^*_{01pq}+a_{01mn}a^*_{00pq})\kappa_{ti}]I_1 \quad (5.146)$$

where

$$I_1 = -\tfrac{1}{2}k^2\kappa_z^2\sigma^2\int_0^\infty \frac{\partial\rho(\xi)}{\partial\xi}e^{-\kappa_z^2\sigma^2(1-\rho(\xi))}\frac{J_1(\kappa_t\xi)}{\kappa_t}\xi d\xi \quad (5.147)$$

I_1 can be evaluated by integration by parts. Setting

$$u_1 = e^{\kappa_z^2\sigma^2\rho(\xi)}-1 \quad (5.148)$$

$$v_1 = \kappa_t\xi J_1(\kappa_t\xi) \quad (5.149)$$

then

$$du_1 = \kappa_z^2\sigma^2\frac{\partial}{\partial\xi}\rho(\xi)e^{\kappa_z^2\sigma^2\rho(\xi)}d\xi \quad (5.150)$$

$$dv_1 = \kappa_t^2\xi J_0(\kappa_t\xi)d\xi \quad (5.151)$$

and

$$I_1 = \frac{-k^2}{2\kappa_t^2} e^{-\kappa_z^2\sigma^2} \int_{\xi=0}^{\xi=\infty} v\,du \tag{5.152}$$

$$= \frac{-k^2}{2\kappa_t^2} e^{-\kappa_z^2\sigma^2} \left((u_1 v_1)\Big|_{\xi=0}^{\xi=\infty} - \int_{\xi=0}^{\xi=\infty} u_1 dv_1 \right) \tag{5.153}$$

$$= \frac{-k^2}{2\kappa_t^2} e^{-\kappa_z^2\sigma^2} \left(\left(\left(e^{\kappa_z^2\sigma^2\rho(\xi)} - 1 \right) \kappa_t \xi J_1(\kappa_t \xi) \right) \Big|_{\xi=0}^{\xi=\infty} - \int_0^{\infty} \left(e^{\kappa_z^2\sigma^2\rho(\xi)} - 1 \right) \kappa_t^2 \xi J_0(\kappa_t \xi) d\xi \right)$$

$$= I_0 \tag{5.154}$$

The evaluation of $u_1 v_1$ at $\xi = \infty$ yields zero if $\rho(\xi)$ tends toward zero faster than $\xi^{-\frac{1}{2}}$, a requirement that has been assumed in the section on the Zeroth Order Scattering term.

This term represents the expected power in a particular direction due to the correlation of height of the surface at one point to the slope at another point.

5.5.4 Second Order Scattering Coefficient

The cross-slope term does not appear in Ulaby *et al.* [48], but does appear later in Fung [15] as part of the Integral Equation Method (IEM) single scattering term, with approximations applied to the polarization amplitudes. In particular, the expansion coefficients higher than zero order have been neglected. The full term is obtained from using (5.19) in (5.118)

with the expected value identities provided by (5.133), (5.135) and (5.134):

$$\begin{aligned}
\frac{k^2}{4\pi A_0}\left\langle S_{mn}S^*_{pq}\right\rangle_{s_1^2} &= \frac{k^2}{4\pi\sin^2\theta_i}\iint_{-\infty}^{\infty} e^{j\kappa_x u + j\kappa_y v} \\
&\quad \left\langle \left(a_{10mn}Z_l + a_{01mn}Z_t\right)\left(a^*_{10pq}Z_l + a^*_{01pq}Z_t\right)e^{j\kappa_z(z-z')}\right\rangle du dv \qquad (5.155) \\
&= \frac{-k^2\sigma^2}{4\pi\sin^2\theta_i}\int_0^{\infty}\int_{2\pi} e^{j\kappa_x\xi\cos\alpha + j\kappa_y\xi\sin\alpha} \\
&\quad \left(a_{10mn}(\cos\alpha\cos\phi_i + \sin\alpha\sin\phi_i) + a_{01mn}(\sin\alpha\cos\phi_i - \cos\alpha\sin\phi_i)\right) \\
&\quad \left(a^*_{10pq}(\cos\alpha\cos\phi_i + \sin\alpha\sin\phi_i) + a^*_{01pq}(\sin\alpha\cos\phi_i - \cos\alpha\sin\phi_i)\right) \\
&\quad \left(\frac{\partial^2}{\partial\xi^2}\rho(\xi) - \frac{1}{\xi}\frac{\partial}{\partial\xi}\rho(\xi) + \kappa_z^2\sigma^2\left(\frac{\partial}{\partial\xi}\rho(\xi)\right)^2\right)e^{-\kappa_z^2\sigma^2(1-\rho(\xi))}d\alpha\xi d\xi \\
&- \frac{k^2\sigma^2}{4\pi\sin^2\theta_i}\int_0^{\infty}\int_{2\pi} e^{j\kappa_x\xi\cos\alpha + j\kappa_y\xi\sin\alpha} \\
&\quad \left(a_{10mn}a^*_{10pq} + a_{01mn}a^*_{01pq}\right. \\
&\quad \left. + \left(a_{10mn}a^*_{01pq} + a_{01mn}a^*_{10pq}\right)(\cos\phi_i\sin\phi_i - \sin\phi_i\cos\phi_i)\right) \\
&\quad \frac{\partial}{\partial\xi}\rho(\xi)e^{-\kappa_z^2\sigma^2(1-\rho(\xi))}d\alpha d\xi \qquad (5.156)
\end{aligned}$$

Upon expanding the trigonometric products, the terms independent of the azimuthal variable of integration, α, are accumulated into the second integral, and both integrations over

α are evaluated with (5.139):

$$\frac{k^2}{4\pi A_0}\langle S_{mn}S_{pq}^*\rangle_{s_1^2} = \frac{-k^2\sigma^2}{8\pi\sin^2\theta_i}\int_0^\infty \frac{-2\pi J_2(\kappa_t\xi)}{\kappa_t^2}$$
$$\left((a_{10mn}a_{10pq}^* - a_{01mn}a_{01pq}^*)\left(\left(\kappa_x^2-\kappa_y^2\right)\cos 2\phi_i + 2\kappa_x\kappa_y\sin 2\phi_i\right)\right.$$
$$\left.+(a_{10mn}a_{01pq}^* + a_{01mn}a_{10pq}^*)\left(-\left(\kappa_x^2-\kappa_y^2\right)\sin 2\phi_i + 2\kappa_x\kappa_y\cos 2\phi_i\right)\right)$$
$$\left(\frac{\partial^2}{\partial\xi^2}\rho(\xi) - \frac{1}{\xi}\frac{\partial}{\partial\xi}\rho(\xi) + \kappa_z^2\sigma^2\left(\frac{\partial}{\partial\xi}\rho(\xi)\right)^2\right)e^{-\kappa_z^2\sigma^2(1-\rho(\xi))}\xi d\xi$$
$$-\frac{k^2\sigma^2}{8\pi\sin^2\theta_i}\int_0^\infty 2\pi J_0(\kappa_t\xi)(a_{10mn}a_{10pq}^* + a_{01mn}a_{01pq}^*)$$
$$\left(\frac{\partial^2}{\partial\xi^2}\rho(\xi) + \frac{1}{\xi}\frac{\partial}{\partial\xi}\rho(\xi) + \kappa_z^2\sigma^2\left(\frac{\partial}{\partial\xi}\rho(\xi)\right)^2\right)e^{-\kappa_z^2\sigma^2(1-\rho(\xi))}\xi d\xi \tag{5.157}$$

Recognizing that

$$\kappa_{li}^2 - \kappa_{ti}^2 = 2\kappa_x\kappa_y\sin 2\phi_i + \left(\kappa_x^2-\kappa_y^2\right)\cos 2\phi_i \tag{5.158}$$

$$2\kappa_{li}\kappa_{ti} = 2\kappa_x\kappa_y\cos 2\phi_i - \left(\kappa_x^2-\kappa_y^2\right)\sin 2\phi_i \tag{5.159}$$

the second order expressions reduce to

$$\frac{k^2}{4\pi A_0}\langle S_{mn}S_{pq}^*\rangle_{s_1^2} = \frac{I_3}{2\kappa_z^2\sin^2\theta_i}\left((a_{10mn}a_{10pq}^* - a_{01mn}a_{01pq}^*)\left(\kappa_{li}^2-\kappa_{ti}^2\right)\right.$$
$$\left.+(a_{10mn}a_{01pq}^* + a_{01mn}a_{10pq}^*)2\kappa_{li}\kappa_{ti}\right)$$
$$+ \frac{I_2}{2\kappa_z^2\sin^2\theta_i}\kappa_t^2(a_{10mn}a_{10pq}^* + a_{01mn}a_{01pq}^*) \tag{5.160}$$

where

$$I_2 = \frac{-k^2\kappa_z^2\sigma^2}{2\kappa_t^2}\int_0^\infty J_0(\kappa_t\xi)\left(\frac{\partial^2}{\partial\xi^2}\rho(\xi)+\frac{1}{\xi}\frac{\partial}{\partial\xi}\rho(\xi)+\kappa_z^2\sigma^2\left(\frac{\partial}{\partial\xi}\rho(\xi)\right)^2\right)e^{-\kappa_z^2\sigma^2(1-\rho(\xi))}\xi d\xi \tag{5.161}$$

$$I_3 = \frac{k^2\kappa_z^2\sigma^2}{2\kappa_t^2}\int_0^\infty J_2(\kappa_t\xi)\left(\frac{\partial^2}{\partial\xi^2}\rho(\xi)-\frac{1}{\xi}\frac{\partial}{\partial\xi}\rho(\xi)+\kappa_z^2\sigma^2\left(\frac{\partial}{\partial\xi}\rho(\xi)\right)^2\right)e^{-\kappa_z^2\sigma^2(1-\rho(\xi))}\xi d\xi \tag{5.162}$$

Integrating I_2 by parts with

$$u_2 = \frac{\partial}{\partial\xi}\left(e^{\kappa_z^2\sigma^2\rho(\xi)}-1\right) = \kappa_z^2\sigma^2 e^{\kappa_z^2\sigma^2\rho(\xi)}\frac{\partial}{\partial\xi}\rho(\xi) \tag{5.163}$$

$$du_2 = \frac{\partial^2}{\partial\xi^2}\left(e^{\kappa_z^2\sigma^2\rho(\xi)}-1\right)d\xi = \kappa_z^2\sigma^2\left(\frac{\partial^2}{\partial\xi^2}\rho(\xi)+\kappa_z^2\sigma^2\left(\frac{\partial}{\partial\xi}\rho(\xi)\right)^2\right)e^{\kappa_z^2\sigma^2\rho(\xi)}d\xi \tag{5.164}$$

$$v_2 = \kappa_t\xi J_0(\kappa_t\xi) \tag{5.165}$$

$$dv_2 = \kappa_t(J_0(\kappa_t\xi)-\kappa_t\xi J_1(\kappa_t\xi))d\xi \tag{5.166}$$

it can be shown that

$$I_2 = \frac{-k^2}{2\kappa_t^3} e^{-\kappa_z^2\sigma^2} \int_{\xi=0}^{\xi=\infty} v_2 du_2 - \frac{k^2\kappa_z^2\sigma^2}{2\kappa_t^2} e^{-\kappa_z^2\sigma^2} \int_{\xi=0}^{\xi=\infty} J_0(\kappa_t\xi) \frac{\partial}{\partial\xi}\rho(\xi) e^{\kappa_z^2\sigma^2\rho(\xi)} d\xi \tag{5.167}$$

$$= \frac{-k^2}{2\kappa_t^3} e^{-\kappa_z^2\sigma^2} \left((u_2 v_2)\Big|_{\xi=0}^{\xi=\infty} - \int_{\xi=0}^{\xi=\infty} u_2 dv_2 \right)$$
$$- \frac{k^2\kappa_z^2\sigma^2}{2\kappa_t^2} e^{-\kappa_z^2\sigma^2} \int_{\xi=0}^{\xi=\infty} J_0(\kappa_t\xi) \frac{\partial}{\partial\xi}\rho(\xi) e^{\kappa_z^2\sigma^2\rho(\xi)} d\xi \tag{5.168}$$

$$= \frac{-k^2}{2\kappa_t^3} e^{-\kappa_z^2\sigma^2} \left(\left(\frac{\partial}{\partial\xi}\left(e^{\kappa_z^2\sigma^2\rho(\xi)} - 1 \right) \kappa_t\xi J_0(\kappa_t\xi) \right) \Big|_{\xi=0}^{\xi=\infty} \right.$$
$$\left. - \kappa_z^2\sigma^2 \int_{\xi=0}^{\xi=\infty} e^{\kappa_z^2\sigma^2\rho(\xi)} \frac{\partial}{\partial\xi}\rho(\xi)\kappa_t (J_0(\kappa_t\xi) - \kappa_t\xi J_1(\kappa_t\xi)) d\xi \right)$$
$$- \frac{k^2\kappa_z^2\sigma^2}{2\kappa_t^2} e^{-\kappa_z^2\sigma^2} \int_{\xi=0}^{\xi=\infty} J_0(\kappa_t\xi) \frac{\partial}{\partial\xi}\rho(\xi) e^{\kappa_z^2\sigma^2\rho(\xi)} d\xi \tag{5.169}$$

$$= -\tfrac{1}{2} k^2\kappa_z^2\sigma^2 e^{-\kappa_z^2\sigma^2} \int_{\xi=0}^{\xi=\infty} \frac{\partial}{\partial\xi}\rho(\xi) e^{\kappa_z^2\sigma^2\rho(\xi)} \frac{J_1(\kappa_t\xi)}{\kappa_t} \xi d\xi \tag{5.170}$$

$$= I_1 = I_0 \tag{5.171}$$

For I_3, integration by parts with u_2 and du_2 above together with

$$v_3 = \kappa_t\xi J_2(\kappa_t\xi) \tag{5.172}$$

$$dv_3 = \kappa_t(\kappa_t\xi J_1(\kappa_t\xi) - J_2(\kappa_t\xi)) d\xi \tag{5.173}$$

yields

$$I_3 = \frac{k^2\kappa_z^2\sigma^2}{2\kappa_t^2}\int_0^\infty J_2(\kappa_t\xi)\left(\frac{\partial^2}{\partial\xi^2}\rho(\xi) - \frac{1}{\xi}\frac{\partial}{\partial\xi}\rho(\xi) + \kappa_z^2\sigma^2\left(\frac{\partial}{\partial\xi}\rho(\xi)\right)^2\right)e^{-\kappa_z^2\sigma^2(1-\rho(\xi))}\xi d\xi \tag{5.174}$$

$$= \frac{k^2}{2\kappa_t^3}e^{-\kappa_z^2\sigma^2}\int_0^\infty v_3 du_2 - \frac{k^2\kappa_z^2\sigma^2}{2\kappa_t^2}e^{-\kappa_z^2\sigma^2}\int_0^\infty J_2(\kappa_t\xi)\frac{1}{\xi}\frac{\partial}{\partial\xi}\rho(\xi)e^{\kappa_z^2\sigma^2\rho(\xi)}\xi d\xi \tag{5.175}$$

$$\begin{aligned} &= \frac{k^2}{2\kappa_t^3}e^{-\kappa_z^2\sigma^2}\left((u_2v_3)|_0^\infty - \int_0^\infty u_2 dv_3\right) \\ &\quad - \frac{k^2\kappa_z^2\sigma^2}{2\kappa_t^2}e^{-\kappa_z^2\sigma^2}\int_0^\infty J_2(\kappa_t\xi)\frac{1}{\xi}\frac{\partial}{\partial\xi}\rho(\xi)e^{\kappa_z^2\sigma^2\rho(\xi)}\xi d\xi \end{aligned} \tag{5.176}$$

$$\begin{aligned} &= \frac{k^2}{2\kappa_t^3}e^{-\kappa_z^2\sigma^2}\left(\left(\frac{\partial}{\partial\xi}\left(e^{\kappa_z^2\sigma^2\rho(\xi)}-1\right)\kappa_t\xi J_2(\kappa_t\xi)\right)\Big|_0^\infty\right. \\ &\quad \left. - \int_0^\infty \kappa_z^2\sigma^2 e^{\kappa_z^2\sigma^2\rho(\xi)}\frac{\partial}{\partial\xi}\rho(\xi)\kappa_t(\kappa_t\xi J_1(\kappa_t\xi) - J_2(\kappa_t\xi))d\xi\right) \\ &\quad - \frac{k^2\kappa_z^2\sigma^2}{2\kappa_t^2}e^{-\kappa_z^2\sigma^2}\int_0^\infty J_2(\kappa_t\xi)\frac{1}{\xi}\frac{\partial}{\partial\xi}\rho(\xi)e^{\kappa_z^2\sigma^2\rho(\xi)}\xi d\xi \end{aligned} \tag{5.177}$$

$$= \frac{-k^2\kappa_z^2\sigma^2}{2\kappa_t}e^{-\kappa_z^2\sigma^2}\int_0^\infty e^{\kappa_z^2\sigma^2\rho(\xi)}\frac{\partial}{\partial\xi}\rho(\xi)J_1(\kappa_t\xi)\xi d\xi \tag{5.178}$$

$$= I_1 = I_0 \tag{5.179}$$

Therefore,

$$\begin{aligned} \frac{k^2}{4\pi A_0}\langle S_{mn}S_{pq}^*\rangle_{s_1^2} &= \frac{I_0}{2\kappa_z^2\sin^2\theta_i}\left(\kappa_t^2\left(a_{10mn}a_{10pq}^* + a_{01mn}a_{01pq}^*\right)\right. \\ &\quad + \left(\kappa_{li}^2 - \kappa_{ti}^2\right)\left(a_{10mn}a_{10pq}^* - a_{01mn}a_{01pq}^*\right) \\ &\quad \left. + 2\kappa_{li}\kappa_{ti}\left(a_{10mn}a_{01pq}^* + a_{01mn}a_{10pq}^*\right)\right) \end{aligned} \tag{5.180}$$

Since $\kappa_t^2 = \kappa_{li}^2 + \kappa_{ti}^2$, the second order term further simplifies to

$$\begin{aligned}\frac{k^2}{4\pi A_0}\langle S_{mn}S_{pq}^*\rangle_{s_1^2} &= \frac{I_0}{\kappa_z^2\sin^2\theta_i}\Big(\kappa_{li}^2 a_{10mn}a_{10pq}^* + \kappa_{ti}^2 a_{01mn}a_{01pq}^* \\ &\quad + \kappa_{li}\kappa_{ti}\big(a_{10mn}a_{01pq}^* + a_{01mn}a_{10pq}^*\big)\Big) \end{aligned} \tag{5.181}$$

This term represents the expected power in a particular direction due to the correlation of slope of the surface at one point to the slope at another point.

Combining the previous three terms together, the expected value of the scattering coefficients is

$$\begin{aligned}\frac{k^2}{4\pi A_0}\langle S_{mn}S_{pq}^*\rangle_{s^0+s^1+s_1^2} &= \frac{k^2}{4\pi A_0}\langle S_{mn}S_{pq}^*\rangle_{s^0} + \frac{k^2}{4\pi A_0}\langle S_{mn}S_{pq}^*\rangle_{s^1} + \frac{k^2}{4\pi A_0}\langle S_{mn}S_{pq}^*\rangle_{s_1^2} \\ &= I_0\left(a_{00mn} - \left(\frac{a_{10mn}}{\sin\theta_i}\frac{\kappa_{li}}{\kappa_z} + \frac{a_{01mn}}{\sin\theta_i}\frac{\kappa_{ti}}{\kappa_z}\right)\right) \\ &\times \left(a_{00pq} - \left(\frac{a_{10pq}}{\sin\theta_i}\frac{\kappa_{li}}{\kappa_z} + \frac{a_{01pq}}{\sin\theta_i}\frac{\kappa_{ti}}{\kappa_z}\right)\right)^* \end{aligned} \tag{5.182}$$

This term has been derived by Fung [15] in his Integral Equation Method (IEM), albeit with approximations in the derivation of the coefficients a.

Another second order scattering term is given by (5.119) which, upon using (5.18) and

(5.20), is

$$\frac{k^2}{4\pi A_0}\left\langle S_{mn}S_{pq}^*\right\rangle_{s_2^2}=\frac{k^2}{4\pi\sin^2\theta_i}\iint_{-\infty}^{\infty}e^{j\kappa_x u+j\kappa_y v}\left(\left\langle\left(a_{00mn}\left(a_{20pq}^*Z_l^2+a_{11pq}^*Z_lZ_t+a_{02pq}^*Z_t^2\right)\right.\right.\right.$$
$$\left.+\left(a_{20mn}Z_l^2+a_{11mn}Z_lZ_t+a_{02mn}Z_t^2\right)a_{00pq}^*\right)e^{j\kappa_z(z-z')}\Big\rangle$$
$$\left.-m^2e^{-\kappa_z^2\sigma^2}\left(a_{00mn}a_{20pq}^*+a_{20mn}a_{00pq}^*+a_{00mn}a_{02pq}^*+a_{02mn}a_{00pq}^*\right)\right)$$
$$dudv \tag{5.183}$$

Converting from rectangular to polar coordinates, and using the expected value identities (5.128), (5.129) and (5.127), results in

$$\begin{aligned}\frac{k^2}{4\pi A_0}\left\langle S_{mn}S_{pq}^*\right\rangle_{s_2^2} &= \frac{-k^2\sigma^2}{4\pi\sin^2\theta_i}\int_0^{\infty}\int_{2\pi}e^{j\kappa_x\xi\cos\alpha+j\kappa_y\xi\sin\alpha}\\
&\left(\left(a_{00mn}a_{20pq}^*+a_{20mn}a_{00pq}^*\right)\cos^2(\alpha-\phi_i)\right.\\
&+\left(a_{00mn}a_{11pq}^*+a_{11mn}a_{00pq}^*\right)\sin(\alpha-\phi_i)\cos(\alpha-\phi_i)\\
&\left.+\left(a_{00mn}a_{02pq}^*+a_{02mn}a_{00pq}^*\right)\sin^2(\alpha-\phi_i)\right)\\
&\kappa_z^2\sigma^2\left(\frac{\partial}{\partial\xi}\rho(\xi)\right)^2e^{-\kappa_z^2\sigma^2(1-\rho(\xi))}d\alpha\xi d\xi\\
&+\frac{k^2m^2}{4\pi\sin^2\theta_i}\int_0^{\infty}\int_{2\pi}e^{j\kappa_x\xi\cos\alpha+j\kappa_y\xi\sin\alpha}\\
&\left(\left(a_{00mn}a_{20pq}^*+a_{20mn}a_{00pq}^*\right)+\left(a_{00mn}a_{02pq}^*+a_{02mn}a_{00pq}^*\right)\right)\\
&\left(e^{-\kappa_z^2\sigma^2(1-\rho(\xi))}-e^{-\kappa_z^2\sigma^2}\right)d\alpha d\xi\end{aligned} \tag{5.184}$$

Upon employing the Bessel function identity (5.139):

$$\frac{k^2}{4\pi A_0}\langle S_{mn}S^*_{pq}\rangle_{s_2^2} = \frac{I_4}{\kappa_z^2\sin^2\theta_i}\Big(2\kappa_{ti}\kappa_{li}\left(a_{00mn}a^*_{11pq}+a_{11mn}a^*_{00pq}\right) + \left(\kappa_{li}^2-\kappa_{ti}^2\right)\left(a_{00mn}\left(a^*_{20pq}-a^*_{02pq}\right)+\left(a_{20mn}-a_{02mn}\right)a^*_{00pq}\right)\Big) - \frac{I_5-m^2I_0}{\sin^2\theta_i}\left(a_{00mn}\left(a^*_{20pq}+a^*_{02pq}\right)+\left(a_{20mn}+a_{02mn}\right)a^*_{00pq}\right) \tag{5.185}$$

where

$$I_4 = \frac{1}{4}k^2\kappa_z^4\sigma^4\int_0^\infty \frac{J_2(\kappa_t\xi)}{\kappa_t^2}\left(\frac{\partial}{\partial\xi}\rho(\xi)\right)^2 e^{-\kappa_z^2\sigma^2(1-\rho(\xi))}\xi d\xi \tag{5.186}$$

$$I_5 = \frac{1}{4}k^2e^{-\kappa_z^2\sigma^2}\int_0^\infty \kappa_z^2\sigma^4\left(\frac{\partial}{\partial\xi}\rho(\xi)\right)^2 e^{\kappa_z^2\sigma^2\rho(\xi)}J_0(\kappa_t\xi)\xi d\xi \tag{5.187}$$

5.6 Evaluation of I_n integrals for common correlation functions

The integrals I_1, I_2 and I_3 have been shown to be the same as I_0. The integral in I_0, I_4 and I_5 can be further simplified if we assume a form for the correlation function $\rho(\xi)$. For the Gaussian and exponential correlation functions, at least, the integrals may be evaluated when the exponential functions in them are expanded in a Taylor series is done in Ulaby *et al.* [48].

In particular, if it is Gaussian, i.e., $\rho(\xi) = e^{-\xi^2/l^2}$, equations (6.631.1), (9.212.4) and (9.215.1) of Gradshteyn and Ryzhik [19] are employed, and the integrals evaluate to these

converging infinite series:

$$I_0 = \frac{k^2 l^2}{4} e^{-\kappa_z^2 \sigma^2} \sum_{i=1}^{\infty} \frac{(\kappa_z \sigma)^{2i}}{i!i} e^{-\frac{\kappa_t^2 l^2}{4i}} \tag{5.188}$$

$$I_4 = \frac{k^2 l^2}{8} e^{-\kappa_z^2 \sigma^2} \sum_{i=1}^{\infty} \frac{i-1}{i} \frac{(\kappa_z \sigma)^{2i}}{i!i} e^{-\frac{\kappa_t^2 l^2}{4i}} \tag{5.189}$$

$$I_5 = \frac{k^2}{2\kappa_z^2} e^{-\kappa_z^2 \sigma^2} \sum_{i=1}^{\infty} (i-1) \frac{(\kappa_z \sigma)^{2i}}{i!i} \left(1 - \frac{\kappa_t^2 l^2}{4i}\right) e^{-\frac{\kappa_t^2 l^2}{4i}} \tag{5.190}$$

Similarly, if the correlation function is exponential, i.e., $\rho(\xi) = e^{-\xi/l}$, then equations (6.621.1) of Gradshteyn and Ryzhik [19] is used to obtain

$$I_0 = \tfrac{1}{2} k^2 l^2 e^{-\kappa_z^2 \sigma^2} \sum_{i=1}^{\infty} \frac{(\kappa_z \sigma)^{2i}}{(i-1)!(i^2 + \kappa_t^2 l^2)^{\frac{3}{2}}} \tag{5.191}$$

$$I_4 = \frac{3k^2 l^2}{16} e^{-\kappa_z^2 \sigma^2} \sum_{i=2}^{\infty} \frac{(\kappa_z \sigma)^{2i}}{(i-2)!i^4} \; {}_2F_1\left(2, \tfrac{5}{2}, 3; -\kappa_t^2 l^2 / i^2\right) \tag{5.192}$$

$$I_5 = \frac{k^2}{4\kappa_z^2} e^{-\kappa_z^2 \sigma^2} \sum_{i=2}^{\infty} \frac{(\kappa_z \sigma)^{2i}}{i!i} (i-1) \; {}_2F_1\left(1, \tfrac{3}{2}, 1; -\kappa_t^2 l^2 / i^2\right) \tag{5.193}$$

where ${}_2F_1(a,b,c;z)$ is hypergeometric function defined by

$${}_2F_1(a,b,c;z) = \sum_{n=0}^{\infty} \frac{\Gamma(a+n)\Gamma(b+n)\Gamma(c)}{\Gamma(a)\Gamma(b)\Gamma(c+n)} z^n \tag{5.194}$$

and $\Gamma(x)$ is the Gamma function.

The Gaussian-exponential correlation function does not have an analytic solution by this technique of expanding the exponential in a series in the integrals. The series representation for I_0 with a power-law correlation is found in Ulaby *et al.* [48].

5.7 Special Case: Forward Scattering in the Specular Direction

For forward scattering in the specular direction, $\theta_s \to \theta_i, \phi_\Delta \to 0$, so that $\kappa_{li} \to 0$ and $\kappa_{ti} \to 0$, and the general expressions above simplify considerably:

$$\frac{k^2}{4\pi A_0}\langle S_{mn}S^*_{pq}\rangle_{s^0} = I_0 a_{00mn}a^*_{00pq} \tag{5.195}$$

$$\frac{k^2}{4\pi A_0}\langle S_{mn}S^*_{pq}\rangle_{s^1} = 0 \tag{5.196}$$

$$\frac{k^2}{4\pi A_0}\langle S_{mn}S^*_{pq}\rangle_{s_1^2} = 0 \tag{5.197}$$

$$\frac{k^2}{4\pi A_0}\langle S_{mn}S^*_{pq}\rangle_{s_2^2} = \frac{m^2 I_0 - I_5}{\sin^2\theta_i}\left(a_{00mn}\left(a^*_{20pq} + a^*_{02pq}\right) + \left(a_{20mn} + a_{02mn}\right)a^*_{00pq}\right) \tag{5.198}$$

where, for *hh* polarization,

$$a_{00hh} = -2R_{h00}\cos\theta_i \tag{5.199}$$

$$a_{20hh} = -2R_{h20}\sin^2\theta_i\cos\theta_i \tag{5.200}$$

$$a_{02hh} = -2R_{h02}\sin^2\theta_i\cos\theta_i + 2(R_{h00} + R_{v00})\cos^3\theta_i \tag{5.201}$$

For *vv* polarization, the expansion coefficients for R_v are substituted for those of R_h, and *vice versa*. The necessary cross-polarized a coefficients are all zero in the specular scattering direction.

For the principal linear polarizations $pq = hh, hv, vh, vv$, the incoherent specular scattering coefficient can be obtained by setting $mn = pq$ in (5.195) and the resultant expression

in (5.115).

5.8 Special Case: Backscattering

For backscattering, $\theta_i, \theta_s \to \theta$, $\phi_\Delta \to 180°$, and thus $\kappa_{li} = -2k\sin\theta$, $\kappa_{ti} = 0$, and $\kappa_z = 2k\cos\theta$.

$$\frac{k^2}{4\pi A_0}\langle S_{mn}S^*_{pq}\rangle_{s^0} = I_0 a_{00mn}a^*_{00pq} \tag{5.202}$$

$$\frac{k^2}{4\pi A_0}\langle S_{mn}S^*_{pq}\rangle_{s^1} = \frac{I_0}{\cos\theta}\left(a_{00mn}a^*_{10pq} + a_{10mn}a^*_{00pq}\right) \tag{5.203}$$

$$\frac{k^2}{4\pi A_0}\langle S_{mn}S^*_{pq}\rangle_{s_1^2} = \frac{I_0}{\cos^2\theta}\left(a_{10mn}a^*_{10pq} + a_{01mn}a^*_{01pq}\right) \tag{5.204}$$

$$\begin{aligned}\frac{k^2}{4\pi A_0}\langle S_{mn}S^*_{pq}\rangle_{s_2^2} = &\frac{I_4}{\cos^2\theta}\left(\left(a_{00mn}a^*_{20pq} + a_{20mn}a^*_{00pq}\right) - \left(a_{00mn}a^*_{02pq} + a_{02mn}a^*_{00pq}\right)\right)\\ &+ \frac{I_5 - m^2 I_0}{\sin^2\theta}\left(\left(a_{00mn}a^*_{20pq} + a_{20mn}a^*_{00pq}\right) + \left(a_{00mn}a^*_{02pq} + a_{02mn}a^*_{00pq}\right)\right)\end{aligned} \tag{5.205}$$

where for *hh* polarization,

$$a_{00hh} = 2R_{h00}\cos\theta \tag{5.206}$$

$$a_{10hh} = 2R_{h00}\sin^2\theta + R_{h10}\sin 2\theta \tag{5.207}$$

$$a_{01hh} = 0 \tag{5.208}$$

$$a_{20hh} = 2R_{h10}\sin^3\theta + 2R_{h20}\sin^2\theta\cos\theta \tag{5.209}$$

$$a_{02hh} = -2(R_{h00} + R_{v00})\cos\theta + R_{h02}\sin^2\theta\cos\theta \tag{5.210}$$

For *vv* polarization, the expansion coefficients for R_v are substituted for those of R_h, and *vice versa*. The necessary cross-polarized *a* coefficients are all zero in the backscattering direction.

5.9 Behavior of Model

5.9.1 Coherent Scattering

The traditional Physical Optics coherent scattering term predicts that the coherent scattering from a rough surface is the same as for a smooth surface, except reduced by a multiplicative factor of $e^{-2k^2\sigma^2\cos^2\theta_i}$. Scattering is in the specular direction only, and cross-polarized scattering is nonexistent. This factor does not effect scattering at grazing (where $\theta_i = 90°$ and $\cos\theta_i = 0$) but is most pronounced at nadir, where a dramatic decrease in the coherently reflected power occurs as the rms surface height σ increases.

At an interface for which η_2/η_1 is purely real, such as an interface between air and a solid dry dielectric, the Brewster angle is distinct and the minimum is theoretically zero. The zeroth order scattering term does not effect the location of the Brewster angle, which is determined solely by the electrical parameters of the material. For non-magnetic materials, the formula $\tan\theta_B = \sqrt{\varepsilon_2/\varepsilon_1}$ for the Brewster angle is given in countless basic textbooks on electromagnetics.

The Physical Optics *v*-polarized rough surface reflection coefficient, through the second order derived in this chapter, is shown in Figure 5.5 for varying surface slopes but fixed dielectric and rms height. With the addition of the second order reflection coefficient, the level

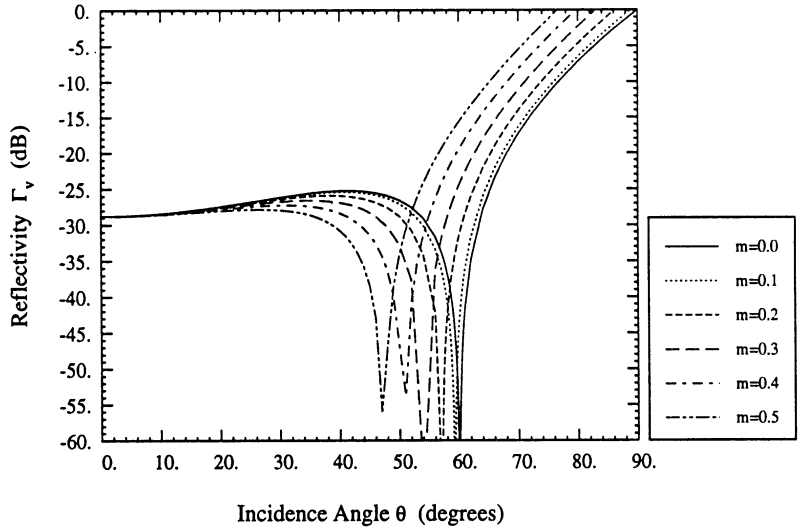

Figure 5.5: v-polarized reflectivity for a non-magnetic rough surface with $\varepsilon_r = 3.0 - j0.0$ and normalized rms height $k\sigma = 1.0$. The rms slope varies from $m = 0$ to $m = 0.5$. The curves include the zeroth and second order reflection coefficients.

of the coherent scattering does not significantly change, as much as the angular pattern compresses toward nadir. In particular, level of the reflection coefficient at nadir is unchanged and the Brewster angle now migrates toward nadir. The v-polarized reflection coefficient, thru second order, is given by

$$R_v^{PO} = R_{vv}^{(0)} + R_{vv}^{(2)} \tag{5.211}$$

$$= \left(R_{v00} - m^2 \left((R_{v00} + R_{h00}) \frac{\cos^2\theta_i}{\sin^2\theta_i} - (R_{v20} + R_{v02}) \right) \right) e^{-2k^2\sigma^2\cos^2\theta_i} \tag{5.212}$$

Neglecting R_{v20} and R_{v02}, and employing (5.104),

$$R_v^{PO} \approx \left(\frac{\eta_1 \cos\theta_i - \eta_2 \cos\theta_t}{\eta_1 \cos\theta_i + \eta_2 \cos\theta_t} - m^2 \left(\frac{2\eta_1\eta_2 (k_2^2/k_1^2 - 1)\cos^2\theta_i}{(\eta_2 \cos\theta_i + \eta_1 \cos\theta_t)(\eta_1 \cos\theta_i + \eta_2 \cos\theta_t)} \right) \right) e^{-2k^2\sigma^2\cos^2\theta_i} \tag{5.213}$$

which, for a boundary between non-magnetic media (ie. $\mu_1 = \mu_2$), reduces to

$$R_v^{PO} \approx \left((\sqrt{\varepsilon_r}\cos\theta_i - \cos\theta_t) - m^2 \left(\frac{2\sqrt{\varepsilon_r}(\varepsilon_r - 1)\cos^2\theta_i}{\cos\theta_i + \sqrt{\varepsilon_r}\cos\theta_t} \right) \right) \frac{e^{-2k^2\sigma^2\cos^2\theta_i}}{\sqrt{\varepsilon_r}\cos\theta_i + \cos\theta_t} \tag{5.214}$$

where $\varepsilon_r = \varepsilon_2/\varepsilon_1$. At the Brewster angle, that is, when $\theta_i = \theta_B$, $\left|R_v^{PO}\right|$ is a minimum. For a real dielectric, R_v is real and $R_v^{PO} = 0$ at the Brewster angle. Using Snell's Law, $\sin\theta_i = \sqrt{\varepsilon_r}\sin\theta_t$, this can be reduced to a quadratic equation in $\cos^2\theta_B$, the solution of which is

$$\cos^2\theta_B = \frac{(\varepsilon_r + 1) - 4m^2\varepsilon_r \pm \sqrt{(\varepsilon_r + 1)^2 - 8m^2\varepsilon_r(\varepsilon_r - 1)}}{8m^2\varepsilon_r(m^2\varepsilon_r - 1)} \tag{5.215}$$

If we assume small slopes such that $m^2 \ll (\varepsilon_r + 1)^2/8\varepsilon_r(\varepsilon_r - 1)$, then the square root can be expanded in a Taylor series to produce

$$\cos^2\theta_B = \frac{1}{(\varepsilon_r + 1)(1 - m^2\varepsilon_r)} \tag{5.216}$$

which is equivalent to

$$\tan^2\theta_B = \varepsilon_r\Big(1-m^2(\varepsilon_r+1)\Big) \tag{5.217}$$

which demonstrates that the effect of the roughness is to reduce the effective dielectric, moving the Brewster angle in toward nadir as the rms slope increases. The actual shift in the Brewster angle due to roughness is

$$\Delta\theta_B = \theta_B - \theta_B|_{m=0} = \tan^{-1}\sqrt{\varepsilon_r(1-m^2(\varepsilon_r+1))} - \tan^{-1}\sqrt{\varepsilon_r} \tag{5.218}$$

$$\approx -\tfrac{1}{2}\sqrt{\varepsilon_r}m^2 \tag{5.219}$$

A more precise analysis, using symbolic math analysis software, on (5.212) not neglecting the terms $R_{v20}+R_{v02}$, yields the result that, to the lowest order of m,

$$\Delta\theta_B = -m^2\frac{\varepsilon_r^4+4\varepsilon_r^3+3\varepsilon_r^2+6\varepsilon_r+2}{2\varepsilon_r^{3/2}(\varepsilon_r+1)^2} \tag{5.220}$$

That this expression reduces to (5.219) for large ε_r indicates that the higher order expansion coefficients become negligible at least as far as the Brewster angle as the dielectric increases.

Greffet [20] analyzed a one-dimensional rough surface with a Gaussian correlation using a Small Perturbation technique and derived a similar result for the dependence of the location of the Brewster angle on the surface roughness. This result is similar to Greffet's in that the Brewster angle migrates toward nadir as σ^2, but differs in that his results indicate a l^{-1} dependence, in contrast to the l^{-2} dependence in (5.219) and (5.220). In addition, Gr-

effet asserts that even for non-magnetic, real dielectric media, the rough surface Brewster angle is not a null, but a minimum, whereas this result indicates that such surfaces should always create a coherent null.

The fourth order reflection coefficients do not change the magnitude of the total reflection coefficient by more than 3 dB or location of the Brewster angle by more than 1° unless slopes are on the order of unity or more, at which point this single scattering model itself is no longer valid. In addition, neither the second order nor fourth order coefficients change the magnitude of the total h polarized reflection coefficient by more than 3 dB unless the slopes are on the order of unity.

5.9.2 Incoherent Scattering

The Physical Optics development guarantees a separation of the effects of the surface electrical characteristics and the roughness characteristics. The electrical characteristics are contained entirely in the local reflection coefficients; the roughness characteristics are contained entirely in the integrals I_0, I_4, and I_5.

5.9.2.1 Co-polarized scattering in the Plane of Incidence

The form of equation (5.182) appears in the Integral Equation Method (IEM) [15]. However, the IEM neglects the expansion of the local reflection coefficients given by (5.28) and (5.29). For specular scattering this makes no difference because, of the terms computed in this chapter, only the zeroth order term contributes to specular scattering. For backscattering, however, the inclusion of R_{v10} and R_{h10} make the first and second order terms non-negligible.

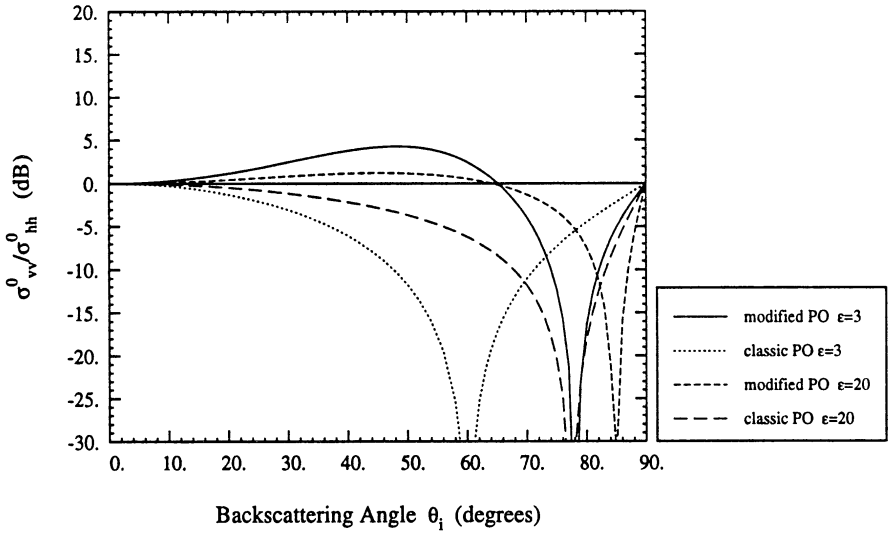

Figure 5.6: Ratio of *vv* to *hh* backscatter. The Physical Optics predicts that *hh* exceeds *vv* by the same ratio as the ratio of the smooth surface reflectivities. The IEM model for these terms agrees with PO. The inclusion of R_{v10} and R_{h10} coefficients results in an angular dependence where *vv* exceeds *hh* for angles less than 60°. This is much more like SPM than the PO is. The curves shown are for nonmagnetic surfaces with dielectric of $\varepsilon_r = 3.0 - j0.0$ and $\varepsilon_r = 20.0 - j0.0$. These curves are independent of the surface roughness characteristics and only very weakly dependent on the imaginary part of the dielectric.

Without the higher order terms of the local reflection coefficients, the ratio of σ^0_{vv} to σ^0_{hh} in the plane of incidence is always the same as the square of the ratio of R_{v00} to R_{h00} for the same angle of incidence. As a result, σ^0_{vv} is always less than σ^0_{hh} in the Physical Optics solution. This is in contrast to the Geometric Optics solution, which does not distinguish between polarizations, and the Small Perturbation Method, which predicts that σ^0_{vv} always exceeds σ^0_{hh}.

With the inclusion of R_{v10} and R_{h10} in the terms strictly proportional to I_0 (that is, the terms that appear in IEM and in (5.182)), the ratio $\sigma^0_{vv}/\sigma^0_{hh}$ in the plane of incidence can be either greater than or less than unity, depending on the choice of bistatic angles and the

surface dielectric. Since all the surface roughness characteristics are contained in I_0, this ratio is independent of rms surface height, the rms surface slope, the correlation length, or even the correlation function. Figure 5.6 shows this ratio for two nonmagnetic surfaces, one with a dielectric $\varepsilon_r = 3$ and the other with $\varepsilon_r = 20$, for backscattering. With these more complete terms the backscattering Brewster angle moves very close to grazing. From nadir out to about 50°, the addition of the first and second order terms appears to reverse the ratio from negative to an equal but positive amount. Both the modified Physical Optics and the Small Perturbation Method predict that the ratio $\sigma^0_{vv}/\sigma^0_{hh}$ has an angular dependence of $\sec^2\theta_i$, at least from 0° thru about 40°, however, the modified Physical Optics and the Small Perturbation Method do not agree on the dependence on ε_r. The only effect of the imaginary part of the dielectric on both the Physical Optics approach and the modified Physical Optics approaches is to change the Brewster null to a minimum; the curves are not changed appreciably away from the null with a nonzero imaginary dielectric.

In specular scattering, all terms other than the zeroth order term are identically zero for co-polarized incoherent scattering. As a result, the Brewster null for σ^0_{vv} in specular scattering is preserved. The angle at which this Brewster null occurs is the same as for the smooth surface Brewster angle. Terms derived from

$$\left\langle \left| U^{(2)}_{pq} \right|^2 e^{j\kappa_z(z-z')} \right\rangle - \left| \left\langle U^{(2)}_{pq} e^{j\kappa_z z} \right\rangle \right|^2, \tag{5.221}$$

are the lowest order incoherent terms which are non-zero at this set of bistatic angles. Figure 5.7 shows that inclusion of these terms changes the *vv* null to a minimum at -44 dB, but at this level it does not otherwise appreciably change the pattern.

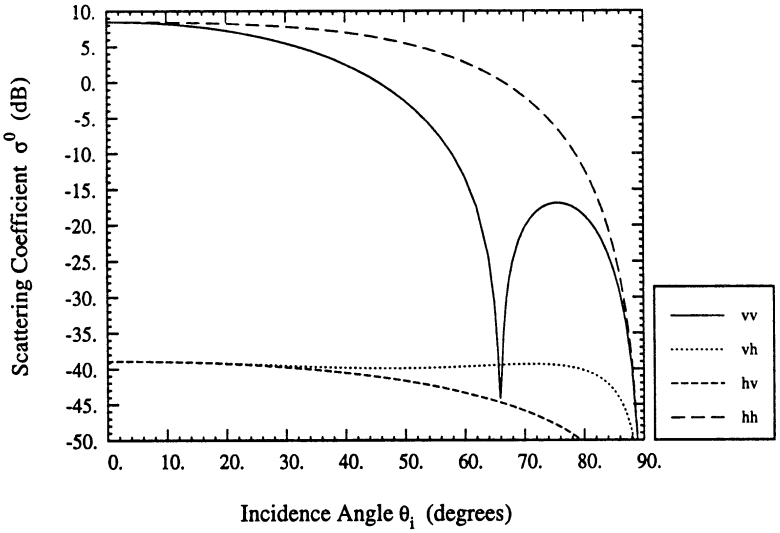

Figure 5.7: Incoherent scattering coefficients in the specular scattering direction ($\theta_s = \theta_i$ and $\phi_\Delta = 0°$) for a nonmagnetic rough surface with $\varepsilon_r = 5.0 - j0.0$ and a Gaussian correlation function with $k\sigma = 0.5$ and $kl = 10.0$. Cross polarized scattering in the plane of incidence are due exclusively to a_{11pq} coefficients; the minimum in the σ^0_{vv} is not a null due to inclusion of a_{20vv} and a_{02vv} coefficients.

The terms proportional to I_4 and I_5 move the level of scattering by only small amounts. At nadir incidence, $R_{v00} = -R_{h00}$ and this results in the change of level for *vv* to be raised while the level of *hh* is reduced by the same amount. The changes induced by these terms are negligible, indicating that the terms strictly proportional to I_0 probably should be considered the appropriate Physical Optics solution to rough surface scattering.

5.9.2.2 Cross polarized scattering in the plane of incidence

Cross polarized scattering in the plane of incidence is identically zero for all the terms derived in this chapter. Terms derived from (5.221), in particular, terms proportional to $|a_{11pq}|^2$, are the lowest order cross-polarized terms which are non-zero in the plane of inci-

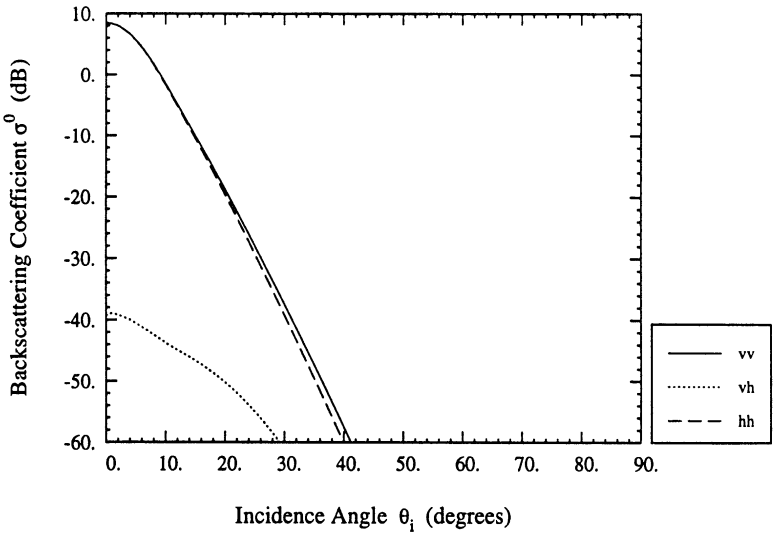

Figure 5.8: Backscattering coefficients for a nonmagnetic rough surface with $\varepsilon_r = 5.0 - j0.0$ and a Gaussian correlation function with $k\sigma = 0.5$ and $kl = 10.0$. Backscattering corresponds to ($\theta_s = \theta_i$ and $\phi_\Delta = 180°$) Cross polarized scattering in the plane of incidence is due exclusively to a_{11pq} coefficients. At backscattering, $a_{11hv} = -a_{11vh}$ and as a result, $\sigma^0_{hv} = \sigma^0_{vh}$.

dence. Figure 5.7 shows the level of these cross-polarized terms relative to the co-polarized terms in the specular scattering direction; Figure 5.8 shows all the backscattering coefficients for the same surface in the backscattering direction. For a backscattering geometry, $a_{11vh} = -a_{11hv}$, resulting in $\sigma^0_{vh} = \sigma^0_{hv}$, which must be true due to reciprocity. This is somewhat surprising result because Physical Optics does not incorporate reciprocity explicitly in the tangent-plane approximation. In other words, preference is given to the incidence angle θ_i over θ_s in the calculation of the local reflection coefficients; θ_s is completely ignored their calculation.

5.9.2.3 Effect of the correlation function on backscatter

The correlation function has a dramatic effect on backscatter as predicted by Physical

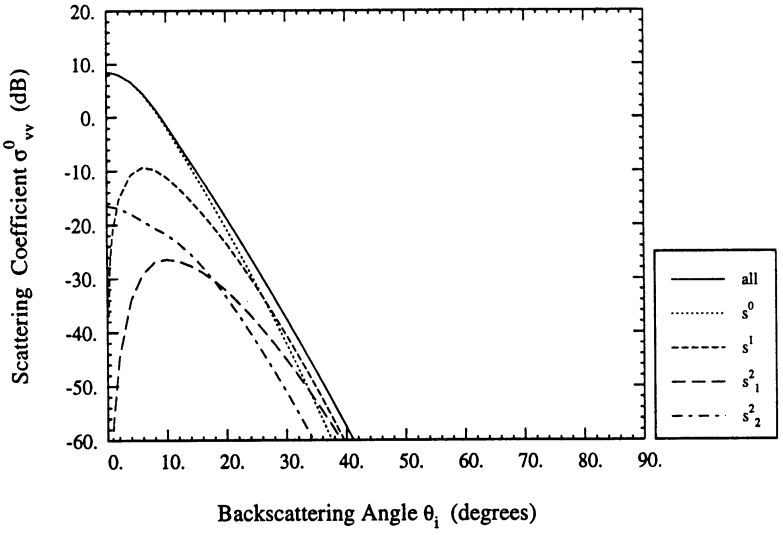

Figure 5.9: σ^0_{vv} vs. backscattering angle for a nonmagnetic rough surface with $\varepsilon_r = 5.0 - j0.0$ and a Gaussian correlation function with $k\sigma = 0.5$ and $kl = 10.0$.

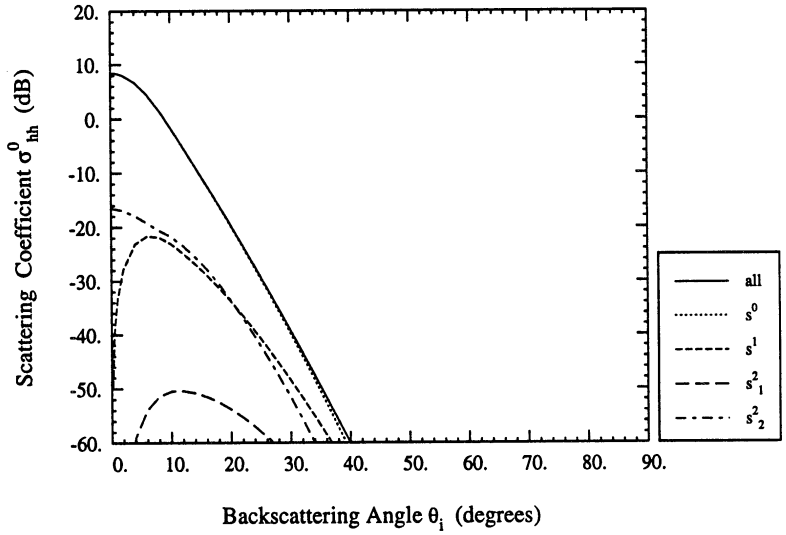

Figure 5.10: σ^0_{hh} vs. backscattering angle for a nonmagnetic rough surface with $\varepsilon_r = 5.0 - j0.0$ and a Gaussian correlation function with $k\sigma = 0.5$ and $kl = 10.0$.

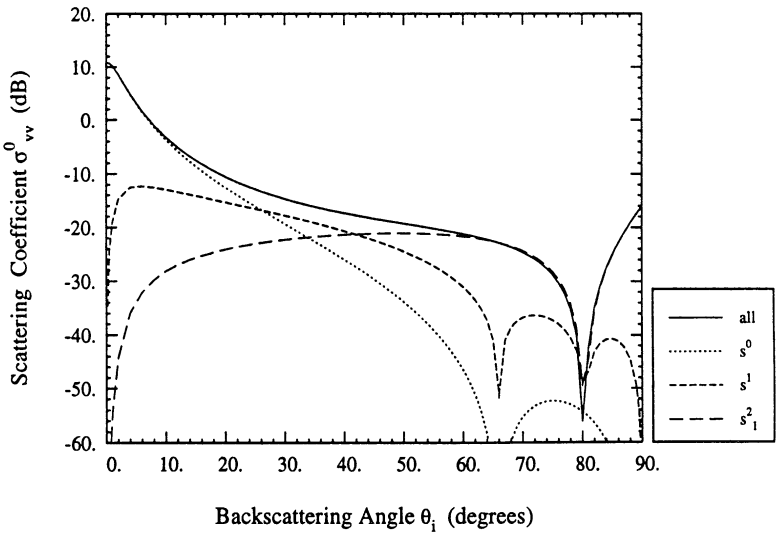

Figure 5.11: σ^0_{vv} vs. backscattering angle for a nonmagnetic rough surface with $\varepsilon_r = 5.0 - j0.0$ and an exponential correlation function with $k\sigma = 0.5$ and $kl = 10.0$.

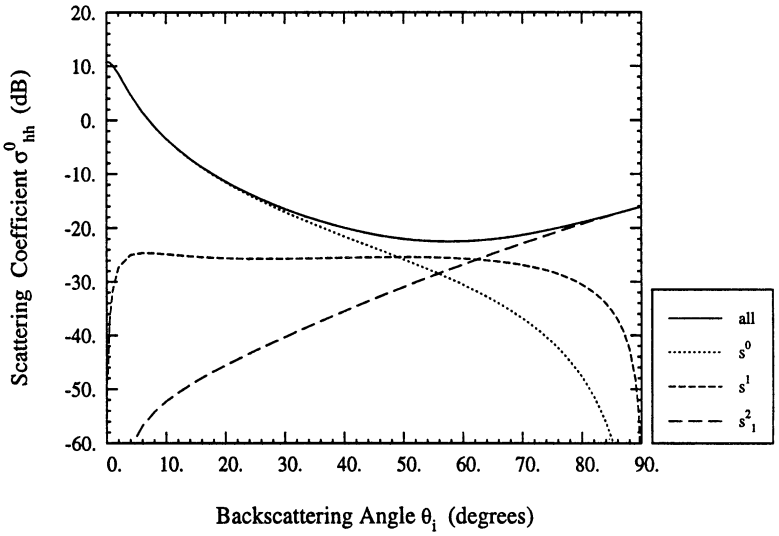

Figure 5.12: σ^0_{hh} vs. backscattering angle for a nonmagnetic rough surface with $\varepsilon_r = 5.0 - j0.0$ and an exponential correlation function with $k\sigma = 0.5$ and $kl = 10.0$.

Optics. This is true also for the modified Physical Optics. A comparison between an exponential and Gaussian correlation function is given in Figure 5.9 through Figure 5.12, for a surface with otherwise identical characteristics.

The higher order terms increase the level of the backscatter away from nadir; at nadir they are negligible. The level for the modified Physical Optics for the Gaussian correlation is increased to the point that the co-polarized scattering agrees more closely with Geometric Optics than Physical Optics does. The pattern still drops off very fast with increasing angle of incidence, however.

This is in stark contrast to the case for the exponential correlation. The additional terms provided by the modified Physical Optics dramatically increases the backscattering for angles away from nadir, to the point where it actually increases with increasing incidence angle and is not infinitesimally small at grazing. This is a reflection of the fact that the exponential correlation is not a strictly valid correlation function, and that the slope for an exponential surface is undefined. The interaction between a grazing incidence wave and a surface with arbitrarily many vertical facets would be large indeed, if such a surface were realizable. Near grazing multiple scattering becomes very important and heuristic shadowing functions often are used on single scattering theories to reduce scattering from them. Shadowing functions are not used in this chapter.

These plots lend credence to the conclusions of Chen and Fung [8], namely that the Physical Optics incoherent backscattering is valid only for angles less than 30°. At 30°, the higher order terms are becoming significant in the modified Physical Optics model.

CHAPTER 6

Results and Comparisions with Theory

A number of measurements were made of rough surfaces sculpted on sand in the Bistatic Measurement Facility, for the purpose of comparing measurements to theoretical predictions. This chapter summarizes the results of these measurements.

6.1 Surface Characterizations

The surface profiler is described in Section 3.3. It was used to characterize the rms height and the correlation function of the surfaces measured in this chapter, including the correlation of the surface shown in Figure 2.4, for which radar data is shown in Figure 6.4.

The correlation function was generated by averaging the individual autocorrelations of 3 linear profiles of the surface. Experimentation has shown that only 3 profile measurements averaged together are necessary to roughly determine the correlation length of the surfaces, but many more are needed to demonstrate that the correlation function tends toward zero beyond a few correlation lengths. As a result of the negative values of the correlation function, the integral (5.141) may yield values which are obviously incorrect. Therefore, from the surface profiles measured an average correlation function is derived, and from this a cor-

relation length is determined. The distance measuring instrument in the profiler had a sufficiently large rms error (± 2 mm per data point) that filtering had to be done to the measured profiles to minimize the measurement noise. This results in a less than best estimate of the correlation function and correlation length. While these estimates are adequate for specular scattering, where scattering is not strongly dependent on the exact correlation function and length, the backscattering data could be grossly overestimated with an exponential correlation and even more grossly underestimated with a Gaussian correlation.

6.2 Coherent Scattering

The coherent scattering data presented here has first been published in [11]. Figure 6.1 shows measurements of the reflection coefficient for a smooth dry surface with $k\sigma < 0.2$ (the rms height σ was smaller than 1 mm, the measurement precision of the laser profileometer). The curves in Figure 6.1 were calculated using the Fresnel reflection coefficient formulas given by (2.75) and (2.76) for a surface with a relative dielectric constant $\varepsilon_r = 3.0 + j0$. The dielectric constant for the sand medium was measured by a dielectric probe, which gave a value of $\varepsilon' = 3.0$ for the real part and a value of $\varepsilon'' < 0.03$ for the imaginary part. Because $\varepsilon''/\varepsilon' \ll 1$ and the inclusion of ε'' as high as 0.05 does not significantly change the results of any of the calculations in this chapter, it was ignored. The excellent agreement between the measured data and the calculated curves presented in Figure 6.1 provides testimony to the measurement accuracy of the system.

Figure 6.2 compares measured values of the power reflection coefficient Γ with curves calculated using modified Physical Optics (equation (5.212)) for surfaces with $k\sigma = 0.515$,

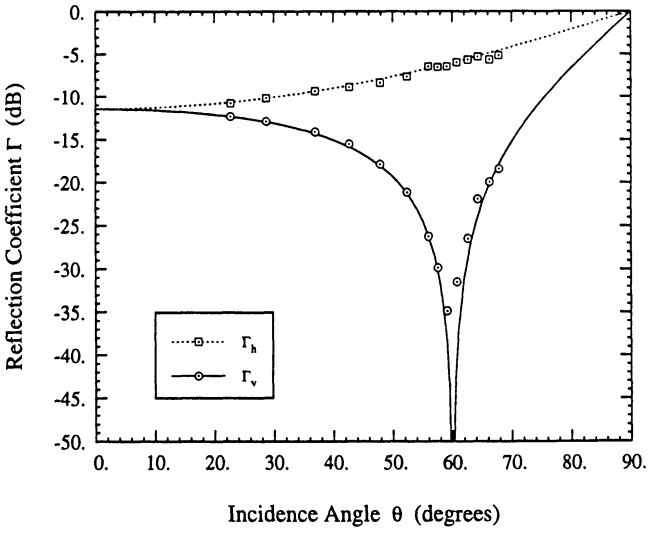

Figure 6.1: Measured coherent reflectivity of a smooth surface with $\varepsilon_r = 3.0$ and $k\sigma < 0.2$: squares denote horizontal polarization and circles denote vertical polarization. Continuous curves are smooth surface reflection coefficients. The angle of minimum reflectivity for vertical polarization is 60°.

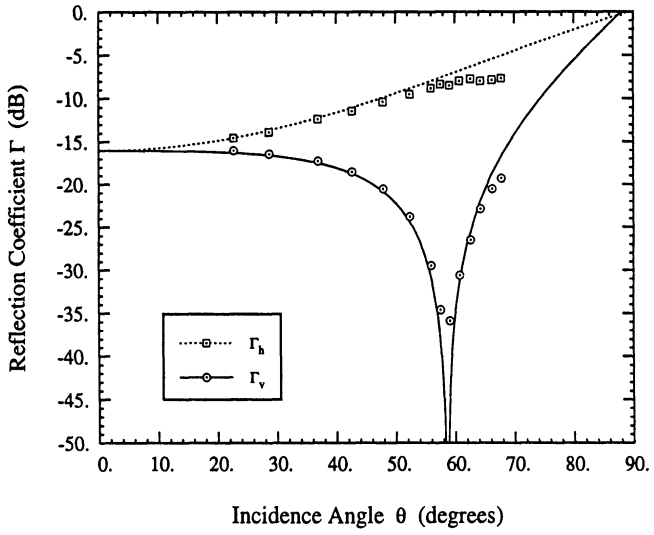

(a) $k\sigma = 0.515; kl = 5.4$

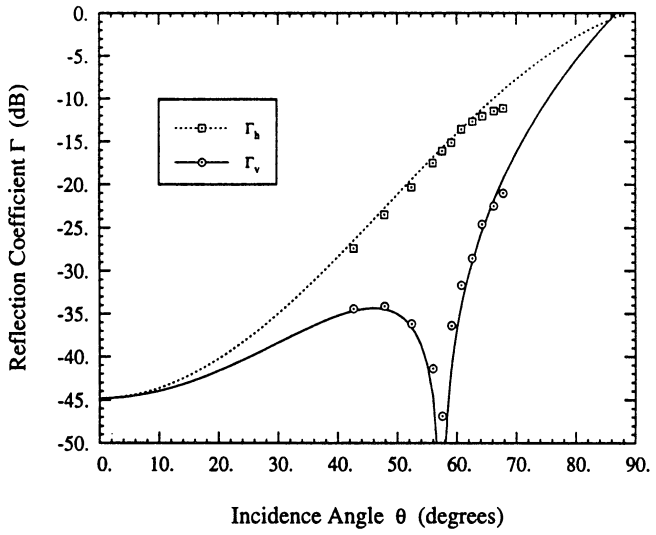

(b) $k\sigma = 1.39; kl = 10.6$

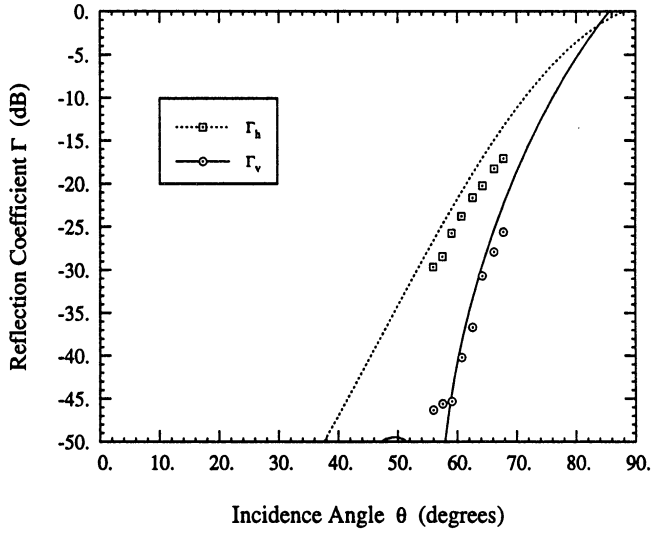

(c) $k\sigma = 1.94; kl = 11.8.$

Figure 6.2: Measured coherent reflectivity of three rough surfaces. Continuous curves are predictions based on modified Physical Optics. In all cases, the surfaces have a relative dielectric constant $\varepsilon_r = 3.0$.

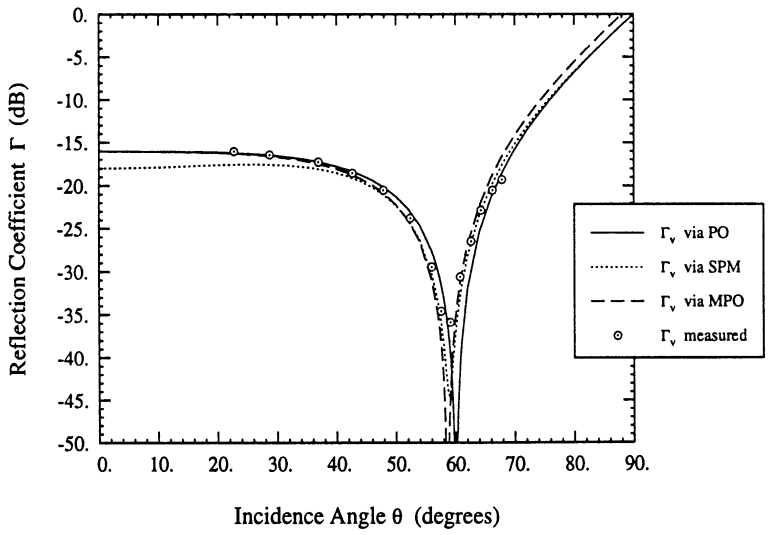

Figure 6.3: Comparison of measured coherent reflectivity of a slightly rough surface with $\varepsilon_r = 3.0$ and $k\sigma = 0.5$ with the predictions of Physical Optics, Small Perturbation, and modified Physical Optics for vertical polarization.

1.39, and 1.94. Good overall agreement is observed between theory and experimental observations, especially in the region of the location of the Brewster angle, which exhibits a slight shift towards decreasing angle of incidence; the Brewster angle shifts from 60.0° for the smooth surface shown in Figure 6.1 to 57.5° for the surface with $k\sigma = 1.39$ (Figure 6.2(b)) and to about 56.0° for the surface with $k\sigma = 1.94$ (Figure 6.2(c)). The shift is toward decreasing angle of incidence, which is the direction predicted by the Small Perturbation Method. While the Small Perturbation Method can be used to explain the data in Figure 6.2(a), it fails for surfaces in Figure 6.2(b) and (c) because they are too rough for the model. The measured vertical polarized reflectivity data in Figure 6.2(a) is shown again in Figure 6.3, together with the predictions of Physical Optics, Small Perturbation, and modified Physical Optics. Physical Optics does not exhibit the shift in the Brewster angle evident

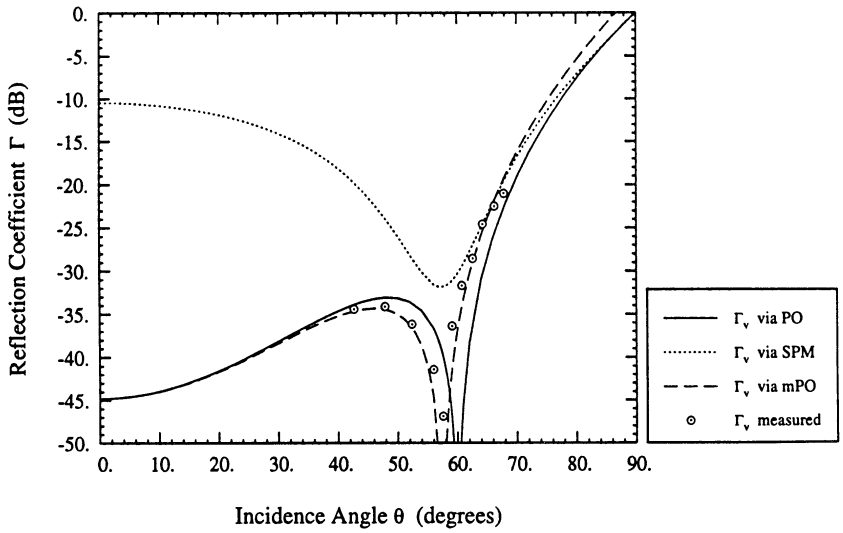

Figure 6.4: Comparison of measured coherent reflectivity of a moderately rough surface with $\varepsilon_r = 3.0$ and $k\sigma = 1.4$ with the predictions of Physical Optics, Small Perturbation, and modified Physical Optics for vertical polarization.

in the data. Both Small Perturbation and the modified Physical Optics predict the level and the shift in the vicinity of the Brewster angle, but Physical Optics and modified Physical Optics match the data better than Small Perturbation at nadir. The measured vertical polarized reflectivity data shown in Figure 6.2(b) is from a considerably rougher surface, and is shown for comparison with the predictions of the models in (6.4). The data is clearly out of the range of validity for the Small Perturbation model, and the Physical Optics prediction fails at the Brewster angle. The modified Physical Optics prediction is very close to the data.

By way of summary, Figure 6.5 shows the dependence of the q-polarized normalized

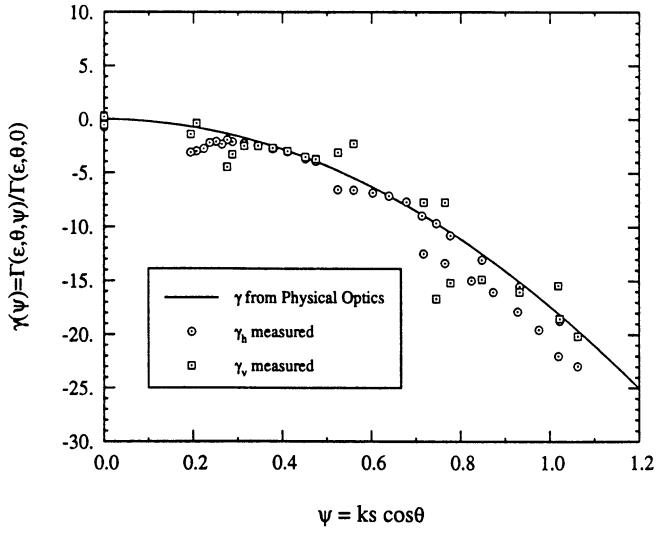

Figure 6.5: The reduction of coherent scattering from a surface due to roughness. Shown is the measured coherent reflectivity of several surfaces (all with with $\varepsilon' = 3$) but differing roughness parameters $\psi = k\sigma\cos\theta_i$, normalized to the reflection coefficient of a smooth surface. The angles of incidence range from 20° to 70° and the roughness $k\sigma$ ranges from 0 to 2. The continuous curve is the zeroth order Physical Optics prediction for surfaces with Gaussian-height probability densities.

power reflection coefficient γ_q on the zeroth order roughness parameter ψ, where

$$\gamma_q(\psi) = \frac{\Gamma_q(\varepsilon_r,\theta,\psi)}{\Gamma_{q0}(\varepsilon_r,\theta,0)} = \frac{\left|R_{qq}^{(0)}\right|^2}{\left|R_{q00}\right|^2} \tag{6.1}$$

$$= e^{-4\psi^2} \tag{6.2}$$

and $\psi = k\sigma\cos\theta$. Data similar to this has last appeared in Beckmann and Spizzichino [3], although not with the dynamic range presented here.

6.3 Incoherent Scattering

6.3.1 Specular Direction

As was discussed previously in Chapter 5, the expression for the bistatic scattering coefficient consists of a number of terms. The specular scattering direction is the special case in which $\theta_s = \theta_i$, $\phi_\Delta = 0$ and thus $\kappa_t = 0$. In this direction, most terms above the zeroth order are identically zero. Figure 6.6(a) shows the measured values of σ^0_{vv} and σ^0_{hh} for a slightly rough surface with $k\sigma = 0.515$, plotted as a function of incidence angle, as well as plots for the same quantities calculated in accordance with the results of Chapter 5. While a higher order term exists which would prevent the forward scattering Brewster minimum from being a null, its value depends on the rms slope of the surface. Since the surface correlation function has been assumed to be exponential, the slope is undefined. A possible rectification for this dilemma is to assume a Gaussian- exponential correlation function, so that the integrals in the modified Physical Optics model behave as if the correlation were exponential, yet there is a well defined slope. Unfortunately, this implies an additional free parameter, the rms slope m, which the author has been unable to directly measure.

For the rougher surfaces shown in Figure 6.6(b) and (c) with $k\sigma = 1.39$ and 1.94, the zeroth order model overestimates the level of σ^0.

6.3.2 Within the Plane of Incidence

Specular scattering can be considered a special case of scattering in the plane of incidence. Figure 6.7 depicts $\sigma^0{}_{hh}$ in the plane of incidence for a transmitter fixed at $\theta_i = 45°$.

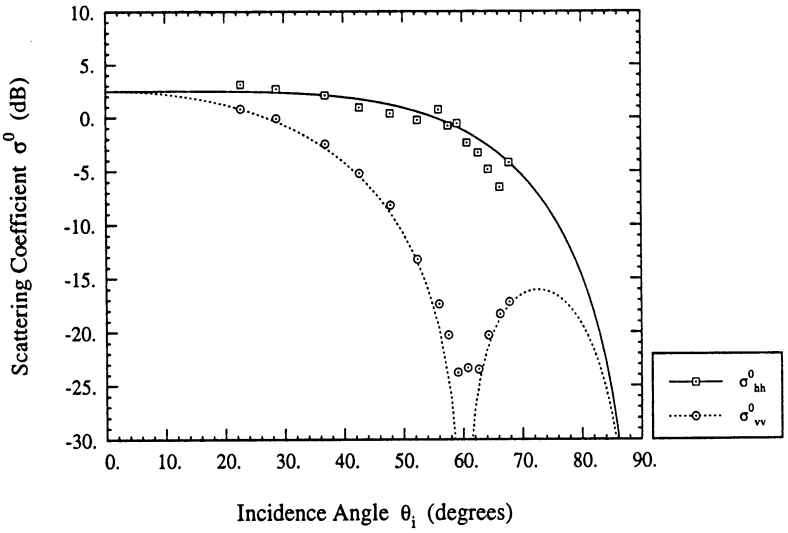

(a) $k\sigma = 0.515; kl = 5.4$

Figure 6.8 shows $\sigma^0{}_{vv}$ for the same surface under the same conditions. Also shown are three predictions of theories discussed in this dissertation: the Geometric Optics, Physical Optics and modified Physical Optics. For the Physical Optics approaches, a power-law correlation was used, as it best fit the profile data. The negative angles of incidence in these plots and those to follow should be interpreted as positive angles of incidence at an azimuthal angle 180° away. For example, $\theta_s = -30°$ in Figure 6.8 should be interpreted as $\theta_s = 30°$ at $\phi_\Delta = 180°$. As the angle of incidence in both figures is $\theta_i = 45°$, the specular scattering direction is at $\theta_s = 45°$ and the backscattering direction is at $\theta_s = -45°$.

In Figure 6.7 the predictions for Physical Optics and modified Physical Optics overlap, but neither of these nor Geometric Optics can be said to predict the data very well. Physical Optics is uniformly too low; in Figure 6.8 Physical Optics and the modified Physical Optics are distinct yet the predictions are almost uniformly too high.

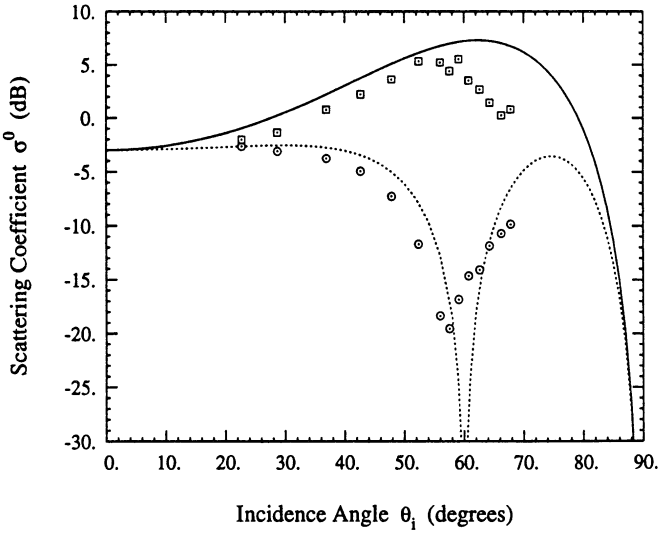

(b) $k\sigma = 1.39; kl = 10.6$

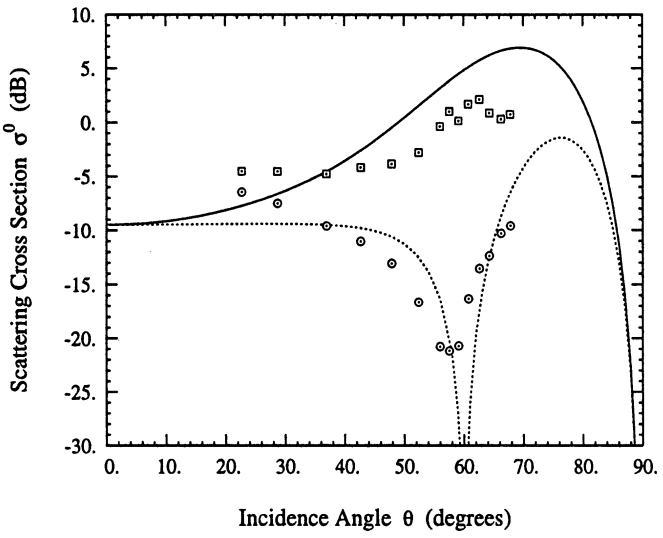

(c) $k\sigma = 1.94; kl = 11.8$

Figure 6.6: Measured co-polarized specular scattering coefficient for three rough surfaces. Continuous curves are based on Physical Optics: the dashed curve corresponds to the zeroth-order term for σ^0_{vv}, the dotted curve corresponds to σ^0_{hh}. The surface has a relative dielectric constant $\varepsilon_r = 3.0$ and an exponential correlation function was used.

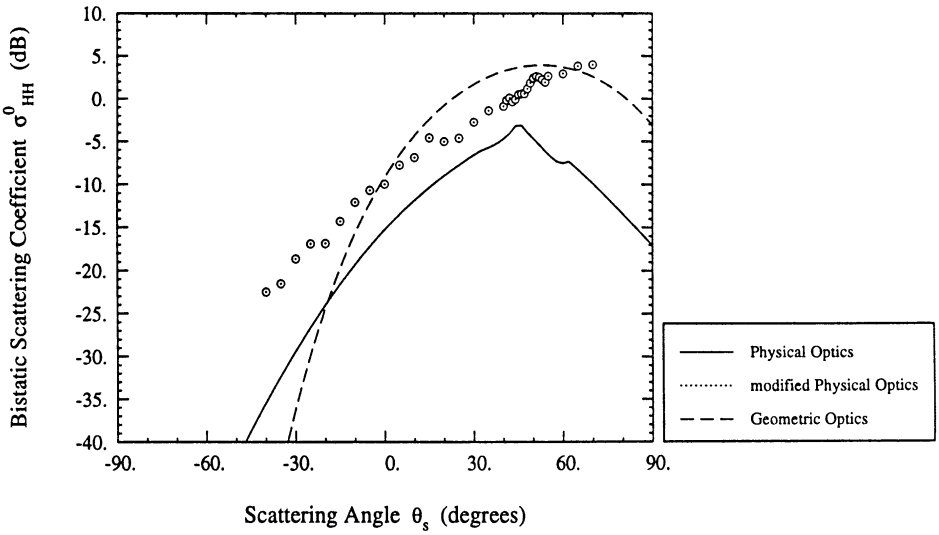

Figure 6.7: *hh*-polarized scattering in the plane of incidence ($\phi_\Delta = 0°$). The surface has a dielectric of $\varepsilon_r = 3.0 - j0.0$ and roughness parameters $k\sigma = 1.44$ and $kl = 11.5$. The transmitter was fixed at $\theta_i = 45°$. The circles represent measured data points; the curves are theoretical predictions. A power-law correlation was used, which best fit the profile data.

The measured σ^0_{hh} in Figure 6.7 does not peak at the specular direction, as all three models predict. The peak is further toward grazing reception than the specular direction, but how much cannot be determined as the Bistatic Measurement Facility cannot make accurate measurements beyond $\theta_s = 70°$. The trend in Figure 6.8 for σ^0_{vv} definitely shows that the scattering peaks near or slightly to the nadir side of the specular direction.

6.3.3 Outside of Plane of Incidence

Measurements in the $\phi_\Delta = 45°$ plane are shown in Figure 6.9 through Figure 6.11 and in the $\phi_\Delta = 90°$ plane in Figure 6.12 and Figure 6.13. In Figure 6.9, all three scattering theories can be seen to match the σ^0_{hh} data in the $\phi_\Delta = 45°$ plane reasonably well, particularly where the scattering is largest. The two Physical Optics approaches are slightly better than the

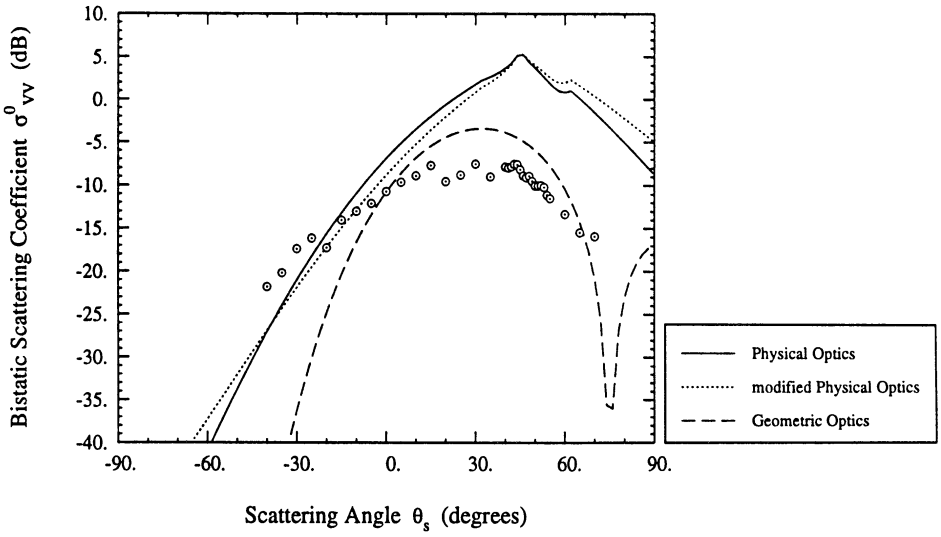

Figure 6.8: *vv*-polarized scattering in the plane of incidence ($\phi_\Delta = 0°$). The surface has a dielectric of $\varepsilon_r = 3.0 - j0.0$ and roughness parameters $k\sigma = 1.44$ and $kl = 11.5$. The transmitter was fixed at $\theta_i = 45°$. The circles represent measured data points; the curves are theoretical predictions. A power-law correlation was used, which best fit the profile data.

Geometric Optics in this case.

All three predictions are uniformly too low in Figure 6.10, but the two Physical Optics patterns seem to capture the shape of the data better than the Geometric Optics. While the Physical Optics prediction is at least 10 dB too low everywhere, the modified Physical Optics is too low by about 5 dB everywhere.

Figure 6.11 shows some interesting features of the three scattering theories, as well as the measurements: the modified Physical Optics model is seen to have the same pattern null as the Geometric Optics model, while having the angular pattern of Physical Optics, except for being higher by about 10 dB, away from the null. This is due to the fact that the modified Physical Optics model accounts for the surface slopes, like Geometric Optics, but unlike the

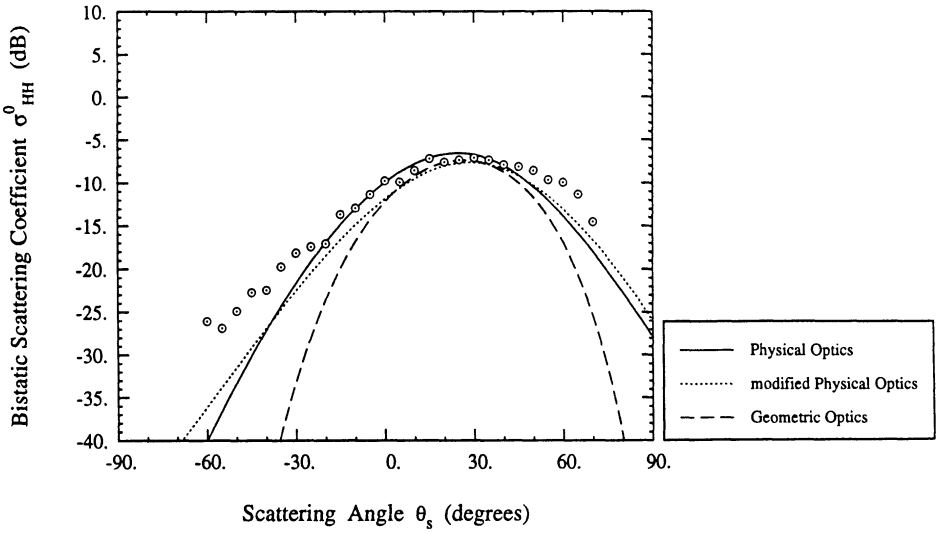

Figure 6.9: *hh*-polarized scattering in the $\phi_\Delta = 45°$ plane. The surface has a dielectric of $\varepsilon_r = 3.0 - j0.0$ and roughness parameters $k\sigma = 1.44$ and $kl = 11.5$. The transmitter was fixed at $\theta_i = 45°$. The circles represent measured data points; the curves are theoretical predictions. A power-law correlation was used, which best fit the profile data.

Physical Optics model. The agreement between the data and the modified Physical Optics model is excellent.

Figure 6.12 shows σ^0_{vh} in the plane thru nadir that is perpendicular to the direction of incident propagation as projected onto the surface. The symmetry is apparent in both the model predictions and the measurements. Despite the agreement between the models, the data is 10 dB lower at a nadir-looking receiver.

There is much more agreement between not just the models, but also the models and the data, in Figure 6.13. While the Geometric Optics apparently predicts the scattering very accurately within 30° of nadir, but the two Physical Optics approaches do a better job of predicting the overall pattern out to about 70°. While Physical Optics is low by about 15 dB

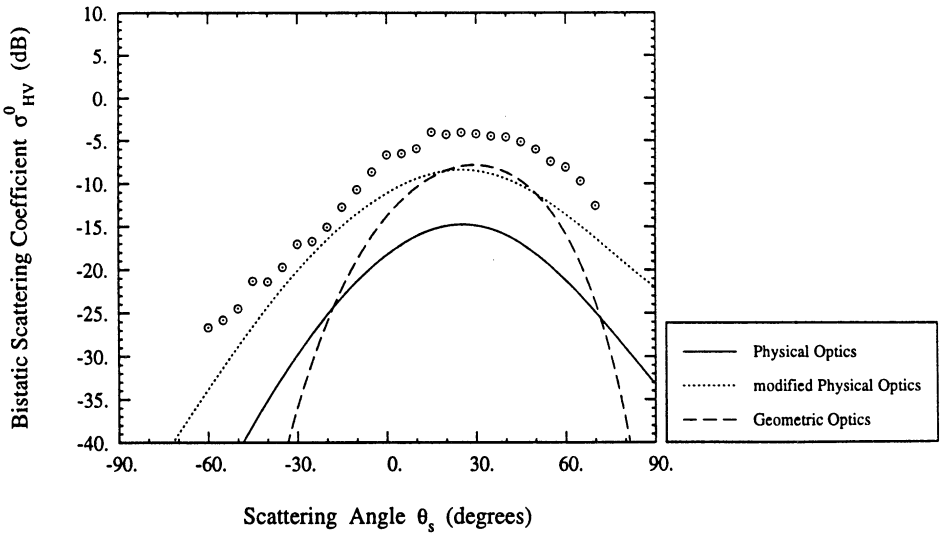

Figure 6.10: *hv*-polarized scattering in the $\phi_\Delta = 45°$ plane. The surface has a dielectric of $\varepsilon_r = 3.0 - j0.0$ and roughness parameters $k\sigma = 1.44$ and $kl = 11.5$. The transmitter was fixed at $\theta_i = 45°$. The circles represent measured data points; the curves are theoretical predictions. A power-law correlation was used, which best fit the profile data.

at $\theta_s = -70°$, the modified Physical Optics model is not low by more than about 5 dB for all scattering angles.

6.4 Summary

The Bistatic Measurement Facility was used to make a number of measurements of bistatic radar scattering, including coherent scattering and incoherent scattering. All surfaces measured had a dielectric constant of $\varepsilon_r = 3.0 - j0.0$.

For the coherent scattering, the Physical Optics model agrees overall with the level of scattering, and the Small Perturbation agrees with the migration of the Brewster angle with roughness, but only the modified Physical Optics model developed in Chapter 5 does both.

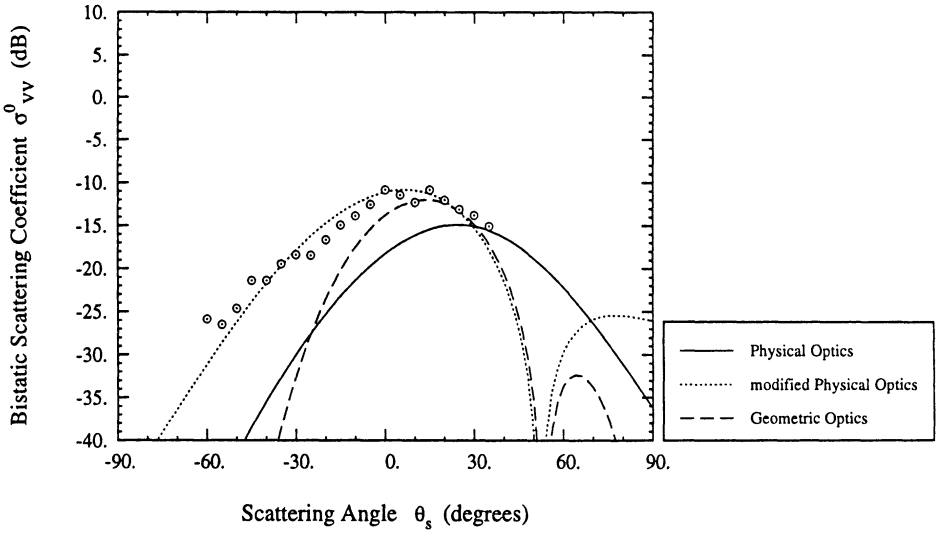

Figure 6.11: *vv*-polarized scattering in the $\phi_\Delta = 45°$ plane. The surface has a dielectric of $\varepsilon_r = 3.0 - j0.0$ and roughness parameters $k\sigma = 1.44$ and $kl = 11.5$. The transmitter was fixed at $\theta_i = 45°$. The circles represent measured data points; the curves are theoretical predictions. A power-law correlation was used, which best fit the profile data.

For incoherent scattering, measurements were made of several surfaces of differing rms surface height in the specular direction. The Physical Optics and modified Physical Optics models agree in the specular direction, and agreed with the data for the slightly rough surface of $k\sigma = 0.5$. The two Physical Optics models agree qualitatively with the specular scattering data up to $k\sigma = 2$.

Scattering from a surface of rms roughness $k\sigma = 1.4$ was measured in three planes of constant azimuth with the transmitter fixed at $\theta_i = 45°$. Neither Physical Optics model nor the Geometric Optics model adequately predicted scattering in the plane of incidence (the $\phi_\Delta = 0°$ plane); but in the $\phi_\Delta = 45°$ and $\phi_\Delta = 90°$ planes, the modified Physical Optics model modestly outperforms both Geometric Optics and Physical Optics.

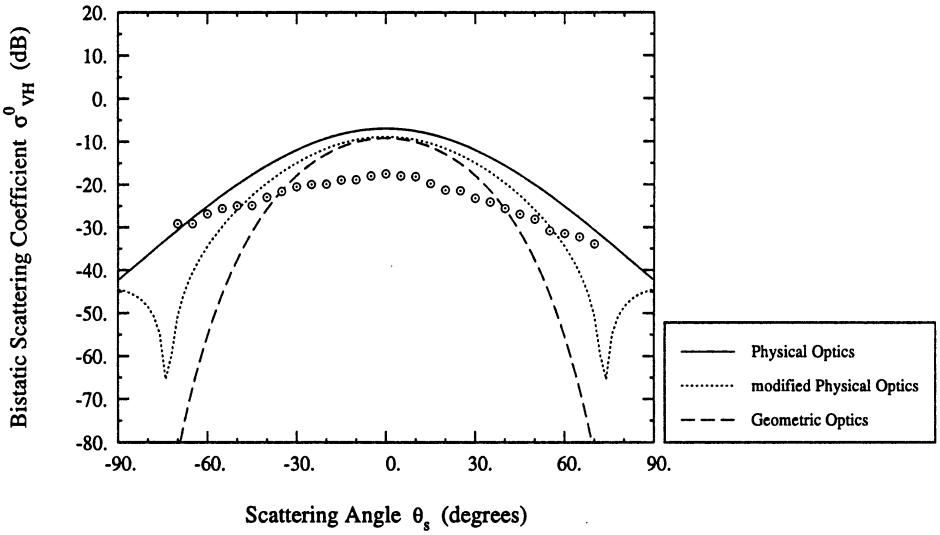

Figure 6.12: *vh*-polarized scattering in the $\phi_\Delta = 90°$ plane. The surface has a dielectric of $\varepsilon_r = 3.0 - j0.0$ and roughness parameters $k\sigma = 1.44$ and $kl = 11.5$. The transmitter was fixed at $\theta_i = 45°$. The circles represent measured data points; the curves are theoretical predictions. A power-law correlation was used, which best fit the profile data.

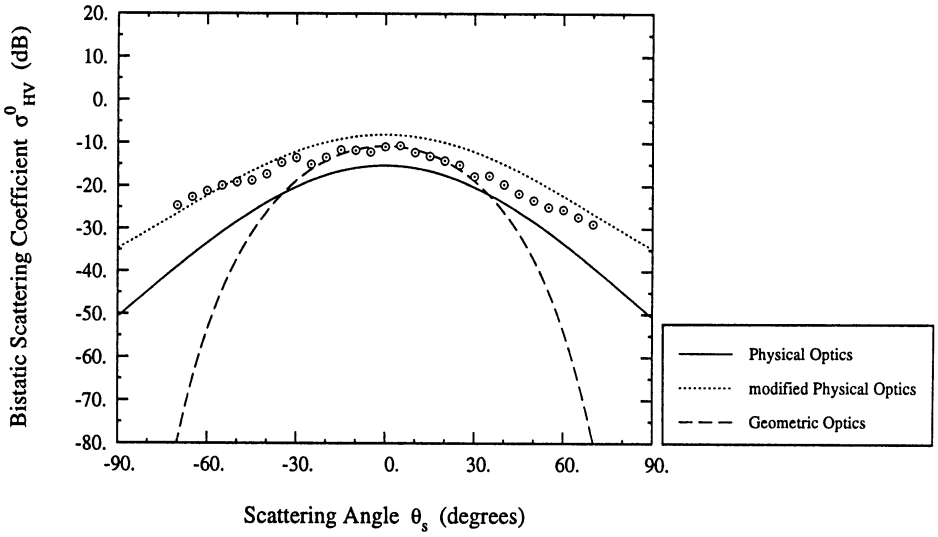

Figure 6.13: *hv*-polarized scattering in the $\phi_\Delta = 90°$ plane. The surface has a dielectric of $\varepsilon_r = 3.0 - j0.0$ and roughness parameters $k\sigma = 1.44$ and $kl = 11.5$. The transmitter was fixed at $\theta_i = 45°$. The circles represent measured data points; the curves are theoretical predictions. A power-law correlation was used, which best fit the profile data.

CHAPTER 7

An Application of Bistatic Surface Scattering: MIMICS model modification

7.1 Model Derivation

This chapter presents a redevelopment of the first order radiative transfer equations used to model forest and crop backscattering, in a software package known as the Michigan Microwave Canopy Scattering Model (MIMICS) [51]. In that package, the ground has been modeled as a specular surface, with ground backscatter and a specular ground-trunk interaction being the only interactions which were included. In the development to follow, the restriction that the ground surface below the forest be specular is lifted, a second-order scattering process involving specular scatter from the ground with trunks is derived, and the assumptions and errors introduced to achieve a tractable solution are explored.

7.1.1 Incorporation of a Rough Ground

As is done in [15], incorporation of a rough ground in the radiative transfer solution for scattering from vegetation involves replacing an otherwise specular surface reflection

coefficient with a rough surface operator, which consists of an integration over elevation and azimuthal angles of a coherent reflection coefficient and an incoherent scattering matrix:

$$\mathbf{R}(\mu) \rightarrow \int_0^1 \int_{2\pi} \left(\mathbf{R}_0(\mu')\delta(\mu-\mu')\delta(\phi-\phi') + \mathbf{G}(\mu,\phi;\mu',\phi')\right) d\phi' d\mu' \qquad (7.1)$$

or

$$\mathbf{R}(\mu_0) \rightarrow \int_0^1 \int_{2\pi} \left(\mathbf{R}_0(\mu_0)\delta(\mu'-\mu_0)\delta(\phi'-\phi_0) + \mathbf{G}(\mu',\phi';\mu_0,\phi_0)\right) d\phi' d\mu' \qquad (7.2)$$

where $\mathbf{R}_0$ is the coherent Mueller matrix for a rough surface (to be distinguished from the coherent Mueller matrix $\mathbf{R}$ for a smooth surface which is being replaced), $\delta(x'-x)$ is the Dirac delta function, and $\mathbf{G}$ is the bistatic incoherent Mueller matrix for the rough surface.

The first substitution involves integration over incident variables (when scattering from the ground is temporally after scattering from other objects) and the second involves integration over the scattering variables (when scattering from the ground temporally precedes scattering from other objects). Under this substitution, the bistatic MIMICS model becomes

$$\mathbf{I}_1^s(\mu,\phi) = \mathbf{T}\mathbf{I}_0 \qquad (7.3)$$

$$= \left(\mathbf{T}_0 + \mathbf{T}_{1g} + \mathbf{T}_{1rcr} + \mathbf{T}_{1cr} + \mathbf{T}_{1rc} + \mathbf{T}_{1c} + \mathbf{T}_{1tr} + \mathbf{T}_{2tg} + \mathbf{T}_{1rt} + \mathbf{T}_{2gt}\right)\mathbf{I}_0 \qquad (7.4)$$

$$\mathbf{T}_0 = e^{-\kappa_c^+ d/\mu}\mathbf{R}_0'(\mu)e^{-\kappa_c^- d/\mu_0}\delta(\mu-\mu_0)\delta(\phi-\phi_0) \tag{7.5}$$

$$\mathbf{T}_{1g} = e^{-\kappa_c^+ d/\mu}e^{-\kappa_t^+ H_t/\mu}\mathbf{G}(\mu,\phi;\mu_0,\phi_0)e^{-\kappa_t^- H_t/\mu_0}e^{-\kappa_c^- d/\mu_0} \tag{7.6}$$

$$\mathbf{T}_{1rcr} = \frac{1}{\mu}e^{-\kappa_c^+ d/\mu}\mathbf{R}_0'(\mu)\int_{-d}^{0} e^{-\kappa_c^-(z'+d)/\mu}\mathbf{P}_c(-\mu,\phi;\mu_0,\phi_0)e^{-\kappa_c^+(z'+d)/\mu_0}\mathbf{R}_0'(\mu_0)e^{-\kappa_c^- d/\mu_0}dz' \tag{7.7}$$

$$\mathbf{T}_{1cr} = \frac{1}{\mu}e^{-\kappa_c^+ d/\mu}\mathbf{R}_0'(\mu)\int_{-d}^{0} e^{-\kappa_c^-(z'+d)/\mu}\mathbf{P}_c(-\mu,\phi;-\mu_0,\phi_0)e^{\kappa_c^- z'/\mu_0}dz' \tag{7.8}$$

$$\mathbf{T}_{1rc} = \frac{1}{\mu}\int_{-d}^{0} e^{\kappa_c^+ z'/\mu}\mathbf{P}_c(\mu,\phi;\mu_0,\phi_0)e^{-\kappa_c^+(z'+d)/\mu_0}\mathbf{R}_0'(\mu_0)e^{-\kappa_c^- d/\mu_0}dz' \tag{7.9}$$

$$\mathbf{T}_{1c} = \frac{1}{\mu}\int_{-d}^{0} e^{\kappa_c^+ z'/\mu}\mathbf{P}_c(\mu,\phi;-\mu_0,\phi_0)e^{\kappa_c^- z'/\mu_0}dz' \tag{7.10}$$

$$\mathbf{T}_{1tr} = \frac{1}{\mu}e^{-\kappa_c^+ d/\mu}e^{-\kappa_t^+ H_t/\mu}\int_0^1\int_{2\pi}\mathbf{R}_0(\mu')\delta(\mu-\mu')\delta(\phi-\phi')\int_{-d'}^{-d} e^{-\kappa_t^-(z'+d')/\mu'}$$
$$\mathbf{P}_t(-\mu',\phi';-\mu_0,\phi_0)e^{\kappa_t^-(z'+d)/\mu_0}dz'd\phi'd\mu'e^{-\kappa_c^- d/\mu_0} \tag{7.11}$$

$$= \frac{1}{\mu}e^{-\kappa_c^+ d/\mu}e^{-\kappa_t^+ H_t/\mu}\mathbf{R}_0(\mu)\int_{-d'}^{-d} e^{-\kappa_t^-(z'+d')/\mu}\mathbf{P}_t(-\mu,\phi;-\mu_0,\phi_0)$$
$$e^{\kappa_t^-(z'+d)/\mu_0}dz'e^{-\kappa_c^- d/\mu_0} \tag{7.12}$$

$$\mathbf{T}_{2tg} = \frac{1}{\mu}e^{-\kappa_c^+ d/\mu}e^{-\kappa_t^+ H_t/\mu}\int_0^1\int_{2\pi}\mathbf{G}(\mu,\phi;\mu',\phi')\int_{-d'}^{-d} e^{-\kappa_t^-(z'+d')/\mu'}$$
$$\mathbf{P}_t(-\mu',\phi';-\mu_0,\phi_0)e^{\kappa_t^-(z'+d)/\mu_0}dz'd\phi'd\mu'e^{-\kappa_c^- d/\mu_0} \tag{7.13}$$

$$\mathbf{T}_{1rt} = \frac{1}{\mu}e^{-\kappa_c^+ d/\mu}\int_0^1\int_{2\pi}\int_{-d'}^{-d} e^{\kappa_t^+(z'+d)/\mu}\mathbf{P}_t(\mu,\phi;\mu',\phi')e^{-\kappa_t^+(z'+d')/\mu'}dz'$$
$$\mathbf{R}_0(\mu_0)\delta(\mu'-\mu_0)\delta(\phi'-\phi_0)d\phi'd\mu'e^{-\kappa_t^- H_t/\mu_0}e^{-\kappa_c^- d/\mu_0} \tag{7.14}$$

$$= \frac{1}{\mu}e^{-\kappa_c^+ d/\mu}\int_{-d'}^{-d} e^{\kappa_t^+(z'+d)/\mu}\mathbf{P}_t(\mu,\phi;\mu_0,\phi_0)e^{-\kappa_t^+(z'+d')/\mu_0}dz'$$
$$\mathbf{R}_0(\mu_0)e^{-\kappa_t^- H_t/\mu_0}e^{-\kappa_c^- d/\mu_0} \tag{7.15}$$

$$\mathbf{T}_{2gt} = \frac{1}{\mu}e^{-\kappa_c^+ d/\mu}\int_0^1\int_{2\pi}\int_{-d'}^{-d} e^{\kappa_t^+(z'+d)/\mu}\mathbf{P}_t(\mu,\phi;\mu',\phi')e^{-\kappa_t^+(z'+d')/\mu'}dz'$$
$$\mathbf{G}(\mu',\phi';\mu_0,\phi_0)d\phi'd\mu'e^{-\kappa_t^- H_t/\mu_0}e^{-\kappa_c^- d/\mu_0} \tag{7.16}$$

where

$$\mathbf{R}_0'(\mu) = e^{-\boldsymbol{\kappa}_t^+ H_t/\mu}\mathbf{R}_0(\mu)e^{-\boldsymbol{\kappa}_t^- H_t/\mu} \tag{7.17}$$

$\mathbf{T}_0$ represents the zeroth-order solution of the radiative transfer equation. Also known as **ds** in [51]. While this term can be mathematically included in the solution, the existence of the delta functions means that it must be treated separately from the rest: it essentially represents a coherent reflection coefficient. Like coherent reflectivity for bare rough surfaces, to convert it to the same units as the incoherent scattering (like a σ^0) requires knowledge of sensor parameters (like beamwidth, range, etc). For backscattering, this only becomes significant near nadir, at which point other problems also manifest themselves (apparently).

$\mathbf{T}_{1g}$ is a direct effect of making the surface in MIMICS rough. It does not appear in Appendix A of [51] but is considered separately (for backscattering) in Section 2 of [51], where it is called $\mathbf{T}_g$. It consists of the rough surface bistatic scattering as attenuated by the canopy and trunk layers.

$\mathbf{T}_{1rcr}$ describes energy which is coherently scattered by the ground, then incoherently scattered by the canopy, then coherently scattered by the ground again, before exiting the forest. Also known as **Term 1** in [51].

$\mathbf{T}_{1cr}$ describes energy which is incoherently scattered by the canopy, then coherently scattered by the ground, before exiting the forest. Also known as **Term 2a** in [51].

$\mathbf{T}_{1rc}$ describes energy which is coherently scattered by the ground, then incoherently scattered by the canopy, before exiting the forest. Also known as **Term 2b** in [51].

$\mathbf{T}_{1c}$ describes energy which is incoherently scattered by the canopy, before exiting the

forest. Also known as **Term 3** in [51].

The first-order terms involving canopy scattering do not involve incoherent scattering by the ground because that is a second-order (or higher) effect.

$\mathbf{T}_{2tg}$ and $\mathbf{T}_{1tr}$ describe energy which is scattered by the trunks to the ground before exiting the forest. $\mathbf{T}_{1tr}$ involves incoherent scattering by the tree trunks and coherent scattering by the ground while $\mathbf{T}_{2tg}$ is really a second order effect, as evidenced by the remaining integrations over μ' and ϕ'. However, these integrations can often be approximated analytically making this term no more computationally intensive than any first-order term.

$\mathbf{T}_{1tr}$ is also known as **Term 4a** in [51].

$\mathbf{T}_{2tg}$ is a new contribution due to the inclusion of the incoherent rough surface scattering in the first order solution. The triple integral over z', μ' and ϕ' is analytic for some combinations of rough surface models, trunk extinction coefficients, and trunk Mueller matrices.

$\mathbf{T}_{1rt}$ is known as **Term 4b** in [51].

$\mathbf{T}_{2gt}$ is another new term.

7.1.2 Integration over Canopy Depth z'

The integration over canopy depth z' is straightforward and follows exactly that in [51]:

$$\mathbf{T}_{1rcr} = \frac{1}{\mu} e^{-\kappa_c^+ d/\mu} \mathbf{R}_0'(\mu) \mathbf{Q}_c(-\mu, \phi) \mathbf{A}_{rcr}(\mu, \phi; \mu_0, \phi_0) \mathbf{Q}_c^{-1}(\mu_0, \phi_0) \mathbf{R}_0'(\mu_0) e^{-\kappa_c^- d/\mu_0} \tag{7.18}$$

$$\mathbf{T}_{1cr} = \frac{1}{\mu} e^{-\kappa_c^+ d/\mu} \mathbf{R}_0'(\mu) \mathbf{Q}_c(-\mu, \phi) \mathbf{A}_{cr}(\mu, \phi; \mu_0, \phi_0) \mathbf{Q}_c^{-1}(-\mu_0, \phi_0) \tag{7.19}$$

$$\mathbf{T}_{1rc} = \frac{1}{\mu} \mathbf{Q}_c(\mu, \phi) \mathbf{A}_{rc}(\mu, \phi; \mu_0, \phi_0) \mathbf{Q}_c^{-1}(\mu_0, \phi_0) \mathbf{R}_0'(\mu_0) e^{-\kappa_c^- d/\mu_0} \tag{7.20}$$

$$\mathbf{T}_{1c} = \frac{1}{\mu} \mathbf{Q}_c(\mu, \phi) \mathbf{A}_c(\mu, \phi; \mu_0, \phi_0) \mathbf{Q}_c^{-1}(-\mu_0, \phi_0) \tag{7.21}$$

$$\mathbf{T}_{1tr} = \frac{1}{\mu} e^{-\kappa_c^+ d/\mu} e^{-\kappa_t^+ H_t/\mu} \mathbf{R}_0(\mu) \mathbf{Q}_t(-\mu, \phi) \mathbf{A}_{tr}(\mu, \phi; \mu_0, \phi_0) \mathbf{Q}_t^{-1}(-\mu_0, \phi_0) e^{-\kappa_c^- d/\mu_0} \tag{7.22}$$

$$\mathbf{T}_{2tg} = \frac{1}{\mu} e^{-\kappa_c^+ d/\mu} e^{-\kappa_t^+ H_t/\mu} \int_0^1 \int_{2\pi} \mathbf{G}(\mu, \phi; \mu', \phi') \mathbf{Q}_t(-\mu', \phi') \mathbf{A}_{tr}(\mu', \phi'; \mu_0, \phi_0) d\phi' d\mu'$$
$$\mathbf{Q}_t^{-1}(-\mu_0, \phi_0) e^{-\kappa_c^- d/\mu_0} \tag{7.23}$$

$$\mathbf{T}_{1rt} = \frac{1}{\mu} e^{-\kappa_c^+ d/\mu} \mathbf{Q}_t(\mu, \phi) \mathbf{A}_{rt}(\mu, \phi; \mu_0, \phi_0) \mathbf{Q}_t^{-1}(\mu_0, \phi_0) \mathbf{R}_0(\mu_0) e^{-\kappa_t^- H_t/\mu_0} e^{-\kappa_c^- d/\mu_0} \tag{7.24}$$

$$\mathbf{T}_{2gt} = \frac{1}{\mu} e^{-\kappa_c^+ d/\mu} \int_0^1 \int_{2\pi} \mathbf{Q}_t(\mu, \phi) \mathbf{A}_{rt}(\mu, \phi; \mu', \phi') \mathbf{Q}_t^{-1}(\mu', \phi') \mathbf{G}(\mu', \phi'; \mu_0, \phi_0) d\phi' d\mu'$$
$$e^{-\kappa_t^- H_t/\mu_0} e^{-\kappa_c^- d/\mu_0} \tag{7.25}$$

where the extinction terms have been expanded as

$$e^{-\kappa_c z/\mu} = \mathbf{Q}_c(\mu, \phi) \mathbf{D}_c(\mu, \phi; -z/\mu) \mathbf{Q}_c^{-1}(\mu, \phi) \tag{7.26}$$

$$[\mathbf{D}_c(\mu, \phi; -z/\mu)]_{ij} = e^{-\lambda_i(\mu,\phi) z/\mu} \delta_{ij} \tag{7.27}$$

and $\mathbf{Q}$ is a matrix for which the i^{th} column is the i^{th} eigenvector of $\boldsymbol{\kappa}$ and λ_i is the i^{th} eigenvalue of $\boldsymbol{\kappa}$. Also, the $\mathbf{A}$'s are of the form:

$$\mathbf{A}(\mu_s,\phi_s;\mu_i,\phi_i) = \int \mathbf{D}(\pm\mu_s,\phi_s;\pm(z'+\{d,d',0\})/\mu_s)\mathbf{Q}^{-1}(\pm\mu_s,\phi_s)\mathbf{P}(\pm\mu_s,\phi_s;\pm\mu_i,\phi_i)$$
$$\mathbf{Q}(\pm\mu_i,\phi_i)\mathbf{D}(\pm\mu_i,\phi_i;\pm(z'+\{d,d',0\})/\mu_i)dz' \tag{7.28}$$

$$[\mathbf{A}(\mu_s,\phi_s;\mu_i,\phi_i)]_{ij} = f(\pm\lambda_i(\pm\mu_s,\phi_s)/\mu_s,\pm\lambda_j(\pm\mu_i,\phi_i)/\mu_i,\{d,H_t\})$$
$$\left[\mathbf{Q}^{-1}(\pm\mu_s,\phi_s)\mathbf{P}(\pm\mu_s,\phi_s;\pm\mu_i,\phi_i)\mathbf{Q}(\pm\mu_i,\phi_i)\right]_{ij} \tag{7.29}$$

See [51] for the explicit expressions of the $\mathbf{A}$'s.

7.1.3 Integration over Elevation μ' in $\mathbf{T}_{2tg}$ and $\mathbf{T}_{2gt}$

The two new terms, namely $\mathbf{T}_{2gt}$ and $\mathbf{T}_{2tg}$, depend on $\mathbf{P}_t(\mu_s,\phi_s;\mu_i,\phi_i)$ in such a way that they can be approximated as a pair of first-order terms. This is because the form of the trunk phase matrix is as follows ([51], appendix C):

$$\begin{aligned}\mathbf{P}_t(\mu_s,\phi_s;\mu_i,\phi_i) &= \mathbf{P}'_t(\mu_s,\mu_i,\phi_\Delta)\frac{N_tH_t}{\pi}\text{sinc}^2\left(\frac{H_t}{\lambda}(\mu_i-\mu_s)\right)\\ &\approx \mathbf{P}'_t(\mu_s,\mu_i,\phi_\Delta)\frac{N_t\lambda}{\pi}\delta(\mu_i-\mu_s)\end{aligned} \tag{7.30}$$

or, equivalently,

$$\begin{aligned}\mathbf{A}_{rt}(\mu_s,\phi_s;\mu_i,\phi_i) &= \mathbf{A}'_{rt}(\mu_s,\phi_s;\mu_i,\phi_i)\frac{N_tH_t}{\pi}\text{sinc}^2\left(\frac{H_t}{\lambda}(\mu_i-\mu_s)\right)\\ &\approx \mathbf{A}'_{rt}(\mu_s,\phi_s;\mu_i,\phi_i)\frac{N_t\lambda}{\pi}\delta(\mu_i-\mu_s)\end{aligned} \tag{7.31}$$

where N_t is the number density of trunks per square meter, H_t is the height of the trunk layer, and

$$\mathrm{sinc}(x) = \frac{\sin \pi x}{\pi x} \tag{7.32}$$

$$\phi_\Delta = \phi_s - \phi_i \tag{7.33}$$

Then the integration over μ' may take place as follows:

$$\begin{aligned}\mathbf{T}_{2gt} &= \frac{N_t H_t}{\pi\mu} e^{-\kappa_c^+ d/\mu} \mathbf{Q}_t(\mu,\phi) \int_0^1 \int_{2\pi} \mathbf{A}'_{rt}(\mu,\phi;\mu',\phi') \mathbf{Q}_t^{-1}(\mu',\phi') \mathrm{sinc}^2\left(\frac{H_t}{\lambda}(\mu-\mu')\right) \\ &\quad \mathbf{G}(\mu',\phi';\mu_0,\phi_0) d\phi' d\mu' e^{-\kappa_t^- H_t/\mu_0} e^{-\kappa_c^- d/\mu_0} \qquad (7.34) \\ &\approx \frac{N_t \lambda}{\pi\mu} e^{-\kappa_c^+ d/\mu} \mathbf{Q}_t(\mu,\phi) \int_{2\pi} \mathbf{A}'_{rt}(\mu,\phi;\mu,\phi') \mathbf{Q}_t^{-1}(\mu,\phi') \mathbf{G}(\mu,\phi';\mu_0,\phi_0) d\phi' \\ &\quad e^{-\kappa_t^- H_t/\mu_0} e^{-\kappa_c^- d/\mu_0} \qquad (7.35)\end{aligned}$$

The error in approximating the double sinc function as a Dirac delta function is shown in Figure 7.1. The error $\varepsilon_{\mathrm{sinc}}$, defined as

$$\varepsilon_{\mathrm{sinc}} = \left| 1 - \int_0^1 \mathrm{sinc}^2\left(\frac{H_t}{\lambda}(\mu-\mu')\right) d\mu' \right| \tag{7.36}$$

is shown as a function of H_t/λ for several values of μ. Note that $\varepsilon_{\mathrm{sinc}}(1-\mu) = \varepsilon_{\mathrm{sinc}}(\mu)$.

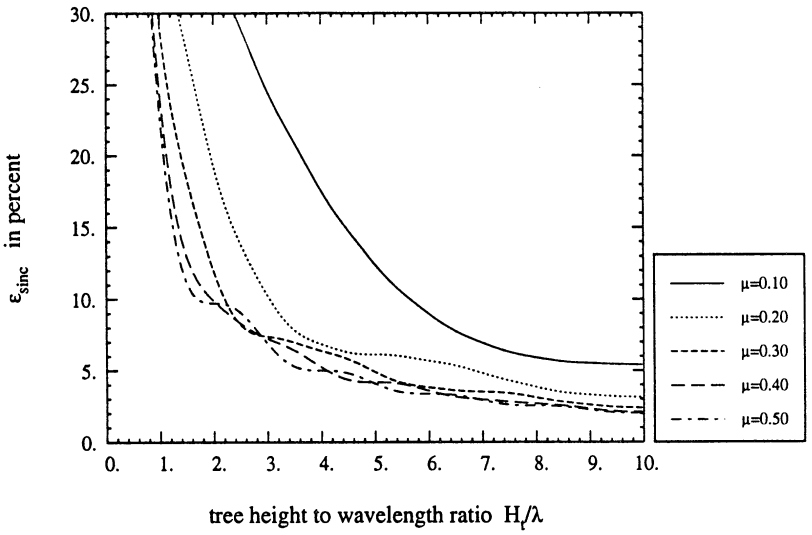

Figure 7.1: Error in approximating the sinc-squared function as a Dirac delta function. The error for $1-\mu$ is the same as for μ. The error is less than 10% for all trunk heights greater than 4 wavelengths and incidence angles between 36° and 78°.

7.1.4 Integration over Azimuth ϕ'

Because the expressions for the phase matrix of the trunk layer are azimuthally isotropic, it can be shown that the extinction coefficients are also azimuthally isotropic:

$$\mathbf{Q}_t(\mu,\phi) = \mathbf{Q}_t(\mu) \tag{7.37}$$

Scattering in the trunk layer can be expressed as a Fourier series:

$$\mathbf{A}'_{rt}(\mu_s,\phi_s;\mu_i,\phi_i) = \mathbf{A}'_{rt}(\mu_s,\mu_i,\phi_\Delta) \tag{7.38}$$

$$= \sum_{k=0}^{\infty} \left[\tilde{\mathbf{A}}^c_{rt}(\mu_s,\mu_i;k)\cos k\phi_\Delta + \tilde{\mathbf{A}}^s_{rt}(\mu_s,\mu_i;k)\sin k\phi_\Delta\right] \tag{7.39}$$

where

$$\tilde{\mathbf{A}}^c_{rt}(\mu_s,\mu_i;k=0) = \frac{1}{2\pi}\int_{2\pi}\mathbf{A}'_{rt}(\mu_s,\mu_i,\phi)d\phi \tag{7.40}$$

$$\tilde{\mathbf{A}}^c_{rt}(\mu_s,\mu_i;k>0) = \frac{1}{\pi}\int_{2\pi}\mathbf{A}'_{rt}(\mu_s,\mu_i,\phi)\cos k\phi d\phi \tag{7.41}$$

$$\tilde{\mathbf{A}}^s_{rt}(\mu_s,\mu_i;k=0) = 0 \tag{7.42}$$

$$\tilde{\mathbf{A}}^s_{rt}(\mu_s,\mu_i;k>0) = \frac{1}{\pi}\int_{2\pi}\mathbf{A}'_{rt}(\mu_s,\mu_i,\phi)\sin k\phi d\phi \tag{7.43}$$

Similarly, if the rough ground is also azimuthally isotropic, then it can also be expressed as a Fourier series:

$$\mathbf{G}(\mu_s,\phi_s;\mu_i,\phi_i) = \mathbf{G}(\mu_s,\mu_i,\phi_\Delta) \tag{7.44}$$

$$= \sum_{k=0}^{\infty}\left[\tilde{\mathbf{G}}^c(\mu_s,\mu_i;k)\cos k\phi_\Delta + \tilde{\mathbf{G}}^s(\mu_s,\mu_i;k)\sin k\phi_\Delta\right] \tag{7.45}$$

where

$$\tilde{\mathbf{G}}^c(\mu_s,\mu_i;k=0) = \frac{1}{2\pi}\int_{2\pi}\mathbf{G}(\mu_s,\mu_i,\phi)d\phi \tag{7.46}$$

$$\tilde{\mathbf{G}}^c(\mu_s,\mu_i;k>0) = \frac{1}{\pi}\int_{2\pi}\mathbf{G}(\mu_s,\mu_i,\phi)\cos k\phi d\phi \tag{7.47}$$

$$\tilde{\mathbf{G}}^s(\mu_s,\mu_i;k=0) = 0 \tag{7.48}$$

$$\tilde{\mathbf{G}}^s(\mu_s,\mu_i;k>0) = \frac{1}{\pi}\int_{2\pi}\mathbf{G}(\mu_s,\mu_i,\phi)\sin k\phi d\phi \tag{7.49}$$

Using the orthogonality of the sine and cosine functions, namely, that

$$\int_{2\pi} \cos m(\phi-\phi')\cos n(\phi'-\phi_0)d\phi' = \pi\cos m(\phi-\phi_0)\delta_{mn}(1+\delta_{m0}) \quad (7.50)$$

$$\int_{2\pi} \sin m(\phi-\phi')\sin n(\phi'-\phi_0)d\phi' = -\pi\cos m(\phi-\phi_0)\delta_{mn}(1-\delta_{m0}) \quad (7.51)$$

$$\int_{2\pi} \cos m(\phi-\phi')\sin n(\phi'-\phi_0)d\phi' =$$

$$\int_{2\pi} \sin m(\phi-\phi')\cos n(\phi'-\phi_0)d\phi' = \pi\sin m(\phi-\phi_0)\delta_{mn} \quad (7.52)$$

where δ_{mn} is the Kronecker delta function: $\delta_{mn} = 1$ if $m = n$ and $\delta_{mn} = 0$ if $m \neq n$. The equations involving the trunks then simplify to:

$$\mathbf{T}_{1tr} = \frac{1}{\mu} e^{-\kappa_c^+ d/\mu} e^{-\kappa_t^+ H_t/\mu} \mathbf{R}_0(\mu)\mathbf{Q}_t(-\mu)\mathbf{A}_{tr}(\mu,\mu_0,\phi-\phi_0)\mathbf{Q}_t^{-1}(-\mu_0)e^{-\kappa_c^- d/\mu_0} \quad (7.53)$$

$$\begin{aligned}\mathbf{T}_{2tg} = &\frac{N_t\lambda}{\mu} e^{-\kappa_c^+ d/\mu} e^{-\kappa_t^- H_t/\mu_0}[2\tilde{\mathbf{G}}^c(\mu,\mu_0;0)\mathbf{Q}_t(-\mu_0)\tilde{\mathbf{A}}_{tr}^c(\mu_0,\mu_0;0) \\ &+ \sum_{k=1}^{\infty}[(\tilde{\mathbf{G}}^c(\mu,\mu_0;k)\mathbf{Q}_t(-\mu_0)\tilde{\mathbf{A}}_{tr}^c(\mu_0,\mu_0;k) \\ &- \tilde{\mathbf{G}}^s(\mu,\mu_0;k)\mathbf{Q}_t(-\mu_0)\tilde{\mathbf{A}}_{tr}^s(\mu_0,\mu_0;k))\cos k(\phi-\phi_0) \\ &+ (\tilde{\mathbf{G}}^c(\mu,\mu_0;k)\mathbf{Q}_t(-\mu_0)\tilde{\mathbf{A}}_{tr}^s(\mu_0,\mu_0;k) \\ &+ \tilde{\mathbf{G}}^s(\mu,\mu_0;k)\mathbf{Q}_t(-\mu_0)\tilde{\mathbf{A}}_{tr}^c(\mu_0,\mu_0;k))\sin k(\phi-\phi_0)]] \\ &\mathbf{Q}_t^{-1}(-\mu_0)e^{-\kappa_c^- d/\mu_0}\end{aligned} \quad (7.54)$$

$$\mathbf{T}_{1rt} = \frac{1}{\mu} e^{-\kappa_c^+ d/\mu} \mathbf{Q}_t(\mu) \mathbf{A}_{rt}(\mu, \mu_0, \phi - \phi_0) \mathbf{Q}_t^{-1}(\mu_0) \mathbf{R}_0(\mu_0) e^{-\kappa_t^- H_t/\mu_0} e^{-\kappa_c^- d/\mu_0} \tag{7.55}$$

$$\begin{aligned}\mathbf{T}_{2gt} = & \frac{N_t \lambda}{\mu} e^{-\kappa_c^+ d/\mu} \mathbf{Q}_t(\mu) [2\tilde{\mathbf{A}}_{rt}^c(\mu, \mu; 0) \mathbf{Q}_t^{-1}(\mu) \tilde{\mathbf{G}}^c(\mu, \mu_0; 0) \\ & + \sum_{k=1}^{\infty} [(\tilde{\mathbf{A}}_{rt}^c(\mu, \mu; k) \mathbf{Q}_t^{-1}(\mu) \tilde{\mathbf{G}}^c(\mu, \mu_0; k) - \tilde{\mathbf{A}}_{rt}^s(\mu, \mu; k) \mathbf{Q}_t^{-1}(\mu) \tilde{\mathbf{G}}^s(\mu, \mu_0; k)) \cos k(\phi - \phi_0) \\ & + (\tilde{\mathbf{A}}_{rt}^c(\mu, \mu; k) \mathbf{Q}_t^{-1}(\mu) \tilde{\mathbf{G}}^s(\mu, \mu_0; k) + \tilde{\mathbf{A}}_{rt}^s(\mu, \mu; k) \mathbf{Q}_t^{-1}(\mu) \tilde{\mathbf{G}}^c(\mu, \mu_0; k)) \sin k(\phi - \phi_0)]] \\ & e^{-\kappa_t^- H_t/\mu_0} e^{-\kappa_c^- d/\mu_0}\end{aligned} \tag{7.56}$$

7.1.5 Reduction to Backscattering

For backscattering, $\mu = \mu_0$ and $\phi - \phi_0 = \pi$. Substituting these values into the expressions above yields:

$$\mathbf{T}_0 = 0 \tag{7.57}$$

$$\mathbf{T}_{1g} = e^{-\kappa_c^+ d/\mu_0} e^{-\kappa_t^+ H_t/\mu_0} \mathbf{G}(\mu_0, \mu_0, \pi) e^{-\kappa_t^- H_t/\mu_0} e^{-\kappa_c^- d/\mu_0} \tag{7.58}$$

$$\begin{aligned}\mathbf{T}_{1rcr} = & \frac{1}{\mu_0} e^{-\kappa_c^+ d/\mu_0} \mathbf{R}_0'(\mu_0) \mathbf{Q}_c(-\mu_0, \phi_0 + \pi) \mathbf{A}_{rcr}(\mu_0, \phi_0 + \pi; \mu_0, \phi_0) \mathbf{Q}_c^{-1}(\mu_0, \phi_0) \\ & \mathbf{R}_0'(\mu_0) e^{-\kappa_c^- d/\mu_0}\end{aligned} \tag{7.59}$$

$$\mathbf{T}_{1cr} = \frac{1}{\mu_0} e^{-\kappa_c^+ d/\mu_0} \mathbf{R}_0'(\mu_0) \mathbf{Q}_c(-\mu_0, \phi_0 + \pi) \mathbf{A}_{cr}(\mu_0, \phi_0 + \pi; \mu_0, \phi_0) \mathbf{Q}_c^{-1}(-\mu_0, \phi_0) \tag{7.60}$$

$$\mathbf{T}_{1rc} = \frac{1}{\mu_0} \mathbf{Q}_c(\mu_0, \phi_0 + \pi) \mathbf{A}_{rc}(\mu_0, \phi_0 + \pi; \mu_0, \phi_0) \mathbf{Q}_c^{-1}(\mu_0, \phi_0) \mathbf{R}_0'(\mu_0) e^{-\kappa_c^- d/\mu_0} \tag{7.61}$$

$$\mathbf{T}_{1c} = \frac{1}{\mu_0} \mathbf{Q}_c(\mu_0, \phi_0 + \pi) \mathbf{A}_c(\mu_0, \phi_0 + \pi; \mu_0, \phi_0) \mathbf{Q}_c^{-1}(-\mu_0, \phi_0) \tag{7.62}$$

$$\mathbf{T}_{1tr} = \frac{1}{\mu_0} e^{-\kappa_c^+ d/\mu_0} e^{-\kappa_t^+ H_t/\mu_0} \mathbf{R}_0(\mu_0)\mathbf{Q}_t(-\mu_0)\mathbf{A}_{tr}(\mu_0,\mu_0,\pi)\mathbf{Q}_t^{-1}(-\mu_0) e^{-\kappa_c^- d/\mu_0} \tag{7.63}$$

$$= \frac{N_t H_t}{\pi\mu_0} e^{-\kappa_c^+ d/\mu_0} e^{-\kappa_t^+ H_t/\mu_0} \mathbf{R}_0(\mu_0)\mathbf{Q}_t(-\mu_0)\mathbf{A}'_{tr}(\mu_0,\mu_0,\pi)\mathbf{Q}_t^{-1}(-\mu_0) e^{-\kappa_c^- d/\mu_0} \tag{7.64}$$

$$\begin{aligned}\mathbf{T}_{2tg} = &\frac{N_t\lambda}{\mu_0} e^{-\kappa_c^+ d/\mu_0} e^{-\kappa_t^+ H_t/\mu_0} [2\tilde{\mathbf{G}}^c(\mu_0,\mu_0;0)\mathbf{Q}_t(-\mu_0)\tilde{\mathbf{A}}^c_{tr}(\mu_0,\mu_0;0) \\ &+ \sum_{k=1}^{\infty}(-1)^k[\tilde{\mathbf{G}}^c(\mu_0,\mu_0;k)\mathbf{Q}_t(-\mu_0)\tilde{\mathbf{A}}^c_{tr}(\mu_0,\mu_0;k) \\ &- \tilde{\mathbf{G}}^s(\mu_0,\mu_0;k)\mathbf{Q}_t(-\mu_0)\tilde{\mathbf{A}}^s_{tr}(\mu_0,\mu_0;k)]]\mathbf{Q}_t^{-1}(-\mu_0) e^{-\kappa_c^- d/\mu_0}\end{aligned} \tag{7.65}$$

$$\mathbf{T}_{1rt} = \frac{1}{\mu_0} e^{-\kappa_c^+ d/\mu_0}\mathbf{Q}_t(\mu_0)\mathbf{A}_{rt}(\mu_0,\mu_0,\pi)\mathbf{Q}_t^{-1}(\mu_0)\mathbf{R}_0(\mu_0) e^{-\kappa_t^- H_t/\mu_0} e^{-\kappa_c^- d/\mu_0} \tag{7.66}$$

$$= \frac{N_t H_t}{\pi\mu_0} e^{-\kappa_c^+ d/\mu_0}\mathbf{Q}_t(\mu_0)\mathbf{A}'_{rt}(\mu_0,\mu_0,\pi)\mathbf{Q}_t^{-1}(\mu_0)\mathbf{R}_0(\mu_0) e^{-\kappa_t^- H_t/\mu_0} e^{-\kappa_c^- d/\mu_0} \tag{7.67}$$

$$\begin{aligned}\mathbf{T}_{2gt} = &\frac{N_t\lambda}{\mu_0} e^{-\kappa_c^+ d/\mu_0}\mathbf{Q}_t(\mu_0)[2\tilde{\mathbf{A}}^c_{rt}(\mu_0,\mu_0;0)\mathbf{Q}_t^{-1}(\mu_0)\tilde{\mathbf{G}}^c(\mu_0,\mu_0;0) \\ &+ \sum_{k=1}^{\infty}(-1)^k[\tilde{\mathbf{A}}^c_{rt}(\mu_0,\mu_0;k)\mathbf{Q}_t^{-1}(\mu_0)\tilde{\mathbf{G}}^c(\mu_0,\mu_0;k) \\ &- \tilde{\mathbf{A}}^s_{rt}(\mu_0,\mu_0;k)\mathbf{Q}_t^{-1}(\mu_0)\tilde{\mathbf{G}}^s(\mu_0,\mu_0;k)]] e^{-\kappa_t^- H_t/\mu_0} e^{-\kappa_c^- d/\mu_0}\end{aligned} \tag{7.68}$$

Thus, the second order terms involving incoherent bistatic scattering from the ground and scattering by trunks can be analytically derived as an infinite series of Fourier terms, making it little more computationally involved than are the first order terms.

The expressions for the Fourier decomposition of the trunk scattering matrices are given in Section B.1 and for the rough surfaces in Section B.2

7.2 Example: Trunks over a Physical Optics Ground

As an example of the effect of the incorporation of the rough ground on the scattering from a forest, let us examine a realistic example which is also simple enough to analyze. Let us assume that the forest is composed of trees which do not have a significant number of primary or secondary branches which would attenuate or scatter the microwaves. Since the canopy is not a part of the problem we are addressing, let us further assume the forest is deciduous and the observation is during the winter months when no leaves are on the trees. Under these circumstances, the canopy is absent, and we can set $\mathbf{T}_{1rcr} = \mathbf{T}_{1cr} = \mathbf{T}_{1rc} = \mathbf{T}_{1c} = 0$ as well as $e^{-\kappa_c^{\pm} d/\mu_0} = 1$.

Furthermore, if scattering from the surface can be described by the Physical Optics model with a Gaussian correlation function and a correlation length that is large such that $\frac{1}{2}(k_0 l)^2(1-\mu_0^2) \gg i$ for the first several i in the summation of $\Phi_k(k_0\sigma, k_0 l, \mu_0)$, then we can employ the large argument approximation for $I_k(x)$, namely: $I_k(x) \rightarrow \frac{e^x}{\sqrt{2\pi x}}$ and

$$\Phi(k_0\sigma, k_0 l, \mu_0) = \lim_{k_0 l \rightarrow \infty} \Phi_k^{Gaussian}(k_0\sigma, k_0 l, \mu_0, \mu_0) \tag{7.69}$$

$$= \frac{1}{16\pi\sqrt{\pi}\mu_0} \frac{k_0 l}{\sqrt{1-\mu_0^2}} \sum_{i=1}^{\infty} \frac{(2k_0\sigma\mu_0)^{2i}}{i!\sqrt{i}} \tag{7.70}$$

which is independent of the azimuth Fourier index k. Then, the Physical Optics expressions

for the Fourier series components of the incoherent Mueller matrices simplify to:

$$2\tilde{\mathbf{G}}^c(\mu_0,\mu_0;k=0)=\tilde{\mathbf{G}}^c(\mu_0,\mu_0;k>0)=8\mu_0^2\mathbf{R}_{0PO}(\mu_0)\Phi(k_0\sigma,k_0l,\mu_0) \tag{7.71}$$

$$\tilde{\mathbf{G}}^s(\mu_0,\mu_0;k)\approx 0 \tag{7.72}$$

where

$$\mathbf{R}_{0PO}(\mu_0)=e^{-4(k_0\sigma\mu_0)^2}\begin{bmatrix} |R_v|^2 & 0 & 0 & 0 \\ 0 & |R_h|^2 & 0 & 0 \\ 0 & 0 & \Re e\{R_vR_h^*\} & -\Im m\{R_vR_h^*\} \\ 0 & 0 & \Im m\{R_vR_h^*\} & \Re e\{R_vR_h^*\} \end{bmatrix} \tag{7.73}$$

Then the relevant terms in the radiative transfer solution for backscattering become:

$$\mathbf{T}_{1tr} = \frac{N_tH_t}{\pi\mu_0}e^{-\kappa_t^+H_t/\mu_0}\mathbf{R}_{0PO}(\mu_0)\mathbf{Q}_t(-\mu_0)\mathbf{A}'_{tr}(\mu_0,\mu_0,\pi)\mathbf{Q}_t^{-1}(-\mu_0) \tag{7.74}$$

$$\mathbf{T}_{2tg} = \mathbf{T}_{1tr}\sqrt{\pi}\frac{l}{H_t}\frac{\mu_0}{\sqrt{1-\mu_0^2}}\sum_{i=1}^{\infty}\frac{(2k_0\sigma\mu_0)^{2i}}{i!\sqrt{i}} \tag{7.75}$$

$$\mathbf{T}_{1rt} = \frac{N_tH_t}{\pi\mu_0}\mathbf{Q}_t(\mu_0)\mathbf{A}'_{rt}(\mu_0,\mu_0,\pi)\mathbf{Q}_t^{-1}(\mu_0)\mathbf{R}_{0PO}(\mu_0)e^{-\kappa_t^-H_t/\mu_0} \tag{7.76}$$

$$\mathbf{T}_{2gt} = \mathbf{T}_{1rt}\sqrt{\pi}\frac{l}{H_t}\frac{\mu_0}{\sqrt{1-\mu_0^2}}\sum_{i=1}^{\infty}\frac{(2k_0\sigma\mu_0)^{2i}}{i!\sqrt{i}} \tag{7.77}$$

$$\mathbf{T}_{1g} = e^{-\kappa_t^+H_t/\mu}\mathbf{G}(\mu_0,\mu_0,\pi)e^{-\kappa_t^-H_t/\mu_0} \tag{7.78}$$

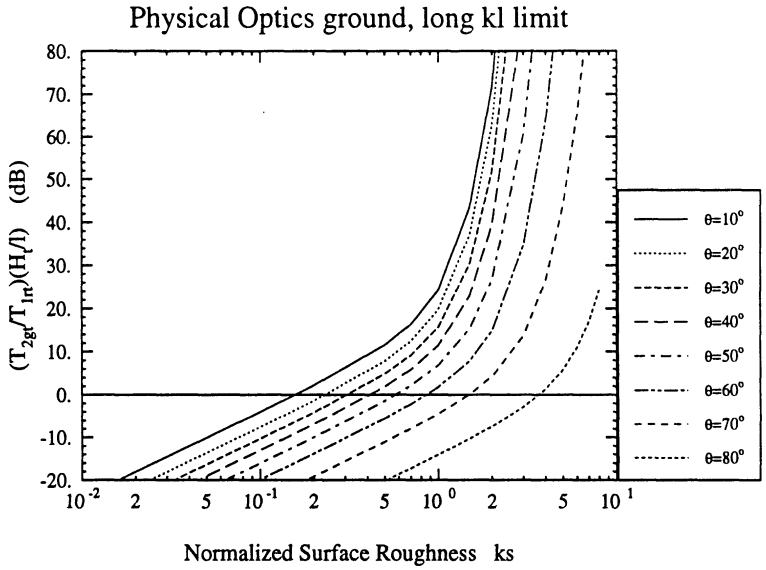

Figure 7.2: Ratio of the second order ground-trunk scattering (incoherent) to the first order ground-trunk scattering (coherent), times the ratio of the trunk height to correlation length, as a function of surface roughness and for several angles of incidence. This is the limiting case for all polarizations for Physical Optics with a long correlation length.

7.3 Significance of Including Ground Roughness

The development of the radiative transfer equation for a set of trunks over a rough ground, while imperfect, has two significances in backscattering models. For co-polarized backscatter, the inclusion of roughness decreases the coherent energy scattered by the ground and off the trunks (and *vice versa*), and includes a new source from bistatic scattering in a cone around each trunk. Under different conditions, direct backscatter from the ground, or the coherent ground-trunk interaction, or the incoherent ground-trunk interaction can dominate the backscattering from a scene. In Figure 7.3, the model shows that the direct backscattering from a rough ground is never significant in a young aspen stand, but depending on the rms surface height, the backscattering can be dominated by the coherent specular ground–

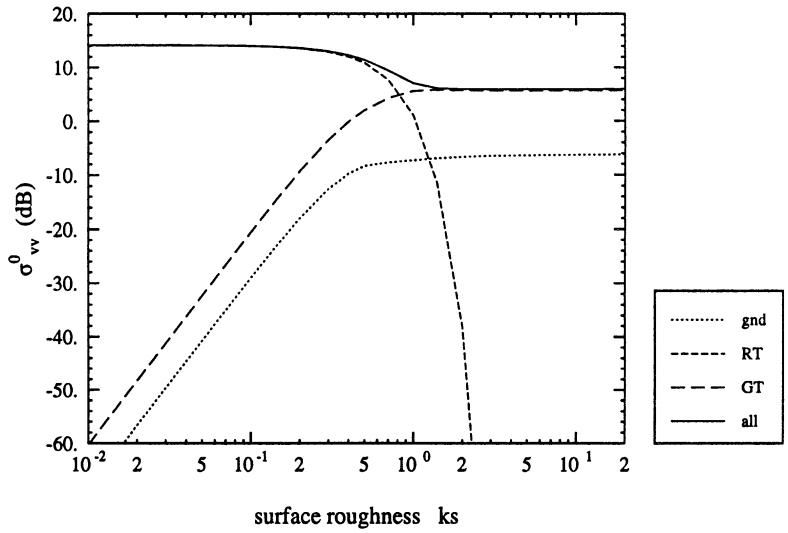

Figure 7.3: Dependence of select terms of forest backscatter on surface rms height. The total *vv*-polarized backscatter from a young aspen stand is dependent on the surface roughness. The dotted curve (marked gnd) represents direct backscatter from the rough ground, the short dashed curve (marked RT) indicates a coherent ground–trunk interaction, the long dashed curve (marked GT) indicates an incoherent bistatic ground–trunk interaction, and the solid curve (marked all) gives the sum of all these contributions. The backscattering angle is $\theta_i = 30°$; and the radar frequency is at L-band ($\lambda = 0.2$ m). At this frequency the aspen trunks have a dielectric of $\varepsilon_{trunk} = 62.3 - j24.3$ and the ground dielectric is $\varepsilon_{gnd} = 13.0 - j2.0$. The trunks are 0.44 m high; the trunk diameter is $ka = 0.4$ and the stalk density $N_t = 6.5$ stalks per square meter.

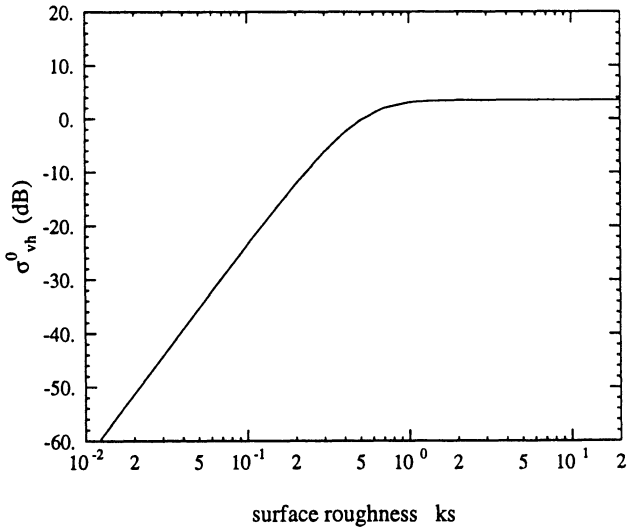

Figure 7.4: Dependence of cross-polarized forest backscatter on surface rms height. Shown is the total *vh*-polarized backscatter from the same young aspen stand in the previous figure. All of the cross-polarized scattering is from the incoherent bistatic ground–trunk interaction. Both direct ground backscatter and the coherent ground–trunk interaction are negligible for cross-polarization.

vertical trunk corner reflector structure, if the surface is sufficiently smooth, or be dominated by a surface bistatic scattering interaction with the trunks, if the surface is sufficiently rough. The overall level of scattering from the scene is different for these two cases. As a function of the normalized rms surface height $k\sigma$, the backscattering from the scene as a whole has one particular constant value for $k\sigma < \frac{1}{2}$, where the coherent specular ground–trunk mechanism dominates, and a different but constant value for $k\sigma > 1$, where the incoherent bistatic ground–trunk mechanism dominates, with a smooth transition zone in the range $\frac{1}{2} < k\sigma < 1$. From a number of runs of the model for differing forest parameters, the difference of the levels of the coherent dominant scattering and incoherent dominant scattering range from about 0 dB to about -10 dB.

Cross-polarized backscatter is virtually non-existent from a trunk-ground scene (with vertical trunks) when the roughness of the ground is ignored. As shown in Figure 7.4, backscattering is dominated by the incoherent bistatic ground-trunk interaction in the entire cone of the trunk, even for relatively smooth surfaces, because the direct ground cross-polarized backscatter and the coherent specular ground–trunk cross-polarized interaction are negligible.

This model is imperfect in the sense that it amplifies the shortcomings of the bistatic surface scattering model employed. For Physical Optics, reciprocity does not hold. For Radiative Transfer, the trunks are not point scatterers as required by the theory.

CHAPTER 8

Conclusions

This chapter provides a summary of the results of this dissertation. Principal contributions are reviewed, and a number of recommendations for future research are given.

8.1 Summary

In Chapter 3, a new Bistatic Measurement Facility is described which was constructed to make accurate measurements of bistatic scattering at X-band frequencies. While bistatic measurements of random rough surfaces are reported in Chapter 6, the Facility was designed to be able to also measure the Mueller matrix of any distributed target, the average field from a distributed target, or the radar cross section of a point target. The only restriction on these targets is that their sizes must be appropriate to fit in the Bistatic Measurement Facility: point targets must be sufficiently small to fit in the Facility's sweet spot and the distributed targets be sufficiently large in extent so that a large number of independent samples can be measured, which is necessary for a quality measurement. Also, while such data does not appear in this dissertation, the Bistatic Measurement Facility is also capable of single antenna backscatter measurements.

In Chapter 4, the theory and techniques to calibrate the Bistatic Measurement Facility are presented. A separate technique is presented for the backscattering calibration and the bistatic calibration. The bistatic calibration developed for this facility uses a single measurement of a commercially available aluminum sheet. Unique verification measurements of an aluminum hemisphere on the calibration plate demonstrate the validity of the calibrations.

In Chapter 5 the Physical Optics problem is attacked with a new and general approach to the expansion of the Stratton–Chu integral in surface slopes. A modified Physical Optics reflection coefficient is derived with this approach and, in Chapter 6, it is shown to very accurately describe the vertically polarized coherent scattering from surfaces. Of the two other classic approaches which predict a reflection coefficient, the Physical Optics reflection coefficient fails to predict a migration of the Brewster angle apparent in the measurements, and the Small Perturbation method, while adequately modeling the measurements of a slightly rough surface, fails dramatically for that of a rougher surface which the modified Physical Optics approach models quite well.

The modified Physical Optics approach also predicts incoherent scattering. In process of deriving the lowest order dependence on the surface statistics of the modified Physical Optics, it is shown that the Physical Optics model for incoherent scattering is incomplete. While the Small Perturbation method predicts *hh* polarized backscattering to exceed *vv* polarized backscattering, Physical Optics predicts just the opposite. The more complete modified Physical Optics model qualitatively agrees with the Small Perturbation method in this regard rather than the Physical Optics model.

In Chapter 6, a number of measurements of a surface with statistics in the traditionally accepted region of validity for the Physical Optics model is compared with the theoreti-

cal models outlined in Chapter 2 and the modified Physical Optics approach. The modified Physical Optics predictions modestly outperforms the Physical Optics predictions in modeling this measured data.

In Chapter 7, the Michigan Microwave Canopy Scattering Model (MIMICS), a model for backscattering from forests, is extended to include a double bounce scattering mechanism which involves rough surface bistatic scattering and scattering from tree trunks. The model demonstrates that, for co-polarization, the level of backscattered power depends on the surface roughness in a crudely binary fashion: if $k\sigma < 1$, coherent specular scattering from the ground dominates other scattering mechanisms involving the ground, while if $k\sigma > 1$, the incoherent bistatic scattering from the ground in a cone around the individual tree trunks dominates other scattering mechanisms involving the ground. In either case, the level of co-polarized backscattered power is otherwise largely independent of the normalized rms surface height $k\sigma$. Also, incoherent bistatic ground–trunk scattering dominates other mechanisms involving the ground for the cross-polarized backscattering, regardless of the roughness of the ground. For both co-polarized and cross-polarized backscatter from a forest scene, direct backscattering from the ground is negligible.

8.2 Results and Contributions

There are five major contributions that may be found in this dissertation:

1) A Bistatic Measurement Facility has been designed and constructed which can polarimetrically measure distributed targets at X-band frequencies. This is the first such facility designed specifically for polarimetric measurements of distributed targets. A number of cal-

ibrated bistatic measurements of characterized rough surfaces are presented in Chapter 6.

2) A calibration and verification technique has been developed to insure that the bistatic measurements from the Bistatic Measurement Facility are accurate.

3) A generalized method for analyzing the Physical Optics model under the tangent plane approximation has been developed. One result of the analysis is that it is discovered that the classic (zeroth order) Physical Optics derivation misses a number of terms which have the same dependence on surface parameters as the lowest order term.

4) One result of this new modified Physical Optics model is that the migration of the coherent scattering Brewster angle with roughness has been experimentally verified and theoretically explained with this model. This theoretical explanation has a wider range of validity than does the only other explanation, the Small Perturbation Model.

5) A modification to the Michigan Microwave Canopy Scattering (MIMICS) model is presented which includes surface roughness in the bistatic trunk-ground scattering mechanisms. For surfaces which are sufficiently rough, the incoherent bistatic ground–trunk interaction dominates all other scattering mechanisms involving the ground, including the direct backscatter from the ground.

8.3 Recommendations for Future Research

With a Bistatic Measurement Facility in place a large volume of data on distributed targets which would benefit the remote sensing community is obtainable. For example, a series of measurements could be conducted which could be used to experimentally determine the region of validity of the Small Perturbation or the modified Physical Optics models. Such

a library of data would be essential to evaluating the validity of not just surface scattering models but also volume and vegetation scattering models. Due to the statistical nature of the scattering problem, a large volume of data is essential to drawing useful conclusions about bistatic scattering.

One very serious problem with the measured surfaces in this dissertation was the characterization of the surface roughness characteristics. Whenever possible, surfaces measured with radar for model verification should be manufactured to particular specifications, rather than sculpted and the profile measured. While this has already been accomplished for surfaces, techniques for designing and manufacturing volume and vegetation targets need to be developed.

The analysis of the Physical Optics approach in chapter 5 contains a number of techniques which are general to nature of the Physical Optics expansion, rather than specific to particular terms. As such, it is theoretically possible to solve all terms simultaneously, resulting in an exact solution to the tangent plane approximation. Also, the development can rather easily be generalized further for surfaces which have nonsymmetric correlation functions or nonzero skewness or kurtosis statistics. The Integral Equation Model (IEM) is a multiple-scattering model which is an outgrowth of the Physical Optics model. As such, many of the techniques developed in this dissertation for evaluating Physical Optics terms could be applied to the IEM as well. This would be a particularly useful exercise, since it is expected that, even for modestly rough surfaces, multiple-scattering processes are significant for such measurables such as cross-polarized backscatter.

While this dissertation presents a tool for evaluating the effects of surface roughness on total backscatter from forests, this model needs to be compared with careful measurements

for which significant ground truth data, especially regarding the surface characteristics, has been acquired.

APPENDICES

APPENDIX A

System User Manual

A.1 Target Preparation

The proper preparation of targets is important to insure that measurements made by the Bistatic Measurement Facility are accurate. This section gives a number of helpful hints for this preparation.

A.1.1 Point Targets

The definition of a radar cross section σ for a point target assumes that the target is illuminated by a plane wave. For this assumption to be true, the target must be sufficiently small so that it fits within the "sweet spot." In both modes the sweet spot is approximately spherical and located at the center of the BMF, but the diameter differs in those two modes as shown in Table 3.1.

A.1.1.1 Locating the Center of the Facility

The center of the Bistatic Scattering Facility is that point at which the two antenna boresights intersect. It is also the point at which the three bistatic axes intersect. The center is

exactly 30 inches off the floor, and the line which passes vertically though the center can be found with the following technique:

Move the inner arch elevation to 0° and the inner arch azimuth to 90°. Move the outer arch elevation such that its uprights are vertical. This should be at -1.5° for this axis. The two pairs of uprights can now be used as visual aids in locating the center of the Bistatic Measurement Facility. Stand close to one of the arch uprights, in the plane of the arch, but not inside the arch. Look across the plane of the arch, from the near upright to the far upright. The plane defined by the left (right) edge of the near upright and the right (left) edge of the far upright of the same arch goes directly through the center the Bistatic Measurement Facility. So does the similar plane defined by the other arch. Since the two arches are now perpendicular to each other, a vertical line going directly through the center of the Bistatic Measurement Facility is well defined. Place the target in the facility such that its center is exactly 30 inches above the floor. Move the target around until it can be verified to be in both planes defined by the two arches.

A.1.1.2 Using the Calibration Plate with Image Theory

The primary purpose of the calibration plate is for the proper calibration of the system. Another use of the calibration plate, used in conjunction with another object, is for verifying the ability of the Bistatic Measurement Facility to measure radar cross sections. The calibration plate shields the BMF from any objects underneath it, which can be a very useful property since the removal of a bulky distributed target is often very inconvenient. The only catch is that the object placed on the plate is now subject to two properties of image theory: first, the object and its mirror image appear in the receiver's field of view, and second, the

target (and its mirror image) are illuminated simultaneously by the transmitter and a mirror image of the transmitter. Probably the most useful target to use with image theory is the hemisphere, because its RCS can be computed exactly and therefore it can be used to verify the operation of the BMF.

A.1.2 Distributed Targets

For distributed targets, the main issues involved in the preparation for a measurement is the proper use of the illuminated area and methods for producing a flat surface.

A.1.2.1 The Illuminated Area

Distributed targets are assumed to be very large with respect to the radar's beamwidth. The region which contributes to scattering is much larger than the sweet spot used for measuring point targets. Since the antenna illumination does not drop off instantly outside the beamwidth, this region is technically infinite in extent, but for almost all scattering situations it suffices to say that the region is where the transmitter and receiver gain pattern product, $G_r G_t$, is within 6 dB of the maximum gain product, which is the gain product at the center of the BMF. This region is known as the illuminated area and is denoted by A_{ill}. A_{ill} depends primarily on the antenna with the smallest beamwidth-range product, βR, and depends on the angle of incidence of this antenna, θ, as $1/\cos\theta$. Therefore, for bistatic mode, the illuminated area is determined by the transmit antenna and its incidence angle, while for backscatter mode, which uses only the horn antenna, the illuminated area is determined solely by the horn antenna and the backscattering angle.

The illuminated area is not directly calculated by the software. Rather, it calculates a

quantity closely related to it, the illumination integral, I_{ill}. See Section 4.5 of Chapter 4 for further discussion of the illumination integral and the formulas used to calculate it.

While A_{ill} is the source of the scattering, it is important to keep all objects which are, or could be, very strong scatterers nowhere near the illuminated area. This is particularly important when the distributed target is a weak scatterer for the bistatic angles and/or polarizations desired, because strong scatterers, even though they might be in sidelobes of the antennas many tens of dB down from boresight, might still contribute the majority of the power received. Such objects include metal objects or anything with metal, water and wet objects (including living things), edges, and objects with planar sides which could specularly reflect from the transmit direction to the receive direction.

A.1.2.2 Making a Flat Surface

An important starting point for many distributed targets is the creation of a flat surface. For measuring volume scattering, a flat surface is useful because it does not scatter in any direction other than the specular direction, thus preventing contamination of the measured volume scattering with surface scattering. For measuring surface scattering, making a flat surface is a good starting point for making rough surfaces because the mean of the rough surface is then more likely to be flat, a requirement of most surface scattering theories.

For distributed targets made from a powdery solid, like sand or soil, the following technique has been found to be the best for creating a flat surface. Level the material as best as one can by hand, then create the final flat surface with a flat surface tool. Such a tool consists of a metal blade, from a strip of sheet metal or angle iron or similar material with a very straight and rigid edge, which is suspended horizontally over the sample holder while the

turntable is made to rotate slowly but continuously. The blade acts like a plow, removing material when it is too high and filling in where it is too low. After one rotation it should be evident where the center of the sample holder is located, as it will be in the center of a small circle of unleveled material. Reposition the blade to pass through the center of that small circle and rotate the turntable again. Repeat the process of locating the center until it is found.

Once the center is found, the blade should be raised or lowered at one or both ends so that it carves a plane on the material instead of a cone. It is also desirable to get the surface as close to 30 inches above the floor as possible. Material may need to be added or removed from the center or the ends of the blade as the turntable rotates. Near the end of this procedure the surface will be flat and level but with a small amount of material being plowed by the blade. At this point the blade should be raised a tiny amount (approximately 1/16 inch) to enable this last material to be incorporated evenly into the flat surface. Once the surface is smooth and the blade no longer plows any material, it can be removed and the flat surface is complete.

A.2 Power Up

The following steps will quickly bring the Bistatic Measurement Facility to its operational state and insure that the bistatic angles are accurate.

A.2.1 Inspection

Make sure no cables have been snagged, disconnected or damaged before attempting to power up the facility. The rail should be cleared of all debris. If the HP-IB or the microwave plumbing is not attached to the network analyzer, do so now.

A.2.2 Apply Power

Power up the instruments in this order: network analyzer, computer monitor, printer (if connected), motor amplifiers, microwave relays, microwave amplifiers, computer cpu. Nothing disastrous will happen if this order is not followed, but the components will have the longest life if this order is used.

A.2.3 Launch The Software

Once the Gateway 2000 PC has booted and produced a DOS prompt, type "win" and press the enter key to launch Windows. After Windows displays the Program Manager, double click the "Visual Basic 3.0" icon to open the Visual Basic directory. In that directory, launch the Visual Basic application by double-clicking the "Microsoft Visual Basic" icon. From the "File" menu, select "Open Project..." The project to open is "sigzero.mak" in the "c:\bistatic" directory. Press the F5 key or select "Start" under the "Run" menu to execute the Bistatic Measurement Facility software. The software will display the main form, as shown in Figure A.1, and await user instructions.

In the following discussion, a number of terms, like "radio button" or "form," are used. These are the Visual Basic terms for these standard Graphical User Interface (GUI) soft-

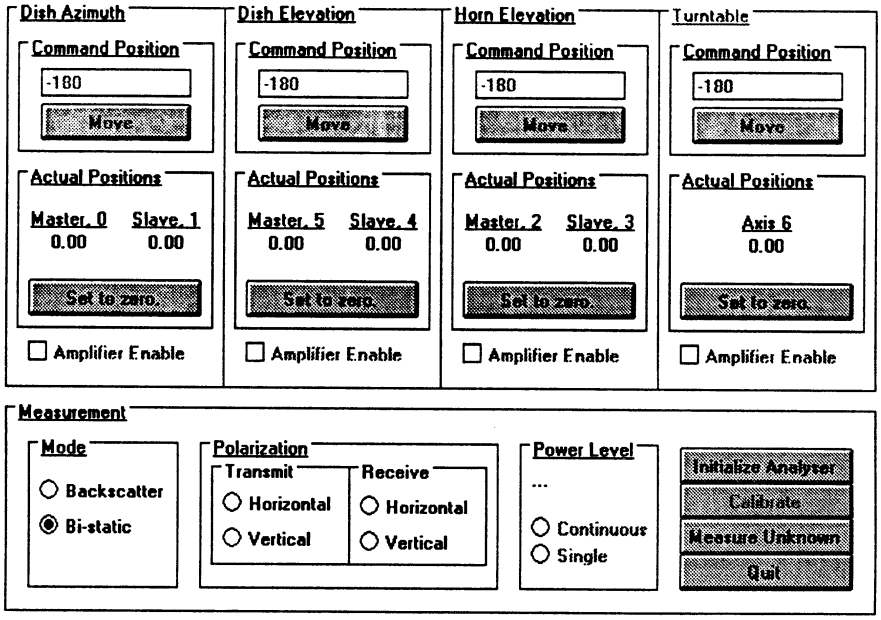

Figure A.1: The Main Form, as it appears when the Bistatic Measurement Facility software is launched.

ware items and the user is referred to that documentation for detailed explanations of their appearance and properties.

A.2.4 Zero Axes

The physical axes of the system do not have absolute encoders, home or limit switches, or other means of determining absolute position without user intervention. Thus the axes must have their zero positions set by the user. The following paragraphs describe how to put the three bistatic axes into the zero position manually. The software should be running during this process, so that the axes, once in the correct position, can be powered up and thus prevent any inadvertent motion from taking them from the zero position. This is done in the main form of the software by clicking the "Set to Zero" button for the appropriate axis, then clicking the "Amplifier Enable" checkbox to apply power to the motors, thus keeping them

at the correct zero position. If the axes have have not had their amplifiers disabled since the last time the axes were zeroed, they do not need to be re-zeroed at this time.

A.2.4.1 Inner-arch Azimuth

The inner arch azimuth axis zero position is where the inner arch axis of rotation is aligned with the outer arch axis of rotation, and the cables go around the sample holder. (The facility is designed to have the cars in the exact same position, but with the cables going around a spool on the floor instead. That is the 360° position.) Since it is hard to align the axes themselves (the big sprockets obstruct vision), the alignment can be checked by making sure the edges of the inner arch car are in line with the edges of the outer arch stand. The cars cannot be pushed directly into position because the cars' driven wheels are directly attached to a worm gear, which locks when torque is applied to the output shaft. Therefore, if a car needs to be moved, the driven wheel must be used to move it or the driven wheel must be lifted off the floor to allow the other wheels to roll. If a car needs to be moved for proper alignment, pick it up near the driven wheel until the driven wheel is not in contact with the floor and slide the car around on the rail. Be careful to put the car back down on the rail properly. When both cars are properly aligned with the stands, the "Dish Azimuth" axis may be "set to zero" with the softkey. Then enable the amplifiers for this axis to prevent any inadvertent motion, such as that induced by manually zeroing the inner arch elevation.

A.2.4.2 Inner-arch Elevation

For the inner arch, the zero position is with both arch uprights in the vertical position. If the center of the arch, where the antenna is located, can be reached, move the arch toward

vertical by applying an upward force on the arch at that point. Do not apply any force directly to the antenna, as that may misalign it. After the arch is sufficiently upright that the center of the arch is out of reach, the arch uprights can be moved toward vertical with the aid of an assistant (one person on each upright near the axis), or solo, if one is careful to move each side only a little at a time. Do not move one side so hard as to "pull" the other side along with it. Confirm that the arch uprights are both vertical with the aid of a carpenter's level. If one upright needs adjustment, be sure to remeasure both uprights with the carpenter's level before proceeding. Once the inner arch has been set to vertical, the "Dish Elevation" axis may be "set to zero" *via* the softkey. Then enable the amplifiers for this axis to prevent any inadvertent motion.

A.2.4.3 Outer-arch Elevation

For the outer arch elevation, the procedure is the same as for the inner arch elevation, except for a few additional steps after the arch has been "set to zero." The software recognizes the outer arch as the "Horn Elevation," so that is the axis which now must be "set to zero" and "enabled." Because the antenna on the outer arch is mounted on the side of the arch instead of the center like the antenna on the inner arch, it is now not at vertical, but instead is off by a few degrees. After the amplifiers have been enabled, type "1.5" in the command position for the "Horn Elevation," then hit the "Move" softkey. Wait until the actual positions agree with each other and are within one count of the command position (for both elevation axes, one count is about 0.05°). Then disable the "Horn Elevation" axis, set it to zero, and re-enable the axis.

A.3 Using the Software

Now that the Bistatic Facility's axes have been aligned and the motor amplifiers for each axis have been enabled, all interactions between the user and the bistatic facility itself (not including the targets) can be done with the software.

A.3.1 Moving the Antennas

Each bistatic axis has a frame in the main form (see Figure A.1) which has exclusive control over the motion of that axis. In addition to the "Set to Zero" command button and the "Amplifier Enable" checkbox, both explained in Section A.2.4, there is a text box and "Move" command button for the motion of the axis. The "Actual Position" frame has labels which display the logical axis numbers for the master and slaved axes associated with the bistatic axis, as well as their current positions (in degrees).

A.3.2 Set the Mode

The mode, backscatter or bistatic, must be set using the radio buttons on the lower left side of the main form. The default mode is bistatic. Pressing one of these radio buttons will cause the software to initialize the network analyzer for the appropriate mode, but will also erase all calibration data and invalidate the current calibration. The system is ready for either making raw measurements or for calibrating.

If the system is in backscatter mode, the entire inner arch is superfluous to the operation of the system. Therefore, it should be moved to a position such that it is out of the way for making measurements. Moving the inner arch elevation to +90° or -90° will keep it entirely

out of the field of view of the backscatter antenna, regardless of the backscattering angle of incidence.

A.3.3 Initialize the Network Analyzer

If the mode was not explicitly set, that is, it was left in bistatic mode, the network analyzer must be initialized by clicking the "Initialize Analyzer" command button. This command button puts the network analyzer into a known state, but does not, by itself, invalidate a completed calibration. Anytime the front panel of the network analyzer has been accessed, re-initializing the network analyzer with this command button before doing anything else with the software is highly encouraged.

A.3.4 Raw Measurements

Raw measurements can be done in two ways, manually from the main form, or with all the polarizations done at once in the measurement form. Either way, the bistatic angles must be set using the axis controls in the main form. Within the main form, the user also has control of the polarization state of the facility *via* the polarization frame, and the raw power level of the signal received at the network analyzer may be read with the power level frame.

Within the power level frame, which is enabled only after the NWA has been initialized, there are two command buttons. The "Single" command button takes a single trace of the network analyzer and reports the power at the center frequency. The "Continuous" command button repeatedly makes single traces and updates the power at the center frequency

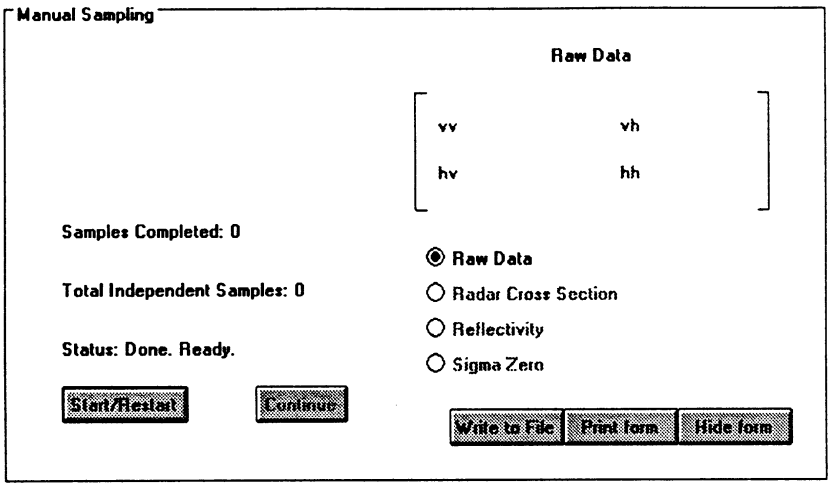

Figure A.2: The Measurement Form, for manual sampling, as it appears when the Bistatic Measurement Facility is not calibrated.

as it gets it. The "Continuous" command button may be turned off by clicking the "Single" command button, or by doing various other actions (such as starting a calibration or measurement).

The radio buttons in the polarization frame control the settings of the polarization switches that are part of the antenna assemblies. The software cannot detect whether the power is applied to the microwave switches, so it is the user's responsibility to ensure that the microwave relay power switch is on.

By clicking the "Measure Unknown" command button and then clicking "Manual" in the menu, the measurement form appears as shown in Figure A.2. The only type of measurement enabled at this point is the raw data, which measures the center frequency power for each polarization and reports the value without applying any calibration, conversion or statistical analysis. The major difference between this measurement and that done from the

main form, other than the fact that all four polarizations are done, is that measurements made in the measurement form have an averaging factor set to 8 on the network analyzer, while that done from the main form has the averaging off (which is the same as an averaging factor of 1). Thus raw measurements done in the measurements form has a signal to noise ratio 9 dB greater than that made from the main form.

Raw measurements have limited usefulness, as their numbers can only be compared to other numbers generated in exactly the same fashion, ie. on that particular bistatic facility. Thus the raw measurements are useful primarily in troubleshooting. For example, the operation of the polarization switches can be easily verified by moving the antennas into the specular angles for a calibration plate, then measuring the plate in the different polarization states.

A.3.5 Calibration

In order to make meaningful measurements, the system must be calibrated. This can be done by clicking the "Calibrate" command button on the main form, which loads the calibration form appropriate for the mode the system is in. Refer to Chapter 4 for a theoretical background to the calibration process. The next two sections describe the recommended procedures for calibrating the Bistatic Measurement Facility for backscattering and bistatic scattering.

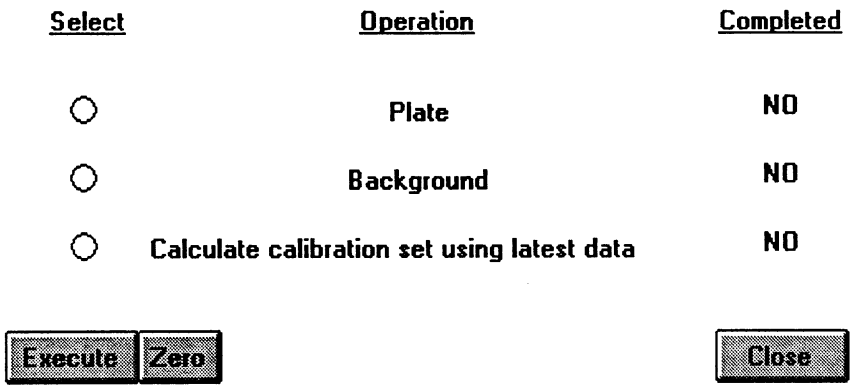

Figure A.3: The Calibration Form, as it appears when the Bistatic Measurement Facility is in backscatter mode.

A.3.6 Backscatter Calibration Procedure

With the software displaying the backscattering calibration form, which is shown in Figure A.3, three radio buttons and either two or three command buttons appear. The radio buttons are labeled "Plate", "Background", and "Calculate calibration set using latest data". They are used to determine the next object upon which the software will act, but selecting them in and of themselves does not do anything. To the right of the radio buttons is a column displaying the status for each object. Possible messages in the status column are: "NO", meaning that no action has yet taken place with that object; "Working", meaning that the software is busy with that object; and a time, which indicates when the last action on that object was completed. The background has an additional status: "0'd" and a time, indicating that the last action on the background was a deletion of the background data and when it happened.

The command buttons are used for telling the software to do something, and are labeled "Execute", "Zero", and "Close". The "Close" command button is used to exit the form and return to the main form, and can be used at any time during the calibration procedure. The "Execute" command button is used to either measure the plate or background, or to calculate the calibration set. The "Zero" command button only applies to the "Background" radio button, so it only appears if that radio button is selected, and is used to erase the measured data for the background target. In effect, it returns the background data to the state it was when the calibration form was first entered; that is, the background is unmeasured.

The following order of steps is recommended for backscattering calibration.

A.3.6.1 Position Calibration Target

Place a large sheet of aluminum at the center of the Bistatic Facility. It must be flat and level, and at a height equal to the axis of rotation of the bistatic facility (30 inches off the floor).

A.3.6.2 Position The Backscattering Antenna

From the main form in the software, move the antenna to 0°. If the inner arch is positioned such that it is between -20° and +20°, it will also need to be moved to prevent it from affecting the calibration measurement.

A.3.6.3 Measure The Calibration Target

Make sure the "Plate" radio button is selected, then click on the "Execute" command button. The status column will show "Working" for about 30 seconds then display the time

when the measurement was completed.

A.3.6.4 Measure The Background (optional)

The object of this measurement is to determine how much of the calibration measurement is due to scattering from other than the calibration target. We have found that the calibration measurement on this bistatic facility has such a large signal to background ratio that this measurement is not necessary for accurate calibration. However, should the system change so that the signal to background ratio be substantially reduced (to 30 dB or less), this measurement would be essential. About the only thing which could cause such a reduction is damage to microwave components, which could then introduce internal reflections within the microwave plumbing and multipath with the same length as the direct path involving the calibration target.

With the same aluminum plate in the same location, the background can be measured by moving the outer arch away from the specular direction. We recommend that it be moved to more than 30° away from nadir for a valid background measurement. In this position, the plate will not scatter any energy back toward the antenna, and the time-gating on the network analyzer will prevent other nearby objects from being measured. Again, the inner arch must not be within the field of view of the backscattering antenna. Select the "Background" radio button, and then select the "Execute" command button. The status will display "Working" for about 30 seconds then display the time the measurement was completed.

A.3.6.5 Calculate The Calibration Set

Anytime a valid "plate" measurement has been completed, the calibration set may be calculated. Select the "Calculate calibration set using latest data" radio button then select the "Execute" command button. The software will then calculate the calibration set using the STCT algorithm and display the time it was completed.

A.3.6.6 Leave The Calibration Form

Remove the calibration plate (unless it is going to be used for measurements) and select the "Close" command button to return to the main form. The bistatic system is now calibrated in backscatter mode and is ready for measurements, as described in Section A.3.8 of Chapter A.

A.3.7 Bistatic Calibration Procedure

With the software displaying the bistatic calibration form, which is shown in Figure A.4, five radio buttons and either two or three command buttons appear. The radio buttons are labeled "Plate w/ Dish unrotated", "Background w/ Dish unrotated", "Plate w/ Dish rotated 45 degrees", "Background w/ Dish rotated 45 degrees", and "Calculate calibration set using latest data". These are used to determine the next object upon which the software will act, but selecting them in and of themselves does not do anything. To the right of the radio buttons is a column displaying the status for each object. Possible messages in the status column are: "NO", meaning that no action has yet taken place with that object; "Working", meaning that the software is busy with that object; and a time, which indicates the when

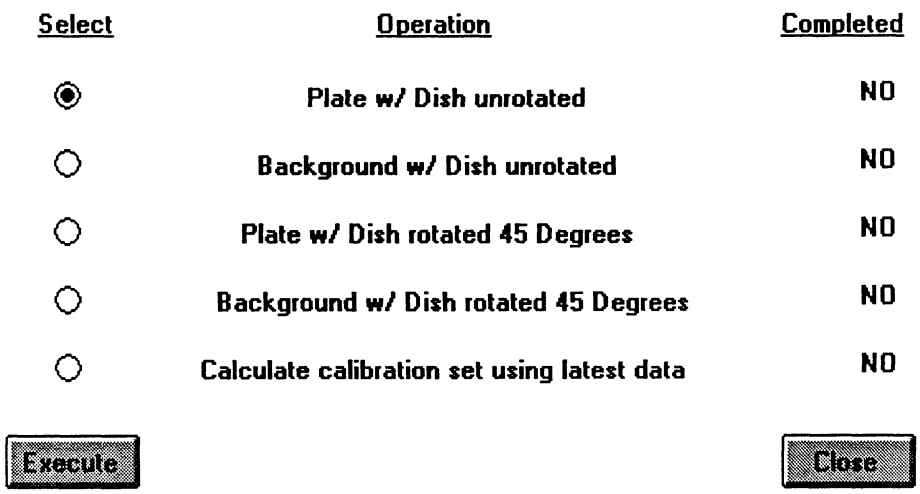

Figure A.4: The Calibration Form, as it appears when the Bistatic Measurement Facility is in bistatic mode.

the last action on that object was completed. The three middle objects have an additional status: "0'd" and a time, indicating that the last action on that object was a deletion of the measured data and when it happened.

The command buttons are used for telling the software to do something, and are labeled "Execute", "Zero", and "Close". The "Close" command button is used to exit the form and return to the main form, and can be used at any time during the calibration procedure. The "Execute" command button is used to either measure the plate or background, or to calculate the calibration set. The "Zero" command button only applies to the three middle radio buttons, so it only appears if one of those radio buttons is selected, and is used to erase the measured data for those targets. In effect, it returns the data for that object to the state it was when the calibration form was first entered, that is, unmeasured.

The only measurement essential for calculating the calibration coefficients is the "Plate with dish unrotated" measurement. The "Plate with dish rotated 45 degrees" is used to insure that the calculation of the calibration coefficients does not involve the division by very small numbers (see the previous section on the bistatic calibration theory). Experience has shown that those small numbers are not sufficiently small (compared to the noise in those numbers) to necessarily cause problems. The object of the two background measurements associated with each plate measurement is to determine how much of the calibration measurement is due to scattering from other than the calibration target. We have found that calibration measurements on this bistatic facility has such a large signal to background ratio that these measurements are not necessary for accurate calibration. However, should the system change so that the signal to background ratio be substantially reduced (to 30 dB or less), this measurement would be essential. About the only thing which could cause such a reduction is damage to microwave components, which could then introduce internal reflections within the microwave plumbing and multipath with the same length as the direct path involving the calibration target.

The following order of steps is recommended for bistatic calibration.

A.3.7.1 Position The Calibration Target

Place a large sheet of aluminum at the center of the Bistatic Facility. It must be flat and level, and at a height equal to the axis of rotation of the bistatic facility (30 inches off the floor).

A.3.7.2 Rotate The Dish (optional)

Lower the dish antenna to an elevation where the the bolt holding the dish assembly to the I-beam of the arch is accessible. Depending on the height of the user, this can be done by sending the dish elevation to about 70° or so. Use a 7/16 inch nut driver or wrench to loosen the bolt about one turn. Do not remove the bolt, as it is the only thing holding the Dish antenna assembly onto the arch. Rotate the Dish assembly about its boresight direction, that is, rotate it around the shaft of the bolt, about 45° counterclockwise (as viewed with the bolt visible). The cables attached to the dish assembly should prevent it from being rotated in the wrong direction. Tighten the bolt which holds the dish assembly onto to the arch.

A.3.7.3 Position The Antennas In The Specular Direction (optional)

From the main form in the software, move the Horn Elevation to some angle θ_{rc} where $20° < \theta_{rc} < 60°$. An angle of 35° is recommended. The Dish Azimuth must be set at 0° and the Dish Elevation must be the same as the Horn Elevation. This is the specular direction; with the antennas in these positions and the plate properly located, the measured scattered power will be at a maximum.

A.3.7.4 Measure The Plate With Rotation (optional)

Make sure the "Plate w/ dish rotated" radio button is selected, then click on the "Execute" command button. The status column will show "Working" for about 30 seconds then display the time when it was completed.

A.3.7.5 Measure The Background With Rotation (optional)

With the same aluminum plate in the same location, the background can be measured by moving both antennas in elevation equal amounts but in opposite directions. This allows the direct path between antennas to be unaffected while removing the calibration target. We recommend that the antennas be moved by more than 30° away from specular direction for a valid background measurement. In this position, the plate will not scatter any energy back toward the antenna, and the time-gating on the network analyzer will prevent other nearby objects from being measured. Select the "Background w/ dish rotated 45 degrees" radio button, and then select the "Execute" command button. The status will display "Working" for about 30 seconds then display the time the measurement was completed.

A.3.7.6 Unrotate The Dish (optional)

Following similar procedures used to rotate the dish, return the dish to its normal orientation. Remember to tighten the bolt which holds the dish assembly onto the arch.

A.3.7.7 Measure The Background Without Rotation (optional)

With the same aluminum plate in the same location, the background can be measured by moving both antennas in elevation equal amounts but in opposite directions away from the specular direction. This allows the direct path between antennas to be unaffected while removing the calibration target. We recommend that the antennas be moved by more than 30° away from the specular direction for a valid background measurement. In this position, the plate will not scatter any energy back toward the antenna, and the time-gating on the network

analyzer will prevent other nearby objects from being measured. Select the "Background w/ dish unrotated" radio button, and then select the "Execute" command button. The status will display "Working" for about 30 seconds then display the time the measurement was completed.

A.3.7.8 Move The Antennas To The Specular Direction

From the main form in the software, move the Horn Elevation to some angle θ_{rc} where $20° < \theta_{rc} < 60°$. An angle of 35° is recommended. The Dish Azimuth must be set at 0° and the Dish Elevation must be the same as the Horn Elevation. This is the specular direction; with the antennas in these positions and the plate properly located, the measured scattered power will be at a maximum.

A.3.7.9 Measure The Plate Without Rotation

Make sure the "Plate w/ dish unrotated" radio button is selected, then click on the "Execute" command button. The status column will show "Working" for about 30 seconds then display the time when it was completed.

A.3.7.10 Calculate Calibration Set

Anytime a valid "Plate w/ dish unrotated" measurement has been completed, the calibration set may be calculated. Select the "Calculate calibration set using latest data" radio button then select the "Execute" command button. The software will then calculate the calibration set and display the time it was completed.

A.3.7.11 Leave The Calibration Form

Remove the calibration plate (unless it is going to be used for measurements) and select the "Close" command button to return to the main form. The bistatic system is now calibrated in bistatic mode and is ready for measurements, as described in Section A.3.8 of Chapter A.

A.3.8 Calibrated Measurements

Upon first entering the measurement form, only the menu is visible. One of the two items on the menu, "Manual" or "Automatic," must be clicked, which will show the measurement form.

Manual sampling refers to the fact that the software waits for the user to modify the target in some fashion between measuring independent samples. The user must acknowledge to the software (*via* the "Continue" command button) that the target has been set to a new independent sample before the BMF will make further measurements.

In automatic sampling, the software rotates the target on the turntable to generate new spatial independent samples between measurements, thus not requiring user intervention. However, entering automatic sampling without the proper turntable controller attached will cause the software to go into a loop which can be escaped only by stopping the program.

These two menu items may be clicked any time the measurement form is open.

A.3.8.1 Manual Sampling

The measurement form for manual sampling, as shown in Figure A.5, displays information in two columns side by side:

On the left, from top to bottom, is a display of the spatial samples completed, the total number of independent samples measured for the current measurement sequence, the current status of the Bistatic Measurement Facility, and finally two command buttons, one for (re-)starting a measurement and a second for continuing a measurement already started.

On the right, from top to bottom, is a 2×2 array of the measured data, four radio buttons showing the type of information to be displayed in the array, and three command buttons. The radio buttons are entitled "Raw Data", "Radar Cross Section", "Reflectivity", and "Sigma Zero." The title of the array matches that of the radio button which has been selected. The three command buttons, which are always visible and enabled, are, from left to right, "Write to File," "Print Form," and "Hide Form."

When the "Radar Cross Section" radio button is selected, as in Figure A.5, an additional command button and check box appear which have to do with background subtraction. The command button is captioned "Measure Bkgnd" and is used to measure the background for a point target (ie. the scene with just the target itself removed, but with all support structures and bistatic angles unchanged). The measurement of a background occurs in the same fashion as any other measurement, and it takes the same time to complete, but the data is stored in a temporary array. If this check box, captioned "Subtract Bkgnd", is turned on (off), the RCS is recalculated and displayed with the background subtracted (ignored).

The "Start/Restart" command button on the left side of the form is used to reset the statis-

measurement type	integer code
Raw Data	0
RCS	1
Reflectivity	2
Sigma Zero	3

Table A.1: Integer codes in the final column of output files

tics used to generate the reflectivity and the scattering coefficient, and start the measurement of the first sample. The "Continue" command button is used to measure an additional sample, and can be used repeatedly to measure an arbitrary number of samples.

Clicking the "Write to File" command button will cause certain information on the current measurement to be written as a single line at the the end of the file *c:\patterns\bmf.dat*. The information is written in ASCII in this order: outside arch elevation, inside arch elevation, inside arch azimuth, the four elements of the array of measured data (vv, vh, hv, hh), and an integer indicating which of the radio buttons is active (and therefore, what kind of data is being written to the file). The bistatic angles are recorded in degrees, the measured data is recorded in dB or dBsm, as appropriate, and the integer has one of the four values given in Table A.1.

Clicking the "Print Form" command button will cause the measurement form to be printed on a properly configured printer which is connected in some fashion to the computer. The computer system is delivered with the assumption that a printer is attached to the printer port LPT1, but the user may reconfigure the default printer with other software provided with Windows. If no printer is attached, any attempt to use this command button will be ignored.

Clicking the "Hide Form" command button will cause the measurement form to be hid-

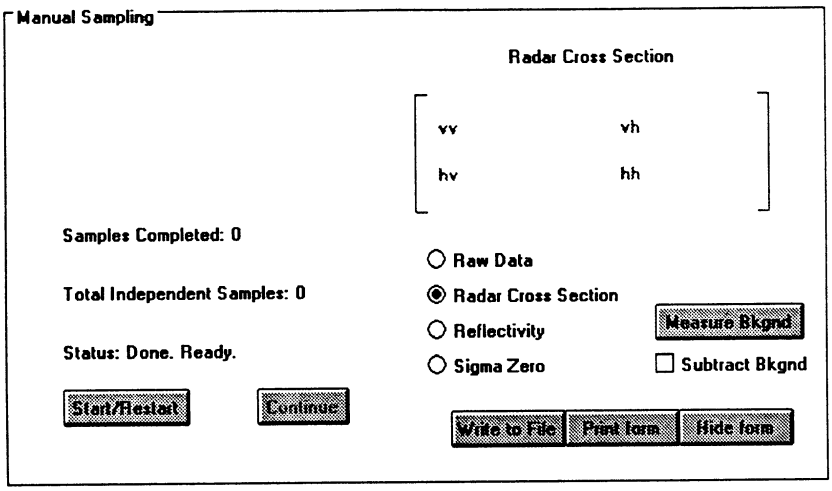

Figure A.5: The Measurement Form, for manual sampling, as it appears when the Bistatic Measurement Facility has been calibrated and RCS is the chosen measurement unit.

den, returning the user to the main form.

See Section 4.5 of Chapter 4 for explanations of the precise meanings of the different types of data that the Bistatic Measurement Facility can produce.

A.3.8.2 Automatic Sampling

Clicking the "Automatic" menu option brings up the same form as does clicking the "Manual" menu option, but with a few additional pieces of information: two text boxes and an additional command button. The measurement form for automatic sampling is shown in Figure A.6. Refer to the manual sampling section above for explanations of the form elements that appear in common between the two sampling methods.

On top of the left hand side are two text boxes for entering information regarding the use of the turntable. The first text box is for entering the number of degrees the turntable should

rotate between independent samples, and the second is for entering the maximum number of independent spatial samples (the number of times the turntable is rotated and the target is measured).

There is an additional command button on the left side of the form, with the caption of "Pause." Clicking this command button will cease program execution, but only after the current sample measurement has been completed. This allows the user to do something with the target or the BMF without invalidating a measurement or having to wait for the measurement sequence to complete. Anytime the software has been paused, and the measurement of that particular spatial location has been completed, the measurement sequence can be continued indefinitely with the "Continue" command button or restarted with the "Start/Restart" command button.

Manual sampling is the same as Automatic sampling except that the turntable is ignored, and that the software tells itself to pause anytime "Start/Restart" or "Continue" has been clicked.

A.4 Examples of Measurements

The following two examples demonstrate the use of the software to make specific measurements. In addition, some practical hints for setting up measurements are given. The hemisphere measurement is useful for confirming the operation of the Bistatic Measurement Facility. The rough surface measurement is a typical measurement of an unknown target and demonstrates the ability of the BMF to separate reflectivity from a scattering coefficient.

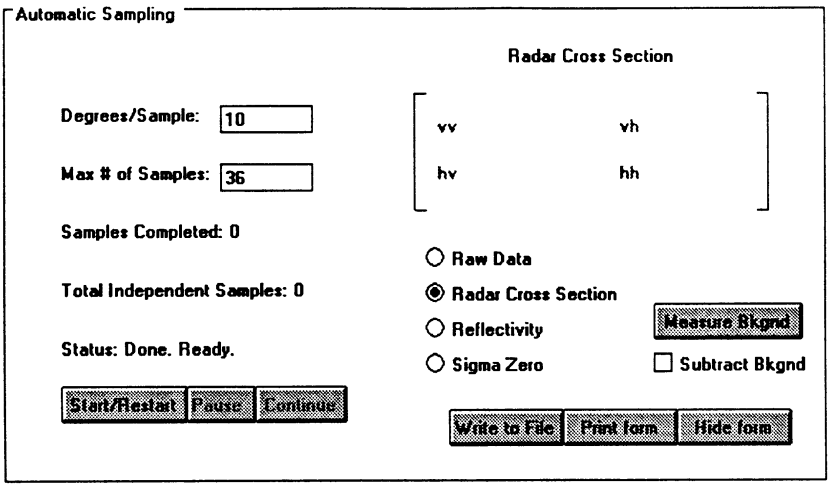

Figure A.6: The Measurement Form, for automatic sampling, as it appears when the Bistatic Measurement Facility has been calibrated and RCS is the chosen measurement unit.

A.4.1 Backscattering RCS of hemisphere on a conducting half-space

The hemisphere and its mirror image create a sphere, for which the scattering characteristics are known exactly. The formulation of the scattering from a sphere is given in Bohren and Huffman [4], Chapter 4, and a Fortran 77 program which calculates the RCS of a hemisphere on a ground plane is provided with the BMF. This code has as its heart a subroutine "bhmie" based on the fortran code in the appendix of [4]. In addition, the software provided includes a subroutine "scatter", which calls "bhmie" and converts the scattering coefficients from the coordinate system in [4] to the coordinate system shown in Figure 2.1. The main routine calls these subroutines and applies image theory to calculate the RCS of a hemisphere as it would be measured with the BMF. This code, which runs (at least) under f77 on a Sun 4, likely needs only minor modifications to run under the local fortran compiler. As

described in Section A.1.1.2, the radar cross section is then given by the interference pattern of the sphere illuminated by the transmitter (a plane wave incident at θ_t) and its image (another plane wave incident at $180° - \theta_t$).

Upon launching the BMF software, select the Backscatter mode in the main form, and set up the calibration sheet. Move inner arch out of the way; make sure the outer arch is at 0° and calibrate (without a background). Refer to Section A.3.6 for the backscatter calibration procedure. Do not remove the calibration sheet, it will become part of the measurement. The system is now ready for making measurements and the only trick is to properly position the target. Find the center of the BMF as described in Section A.1.1.1. Once the hemisphere is located at the center of the BMF, marking a circle on the plate with a mechanical pencil around the circumference of the hemisphere can be helpful to quickly but precisely relocate the hemisphere at the center of the BMF without having to use the arches.

Again, move the inner arch out of the way. Move the outer arch to the desired angle and enter the measurement form. Choose manual sampling. Click the RCS radio button and click the Start/Restart command button. When the measurement is complete and an RCS is displayed, remove the hemisphere and click the "Measure Bkgnd" command button. When this is complete, the RCS of the hemisphere at this angle can be viewed both with and without background subtraction by checking or unchecking the "Subtract Bkgnd" check box. The order in which the target and its background are measured can be reversed. The system is ready to be moved to a new backscattering angle for a new measurement.

By this technique it can be easily shown that the background is very significant at angles near nadir, where the specular flash from the plate is large, but is negligible at angles far from nadir.

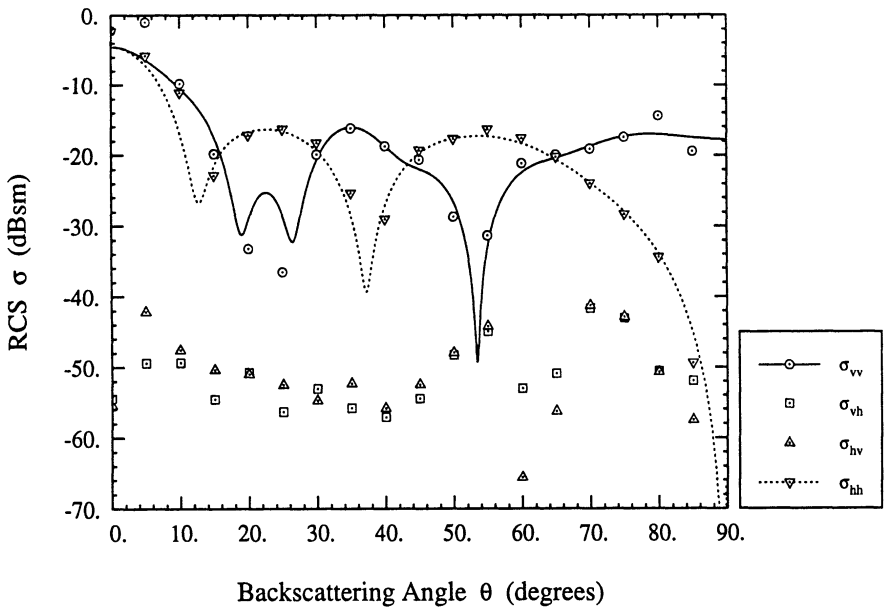

Figure A.7: Typical Bistatic Measurement Facility results for a conducting 3-3/16 inch diameter hemisphere on a calibration plate. The curves show the theoretical results as computed by the code mentioned in this section. The corrected system isolation is evident from the reported values for cross-polarization, since their theoretical values are zero. The agreement near nadir is poor because the hemisphere shields part of the calibration plate which contributes significantly to the background. The agreement for σ_{vv} near grazing is poor because the time-gate does not eliminate interactions between the hemisphere and the edge of the calibration plate (the same interaction for *hh* polarization is extremely small).

Typical results of the measurement of a hemisphere on the calibration plate are shown in Figure A.7. The points show the measured Radar Cross Section, and the curves are results of the software mentioned in this section.

Section	Task
A.2.1	Inspect the BMF
A.2.2	Power up the BMF
A.2.3	Launch the BMF software
A.2.4	Zero the BMF axes
A.3.1	Move the Dish Elevation to +30°
A.3.2	Click Backscatter Mode radio button
A.3.5	Click Calibrate command button
A.3.6	Position Calibration target
A.3.6	Click Plate radio button and Execute
A.3.6	Click Calculate radio button and Execute
A.3.6	Click Close command button
A.3.1	Move the Dish Elevation to 0°
A.3.1	Move the Dish Azimuth to +90°
A.3.1	Move the Horn Elevation to -2°
A.1.1.1	Place the hemisphere at the center of the BMF
A.3.1	Move the Dish Elevation to +30°
A.3.1	Move the Horn Elevation to desired backscatter angle
A.3.4	Click the Measure Unknown command button
A.3.8	Click Manual in the menu
A.3.8	Click the Radar Cross Section radio button
A.3.8	Click the Start/Restart command button
A.3.8	Remove the hemisphere
A.3.8	Click the Measure Bkgnd command button
A.3.8	Click the Subtract Bkgnd check box
A.3.8	Read the RCS in the array

Table A.2: Hemisphere Measurement Cross Reference and Checklist

A.4.2 Reflectivity and Specular Scattering Coefficient of a rough surface

Prepare a smooth surface as outlined in Section A.1.2.2. Place the calibration plate directly onto the surface in the region of the illuminated area. Put the BMF into bistatic mode and calibrate as described in Section A.3.7, with the antennas in the (or in one of the) elevation angles to be used for measuring. Carefully remove the calibration plate, so as not to disturb the smooth surface underneath (an assistant at this point is invaluable). Perturb the surface to the desired roughness.

The surface is now ready for measuring. If the automatic sampling is working, enter the measurement form, click on "Automatic" in the menu, enter the desired number of spatial samples and their angular separation in the appropriate text boxes, and click the start command button. If automatic sampling is not usable, use manual sampling in the measurement form, and click the start command button. When the measurement is completed, rotate the sample holder by the amount of the desired angular separation between independent samples and click the continue command button. Repeat the instructions in the last sentence until the desired number of independent samples have been measured.

By clicking the "Reflectivity" radio button, the reflectivity matrix is displayed. Clicking the "Sigma Zero" radio button displays the scattering coefficient matrix. These radio buttons can be clicked at any time during the measurement cycle to show how the variations in these numbers decrease as the number of independent samples increases.

If the reflectivity and/or scattering coefficient are desired at other angles, move the bistatic arches (*via* the controls in the main form), and repeat the directions in the last two

paragraphs. The reflectivity does not have a scientific meaning for a surface away from the specular direction, however.

Once the measurement is complete, the surface may be characterized by inserting a long piece of sheet metal edgewise into the surface, and tracing the intersection of the surface and the sheet metal onto the sheet metal with a pencil or with spray paint. Remove the sheet metal and digitize the traced curve. Use the data to estimate the rms surface height and correlation length. This technique is not the most accurate, as it disturbs the surface which is measured, but it is one of the easiest. The accuracy can be improved somewhat by taking several "slices" of the surface.

Section	Task
A.2.1	Inspect the BMF
A.2.2	Power up the BMF
A.2.3	Launch the BMF software
A.2.4	Zero the BMF axes
A.1.2.2	Prepare a smooth target surface
A.3.2	Click Bistatic Mode radio button
A.3.1	Move the Dish Elevation to 35°
A.3.1	Move the Horn Elevation to 35°
A.3.1	Move the Dish Azimuth to 0°
A.3.5	Click Calibrate command button
A.3.6	Position Calibration target
A.3.6	Click Plate radio button and Execute
A.3.6	Click Calculate radio button and Execute
A.3.6	Click Close command button
A.4.2	Remove the Calibration Target
A.4.2	Make a rough surface
A.3.1	Move the Dish Elevation to desired angle
A.3.1	Move the Horn Elevation to the same angle
A.3.4	Click the Measure Unknown command button
A.3.8	Click Manual in the menu
A.3.8	Click the Reflectivity radio button
A.3.8	Click the Start/Restart command button
A.3.8	Move target & click the Continue command button (repeat for independent samples)
A.3.8	Read the Reflectivity in the array
A.3.8	Click the Sigma Zero radio button
A.3.8	Read the Scattering Coefficient in the array

Table A.3: Rough Surface Measurement Cross Reference and Checklist

APPENDIX B

Fourier Representations of Some Mueller Matrices

This appendix presents the Fourier decomposition of the Mueller matrices of certain targets for use in the Michigan Microwave Canopy Scattering Model (MIMICS), given by (7.57) thru (7.68), as outlined in Chapter 7. The first section gives the Fourier series representation for two forms of the Mueller matrix for trunks, one for thin cylinders based on a model by Sarabandi, and another for arbitrary diameter cylinders based on a model by Ruck. The second section gives the Fourier series representation for two models for rough surface scattering, the Physical Optics model and the Small Perturbation model.

B.1 Fourier Series Representation of Trunk Phase Matrices

B.1.1 Form of $\mathbf{P}_t'$ for thin trunks

According to Sarabandi [36], the scattering matrix of a vertically oriented thin cylinder of length H_t and diameter, $2a$, where $a \ll \lambda$, can be modeled as

$$\mathbf{S} = \tfrac{1}{2}k_0^2 a^2 H_t \left(\frac{\varepsilon_r - 1}{\varepsilon_r + 1}\right) \operatorname{sinc}\left(\frac{H_t}{\lambda}(\mu_s - \mu_i)\right) \begin{bmatrix} \tfrac{1}{2}(\varepsilon_r+1)\sqrt{1-\mu_i^2}\sqrt{1-\mu_s^2} - \mu_i\mu_s\cos\phi_\Delta & \mu_i \sin\phi_\Delta \\ \mu_s \sin\phi_\Delta & 1 \end{bmatrix} \tag{B.1}$$

Thus,

$$\mathbf{P}_t'(\mu_s, \mu_i, \phi_\Delta) = \frac{\pi}{4}k_0^4 a^4 \left|\frac{\varepsilon_r - 1}{\varepsilon_r + 1}\right|^2 \sum_{n=0}^{2} \tilde{\mathbf{P}}_{tc}^{thin}(\mu_s, \mu_i; n)\cos n\phi_\Delta + \tilde{\mathbf{P}}_{ts}^{thin}(\mu_s, \mu_i; n)\sin n\phi_\Delta \tag{B.2}$$

where

$$\tilde{\mathbf{P}}_{tc}^{thin}(\mu_s,\mu_i;0)=\begin{bmatrix} \frac{1}{4}|\varepsilon_r+1|^2\mu_i'^2\mu_s'^2+\frac{1}{2}\mu_i^2\mu_s^2 & \frac{1}{2}\mu_s^2 & \cdots & 0 & 0 \\ \frac{1}{2}\mu_i^2 & 1 & & 0 & 0 \\ 0 & 0 & & \frac{1}{2}((\varepsilon_r'+1)\mu_i'\mu_s'+\mu_i\mu_s) & -\frac{1}{2}\varepsilon_r''\mu_i'\mu_s' \\ 0 & 0 & & \frac{1}{2}\varepsilon_r''\mu_i'\mu_s' & \frac{1}{2}((\varepsilon_r'+1)\mu_i'\mu_s'-\mu_i\mu_s) \end{bmatrix} \tag{B.3}$$

$$\tilde{\mathbf{P}}_{tc}^{thin}(\mu_s,\mu_i;1)=\begin{bmatrix} -(\varepsilon_r'+1)\mu_i\mu_i'\mu_s\mu_s' & 0 & 0 & 0 \\ 0 & 0 & 0 & 0 \\ 0 & 0 & \mu_i\mu_s & 0 \\ 0 & 0 & 0 & \mu_i\mu_s \end{bmatrix} \tag{B.4}$$

$$\tilde{\mathbf{P}}_{tc}^{thin}(\mu_s,\mu_i;2)=\begin{bmatrix} \frac{1}{2}\mu_i\mu_s & -\frac{1}{2}\mu_s^2 & 0 & 0 \\ -\frac{1}{2}\mu_i^2 & 0 & 0 & 0 \\ 0 & 0 & -\frac{1}{2}\mu_i\mu_s & 0 \\ 0 & 0 & 0 & \frac{1}{2}\mu_i\mu_s \end{bmatrix} \tag{B.5}$$

$$\tilde{\mathbf{P}}_{ts}^{thin}(\mu_s,\mu_i;1)=\begin{bmatrix} 0 & 0 & \frac{1}{2}(\varepsilon_r'+1)\mu_s\mu_i'\mu_s' & -\frac{1}{2}\varepsilon_r''\mu_s\mu_i'\mu_s' \\ 0 & 0 & \mu_s & 0 \\ (\varepsilon_r'+1)\mu_i\mu_i'\mu_s' & 2\mu_i & 0 & 0 \\ \varepsilon_r''\mu_i\mu_i'\mu_s' & 0 & 0 & 0 \end{bmatrix} \tag{B.6}$$

$$\tilde{\mathbf{P}}_{ts}^{thin}(\mu_s,\mu_i;2)=\begin{bmatrix} 0 & 0 & -\mu_i\mu_s^2 & 0 \\ 0 & 0 & 0 & 0 \\ -2\mu_i^2\mu_s & 0 & 0 & 0 \\ 0 & 0 & 0 & 0 \end{bmatrix} \tag{B.7}$$

where k_0 is the freespace wavenumber, $2a$ is the trunk diameter, and $\varepsilon_r=\varepsilon_r'+j\varepsilon_r''$ is the relative dielectric constant of the trunk, $\mu_i'=\sqrt{1-\mu_i^2}=\sin\theta_i$, and $\mu_s'=\sqrt{1-\mu_s^2}=\sin\theta_s$.

B.1.2 Form of $\mathbf{P}_t'$ for other trunks

For trunks which are not thin compared to a wavelength, Ruck *et al.* [34] provide the following solution for the scattering matrix of vertically oriented cylinders:

$$\mathbf{S}=\frac{iH_t}{\pi}\frac{\sqrt{1-\mu_s^2}}{\sqrt{1-\mu_i^2}}\operatorname{sinc}\left(\frac{H_t}{\lambda}(\mu_s-\mu_i)\right) \begin{bmatrix} C_0^{TM}+2\sum_{n=1}^{\infty}C_n^{TM}\cos n\phi_\Delta & 2\sum_{n=1}^{\infty}C_n^{x}\sin n\phi_\Delta \\ -2\sum_{n=1}^{\infty}C_n^{x}\sin n\phi_\Delta & C_0^{TE}+2\sum_{n=1}^{\infty}C_n^{TE}\cos n\phi_\Delta \end{bmatrix} \tag{B.8}$$

where

$$C_n^{TM} = -\left(\frac{V_n P_n - q_n J_n(x_0) J_n(x_1) D_n}{P_n N_n - D_n^2}\right) \tag{B.9}$$

$$C_n^{TE} = -\left(\frac{M_n N_n - q_n J_n(x_0) J_n(x_1) D_n}{P_n N_n - D_n^2}\right) \tag{B.10}$$

$$C_n^{x} = \frac{i2}{\pi x_0 \sqrt{1-\mu_i^2}}\left(\frac{q_n J_n^2(x_1)}{P_n N_n - D_n^2}\right) \tag{B.11}$$

$$x_0 = k_0 a \sqrt{1-\mu_i^2} \tag{B.12}$$

$$x_1 = k_0 a \sqrt{\varepsilon_r - \mu_i^2} \tag{B.13}$$

$$q_n = \frac{n\mu_i}{k_0 a}\left(\frac{1}{\varepsilon_r - \mu_i^2} - \frac{1}{1-\mu_i^2}\right) \tag{B.14}$$

$$D_n = q_n H_n(x_0) J_n(x_1) \tag{B.15}$$

$$V_n = \varepsilon_r M_n^{(1)} - M_n^{(2)} \tag{B.16}$$

$$P_n = P_n^{(1)} - P_n^{(2)} \tag{B.17}$$

$$N_n = \varepsilon_r P_n^{(1)} - P_n^{(2)} \tag{B.18}$$

$$M_n = M_n^{(1)} - M_n^{(2)} \tag{B.19}$$

$$P_n^{(1)} = \frac{H_n(x_0) J_n'(x_1)}{\sqrt{\varepsilon_r - \mu_i^2}} \tag{B.20}$$

$$P_n^{(2)} = \frac{H_n'(x_0) J_n(x_1)}{\sqrt{1-\mu_i^2}} \tag{B.21}$$

$$M_n^{(1)} = \frac{J_n(x_0) J_n'(x_1)}{\sqrt{\varepsilon_r - \mu_i^2}} \tag{B.22}$$

$$M_n^{(2)} = \frac{J_n'(x_0) J_n(x_1)}{\sqrt{1-\mu_i^2}} \tag{B.23}$$

and k_0 is the freespace wavenumber, $2a$ is the trunk diameter, and ε_r is the relative dielectric constant of the trunk. Also, $J_n(x)$ is the Bessel function of the first kind n^{th} order, and $H_n(x)$ is the Hankel function of the first kind n^{th} order: $H_n(x) = H_n^{(1)}(x) = J_n(x) + iY_n(x)$. Thus,

$$\mathbf{P}_t'(\mu_s, \mu_i, \phi_\Delta) = \frac{1-\mu_s^2}{1-\mu_i^2} \sum_{n=0}^{\infty} \tilde{\mathbf{P}}_{tc}'(\mu_i; n) \cos n\phi_\Delta + \tilde{\mathbf{P}}_{ts}'(\mu_i; n) \sin n\phi_\Delta \tag{B.24}$$

where

$$\tilde{\mathbf{P}}_{tc}'(\mu; n) = \begin{bmatrix} |T_{vv}|_n^2 & |T_x|_n^2 & 0 & 0 \\ |T_x|_n^2 & |T_{hh}|_n^2 & 0 & 0 \\ 0 & 0 & \Re e\{T_{vv}T_{hh}^*\}_n - |T_x|_n^2 & -\Im m\{T_{vv}T_{hh}^*\}_n \\ 0 & 0 & \Im m\{T_{vv}T_{hh}^*\}_n & \Re e\{T_{vv}T_{hh}^*\}_n + |T_x|_n^2 \end{bmatrix} \tag{B.25}$$

$$\tilde{\mathbf{P}}_{ts}'(\mu; n) = \begin{bmatrix} 0 & 0 & -\Re e\{T_{vv}T_x^*\}_n & \Im m\{T_{vv}T_x^*\}_n \\ 0 & 0 & \Re e\{T_{hh}T_x^*\}_n & \Im m\{T_{hh}T_x^*\}_n \\ 2\Re e\{T_{vv}T_x^*\}_n & -2\Re e\{T_{hh}T_x^*\}_n & 0 & 0 \\ 2\Im m\{T_{vv}T_x^*\}_n & 2\Im m\{T_{hh}T_x^*\}_n & 0 & 0 \end{bmatrix} \tag{B.26}$$

and

$$|T_{vv}|_0^2 = \left|C_0^{TM}\right|^2 + 2\sum_{m=1}^{\infty}\left|C_m^{TM}\right|^2 \tag{B.27}$$

$$|T_{hh}|_0^2 = \left|C_0^{TE}\right|^2 + 2\sum_{m=1}^{\infty}\left|C_m^{TE}\right|^2 \tag{B.28}$$

$$(T_{vv}T_{hh}^*)_0 = C_0^{TM}C_0^{TE*} + 2\sum_{m=1}^{\infty} C_m^{TM}C_m^{TE*} \tag{B.29}$$

$$|T_x|_0^2 = 2\sum_{m=1}^{\infty}|C_m^x|^2 \tag{B.30}$$

$$|T_{vv}|_{n>0}^2 = 4\sum_{m=0}^{\infty}\Re e\{C_m^{TM}C_{n+m}^{TM*}\} + 2\sum_{m=1}^{n-1} C_m^{TM}C_{n-m}^{TM*} \tag{B.31}$$

$$|T_{hh}|_{n>0}^2 = 4\sum_{m=0}^{\infty}\Re e\{C_m^{TE}C_{n+m}^{TE*}\} + 2\sum_{m=1}^{n-1} C_m^{TE}C_{n-m}^{TE*} \tag{B.32}$$

$$(T_{vv}T_{hh}^*)_{n>0} = 2\sum_{m=0}^{\infty}\left(C_m^{TM}C_{n+m}^{TE*} + C_{n+m}^{TM}C_m^{TE*}\right) + 2\sum_{m=1}^{n-1} C_m^{TM}C_{n-m}^{TE*} \tag{B.33}$$

$$|T_x|_{n>0}^2 = 4\sum_{m=1}^{\infty}\Re e\{C_m^x C_{n+m}^{x*}\} - 2\sum_{m=1}^{n-1} C_m^x C_{n-m}^{x*} \tag{B.34}$$

$$(T_{vv}T_x^*)_{n>0} = -2\left(\sum_{m=1}^{\infty}\left(C_m^{TM}C_{n+m}^{x*} - C_{n+m}^{TM}C_m^{x*}\right) + \sum_{m=0}^{n-1} C_m^{TM}C_{n-m}^{x*}\right) \tag{B.35}$$

$$(T_{hh}T_x^*)_{n>0} = -2\left(\sum_{m=1}^{\infty}\left(C_m^{TE}C_{n+m}^{x*} - C_{n+m}^{TE}C_m^{x*}\right) + \sum_{m=0}^{n-1} C_m^{TE}C_{n-m}^{x*}\right) \tag{B.36}$$

B.2 Fourier Series Representation for Rough Ground

B.2.1 Physical Optics

The traditional (zeroth order) Physical Optics coherent scattering matrix and bistatic incoherent scattering matrix are

$$\mathbf{R}_{0PO}(\mu_i) = \begin{bmatrix} |R_v|^2 & 0 & 0 & 0 \\ 0 & |R_h|^2 & 0 & 0 \\ 0 & 0 & \Re e\{R_v R_h^*\} & -\Im m\{R_v R_h^*\} \\ 0 & 0 & \Im m\{R_v R_h^*\} & \Re e\{R_v R_h^*\} \end{bmatrix} e^{-(2k_0\sigma\mu_i)^2} \tag{B.37}$$

$$\mathbf{G}_{PO}(\mu_i, \mu_s, \phi_\Delta) = \begin{bmatrix} |a_{vv}|^2 & |a_{vh}|^2 & \cdots & \\ |a_{hv}|^2 & |a_{hh}|^2 & & \\ -2a_{vv}a_{hv}^* & 2a_{hh}a_{vh}^* & & \\ 0 & 0 & & \end{bmatrix}$$

$$\cdots \begin{bmatrix} \Re e\{a_{vv}a_{vh}^*\} & \Im m\{a_{vv}a_{vh}^*\} \\ -\Re e\{a_{hh}a_{hv}^*\} & -\Im m\{a_{hh}a_{hv}^*\} \\ \Re e\{a_{vv}a_{hh}^* - a_{vh}a_{hv}^*\} & -\Im m\{a_{vv}a_{hh}^* + a_{vh}a_{hv}^*\} \\ \Im m\{a_{vv}a_{hh}^* - a_{vh}a_{hv}^*\} & \Re e\{a_{vv}a_{hh}^* + a_{vh}a_{hv}^*\} \end{bmatrix}$$

$$\frac{1}{8\pi\mu_s} k_0^2 e^{-(k_0\sigma(\mu_i+\mu_s))^2} \int_0^\infty \left[e^{(k_0\sigma(\mu_i+\mu_s))^2\rho(\xi)} - 1 \right] J_0(\kappa_t\xi)\xi d\xi \tag{B.38}$$

where

$$a_{vv} = R_{v00}(\mu_i + \mu_s)\cos\phi_\Delta \tag{B.39}$$

$$a_{hv} = R_{v00}(1 + \mu_i\mu_s)\sin\phi_\Delta \tag{B.40}$$

$$a_{vh} = R_{h00}(1 + \mu_i\mu_s)\sin\phi_\Delta \tag{B.41}$$

$$a_{hh} = R_{h00}(\mu_i + \mu_s)\cos\phi_\Delta \tag{B.42}$$

$$\kappa_t = k_0\sqrt{\mu_i'^2 + \mu_s'^2 - 2\mu_i'\mu_s'\cos\phi_\Delta} \tag{B.43}$$

and

$$\mu_i' = \sqrt{1-\mu_i^2} = \sin\theta_i \tag{B.44}$$

$$\mu_s' = \sqrt{1-\mu_s^2} = \sin\theta_s \tag{B.45}$$

It is possible to analyze $\tilde{\mathbf{G}}^c$ and $\tilde{\mathbf{G}}^s$ using

$$\frac{1}{2\pi}\int_{2\pi}\sin m\phi_\Delta J_0(\kappa_t x)d\phi_\Delta = 0 \tag{B.46}$$

$$\frac{1}{2\pi}\int_{2\pi}\cos m\phi_\Delta J_0(\kappa_t x)d\phi_\Delta = J_m(k_0 x\mu_i')J_m(k_0 x\mu_s') \tag{B.47}$$

The result is:

$$\tilde{\mathbf{G}}^c(\mu_i,\mu_s;k=0)=\tfrac{1}{2}\Big(\tilde{\mathbf{G}}^{c1}\Phi_2(k_0\sigma,\rho,\mu_i,\mu_s)+\tilde{\mathbf{G}}^{c2}\Phi_0(k_0\sigma,\rho,\mu_i,\mu_s)\Big)e^{-(k_0\sigma(\mu_i+\mu_s))^2} \tag{B.48}$$

$$\tilde{\mathbf{G}}^c(\mu_i,\mu_s;k>0)=\tfrac{1}{2}\tilde{\mathbf{G}}^{c1}(\Phi_{k-2}(k_0\sigma,\rho,\mu_i,\mu_s)+\Phi_{k+2}(k_0\sigma,\rho,\mu_i,\mu_s))e^{-(k_0\sigma(\mu_i+\mu_s))^2}$$
$$+\tilde{\mathbf{G}}^{c2}\Phi_k(k_0\sigma,\rho,\mu_i,\mu_s)e^{-(k_0\sigma(\mu_i+\mu_s))^2} \tag{B.49}$$

$$\tilde{\mathbf{G}}^s(\mu_i,\mu_s;k)=\tfrac{1}{2}(\mu_i+\mu_s)(1+\mu_i\mu_s)\begin{bmatrix} 0 & 0 & \Re e\{R_vR_h^*\} & \Im m\{R_vR_h^*\} \\ 0 & 0 & -\Re e\{R_vR_h^*\} & \Im m\{R_vR_h^*\} \\ -2|R_v|^2 & 2|R_h|^2 & 0 & 0 \\ 0 & 0 & 0 & 0 \end{bmatrix}$$
$$(\Phi_{k-2}(k_0\sigma,\rho,\mu_i,\mu_s)-\Phi_{k+2}(k_0\sigma,\rho,\mu_i,\mu_s))e^{-(k_0\sigma(\mu_i+\mu_s))^2} \tag{B.50}$$

where

$$\tilde{\mathbf{G}}^{c1} = \begin{bmatrix} (\mu_i+\mu_s)^2|R_v|^2 & -(1+\mu_i\mu_s)^2|R_v|^2 & 0 & 0 \\ -(1+\mu_i\mu_s)^2|R_h|^2 & (\mu_i+\mu_s)^2|R_h|^2 & 0 & 0 \\ 0 & 0 & \Re e\{R_vR_h^*\}\mu^+ & -\Im m\{R_vR_h^*\}\mu^- \\ 0 & 0 & \Im m\{R_vR_h^*\}\mu^+ & \Re e\{R_vR_h^*\}\mu^- \end{bmatrix} \tag{B.51}$$

$$\tilde{\mathbf{G}}^{c2} = \begin{bmatrix} (\mu_i+\mu_s)^2|R_v|^2 & (1+\mu_i\mu_s)^2|R_v|^2 & 0 & 0 \\ (1+\mu_i\mu_s)^2|R_h|^2 & (\mu_i+\mu_s)^2|R_h|^2 & 0 & 0 \\ 0 & 0 & \Re e\{R_vR_h^*\}\mu^- & -\Im m\{R_vR_h^*\}\mu^+ \\ 0 & 0 & \Im m\{R_vR_h^*\}\mu^- & \Re e\{R_vR_h^*\}\mu^+ \end{bmatrix} \tag{B.52}$$

and

$$\mu^{\pm} = (\mu_i+\mu_s)^2 \pm (1+\mu_i\mu_s)^2 \tag{B.53}$$

$$\Phi_k(k_0\sigma,\rho,\mu_i,\mu_s) = \frac{k_0^2}{8\pi\mu_s}\int_0^{\infty}\left[e^{(k_0\sigma(\mu_i+\mu_s))^2\rho(\xi)}-1\right]J_k(k_0\xi\mu_i')J_k(k_0\xi\mu_s')\xi d\xi \tag{B.54}$$

for which, if the surface has a Gaussian correlation, ie. $\rho(\xi) = e^{-\xi^2/l^2}$,

$$\Phi_k^{Gaussian}(k_0\sigma,k_0l,\mu_i,\mu_s) = \frac{(k_0l)^2}{16\pi\mu_s}\sum_{i=1}^{\infty}\frac{(k_0\sigma(\mu_i+\mu_s))^{2i}}{i!i}I_k(x)e^{-x}e^{-(k_0l)^2(\mu'_i-\mu'_s)^2/4i} \tag{B.55}$$

where $x = (k_0l)^2\mu_i'\mu_s'/2i$.

B.2.2 Small Perturbation

For the Small Perturbation Method, the coherent reflectivity Mueller matrix is

$$\mathbf{R}_{0SP}(\mu_i) = \begin{bmatrix} \left|R_{v(SPM)}\right|^2 & 0 & 0 & 0 \\ 0 & \left|R_{h(SPM)}\right|^2 & 0 & 0 \\ 0 & 0 & \Re e\left\{R_{v(SPM)}R^*_{h(SPM)}\right\} & -\Im m\left\{R_{v(SPM)}R^*_{h(SPM)}\right\} \\ 0 & 0 & \Im m\left\{R_{v(SPM)}R^*_{h(SPM)}\right\} & \Re e\left\{R_{v(SPM)}R^*_{h(SPM)}\right\} \end{bmatrix} \tag{B.56}$$

where $R_{v,h(SPM)}$ are the vertical and horizontal Small Perturbation Fresnel reflection coefficients, respectively, are given by (2.85) and (2.86) above.

The first order scattering matrix correlation product (see (2.78)) is:

$$\left\langle S^{(1)}_{pq} S^{(1)*}_{mn} \right\rangle = 2\pi A_0 (k_0\sigma)^2 \mu_s^2 f_{pq} f^*_{mn} W(\kappa_x, \kappa_y) \tag{B.57}$$

$$G_{pqmn} = \frac{k_0^2}{4\pi\mu_s A_0} \left\langle S_{pq} S^*_{mn} \right\rangle \tag{B.58}$$

where the f_{pq} are the Small Perturbation scattering amplitudes and $W(\kappa_x, \kappa_y)$ is the surface spectral density given by (2.35).

Then, the Small Perturbation bistatic incoherent scattering matrix is

$$\mathbf{G}_{SP}(\mu_s,\mu_i,\phi_\Delta) = \left[\begin{array}{cc} |f_{vv}|^2 & |f_{vh}|^2 \\ |f_{hv}|^2 & |f_{hh}|^2 \\ 2\Re e\{f_{vv}f_{hv}^*\} & 2\Re e\{f_{hh}f_{vh}^*\} \\ 2\Im m\{f_{vv}f_{hv}^*\} & -2\Im m\{f_{hh}f_{vh}^*\} \end{array}\right. \cdots$$

$$\cdots \left[\begin{array}{cc} \Re e\{f_{vv}f_{vh}^*\} & -\Im m\{f_{vv}f_{vh}^*\} \\ \Re e\{f_{hh}f_{hv}^*\} & \Im m\{f_{hh}f_{hv}^*\} \\ \Re e\{f_{vv}f_{hh}^* + f_{vh}f_{hv}^*\} & -\Im m\{f_{vv}f_{hh}^* - f_{vh}f_{hv}^*\} \\ \Im m\{f_{vv}f_{hh}^* + f_{vh}f_{hv}^*\} & \Re e\{f_{vv}f_{hh}^* - f_{vh}f_{hv}^*\} \end{array}\right]$$

$$\frac{(k\sigma)^2(kl)^2\mu_s}{2} e^{-k^2l^2(\sin^2\theta_i+\sin^2\theta_s)/4} e^{\frac{1}{2}k^2l^2\sin\theta_i\sin\theta_s\cos\phi_\Delta} \tag{B.59}$$

if we re-express the f's as:

$$f_{hh} = f_{hh0} + f_{hhc}\cos\phi_\Delta \tag{B.60}$$

$$f_{hv} = f_{hvs}\sin\phi_\Delta \tag{B.61}$$

$$f_{vh} = f_{vhs}\sin\phi_\Delta \tag{B.62}$$

$$f_{vv} = f_{vv0} + f_{vvc}\cos\phi_\Delta \tag{B.63}$$

with

$$f_{hh0} = \frac{-k\eta_r}{D_H}\frac{\mu_r - 1}{\mu_r}\sin\theta_i \sin\theta_s(1 + R_h) \tag{B.64}$$

$$f_{hhc} = \frac{k}{D_H}(\mu_r - 1)\cos\theta_i \cos\theta_{st}(1 - R_h) - \eta_r(\varepsilon_r - 1)(1 + R_h) \tag{B.65}$$

$$f_{hvs} = \frac{-k}{D_H}((\mu_r - 1)\cos\theta_{st}(1 + R_v) - \eta_r(\varepsilon_r - 1)\cos\theta_i(1 - R_v)) \tag{B.66}$$

$$f_{vhs} = \frac{-k}{D_V}((\mu_r - 1)\cos\theta_i(1 - R_h) - \eta_r(\varepsilon_r - 1)\cos\theta_{st}(1 + R_h)) \tag{B.67}$$

$$f_{vv0} = \frac{-k}{D_V}\frac{\varepsilon_r - 1}{\varepsilon_r}\sin\theta_i \sin\theta_s(1 + R_v) \tag{B.68}$$

$$f_{vvc} = \frac{-k}{D_V}((\mu_r - 1)(1 + R_v) - \eta_r(\varepsilon_r - 1)\cos\theta_i \cos\theta_{st}(1 - R_v)) \tag{B.69}$$

then we can express $\mathbf{G}_{SP}$ as follows:

$$\mathbf{G}_{SP}(\mu_s, \mu_i, \phi_\Delta) = \mathbf{G}_{SP}^{c0}(\mu_s, \mu_i) + \sum_{n=1}^{\infty} \mathbf{G}_{SP}^{cn}(\mu_s, \mu_i)\cos n\phi_\Delta + \mathbf{G}_{SP}^{sn}(\mu_s, \mu_i)\sin n\phi_\Delta \tag{B.70}$$

where

$$\mathbf{G}_{SP}^{c0}(\mu_s,\mu_i) = \tfrac{1}{2}K\left(\mathbf{G}_{SP}^{c(0)}I_0(x) + 2\mathbf{G}_{SP}^{c(1)}I_1(x) + \mathbf{G}_{SP}^{c(2)}I_2(x)\right) \tag{B.71}$$

$$\mathbf{G}_{SP}^{c1}(\mu_s,\mu_i) = K\left(\mathbf{G}_{SP}^{c(0)}I_1(x) + \mathbf{G}_{SP}^{c(1)}(I_0(x)+I_2(x)) + \mathbf{G}_{SP}^{c(2)}\frac{I_1(x)+I_3(x)}{2}\right) \tag{B.72}$$

$$\mathbf{G}_{SP}^{cn}(\mu_s,\mu_i) = K\left(\mathbf{G}_{SP}^{c(0)}I_n(x) + \mathbf{G}_{SP}^{c(1)}(I_{n-1}(x)+I_{n+1}(x)) + \mathbf{G}_{SP}^{c(2)}\frac{I_{n-2}(x)+I_{n+2}(x)}{2}\right) \tag{B.73}$$

$$\mathbf{G}_{SP}^{s0}(\mu_s,\mu_i) = 0 \tag{B.74}$$

$$\mathbf{G}_{SP}^{s1}(\mu_s,\mu_i) = K\left(\mathbf{G}_{SP}^{s(1)}(I_0(x)-I_2(x)) + \mathbf{G}_{SP}^{s(2)}\frac{I_1(x)-I_3(x)}{2}\right) \tag{B.75}$$

$$\mathbf{G}_{SP}^{sn}(\mu_s,\mu_i) = K\left(\mathbf{G}_{SP}^{s(1)}(I_{n-1}(x)-I_{n+1}(x)) + \mathbf{G}_{SP}^{s(2)}\frac{I_{n-2}(x)-I_{n+2}(x)}{2}\right) \tag{B.76}$$

and

$$x = \tfrac{1}{2}(kl)^2\mu_i'\mu_s' \tag{B.77}$$

$$K = \tfrac{1}{2}(k\sigma)^2(kl)^2\mu_s e^{-x}e^{-k^2l^2(\mu_i'-\mu_s')^2/4} \tag{B.78}$$

$$\mathbf{G}_{SP}^{c(0)} = \begin{bmatrix} 2|f_{vv0}|^2 + |f_{vvc}|^2 & |f_{vhs}|^2 & \cdots & 0 & 0 \\ |f_{hvs}|^2 & 2|f_{hh0}|^2 + |f_{hhc}|^2 & & 0 & 0 \\ 0 & 0 & \cdots & \Re e\{2f_{vv0}f_{hh0}^* + f_{vvc}f_{hhc}^* + f_{vhs}f_{hvs}^*\} & -\Im m\{2f_{vv0}f_{hh0}^* + f_{vvc}f_{hhc}^* - f_{vhs}f_{hvs}^*\} \\ 0 & 0 & & \Im m\{2f_{vv0}f_{hh0}^* + f_{vvc}f_{hhc}^* + f_{vhs}f_{hvs}^*\} & \Re e\{2f_{vv0}f_{hh0}^* + f_{vvc}f_{hhc}^* - f_{vhs}f_{hvs}^*\} \end{bmatrix} \tag{B.79}$$

$$\mathbf{G}_{SP}^{c(1)} = \begin{bmatrix} 2\Re e\{f_{vv0}f_{vvc}^*\} & 0 & \cdots & 0 & 0 \\ 0 & 2\Re e\{f_{hh0}f_{hhc}^*\} & & 0 & 0 \\ 0 & 0 & \cdots & \Re e\{f_{vv0}f_{hhc}^* + f_{vvc}f_{hh0}^*\} & -\Im m\{f_{vv0}f_{hhc}^* + f_{vvc}f_{hh0}^*\} \\ 0 & 0 & & \Im m\{f_{vv0}f_{hhc}^* + f_{vvc}f_{hh0}^*\} & \Re e\{f_{vv0}f_{hhc}^* + f_{vvc}f_{hh0}^*\} \end{bmatrix} \tag{B.80}$$

$$\mathbf{G}_{SP}^{c(2)} = \begin{bmatrix} |f_{vvc}|^2 & -|f_{vhs}|^2 & 0 & 0 \\ -|f_{hvs}|^2 & |f_{hhc}|^2 & 0 & 0 \\ 0 & 0 & \Re e\{f_{vvc}f_{hhc}^* - f_{vhs}f_{hvs}^*\} & -\Im m\{f_{vvc}f_{hhc}^* + f_{vhs}f_{hvs}^*\} \\ 0 & 0 & \Im m\{f_{vvc}f_{hhc}^* - f_{vhs}f_{hvs}^*\} & \Re e\{f_{vvc}f_{hhc}^* + f_{vhs}f_{hvs}^*\} \end{bmatrix} \tag{B.81}$$

$$\mathbf{G}_{SP}^{s(1)} = \begin{bmatrix} 0 & 0 & \Re e\{f_{vv0}f_{vhs}^*\} & -\Im m\{f_{vv0}f_{vhs}^*\} \\ 0 & 0 & \Re e\{f_{hh0}f_{hvs}^*\} & \Im m\{f_{hh0}f_{hvs}^*\} \\ 2\Re e\{f_{vv0}f_{hvs}^*\} & 2\Re e\{f_{hh0}f_{vhs}^*\} & 0 & 0 \\ 2\Im m\{f_{vv0}f_{hvs}^*\} & 2\Im m\{f_{hh0}f_{vhs}^*\} & 0 & 0 \end{bmatrix} \tag{B.82}$$

$$\mathbf{G}_{SP}^{s(2)} = \begin{bmatrix} 0 & 0 & \Re e\{f_{vvc}f_{vhs}^*\} & -\Im m\{f_{vvc}f_{vhs}^*\} \\ 0 & 0 & \Re e\{f_{hhc}f_{hvs}^*\} & \Im m\{f_{hhc}f_{hvs}^*\} \\ 2\Re e\{f_{vvc}f_{hvs}^*\} & 2\Re e\{f_{hhc}f_{vhs}^*\} & 0 & 0 \\ 2\Im m\{f_{vvc}f_{hvs}^*\} & 2\Im m\{f_{hhc}f_{vhs}^*\} & 0 & 0 \end{bmatrix} \tag{B.83}$$

BIBLIOGRAPHY

[1] R. T. Austin, *Electromagnetic Wave Scattering by Power-Law Surfaces*, PhD dissertation, University of Michigan, Ann Arbor, 1994.

[2] C. Baylard, J.-J. Greffet, and A. A. Maradudin, "Coherent reflection factor of a random rough surface: applications," *Journal of the Optical Society of America A*, vol. 10, pp. 2637–2647, December 1993.

[3] P. Beckmann and A. Spizzichino, *The Scattering of Electromagnetic Waves from Rough Surfaces*, Pergamon Press, Oxford, 1963.

[4] C. F. Bohren and D. R. Huffman, *Absorbtion and Scattering of Light by Small Particles*, Wiley-Interscience, New York, 1983.

[5] S. L. Broschat, *Numerical Studies of the Phase Perturbation Technique for Random Rough Surface Scattering*, PhD dissertation, University of Washington, Seattle, January 1989.

[6] G. S. Brown, "A comparison of approximate theories for scattering from rough surfaces," *Wave Motion*, vol. 7, pp. 195–205, 1985.

[7] K. S. Chen and A. K. Fung, "An iterative approach to surface scattering simulation," in *Digest*, IEEE International Geoscience and Remote Sensing Symposium (IGARSS '90), pp. 405–408, College Park, MD, 1990.

[8] M. F. Chen and A. K. Fung, "A numerical study of the regions of validity of the Kirchhoff and small-perturbation rough surface scattering models," *Radio Science*, vol. 23, no. 2, pp. 163–170, March 1988.

[9] R. L. Cosgriff, W. H. Peake, and R. C. Taylor, "Terrain scattering properties for sensor system design," Technical Report 181, Ohio State University, 1960.

[10] W. B. Davenport and W. L. Root, *Random Signals and Noise*, McGraw-Hill, New York, 1958.

[11] R. D. De Roo and F. T. Ulaby, "Bistatic specular scattering from rough dielectric surfaces," *IEEE Transactions on Antennas and Propagation*, vol. 42, no. 2, pp. 220–231, February 1994.

[12] R. D. De Roo and F. T. Ulaby, "Authors' reply to comments on bistatic specular scattering from rough dielectric surfaces," *IEEE Transactions on Antennas and Propagation*, vol. 43, no. 2, pp. 225–226, February 1995.

[13] H. J. Eom and W. M. Boerner, "Rough surface incoherent backscattering of a spherical wave," *IEICE Transactions*, vol. E 74, pp. 105–108, January 1991.

[14] A. K. Fung, "On depolarization of electromagnetic waves backscattered from a rough surface," *Planetary Space Science*, vol. 14, pp. 563–568, 1966.

[15] A. K. Fung, *Microwave Scattering and Emission Models and Applications*, Artech House, Norwood, MA, 1993.

[16] A. K. Fung and H. J. Eom, "Multiple scattering and depolarization by a randomly rough Kirchhoff surface," *IEEE Transactions on Antennas and Propagation*, vol. 29, pp. 463–471, May 1981.

[17] A. K. Fung and H. J. Eom, "Coherent scattering of a spherical wave from an irregular surface," *IEEE Transactions on Antennas and Propagation*, vol. 31, pp. 68–72, January 1983.

[18] A. K. Fung and G. W. Pan, "A scattering model for perfectly conducting random surfaces I. model developement," *International Journal of Remote Sensing*, vol. 8, no. 11, pp. 1579–1593, November 1987.

[19] I. S. Gradshteyn and I. M. Ryzhik, *Table of Integrals, Series, and Products*, Academic Press, New York, fourth edition, 1980.

[20] J.-J. Greffet, "Theoretical model of the shift of the Brewster angle on a rough surface," *Optics Letters*, vol. 17, no. 4, pp. 238–240, February 1992.

[21] J. A. Holzer and C. C. Sung, "Scattering of electromagnetic waves from a rough surface. II," *Journal of Applied Physics*, vol. 49, no. 3, pp. 1002–1011, March 1978.

[22] A. Ishimaru and J. S. Chen, "Scattering from very rough surfaces based on the modified second-order Kirchhoff approximation with angular and propagation shadowing," *Journal of the Acoustical Society of America*, vol. 88, no. 4, pp. 1877–1883, 1990.

[23] K. Ivanova, M. A. Michalev, and O. I. Yordanov, "Study of the phase perturbation technique for scattering of waves by rough surfaces at intermediate and large values of the roughness parameter," *Journal of Electromagnetic Waves and Applications*, vol. 4, no. 5, pp. 401–414, 1990.

[24] D. R. Jackson, D. P. Winebrenner, and A. Ishimaru, "Comparison of perturbation theories for rough-surface scattering," *Journal of the Acoustical Society of America*, vol. 83, pp. 961–969, 1988.

[25] D. Kähny, K. Schmitt, and W. Wiesbeck, "Calibration of bistatic polarimetric radar systems," *IEEE Transactions on Geoscience and Remote Sensing*, vol. 30, no. 5, pp. 847–852, September 1992.

[26] T. Kojima, "Scattering of Hermite-Gaussian beams from an irregular surface," *Journal of Applied Physics*, vol. 65, no. 4, pp. 1424–1428, February 1989.

[27] J. C. Leader, "Bidirectional scattering of electromagnetic waves from rough surfaces," *Journal of Applied Physics*, vol. 42, no. 12, pp. 4808–4816, November 1971.

[28] J. C. Leader and W. A. J. Dalton, "Bidirectional scattering of electromagnetic waves from the volume of dielectric materials," *Journal of Applied Physics*, vol. 43, no. 7, pp. 3080–3090, July 1972.

[29] E. R. Mendez and K. A. O'Donnell, "Observation of depolarization and backscattering enhancement in light scattering from Gaussian random surfaces," *Optics Communications*, vol. 61, no. 2, pp. 91–95, January 1987.

[30] M. Nieto-Vesperinas, "Depolarization of electromagnetic waves scattered from slightly rough random surfaces: a study by means of the exinction theorem," *Journal of the Optical Society of America*, vol. 72, no. 5, pp. 539–547, 1982.

[31] K. A. O'Donnell and E. R. Mendez, "Experimental study of scattering from characterized random surfaces," *Journal of the Optical Society of America*, vol. 4, no. 7, pp. 1194–1205, July 1987.

[32] P. Phu, A. Ishimaru, Y. Kuga, and J. S. Chen, "Millimeter wave experiments on the scattering of electromagnetic waves from one-dimensional very rough surfaces,".

[33] S. O. Rice, "Reflection of electromagnetic waves from slightly rough surfaces," *Communications in Pure and Applied Mathematics*, vol. 4, pp. 351–378, 1951.

[34] G. T. Ruck, D. E. Barrick, W. D. Stuart, and C. K. Krichbaum, *Radar Cross Section Handbook*, volume 1, Plenum Press, New York, 1970.

[35] M. Saillard and D. Maystre, "Scattering from metallic and dielectric rough surfaces," *Journal of the Optical Society of America A*, vol. 7, no. 6, pp. 982–990, June 1990.

[36] K. Sarabandi, *Electromagnetic Scattering from Vegetation Canopies*, PhD dissertation, University of Michigan, Ann Arbor, 1989.

[37] K. Sarabandi and F. T. Ulaby, "A convenient technique for polarimetric calibration of single-antenna radar systems," *IEEE Transactions on Geoscience and Remote Sensing*, vol. 28, no. 6, pp. 1022–1033, November 1990.

[38] K. Sarabandi, F. T. Ulaby, and M. A. Tassoudji, "Calibration of polarimetric radar systems with good polarization isolation," *IEEE Transactions on Geoscience and Remote Sensing*, vol. 28, no. 1, pp. 70–75, January 1990.

[39] S. Silver, *Microwave Antenna Theory and Design*, volume M. I. T. Radiation Lab, Series 12, McGraw-Hill, New York, 1947.

[40] J. A. Stratton, *Electromagnetic Theory*, pp. 464–469, McGraw-Hill, New York, 1941.

[41] C. C. Sung and J. A. Holzer, "Scattering of electromagnetic waves from a rough surface," *Applied Physics Letters*, vol. 28, no. 8, pp. 429–431, April 1976.

[42] E. I. Thorsos, "The validity of the Kirchhoff approximation for rough surface scattering using a Gaussian roughness spectrum," *Journal of the Acoustical Society of America*, vol. 83, no. 1, pp. 78–92, January 1988.

[43] E. I. Thorsos, "Acoustic scattering from a Pierson-Moskowitz sea surface," *Journal of the Acoustical Society of America*, vol. 88, pp. 335–349, July 1990.

[44] E. I. Thorsos and D. R. Jackson, "The validity of the perturbation approximation for rough surface scattering using a Gaussian roughness spectrum," *Journal of the Acoustical Society of America*, vol. 86, pp. 261–277, July 1989.

[45] L. Tsang, *Private Communication*, Sep 1994.

[46] L. Tsang, J. A. Kong, and R. T. Shin, *Theory of Microwave Remote Sensing*, Wiley-Interscience, New York, 1985.

[47] F. T. Ulaby and E. C. Elachi, *Radar Polarimetry for Geoscience Applications*, Artech House, Norwood, MA, 1990.

[48] F. T. Ulaby, R. K. Moore, and A. K. Fung, *Microwave Remote Sensing: Active and Passive*, volume 2, Addison-Wesley, Reading, MA, 1982.

[49] F. T. Ulaby, R. K. Moore, and A. K. Fung, *Microwave Remote Sensing: Active and Passive*, volume 3, Artech House, Norwood, MA, 1986.

[50] F. T. Ulaby, T. F. Haddock, and M. E. Coluzzi, "Millimeter-wave bistatic radar measurements of sand and gravel," in *Digest*, IEEE International Geoscience and Remote Sensing Symposium (IGARSS '87), pp. 281–286, Ann Arbor, MI, May 1987.

[51] F. T. Ulaby, K. Sarabandi, K. C. McDonald, M. Whitt, and M. C. Dobson, "Michigan Microwave Canopy Scattering Model (MIMICS)," Technical Report 022486-T-1, The University of Michigan, Ann Arbor, MI, 1988.

[52] G. R. Valenzuela, "Depolarization of EM waves by slightly rough surfaces," *IEEE Transactions on Antennas and Propagation*, vol. 15, pp. 552–557, 1967.

[53] M. W. Whitt and F. T. Ulaby, "A general polarimetric radar calibration technique: Theory and experiment," *IEEE Transactions on Antennas and Propagation*, vol. 39, no. 1, pp. 62–67, January 1991.